



12-1991

## **A Fourier-transform method to measure concentration during solidification of a transparent metal model**

Mary E. Magnani

Follow this and additional works at: [https://trace.tennessee.edu/utk\\_gradthes](https://trace.tennessee.edu/utk_gradthes)

---

### **Recommended Citation**

Magnani, Mary E., "A Fourier-transform method to measure concentration during solidification of a transparent metal model. " Master's Thesis, University of Tennessee, 1991.  
[https://trace.tennessee.edu/utk\\_gradthes/12467](https://trace.tennessee.edu/utk_gradthes/12467)

This Thesis is brought to you for free and open access by the Graduate School at TRACE: Tennessee Research and Creative Exchange. It has been accepted for inclusion in Masters Theses by an authorized administrator of TRACE: Tennessee Research and Creative Exchange. For more information, please contact [trace@utk.edu](mailto:trace@utk.edu).

To the Graduate Council:

I am submitting herewith a thesis written by Mary E. Magnani entitled "A Fourier-transform method to measure concentration during solidification of a transparent metal model." I have examined the final electronic copy of this thesis for form and content and recommend that it be accepted in partial fulfillment of the requirements for the degree of Master of Science, with a major in Engineering Science.

Mary Helen McCay, Major Professor

We have read this thesis and recommend its acceptance:

Monty Smith, Dwayne McCay

Accepted for the Council:

Carolyn R. Hodges

Vice Provost and Dean of the Graduate School

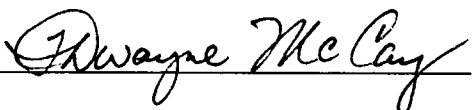

(Original signatures are on file with official student records.)

To the Graduate Council:

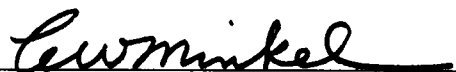
I am submitting herewith a thesis written by Mary E. Magnani entitled "A Fourier-transform Method to Measure Concentration during Solidification of a Transparent Metal Model." I have examined the final copy of this thesis for form and content and recommend that it be accepted in partial fulfillment of the requirements for the degree of Master of Science, with a major in Engineering Science and Mechanics.

  
\_\_\_\_\_  
Mary Helen McCay, Major Professor

We have read this thesis  
and recommend its acceptance:

  
\_\_\_\_\_  
  
\_\_\_\_\_

Accepted for the Council:

  
\_\_\_\_\_  
Associate Vice Chancellor  
and Dean of The Graduate School

## STATEMENT OF PERMISSION TO USE

In presenting this thesis in partial fulfillment of the requirements for a Master's degree at The University of Tennessee, Knoxville, I agree that the Library shall make it available to borrowers under rules of the Library. Brief quotations from this thesis are allowable without special permission, provided that accurate acknowledgment of the source is made.

Permission for extensive quotation from or reproduction of this thesis may be granted by my major professor, or in her absence, by the Head of Interlibrary Services when, in the opinion of either, the proposed use of the material is for scholarly purposes. Any copying or use of the material in this thesis for financial gain shall not be allowed without my written permission.

Signature Mary E. Magnani  
Date December 1991



A FOURIER-TRANSFORM METHOD TO MEASURE CONCENTRATION  
DURING SOLIDIFICATION OF A TRANSPARENT METAL MODEL

A Thesis

Presented for the

Master of Science

Degree

The University of Tennessee, Knoxville

Mary E. Magnani

December 1991

Dedicated to my parents,

John and Susan Yesko

## ACKNOWLEDGMENTS

I would like to thank the members of my thesis committee, Mary Helen McCay, Monty Smith, and Dwayne McCay, for reviewing this research and for giving me the opportunity to work on NASA's Casting and Solidification Technology (CAST) contract. Dr. Smith suggested the application of the Fourier-transform method to solidification work.

Bob Owen of Owen Research, Boulder, Colorado, provided consulting services regarding CAST holography. Dave McIntosh recorded and developed CAST holograms at the Holographic Ground System at NASA Marshall Space Flight Center in Huntsville, Alabama.

The staff of the University of Tennessee Space Institute (UTSI) Library, headed by Mary Lo, were extremely helpful to me as I reviewed the literature.

Many staff personnel from the Center for Laser Applications provided technical and administrative assistance during my two years at UTSI. These include Mike Sharp, Fred Schwartz, Newton Wright, Bruce Hill, Chris Parigger, Mary Helen Brittain, Melissa Weatherford, and Dee Robinette.

My graduate school expenses were partially funded by the Amelia Earhart Fellowship awarded to me by Zonta International, Chicago, Illinois, a women's service organization. Additional financial support came from graduate research assistantships sponsored by UTSI and NASA contract NAS8-37292.

Special thanks go to my coworkers on the CAST project: Jim Goodman, Sam Lowry, Ken Shasteen, Jessica Gass, and John Hopkins. I am especially

grateful to John for teaching me about solidification, for guiding much of my work, and for his support, encouragement, and friendship.

I would like to thank the members of my family, Jack and Sue Yesko, John Yesko, and Patti Yesko, for their love and support throughout my life.

Most of all, I would like to thank my husband Steve Magnani, for his love, support, and encouragement, for keeping me sane, making me laugh, and reminding me what is really important.

Mary E. Magnani  
November, 1991  
Tullahoma, Tennessee

## ABSTRACT

A 1-D implementation of the Fourier-transform method of fringe pattern analysis was designed to measure phase and concentration changes that take place in the diffusion layer during vertical directional solidification of the metal model material, ammonium chloride and water. Fringe patterns were acquired with the laser optical techniques of interferometry and holographic interferometry.

The Fourier-transform method uses Fourier domain processing to decode phase from a pattern of tilt fringes. Manual fringe location is bypassed, and outside information regarding phase is not required. Unlike intensity techniques, the Fourier-transform method filters unwanted irradiance variations and produces a complete phase field. The Fourier-transform method is more automated than many intensity methods. FORTRAN programs written for this project featured the use of a Hanning window for lowpass filtering, accurate determination of the carrier frequency, phase-unwrapping via a recurrence relationship, and base phase subtraction.

Phase and concentration plots of the expected form were produced with the Fourier-transform method. Consistent results were obtained for similar experimental conditions, and the method performed well in comparison with an intensity method. The Fourier-transform method will be used to analyze holograms for an upcoming microgravity flight experiment. The method was successfully applied to fringe patterns produced with holographic interferometry, but poor fringe visibility led to significant noise in the output.

## TABLE OF CONTENTS

Chapter 1: Introduction	1
Chapter 2: Measuring Concentration during Solidification	3
Solidification of Metal Alloys	3
Experimental Measurement of Concentration	10
Chapter 3: The Fourier-transform Method of Fringe Pattern Analysis	21
The Fringe Pattern	21
Techniques of Fringe Pattern Analysis	24
The Fourier-transform Method	32
Enhancements to the Fourier-transform Method	40
Other Versions of the Fourier-transform Method	55
Evaluation of the Fourier-transform Method	60
Chapter 4: Methods	67
Solidification	67
Interferometry	76
Holographic Interferometry	79
Image Translation	89
Fourier-transform Method to Measure Concentration	89
1-D Processing	140
Consistency	143
Comparison with Intensity Methods	144
Base Phase Subtraction	146
Application: Holographic Interferometry	147
Chapter 5: Results	149
1-D Processing	149
Consistency	149
Comparison with Intensity Methods	154
Base Phase Subtraction	160
Application: Holographic Interferometry	168
Discussion of Problems	168
Overall Results	173

Chapter 6: Conclusions	176
Discussion	176
Recommendations	178
List of References	180
Appendices	183
Appendix 1: The Discrete Fourier Transform	184
Appendix 2: Equipment Lists	187
Appendix 3: Program GET_COL	196
Appendix 4: Program CARRIER1	200
Appendix 5: Program CARRIER2	210
Appendix 6: Program AUTO1	229
Appendix 7: Program AUTO2	234
Appendix 8: Program CONCEN1	245
Appendix 9: Program CONCEN2	254
Appendix 10: Raw Data	262
Vita	275

## LIST OF FIGURES

Figure	Page
Figure 1. Typical phase diagram of a metal alloy composed of constituents A and B.	4
Figure 2. Typical density profile during vertical directional solidification of a superalloy.	6
Figure 3. Skeletonizing a fringe pattern.	19
Figure 4. Sketch of a Mach-Zehnder interferometer.	23
Figure 5. Techniques of fringe pattern analysis.	25
Figure 6. Steps in the Fourier-transform procedure. Magnitude of the Fourier transform versus frequency. a) FFT. b) Filter. c) Translate.	35
Figure 7. Phase-unwrapping.	37
Figure 8. Digitization of data leading to an error in the carrier frequency.	49
Figure 9. Typical characteristic curve, illustrating nonlinear film response.	54
Figure 10. Overlap of spectra that are not bandlimited.	62
Figure 11. Scale drawing of the quartz cuvette (Part 1, schematic).	69
Figure 12. Scale drawing of the quartz cuvette (Part 2, specifications).	70
Figure 13. The cuvette assembly. Adapted from [12].	71
Figure 14. Scale drawing of the cuvette assembly. [12]	72
Figure 15. Scale drawing of the copper plate slotted for a thermocouple.	73
Figure 16. The solidification control system. Adapted from [12].	75
Figure 17. Optics system for interferometry.	77



Figure 18. Optics system for holography at the Holographic Ground System. Adapted from [16].	80
Figure 19. Recording and reconstructing a hologram.	82
Figure 20. Optics system for holographic interferometry.	83
Figure 21. Scale drawing of the mount for the optical window.	85
Figure 22. Optical window etched for a vacuum line.	86
Figure 23. Alignment procedure for holographic reconstruction.	87
Figure 24. Flowchart for FORTRAN programs (Part 1).	91
Figure 25. Flowchart for FORTRAN programs (Part 2).	92
Figure 26. Slices of the images analyzed. a) The carrier image. b) The base image. c) The experimental image for Run 64 at 45 seconds.	95
Figure 27. Intensity for the carrier image, $g_c(y)$ vs. $y$ .	97
Figure 28. Fourier transform for the carrier image, $G_c(f)$ vs. $f$ .	99
Figure 29. Ideal lowpass filter for the carrier image, $I(f)$ vs. $f$ .	101
Figure 30. Inverse Fourier transform of ideal lowpass filter, for the carrier image, $i(y)$ vs. $y$ .	102
Figure 31. Hanning window for the carrier image, $h(y)$ vs. $y$ .	104
Figure 32. Inverse Fourier transform of filter modified by Hanning window, for carrier image, $j(y)$ vs. $y$ .	105
Figure 33. Filter modified by Hanning window, for the carrier image, $J(f)$ vs. $f$ .	106
Figure 34. Filtered Fourier transform for the carrier image, $C(f-f_0)$ vs. $f$ .	107

Figure 35. Phase, modulo $2\pi$ , for the carrier image, $\phi_c(y)$ vs. $y$ .	108
Figure 36. Phase for the carrier image, $\phi_c(y)$ vs. $y$ .	109
Figure 37. Intensity for the base image, $g_B(y)$ vs. $y$ .	111
Figure 38. Fourier transform for the base image, $G_B(f)$ vs. $f$ .	112
Figure 39. Ideal lowpass filter for the base image, $I(f)$ vs. $f$ .	114
Figure 40. Inverse Fourier transform of ideal lowpass filter, for the base image, $i(y)$ vs. $y$ .	115
Figure 41. Hanning window for the base image, $h(y)$ vs. $y$ .	116
Figure 42. Inverse Fourier transform of filter modified by Hanning window, for the base image, $j(y)$ vs. $y$ .	117
Figure 43. Filter modified by Hanning window, for the base image, $J(f)$ vs. $f$ .	118
Figure 44. Filtered Fourier transform for the base image, $C(f-f_0)$ vs. $f$ .	119
Figure 45. Phase for the base image, $\phi_B(y)$ vs. $y$ .	120
Figure 46. Intensity for the experimental image, $g_E(y)$ vs. $y$ .	122
Figure 47. Fourier transform for the experimental image, $G_E(f)$ vs. $f$ .	123
Figure 48. Ideal lowpass filter for the experimental image, $I(f)$ vs. $f$ .	125
Figure 49. Inverse Fourier transform of ideal lowpass filter, for the experimental image, $i(y)$ vs. $y$ .	126
Figure 50. Hanning window for the experimental image, $h(y)$ vs. $y$ .	127
Figure 51. Inverse Fourier transform of filter modified by Hanning window, for the experimental image, $j(y)$ vs. $y$ .	128

Figure 52. Filter modified by Hanning window, for the experimental image, $J(f)$ vs. $f$ .	129
Figure 53. Filtered Fourier transform for the experimental image, $C(f-f_0)$ vs. $f$ .	130
Figure 54. Phase for the experimental image, $[\phi_E(y) + \phi_B(y)]$ vs. $y$ .	131
Figure 55. Phase, $\phi_E(y)$ vs. $y$ .	132
Figure 56. Fringe pattern, $p(y)$ vs. $y$ .	134
Figure 57. Index of refraction, $n(y)$ vs. $y$ .	136
Figure 58. Index of refraction with temperature gradient removed, $n(y)$ vs. $y$ .	141
Figure 59. Concentration, $C(y)$ vs. $y$ .	142
Figure 60. Phase plot for adjacent columns.	150
Figure 61. Concentration plot for adjacent columns.	151
Figure 62. Phase plot for consistency check.	152
Figure 63. Concentration plot for consistency check.	153
Figure 64. a) Fourier-transform method at 45 sec. b) Intensity method at 45 sec. c) Fourier-transform method at 75 sec. d) Intensity method at 75 sec.	155
Figure 65. Concentration plot at 45 seconds, comparing three analytical methods.	157
Figure 66. Concentration plot at 75 seconds, comparing three analytical methods.	158
Figure 67. The base phase.	161

Figure 68. Phase plots produced with and without base phase subtraction.	162
Figure 69. Comparison of fringe patterns at 30 seconds, with and without base phase subtraction.	163
Figure 70. Comparison of fringe patterns at 55 seconds, with and without base phase subtraction.	164
Figure 71. Comparison of fringe patterns at 75 seconds, with and without base phase subtraction.	165
Figure 72. Concentration plots produced with and without base phase subtraction.	166
Figure 73. Phase plot for holographic interferometry.	169
Figure 74. Concentration plot for holographic interferometry.	170
Figure 75. Concentration plot for holographic interferometry, comparing Fourier-transform analysis with an intensity method.	171

## LIST OF SYMBOLS

a	Growth parameter (dimensionless)
a(x), a(y), a(x,y)	Background intensity (W/mm <sup>2</sup> )
a <sub>1</sub>	Fourier series coefficient
A	Solvent in a binary alloy
A(f)	Fourier transform of a(x)
A(f,y)	Fourier transform of a(x,y)
A(u,v)	Fourier transform of a(x,y)
A(x,y)	Amplitude of object beam (V/mm)
b(x), b(y), b(x,y)	Fringe visibility (W/mm <sup>2</sup> )
b <sub>1</sub>	Fourier series coefficient
B	Solute in a binary alloy
B(x,y)	Amplitude of reference beam (V/mm)
c(x)	1/2 b(x) exp [jϕ(x)] (W/mm <sup>2</sup> )
c(x,y)	1/2 b(x,y) exp [jϕ(x,y)] (W/mm <sup>2</sup> )
c*(x)	Complex conjugate of c(x) (W/mm <sup>2</sup> )
c*(x,y)	Complex conjugate of c(x,y) (W/mm <sup>2</sup> )
c <sub>1</sub> (x,y)	c(x,y) exp [2πjϕ(u <sub>0</sub> x + v <sub>0</sub> y)] (W/mm <sup>2</sup> )
c'(x,y)	c(x,y) with error in the carrier frequency (W/mm <sup>2</sup> )
c''(x,y)	Minimization function (W/mm <sup>2</sup> )
C, C(y)	Concentration (wt%)

$C(f-f_0)$	Fourier transform of $c(x)$
$C(f-f_0, y)$	Fourier transform of $c(x, y)$
$C(u-u_0, v-v_0)$	Fourier transform of $c(x, y)$
$C^*(f+f_0)$	Complex conjugate of $C(f-f_0)$
$C^*(f+f_0, y)$	Complex conjugate of $C(f-f_0, y)$
$C^*(u+u_0, v+v_0)$	Complex conjugate of $C(u-u_0, v-v_0)$
$C_L, C_L(x)$	Liquid concentration (wt%)
$C_{L1}$	Liquid concentration at temperature $T_1$ (wt%)
$C_{L2}$	Liquid concentration at temperature $T_2$ (wt%)
$C_1$	A specific concentration value (wt%)
$C_p$	Phase complexity measure
$C_{s1}$	Solid concentration at temperature $T_1$ (wt%)
$C_{s2}$	Solid concentration at temperature $T_2$ (wt%)
$C_T$	Concentration at dendrite tips (wt%)
$C_2$	A specific concentration value (wt%)
$C_0$	Bulk concentration (wt%)
$d$	Thickness of container for solidification (mm)
$d_1$	Fourier coefficient
$d_0$	Fourier coefficient
$D$	Diffusion coefficient of solid in the liquid (cm <sup>2</sup> /sec)
$D(x), D(x, y)$	Phase difference between adjacent points (rads)
$e_1$	Fourier coefficient
$E(x, y)$	Electric field (V/mm)

$f(x), f(x,y)$	A spatial function
$\Delta f_1, \Delta f_2$	Frequency shifts produced by Bragg cells (rads/sec)
$f_0$	Spatial carrier frequency (1/mm)
$F(u)$	Fourier transform of $f(x)$
$F(u,v)$	Fourier transform of $f(x,y)$
$g(x), g(y), g(x,y)$	Intensity ( $W/mm^2$ )
$g_B(y)$	Intensity of the base image ( $W/mm^2$ )
$g_C(y)$	Intensity of the carrier image ( $W/mm^2$ )
$g_N(x,y)$	Intensity of Nth interferogram ( $W/mm^2$ )
$g_1(x,y)$	Distorted intensity in region with no phase information ( $W/mm^2$ )
$g_2(x,y)$	Fringe pattern corrected for nonlinear film response ( $W/mm^2$ )
$G$	Temperature gradient ( $^{\circ}C/cm$ )
$G(f)$	Fourier transform of $g(x)$
$G(f,y)$	Fourier transform of $g(x,y)$
$G(u,v)$	Fourier transform of $g(x,y)$
$G_B(f)$	Fourier transform of $g_B(y)$
$G_C(f)$	Fourier transform of $g_C(y)$
$G_E(f)$	Fourier transform of $g_E(y)$
$h(y)$	Hanning window ( $W/mm^2$ )
$h(x,y)$	Nonlinear response of recording medium ( $W/mm^2$ )
$i(y)$	Ideal lowpass filter ( $W/mm^2$ )
$I(f)$	Fourier transform of $i(y)$
$j$	$(-1)^{1/2}$

$j(y)$	Ideal lowpass filter modified by Hanning window ( $W/mm^2$ )
$J(f)$	Fourier transform of $j(y)$
$\lambda$	Wavelength of light (mm)
$m_L$	Slope of the liquidus from the phase diagram ( $^{\circ}C/wt\%$ )
$M_1(x,y), M_2(x,y)$	Filtered intensity patterns in QMM method ( $W/mm^2$ )
$n, n(y)$	Index of refraction (dimensionless)
$n(x,y,z), n(T,C)$	Index of refraction (dimensionless)
$n(x)$	Signal-independent random additive noise ( $W/mm^2$ )
$n_C$	$1.63 \times 10^{-3}$ ( $1/wt\%$ )
$n_T$	$1.73 \times 10^{-4}$ ( $1/^{\circ}C$ )
$n_o$	1.3419 (dimensionless)
$N$	Number of pixels or elements
$p(y)$	Fringe pattern after Fourier processing ( $W/mm^2$ )
$\phi(x), \phi(x,y)$	Phase (rads)
$\phi_B(y)$	Phase change due to the cuvette walls (rads)
$\phi_C(y)$	Phase of the carrier image (rads)
$\phi_C(x), \phi_C(x,y)$	Continuous phase (rads)
$\phi_C^x(x,y)$	Continuous phase in the x direction (rads)
$\phi_D(x), \phi_D(x,y)$	Discontinuous phase (rads)
$\phi_E(y)$	Phase change due to the experiment (rads)
$\phi_{jump}$	Criterion for phase jump (rads)
$\phi_N$	Induced phase shift of Nth interferogram (rads)
$\phi_o(y)$	Phase of the object beam (rads)



$\phi_0(x), \phi_0(x,y)$	Offset phase (rads)
$\phi_0^x(x,y)$	Offset phase in x direction (rads)
$\phi_0^y(x,y)$	Offset phase in y direction (rads)
$\phi_1(x,y)$	Phase of $c_1(x,y)$ (rads)
$\phi'(x,y)$	$\phi(x,y)$ with error in the carrier frequency (rads)
$\phi_R(y)$	Phase of the reference beam (rads)
$r(x,y)$	Sinusoidal reference pattern (W/mm <sup>2</sup> )
R	Rate of movement of the interface (cm/sec)
$S_N$	Signal-to-noise ratio
$\sigma_N$	Standard deviation of $n(x)$
$\sigma_\phi$	Standard deviation of $\phi(x)$
t	Time (sec)
T, T(x)	Temperature (°C)
$T_L$	Initial melting temperature (°C)
$T_1$	A specific temperature value (°C)
$T_1$	Initial melting temperature during solidification of an alloy (°C)
$T_2$	A specific temperature value (°C)
$T_2$	Temperature during solidification of an alloy (°C)
$T_0$	Intercept in a linear temperature plot (°C)
u	Spatial frequency in the x direction (1/mm)
$u_E$	Positioning error in u (1/mm)
$u_E'$	Minimization parameter (1/mm)
$u_0$	Spatial carrier frequency in the x direction (1/mm)

$v$	Spatial frequency in the y direction (1/mm)
$v_E$	Positioning error in $v$ (1/mm)
$v_E'$	Minimization parameter (1/mm)
$v_0$	Spatial carrier frequency in the y direction (1/mm)
$x$	Distance from the solid-liquid interface (cm)

# CHAPTER 1

## INTRODUCTION

In the past decade researchers in the field of metal alloy solidification have turned to techniques based on laser optics. Although lasers cannot be used to study metal alloys directly, optical techniques such as interferometry and holography can be applied to study transparent "metal model" materials. In the metal model experiments, researchers vary the significant solidification parameters (e.g., growth rate, temperature gradient, etc.). Results are then related to the solidification of metals.

Early applications of optical techniques to metal model solidification yielded qualitative results. For example, schlieren filtering was applied to chronicle the general development of the diffusion layer. [1] More recent work relies on optical techniques that can produce quantitative results, such as the use of interferometry to measure concentration in the diffusion layer. [2] [3]

Interferometry produces a pattern of interference fringes which represent changes in the phase of the light travelling through a transparent object. Since phase changes can be related to changes in physical quantities such as concentration, fringe pattern analysis is a valuable quantitative tool. Current work in this field centers on the automation of fringe analysis.

In the same time frame that solidification researchers have experimented with laser optics, fringe analysis researchers have developed and refined an

automated analysis technique known as the Fourier-transform method. In this method, Fourier domain filtering decodes phase information from a fringe pattern. Unlike methods which calculate phase only at fringe extrema, the Fourier-transform method produces a complete field of phase information. The method is quick and accurate.

This project combined two trends: the use of laser optics to study metal models, and the use of the Fourier-transform method to analyze fringe patterns. A fringe pattern for the diffusion layer of a solidifying metal model was produced via interferometry, and computer programs were developed to process the fringes with the Fourier-transform method. The result was a continuous profile of concentration in the diffusion layer. The speed and accuracy of the method will give researchers additional flexibility in analyzing the results of solidification experiments. This Fourier-transform method will be used to analyze hundreds of holograms produced during an upcoming microgravity flight experiment. [4]

## CHAPTER 2

### MEASURING CONCENTRATION DURING SOLIDIFICATION

#### Solidification of Metal Alloys

During the solidification of an alloy composed of solvent A and solute B, solid and liquid concentrations vary with temperature, as represented by the alloy's phase diagram in Figure 1. Solution of initial solute concentration  $C_{L1}$  begins to freeze at temperature  $T_1$ , producing solid of concentration  $C_{S1}$  and liquid of concentration  $C_{L1}$ . Since the solute concentration of the solid material,  $C_{S1}$ , is less than the initial solute concentration  $C_{L1}$ , the balance of solute is rejected into the liquid ahead of the solid-liquid interface. A solute-rich boundary layer thus develops in front of the interface.

The solute concentration of the liquid in front of the interface is therefore higher than the solute concentration of the bulk liquid. The difference in concentration creates a concentration gradient, and diffusion of solute ahead of the interface is initiated. Diffusion is the process whereby particles tend to redistribute as a result of their random thermal motion, migrating from regions of high particle concentration into regions of low particle concentration. [5]

As the temperature is lowered to  $T_2$ , solidification continues, producing solid material of concentration  $C_{S2}$ , and liquid of concentration  $C_{L2}$  at the interface. The liquid concentration  $C_{L2}$  is higher than the concentration of the original liquid,  $C_{L1}$ , so diffusion continues. Solute concentration is highest directly

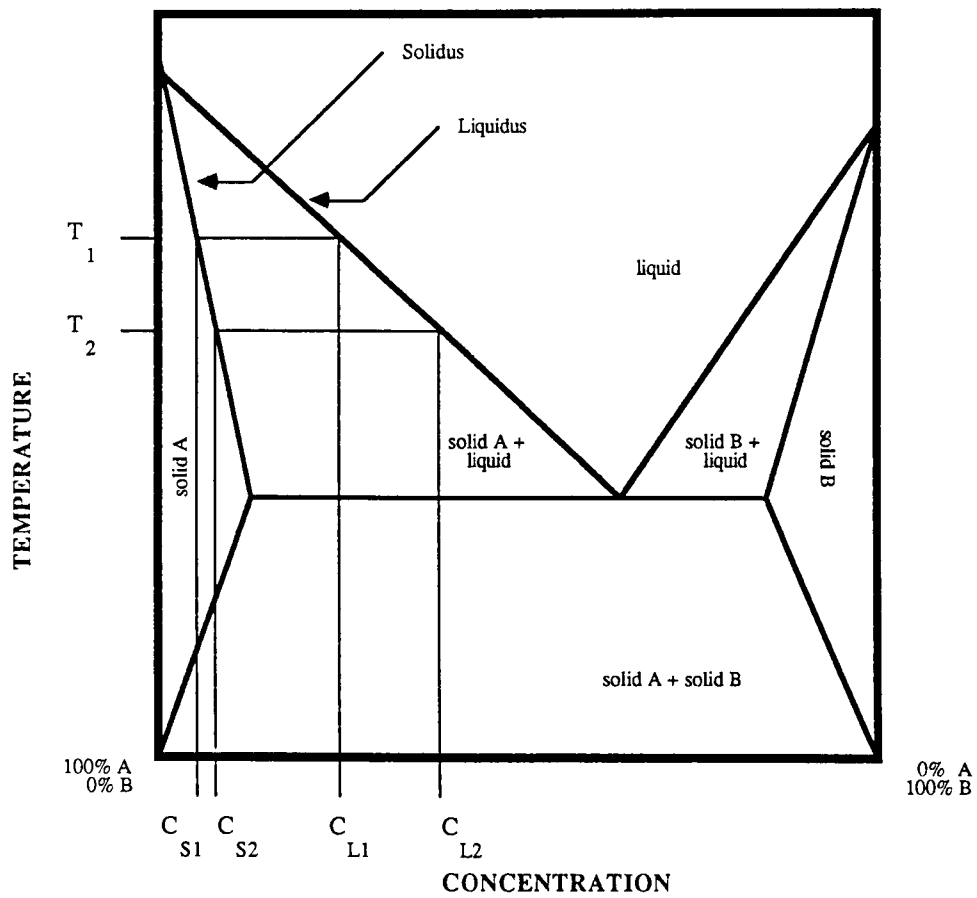


Figure 1. Typical phase diagram of a metal alloy composed of constituents A and B.

in front of the interface, decreasing exponentially until liquid of the bulk concentration is reached. The layer of solution adjacent to the interface, in which a concentration gradient exists, is known as the diffusion layer.

During vertical directional solidification, a positive temperature gradient is applied to a container. Because the temperature at the top of the container is warmer than that at the bottom, warm, less dense liquid sits on top of cooler, denser liquid. If the solute is less dense than the solvent, the liquid in the diffusion layer is lighter than the bulk liquid. Thus when solidification begins from the bottom of the container, a density inversion is created, and a region of maximum density develops. See Figure 2. The potential for buoyant flow exists; light liquid may plume upwards following a process called convective breakdown.

Many alloys solidify dendritically, that is, with a branched, treelike morphology. For steady state dendritic growth, solute distribution is given by: [6]

(Eq. 1.)

$$D \frac{d^2}{dx^2} (C_L) + R \frac{d}{dx} (C_L) = 0.$$

In this equation, D is the diffusion coefficient of solute in the liquid, x is the distance from the dendritic interface, and R is the rate of movement of the interface. The boundary conditions for this equation are:

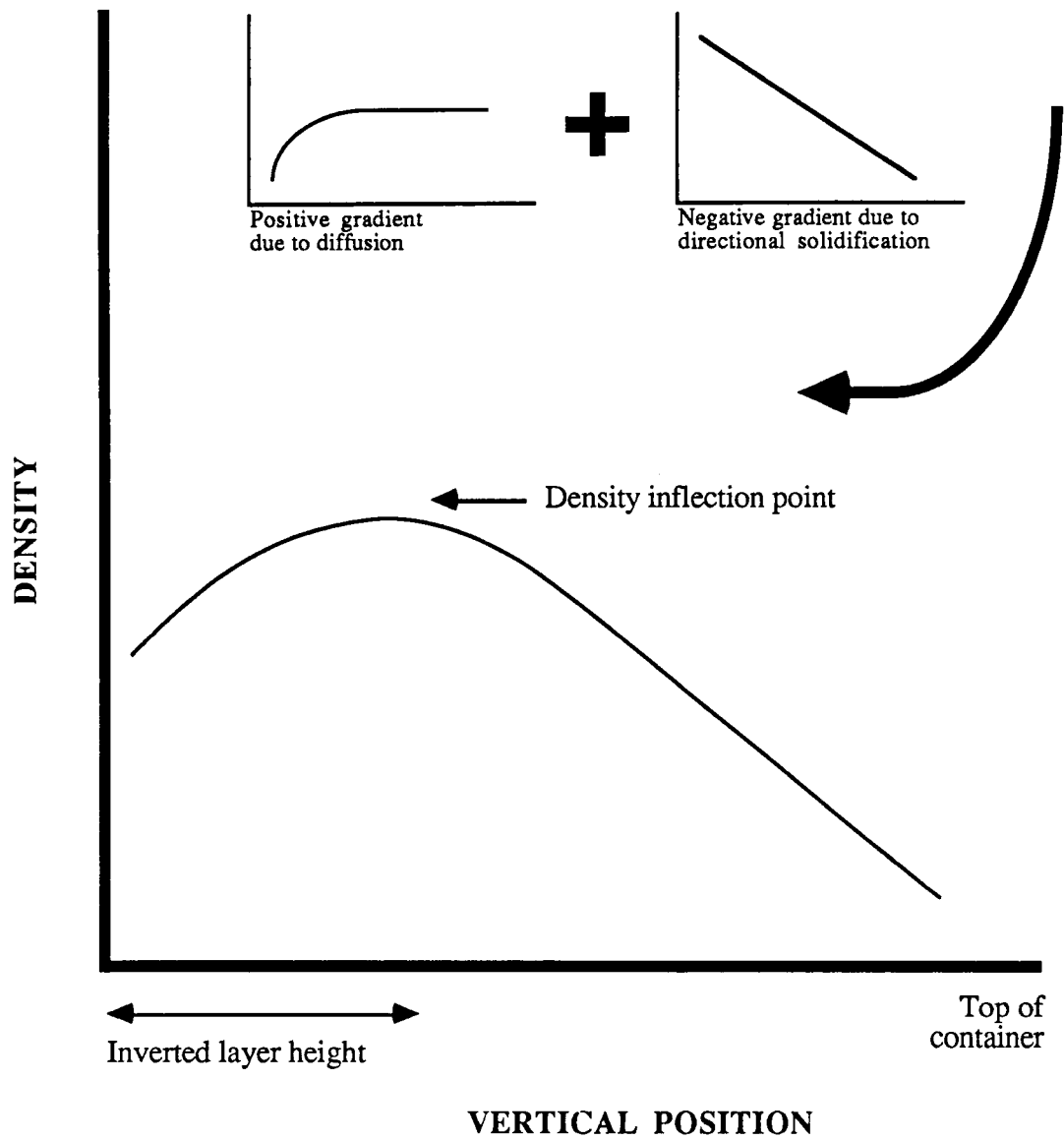


**Figure 2.** Typical density profile during vertical directional solidification of a superalloy.



(Eq. 2.)

$$C_L = C_T \text{ at } x = 0, \text{ and}$$

$$C_L = C_0 \text{ at } x = \text{infinity},$$

where  $C_T$  is the concentration at the dendrite tips, and  $C_0$  is the bulk concentration. A solution to Eq. 1 is:

(Eq. 3.)

$$C_L(x) = C_0 + (C_T - C_0) \exp(-Rx/D).$$

The solution is further specified by evaluating the tip concentration  $C_T$ , as follows. Under steady state conditions, solute conservation at the interface gives:

[6]

(Eq. 4.)

$$R(C_T - C_0) = -D \frac{d}{dx} (C_L)$$

It is assumed that the liquid at any fixed distance behind the dendrite tips is of uniform concentration, with liquid concentration given by the liquidus from the phase diagram. With the added requirement that the liquidus have constant slope  $m_L$ , this assumption leads to: [6]

(Eq. 5.)

$$C_L(x) - C_0 = 1/m_L [T(x) - T_L],$$

where T is the temperature. After differentiating with respect to x, and letting  $dT/dx = G$ , the thermal gradient, the concentration gradient is given by: [6]

(Eq. 6.)

$$\frac{d}{dx} (C_L) = G/m_L.$$

Combining Eq. 4 with Eq. 6 results in:

(Eq. 7.)

$$C_T = (1-a) C_0,$$

where  $a = -DG/m_L RC_0$ . After substituting Eq. 7 into Eq. 3, the solution to Eq. 1 is obtained:

(Eq. 8.)

$$C_L(x) = C_0 [1 - a \exp (-Rx/D)].$$

Steady state growth is not realizable for most growth rates of the metal model used in this project. [7] Therefore, the time-dependent form of Eq. 1 must

be used to determine the profile of the diffusion layer. The time-dependent form is: [6]

(Eq. 9.)

$$\frac{\partial C_L}{\partial t} = D \frac{\partial^2 (C_L)}{\partial x^2} + R \frac{\partial (C_L)}{\partial x}$$

An approximate solution to this equation has been obtained, but it is cumbersome. [6] A control volume approach [8] has also been employed to solve Eq. 9, [1] [2] [9] but it was necessary to use approximations to formulate a needed boundary condition for the tip concentration. Although a control volume approach has been developed to solve a version of Eq. 9 that includes convection, [10] this method requires significant computing resources.

Since concentration and temperature fields at the solid-liquid interface define the composition of the solidifying material, determination of these fields is an important aspect of solidification research. Models can provide significant information, but measurement of concentration during solidification experiments continues to be a valuable tool for researchers. In this project the Fourier-transform method of fringe pattern analysis was used to measure concentration in the diffusion layer of a solidifying metal model material. This approach builds upon the following history of experimental work.

## Experimental Measurement of Concentration

### Ammonium Chloride and Water

One technique for studying the concentration changes in the diffusion layer of a metal is to quench the solidifying interface, "freezing" solidification phenomena for later analysis. Although this technique works directly with the alloy of interest, the interface cannot be observed until a sample is sectioned and prepared. If the quench did not preserve the desired time, or if a time sequence is required, another experiment in the solidification furnace must be initiated.

Since metal model materials solidify like metal alloys, they can be used to study concentration changes during diffusion. The metal model material ammonium chloride and water ( $\text{NH}_4\text{Cl-H}_2\text{O}$ ) has a melting point range near room temperature, making it easier to handle than a molten metal. Like many metal alloys,  $\text{NH}_4\text{Cl-H}_2\text{O}$  solidifies dendritically. Since water is less dense than ammonium chloride, a density inversion develops during  $\text{NH}_4\text{Cl-H}_2\text{O}$  solidification.

Because  $\text{NH}_4\text{Cl-H}_2\text{O}$  is transparent, it can be studied with the techniques of laser optics. As laser light passes through a solidifying system, the entire solidification process can be recorded for later analysis. Optical techniques such as schlieren filtering can be used to process the light, revealing information that the unaided eye cannot see. Because  $\text{NH}_4\text{Cl-H}_2\text{O}$  has a high refractive index, it operates well in optical systems that measure changes in refractive index, such as interferometers. When solidification experiments are complete, the techniques of

digital image processing can be used to compare, enhance, and analyze the recorded images.

All of the following studies used the techniques of laser optics to observe solidifying  $\text{NH}_4\text{Cl-H}_2\text{O}$  systems. The studies differ in the specific optical technique applied, and in the emphasis placed on the diffusion layer and the measurement of concentration.

Johnston and Owen used interferometry to study the vertical solidification of  $\text{NH}_4\text{Cl-H}_2\text{O}$  in low gravity and at one-gravity. [11] Although they measured the thickness of the diffusion layer, solidification was not controlled precisely enough to study the details of the development of the layer. Rather, the concentration difference between the bulk liquid and a plume was measured. To accomplish this, it was noted that fringe patterns in the interferograms changed when temperature and concentration changed. A refractometer, which measures the index of refraction, was used to quantify these relationships. A one percent change in concentration led to a refractive index change of 0.00187, and a one degree Celsius change in temperature led to a refractive index change of 0.00012. The index of refraction changes depicted in a fringe pattern do not distinguish between concentration and temperature. To separate the two effects, measurements were not taken until plumes rose to an area of uniform temperature. In their study Johnston and Owen found that low gravity solidification produces more stable concentration profiles.

McCay and McCay studied the solidification of  $\text{NH}_4\text{Cl-H}_2\text{O}$  with the technique of schlieren filtering. [1] A highly controlled vertical directional

solidification apparatus allowed them to focus on the development of the inverted density layer. The schlieren technique highlighted the layer as a bright band. The thickness of the inverted layer was measured for several growth rates and temperature gradients, and the effects of solidification parameters on the layer were quantified. For example, a slower growth rate led to a thicker inverted density layer, due to an increased concentration of water immediately ahead of the interface. It was also found that pluming significantly decreased the width of the layer.

Gray continued to quantify the effects of solidification parameters on the inverted density layer, but the focus was convective breakdown. [12] [13] Density changes leading to breakdown were visualized with the central dark ground method. In this technique, a dark band or null layer appears at a region of constant index of refraction. In the solidification of  $\text{NH}_4\text{Cl-H}_2\text{O}$ , this region coincides with the region of maximum density, which forms the upper boundary of the inverted density layer. The height and thickness of the null layer were measured for several cooling rates and temperature gradients. Image processing techniques were introduced to solidification work in that video images were digitized, and measurements were taken with a cursor. It was found that the height of the null layer increased as solute built up. When the instability of the inverted density layer led to breakdown, flow occurred in an ordered fashion resembling Benard cells, which are axisymmetric, vortical, hexagonal rings. Following breakdown, the null layer fell, then reached an equilibrium height.

McCay et al. [14] further applied the central dark ground method to study  $\text{NH}_4\text{Cl-H}_2\text{O}$  solidification, measuring the height of the inverted density layer for a matrix of cooling rates, temperature gradients, and initial mushy zone heights. (The mushy zone is a two-phase region composed of solid and liquid components; see the region labelled "solid A + liquid" in Figure 1.) A digital image processor was again used to take measurements. A critical Rayleigh number that was a function of the initial mushy zone height was determined for the system. The Rayleigh number is a quantity used to characterize a system's potential for buoyancy driven flow; convective instability ensues at a critical value of the Rayleigh number.

Several aspects of this study by McCay et al. triggered their next experiments. In their discussion they returned to the idea that changes in temperature and concentration directly affect the index of refraction in a solidifying  $\text{NH}_4\text{Cl-H}_2\text{O}$  system. While Johnston and Owen [11] had quantified the separate relationships, the effect of temperature on index of refraction, and the effect of concentration on index of refraction, McCay et al. combined the two effects. The following equation, which shows the dependence of  $\text{NH}_4\text{Cl-H}_2\text{O}$  refractive index  $n$ , on temperature  $T$ , and concentration  $C$ , was presented:

(Eq. 10.)

$$n = 1.3822 - 1.73 \times 10^{-4}(T - 22^\circ\text{C}) + 1.63 \times 10^{-3}(C - 27.07\text{wt}\%).$$

This equation was not used to calculate concentration profiles. However, in recording the sequence of events in  $\text{NH}_4\text{Cl-H}_2\text{O}$  solidification, it was noted that concentration changes in the diffusion layer produced a refractive index fringe pattern.

In their next study McCay et al. set out to measure these concentration changes. [9] Fringe patterns produced by the central dark ground technique were analyzed to obtain concentration in the following way. Light passing through a solidifying system undergoes a phase shift due to temperature and concentration changes. If the thickness,  $d$ , of the container is thin, the phase shift  $\phi(x,y)$  is given by:

(Eq. 11.)

$$\phi(x,y) = 2\pi / \lambda \int_0^d n(x,y,z) dz.$$

In this expression, the light is travelling in the  $z$ -direction.  $\lambda$  is the wavelength of light, and  $n(x,y,z)$  is the index of refraction at point  $(x,y,z)$  in the container. Assuming that the index of refraction did not vary in the  $z$ -direction, the expression for the phase shift was simplified to:

(Eq. 12.)

$$\phi(x,y) = 2\pi dn(x,y) / \lambda .$$



After central dark ground processing, a camera recorded the intensity  $g(x,y)$  of the resulting fringe pattern:

(Eq. 13.)

$$g(x,y) = a(x,y) + b(x,y) \cos [\phi(x,y)],$$

where  $a(x,y)$  and  $b(x,y)$  are irradiance variations. The location of each fringe was noted, then a relative phase value was assigned such that the phase increased by  $2\pi$  for each fringe. Using Eq. 12, this field of phase values was converted to a field of refractive index values. Finally, index of refraction was converted to concentration with the help of Eq. 10. Since Eq. 10 requires temperature information, the temperature of the solidifying system was measured with thermocouples. The temperature information indicated by fringe spacing in the bulk liquid, where concentration was constant, was also used.

McCay et al. plotted concentration in the diffusion layer against the distance from the solidifying interface. Measured concentrations agreed well with numerical simulations, differing by no more than 0.004 wt%. Although the central dark ground method is a rugged technique, it was noted that the resulting fringes were less visible than interferometric fringes, leading to reduced accuracy.

In further efforts to measure concentration in the diffusion layer, Hopkins turned to the highly visible fringe patterns produced in Mach-Zehnder interferometry. [2] Discrete measurements of phase were converted to a refractive

index field, using the analysis discussed above. In order to isolate concentration in Eq. 10, temperature effects must be subtracted from the refractive index field. After thermocouples were used to verify the linearity of the temperature gradient within the solidifying system, a linear temperature gradient was subtracted. Although interferometry produced a more visible fringe pattern, it was noted that the process of fitting discrete phase values to a continuous curve still led to experimental uncertainty. Selection of fringe extrema is a subjective activity.

In continuing interferometric studies, [3] [7] error in the measured concentration was estimated to be 0.04 wt%. Several findings related to the diffusion layer were reported. Concentration was fit to an exponential form to extrapolate a tip concentration and to determine the characteristic diffusion parameter. Tip concentration was shown to increase linearly during diffusion dominated growth. Comparing tip concentrations predicted by steady state theory with the extrapolated values verified that steady state growth was not achieved.

In these studies further limitations of interferometry were noted, stemming from the low resolution of phase in conventional fringe patterns. Although phase changes began shortly after cooling was initiated, concentration fringes did not appear until 30 seconds after the start of the runs. Thus concentration profiles could not be determined before that time. Due to the limited resolution of fringe data, concentration measurements could not be made directly at the dendrite tips, so it was necessary to extrapolate tip concentrations.

The above studies are similar in that all used the techniques of laser optics to process the light travelling through a solidifying  $\text{NH}_4\text{Cl-H}_2\text{O}$  system.

Christenson and Incropera took a different approach. [15] Rather than using laser optics to produce an image, they used an optical tool to probe  $\text{NH}_4\text{Cl-H}_2\text{O}$  concentration directly. A miniature fiber-optic refractometer was used to measure the amount of laser light passing through a horizontal directional solidification system, thus determining the refractive index of the solution. Although the index of refraction depended on both temperature and concentration, the device was calibrated over the experimental temperature range so that it measured concentration without concurrent temperature measurements. An accuracy of 0.5 wt% was reported, which was sufficient to measure concentration changes due to thermal boundary conditions and initial solution concentrations. However, since the concentration changes across the diffusion layer are on the order of 0.25 wt%, [2] [9] the fiber-optic refractometer is not an appropriate tool for diffusion layer studies.

### Triglycine Sulfate

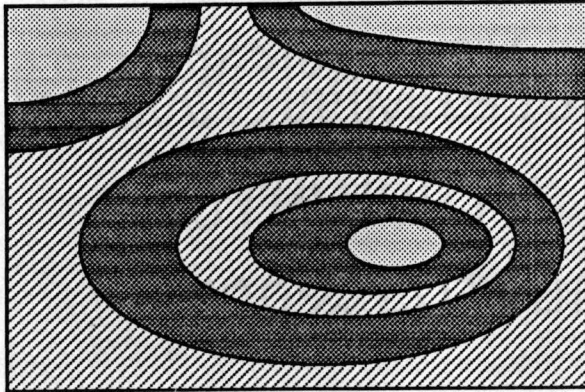
The techniques of laser optics have also been used to study other transparent materials, including triglycine sulfate  $(\text{NH}_2\text{CH}_2\text{COOH})_3(\text{H}_2\text{SO}_4)$ . Fringe pattern analysis was used to measure concentration in the depletion layer of triglycine sulfate (TGS) crystals grown aboard Spacelab 3 in 1985.

TGS experiments were conducted in NASA's Fluid Experiments System (FES). One of the main FES components is its holographic system, which was chosen to maximize the collection of data while minimizing optical set-up. [16] Holograms recorded the phase of light travelling through a solidifying TGS

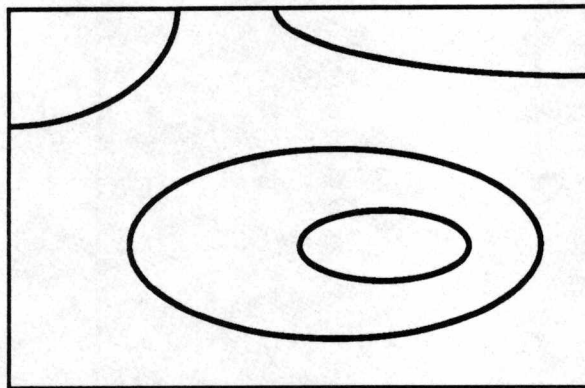
system. After the mission, holograms were developed and reconstructed in the Holographic Ground System (HGS), reproducing the wavefronts created during the experiments. Various optical techniques, including those too difficult to use in orbit, were then applied to the wavefronts. [16] [17]

In one reconstruction technique, interferograms showing refractive index changes in the TGS solution were produced. Tan et al. developed a system to analyze these fringe patterns automatically, yielding concentration profiles of the TGS depletion layer. [18] The system included a low-cost digital image processor with a frame grabber, which was used to digitize the interferograms. Commercial software was then used to pre-process the resulting image, thereby filtering out noise. Fringe detection software was executed to skeletonize the interferogram. The array of elements in a digital image, known as pixels, range in brightness from white to varying shades of gray to black. In the skeleton procedure, all pixels in the image are converted to white or black. The result is a binary pattern of lines representing the center-lines of fringe extrema, a "skeletonized" version of the original fringe pattern. See Figure 3.

The skeleton fringes were numbered such that the phase from fringe to fringe increased by  $2\pi$ . An interpolation routine was used to convert this discrete phase map to a continuous one. Since the TGS seed crystal and its depletion layer were axially symmetric, the Abel inversion was used to convert phase to index of refraction. It was assumed that temperature effects on index of refraction were small compared to concentration effects. [19] [20] Index of refraction was



**BEFORE**



**AFTER**

**Figure 3.** Skeletonizing a fringe pattern.

converted directly to concentration, neglecting any temperature changes.

The automated fringe analysis system was tested before the Spacelab flight with the help of a computer model developed to predict temperature and concentration profiles for the TGS flight experiment. [20] [19] Kroes and Reiss had used a refractometer to quantify the separate effects of concentration and temperature on TGS refractive index. [21] The computer model used this data to calculate index of refraction fields and to synthesize the resulting interferograms. Fringes were rounded off to simulate flight interferograms, then analyzed with the automated fringe analysis system. In this way, a known refractive index pattern was compared with the refractive index pattern calculated by the automated system. The results of these tests were not reported.

The fringe analysis procedure used in the TGS experiments is more automated than the manual technique discussed earlier for  $\text{NH}_4\text{Cl-H}_2\text{O}$ . However, both the TGS method and the  $\text{NH}_4\text{Cl-H}_2\text{O}$  method centered around identification of fringe extrema. For this reason they are categorized as intensity methods. Intensity methods are just one class of fringe pattern analysis techniques.

## CHAPTER 3

### THE FOURIER-TRANSFORM METHOD OF FRINGE PATTERN ANALYSIS

#### The Fringe Pattern

Various optical techniques produce fringe patterns with the intensity:

(Eq. 14.)

$$g(x,y) = a(x,y) + b(x,y) \cos [2\pi f_0 x + \phi(x,y)],$$

where  $a(x,y)$  represents the variation in background intensity, and  $b(x,y)$  represents the variation in fringe visibility.  $f_0$  is a measure of the tilt between interfering wavefronts, and  $\phi(x,y)$ , the phase, is the desired information. It can be seen that the phase is encoded within the intensity of the fringe pattern. The goal of fringe pattern analysis, then, is to decode the desired phase information. Since phase changes can be related to changes in such physical quantities as density, pressure, and temperature, fringe pattern analysis can be used to measure these quantities.

Mach-Zehnder interferometry is a specific example of an optical technique that produces a fringe pattern of the form given in Eq. 14. In this technique, fringes are formed when an object beam and a reference beam are interfered. See

Figure 4. The object beam passes through a transparent object and carries the desired phase information,  $\phi(x,y)$ . In phasor notation the electric field component of the object beam is represented by  $A(x,y) \exp[j\phi(x,y)]$ . The reference beam is represented by  $B(x,y) \exp[-j2\pi f_0 x]$ , where  $f_0$  is proportional to the tilt of the reference beam with respect to the object beam. In these expressions,  $A(x,y)$  and  $B(x,y)$  give the variation of the amplitude of the beams with position.

When the two beams are combined, the electric field  $E(x,y)$  at the detector is the sum of the two electric field components:

(Eq. 15.)

$$E(x,y) = A(x,y) \exp [j\phi(x,y)] + B(x,y) \exp [-j2\pi f_0 x].$$

The intensity at the detector,  $g(x,y)$ , is equal to the quantity  $|E(x,y)|^2$ . After expanding both terms of  $E(x,y)$  with Euler's formula, and applying trigonometric identities, the following intensity expression is obtained:

(Eq. 16.)

$$g(x,y) = [A^2(x,y) + B^2(x,y)] + 2 A(x,y) B(x,y) \cos [2\pi f_0 x + \phi(x,y)].$$

After making the substitutions  $a(x,y) = A^2(x,y) + B^2(x,y)$ , and  $b(x,y) = 2 A(x,y) B(x,y)$ , it can be noted that the form of Eq. 16 is exactly that of Eq. 14.



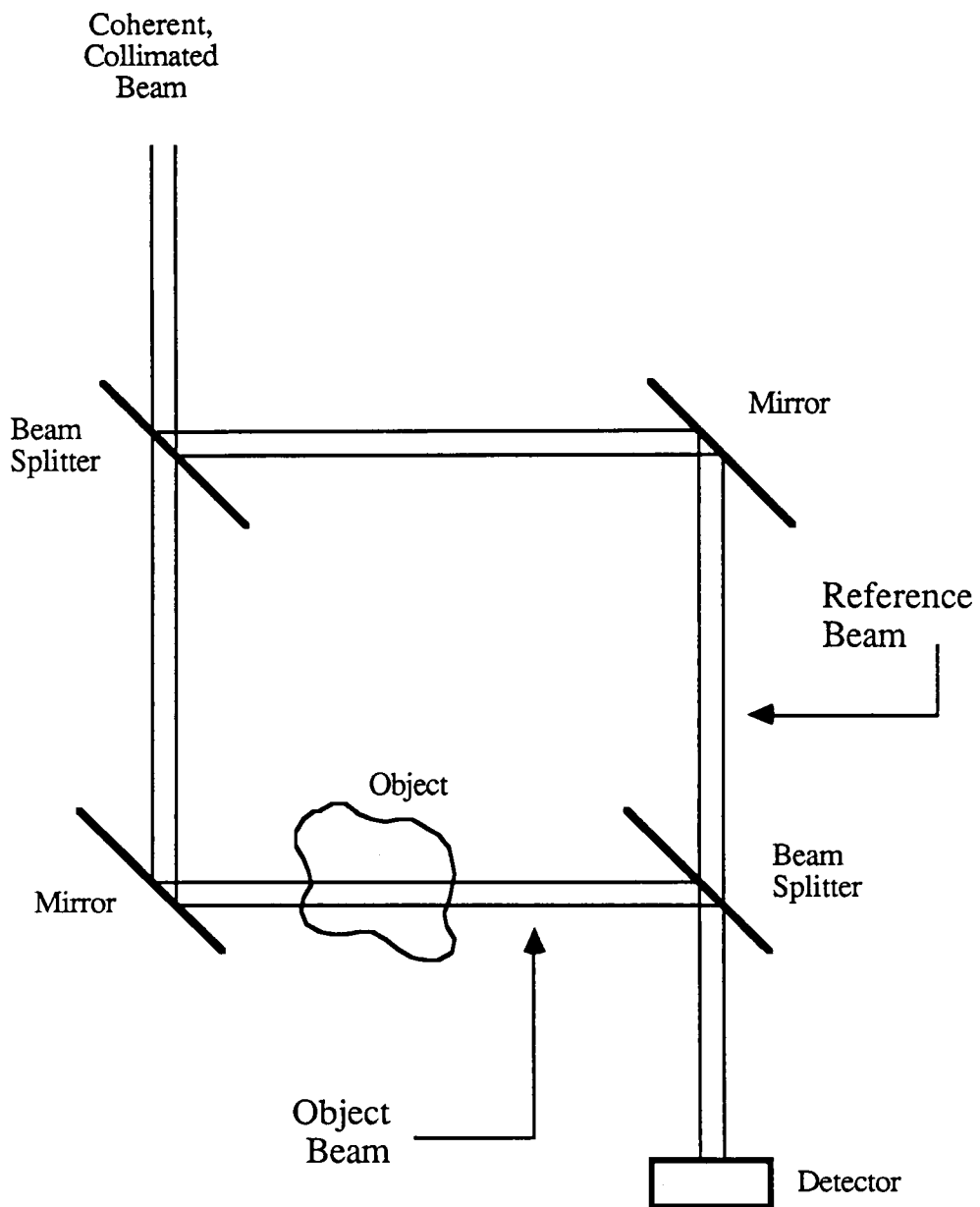


Figure 4. Sketch of a Mach-Zehnder interferometer.

## Techniques of Fringe Pattern Analysis

The goals of all fringe pattern analysis techniques are similar: to decode phase information from intensity, and to relate the phase to a physical quantity of interest, such as temperature. As the speed and accuracy of modern fringe pattern analysis increase, optical techniques such as interferometry become more useful as measurement tools. Excellent reviews of fringe pattern analysis are given by Reid [22] and Hesselink. [23]

Fringe pattern analysis techniques are divided into two classes, intensity techniques and phase techniques. See Figure 5.

### Intensity Techniques

Intensity techniques identify and track fringe extrema, also known as fringe contours. Phase information between the contours is disregarded. Since the fringe pattern is a periodic sinusoid, each contour represents a phase change of  $2\pi$ .

In intensity techniques, the reference beam is adjusted to eliminate tilt with respect to the object beam. Since  $f_0$  in Eq. 14 is thus set to zero, the resultant intensity is:

(Eq. 17.)

$$g(x,y) = a(x,y) + b(x,y) \cos [\phi(x,y)].$$

## Techniques of Fringe Pattern Analysis

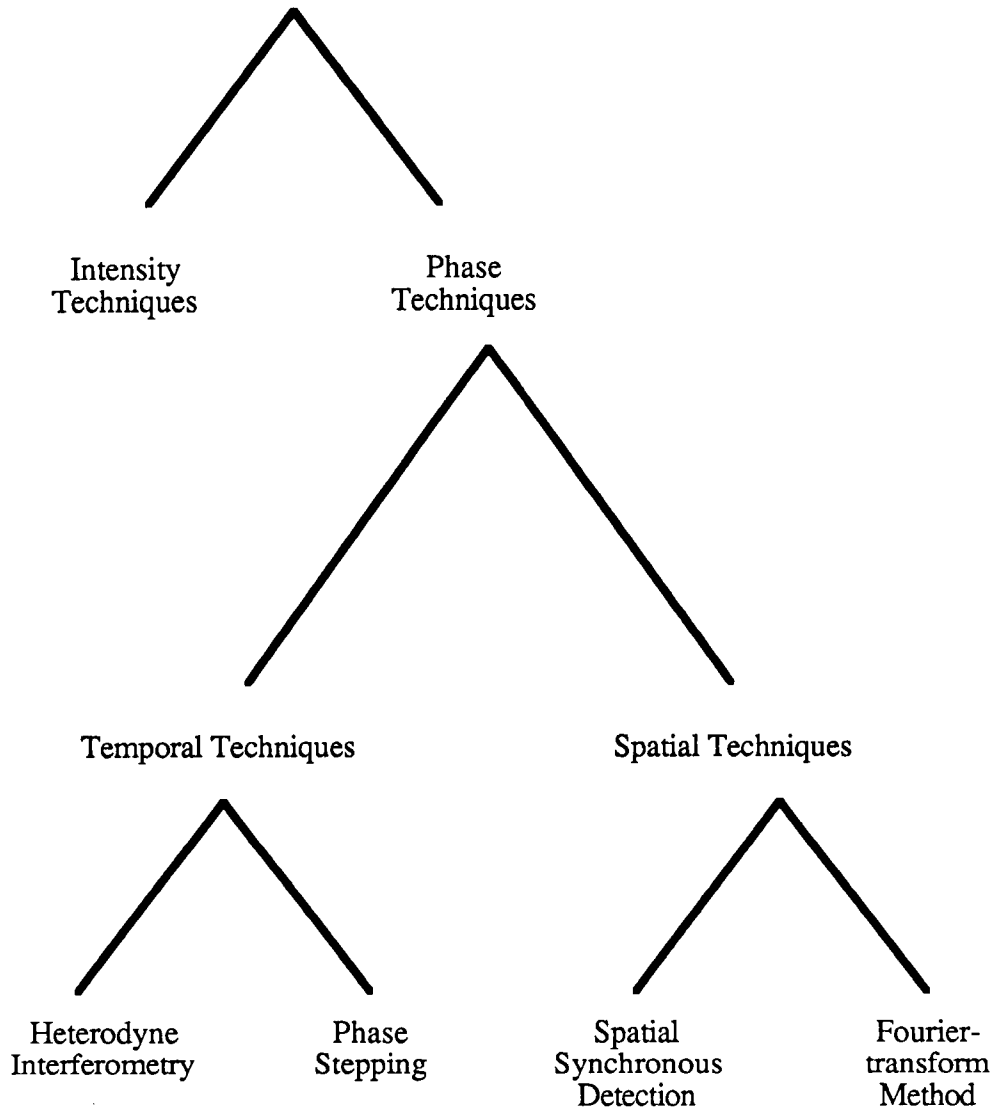


**Figure 5.** Techniques of fringe pattern analysis.

Intensity techniques then proceed as follows:

- 1) Digital filtering is used to improve fringe quality.
- 2) The fringe pattern is skeletonized into a line pattern representing fringe extrema.
- 3) The skeletonized fringes are numbered, and phase values are assigned to each fringe, either automatically or interactively.
- 4) Interpolation or sinusoidal fitting is used to obtain the phase at points between the skeletonized fringes.

### Phase Techniques

Phase techniques introduce a known phase shift to obtain a unique decoding of phase from intensity. There are two classes of phase techniques, temporal and spatial.

In temporal phase techniques, the phase shift is introduced over time. One example is heterodyne interferometry, known also as electronic heterodyning. [22] In this form of interferometry, Bragg cells (a type of electro-optic modulator) produce unequal frequency shifts,  $\Delta f_1$  and  $\Delta f_2$ , in the interfering laser beams. A photoelectric detector generates an AC photocurrent in response to the incident intensity, which now depends on sum and difference terms involving  $\Delta f_1$  and  $\Delta$

$f_2$ . The bandwidth of the detector is designed to detect only the component of intensity directly dependent on the desired phase. The phase of the AC photocurrent at each location is then the same as the desired phase at that location.

A second example of a temporal phase technique is phase stepping, also referred to as quasi-heterodyne interferometry. [22] [23] In this procedure, a computer controlled piezo-electric translator moves the reference mirror in discrete steps, and an interferogram is recorded after each movement. If  $(M + 1)$  interferograms are to be recorded, the phase of the reference beam is changed by  $2\pi/M$  with each step. The intensity of the interferograms is given by:

(Eq. 18.)

$$g_N(x,y) = a(x,y) + b(x,y) \cos [\phi(x,y) + \phi_N],$$

where  $\phi_N$  is the induced phase shift in the reference beam, for the Nth interferogram. The Fourier series coefficients are computed:

(Eq. 19.)

$$a_1 = [ \sum_{N=0}^M g_N(x,y) \cos (2\pi N/M) ], \text{ and}$$

$$b_1 = [ \sum_{N=0}^M g_N(x,y) \sin (2\pi N/M) ].$$

The phase at each location is then determined by:

(Eq. 20.)

$$\phi(x,y) = \arctan (b_1 / a_1).$$

The spatial synchronous detection methods developed by Womack [24] are examples of spatial phase techniques. While temporal phase techniques use a phase shift over time, spatial phase techniques introduce a phase shift over the physical extent of the interferogram. The phase shift is provided by a large tilt in the reference beam.

Womack's methods are based on the general concept of synchronous detection, in which an unknown signal is multiplied by a sinusoidal reference, then integrated to isolate the low frequency part of the product. One of his algorithms, the quadrature multiplicative moire (QMM) method, begins with an interferogram having substantial tilt in the reference beam. The intensity is that of the general fringe pattern given by Eq. 14, and is repeated here:

$$g(x,y) = a(x,y) + b(x,y) \cos [2\pi f_0 x + \phi(x,y)],$$

A sinusoidal reference pattern,  $r(x,y)$ , is generated by a computer:

(Eq. 21.)

$$r(x,y) = \cos (2\pi f_0 x).$$

A lowpass filter applied to the product of these two patterns gives:

(Eq. 22.)

$$M_1(x,y) = 1/2 b(x,y) \cos [\phi(x,y)].$$

A second sinusoidal reference pattern is generated by shifting the phase of the first reference pattern by  $\pi/2$ . Multiplication and lowpass filtering result in:

(Eq. 23.)

$$M_2(x,y) = - 1/2 b(x,y) \sin [\phi(x,y)].$$

The desired phase is then computed:

(Eq. 24.)

$$\phi(x,y) = - \arctan [M_2(x,y) / M_1(x,y)].$$

Another example of a spatial phase technique is the Fourier-transform method developed by Takeda et al. [25] In this method, a tilted reference beam is again used to decode desired phase information, this time with the help of Fourier transform techniques.

## Evaluation

Before turning to the Fourier-transform method, this section concludes with a comparison of the general classes of fringe pattern analysis. A specific evaluation of the Fourier-transform method is given later.

In comparing intensity techniques to phase techniques, Reid notes that intensity techniques are general purpose, requiring little knowledge of the fringe pattern to be analyzed. Verification is simple in that a graphical representation of the fringe extrema can be compared with the actual interferogram. [22]

However, the sensitivity of intensity techniques is limited to  $2\pi$  because phase variations less than  $2\pi$  do not create fringe contours. In contrast, phase techniques make use of information between fringe extrema to yield a complete field of phase data. Thus phase techniques are more sensitive than intensity techniques.

In addition, phase techniques achieve higher accuracy by separating the desired phase information from variations in background intensity and fringe visibility, i.e.,  $a(x,y)$  and  $b(x,y)$ . For example, the accuracy of heterodyne interferometry approaches  $2\pi/1000$ , which is two to three orders of magnitude greater than that achieved with intensity techniques. [22]

Phase techniques also determine the sign of the phase. From contour to contour, intensity techniques cannot distinguish increases and decreases in phase. In a topography application, for example, outside knowledge of depression and



elevation would have to be used in conjunction with an intensity technique, in order to determine if the phase increases or decreases between contours.

In general, phase techniques are more amenable to computer automation than intensity techniques. No operator interaction is required to number fringes or to touch up the unreliable phase maps often produced by intensity techniques. [26] The tilt used in many phase techniques straightens the fringes and gives them a relatively uniform separation, easing the use of computer vision algorithms. [27]

Comparisons can also be made between temporal phase techniques and spatial phase techniques. The temporal techniques are characterized by less complicated data processing. [23] Phase measurement is very direct, particularly in the case of heterodyne interferometry.

In contrast, the spatial techniques are characterized by less complicated data acquisition. [23] Frequency modulation is unnecessary, as is the piezoelectric translator. However, the tilt induced by the spatial techniques requires them to operate at high fringe densities, so a high resolution detector is needed. [24]

With the spatial techniques, only one interferogram is required for analysis. Temporal techniques, however, call for a series of interferograms at different times, a requirement that limits the speed of data capture. [22] This inhibits the use of temporal techniques with transient phenomena, such as rapidly changing plasma flows, where it may be difficult to obtain several images before significant changes occur. [24]

Sources of error in the temporal techniques and the spatial techniques also differ. Error in the temporal techniques is generally due to imprecision in the phase steps, while error in the spatial techniques is tied to the performance of filters. [24]

### The Fourier-transform Method

The Fourier-transform method, a spatial phase technique of fringe pattern analysis, was developed by Takeda et al. [25] It operates on the general fringe pattern given by Eq. 14. When the analysis is conducted for a fixed value of  $y$ , Eq. 14 can be rewritten in 1-D notation:

(Eq. 25.)

$$g(x) = a(x) + b(x) \cos [2\pi f_0 x + \phi(x)].$$

In this equation  $f_0$ , a measure of the tilt between interfering wavefronts, is known as the carrier frequency. In the Fourier domain, the tilt acts to separate information components from each other and from some of the spurious intensity variations. The combination of tilt and Fourier domain processing is the hallmark of the Fourier-transform method.

## The Fourier-transform Procedure

The overall goal of the Fourier-transform procedure is to decode the phase,  $\phi(x)$ , from the recorded intensity  $g(x)$ . The procedure includes the following steps:

- 1) Eq. 25 is rewritten, with the help of Euler's formula:

(Eq. 26.)

$$g(x) = a(x) + c(x) \exp(2\pi j f_0 x) + c^*(x) \exp(-2\pi j f_0 x).$$

In this equation,  $c(x) = 1/2 b(x) \exp [j\phi(x)]$ , and \* indicates the complex conjugate.

- 2) The fast Fourier transform (FFT) is applied to compute the discrete Fourier transform of the fringe pattern. The Fourier transform is given by:

(Eq. 27.)

$$G(f) = A(f) + C(f-f_0) + C^*(f+f_0),$$

where capital letters represent the Fourier spectra, and where  $f$  represents the spatial frequency. For more information on the discrete Fourier transform, see Appendix 1.

In most cases  $a(x)$ ,  $b(x)$ , and  $\phi(x)$  vary slowly in comparison with the variation introduced by the carrier frequency  $f_0$ . For this reason the Fourier transform consists of three distinct regions, corresponding to the three terms in Eq. 27. The trimodal function  $G(f)$  has peaks at  $-f_0$ ,  $f_0$ , and the origin, as shown in Figure 6a).

3) The spectrum  $C(f-f_0)$  is isolated with a filter. The effects of the varying background intensity, represented by  $a(x)$ , are thus eliminated. See Figure 6b).

4) The spectrum  $C(f-f_0)$  is translated to the origin, by the distance  $f_0$ . Due to the translation property of the discrete Fourier transform, the resulting spectrum is  $C(f)$ . See Figure 6c).

5) The inverse FFT of  $C(f)$  is computed, to obtain  $c(x)$ .

6) The phase is calculated by taking the imaginary part of the complex log:

(Eq. 28.)

$\ln [c(x)] = \ln [1/2 b(x)] + j\phi(x)$ , and

$\phi(x) = \text{Im} \{ \ln [c(x)] \}$ .

Alternatively, the phase can be computed by using: [27]

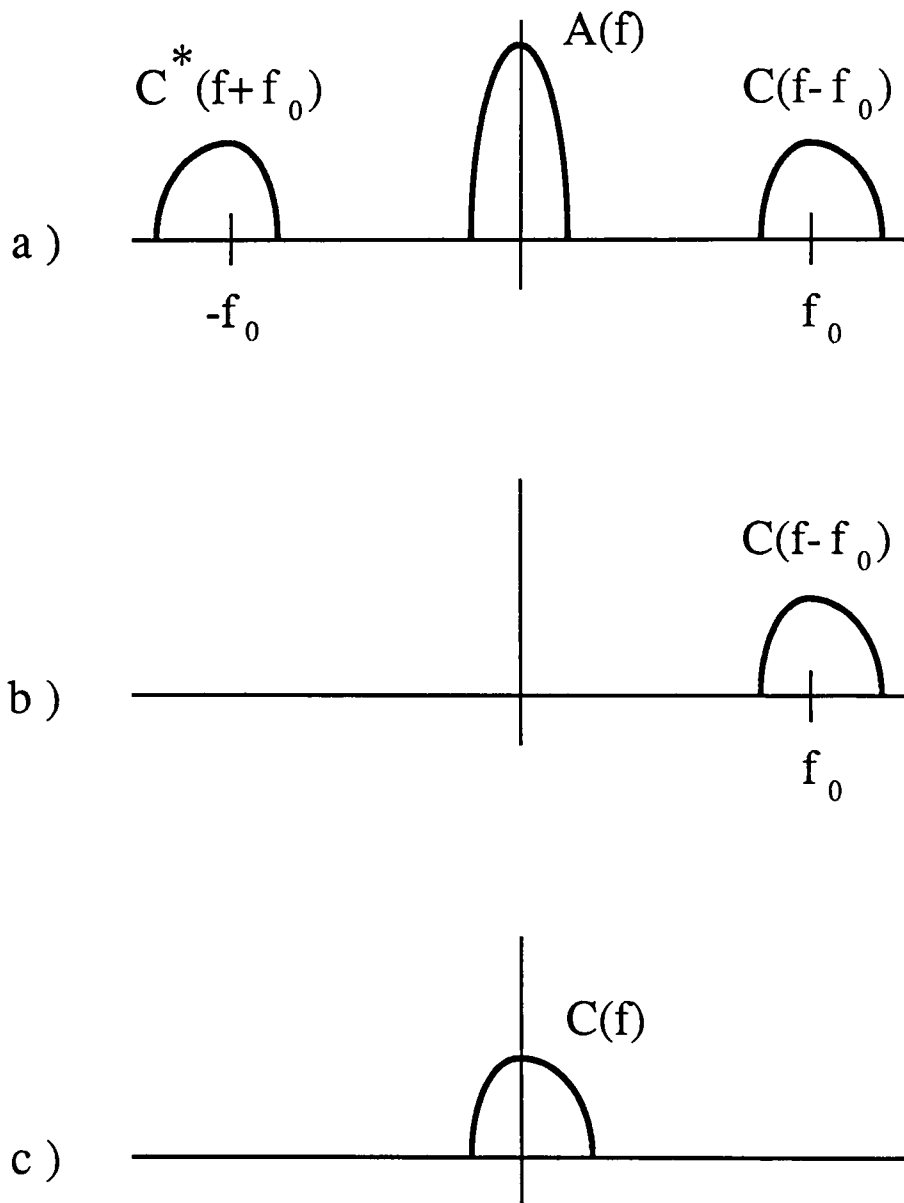


**Figure 6.** Steps in the Fourier-transform procedure. Magnitude of the Fourier transform versus frequency. a) FFT. b) Filter. c) Translate.

(Eq. 29.)

$$\phi(x) = \arctan \{Im [c(x)] / Re [c(x)]\}.$$

With either method, the effects of the varying fringe visibility,  $b(x)$ , are eliminated.

### Phase-unwrapping

All values of phase computed in this way fall in a  $2\pi$  range. Thus the complete phase field often contains discontinuities, or phase jumps. Phase-unwrapping, also known as phase continuation, is used to detect and correct phase jumps. The result is a continuous phase profile. See Figure 7.

Two approaches to phase-unwrapping are discussed here. The first, developed by Takeda et al., [25] computes an offset phase which is added to the discontinuous phase, to obtain the continuous phase:

(Eq. 30.)

$$\phi_c(x) = \phi_D(x) + \phi_o(x).$$

To compute the offset for each point, the phase difference between adjacent points is calculated:

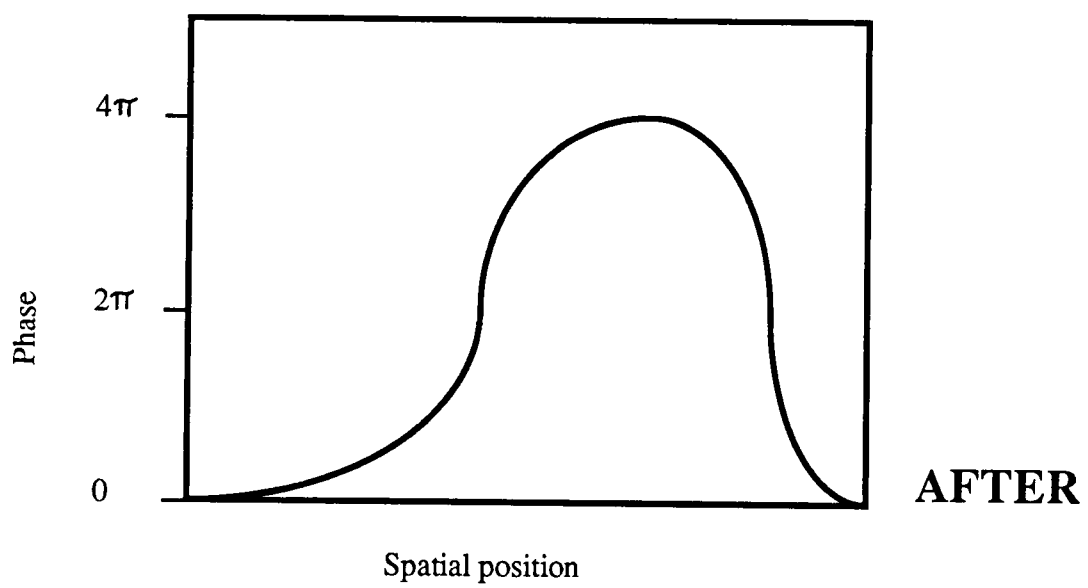
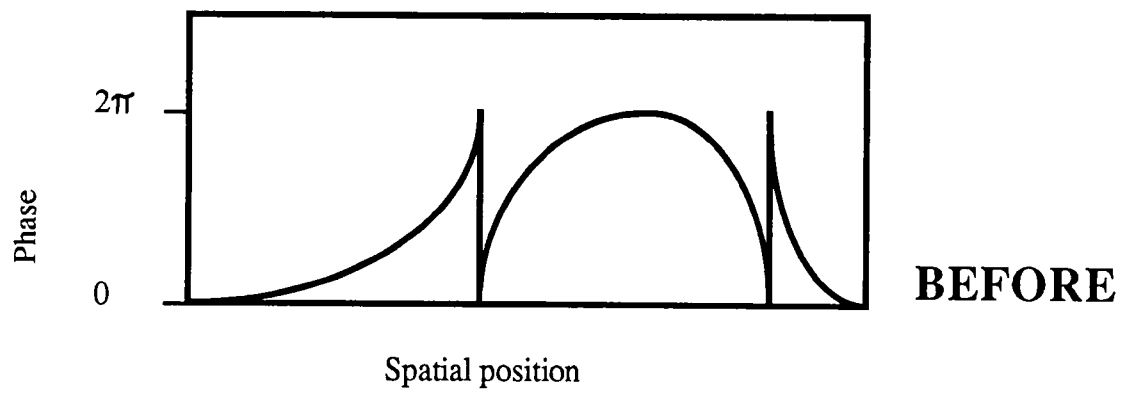


**Figure 7.** Phase-unwrapping.

(Eq. 31.)

$$D(x_k) = \phi_D(x_k) - \phi_D(x_{k-1}).$$

If the phase is continuous, the absolute value of  $D(x_k)$  is less than  $2\pi$ . Where a phase jump occurs, however, the value approaches  $2\pi$ . The direction of the phase jump is given by the sign of  $D(x_k)$ .

A criterion for a phase jump,  $\phi_{\text{jump}}$ , is set. Takeda et al., for example, use  $\phi_{\text{jump}} = (0.9 \times 2\pi)$ . The offset of the first point,  $\phi_o(x_1)$ , is set to zero. Offsets for subsequent points are determined by comparing  $D(x_k)$  to  $\phi_{\text{jump}}$ . If a positive phase jump is detected, the current offset is obtained by subtracting  $2\pi$  from the offset of the previous point. If a negative phase jump is detected,  $2\pi$  is added to the previous offset.

In summary:

(Eq. 32.)

$$\begin{aligned} \phi_o(x_1) &= 0, \\ \phi_o(x_k) &= \begin{cases} \phi_o(x_{k-1}) - 2\pi & \text{if } D(x_k) \geq \phi_{\text{jump}}, \\ \phi_o(x_{k-1}) + 2\pi & \text{if } D(x_k) \leq -\phi_{\text{jump}}, \\ \phi_o(x_{k-1}) & \text{otherwise, and} \end{cases} \\ \phi_c(x) &= \phi_D(x) + \phi_o(x). \end{aligned}$$



A more elegant approach to phase-unwrapping, based on a recurrence relationship, was developed by Macy. [27] This approach requires less computation time than that of Takeda et al. It begins with an expression for the continuous, or unwrapped phase:

(Eq. 33.)

$$\phi_C(x) = \phi_D(x) + 2m\pi,$$

where  $m$  is a positive or negative integer. That is, the unwrapped phase is obtained from the discontinuous phase by adding some multiple of  $2\pi$ .

The change in phase from fringe to fringe is  $2\pi$ . Macy's method proceeds by noting that the maximum change in phase between adjacent pixels is  $\pi$ , since there must be at least two pixels per fringe. The maximum change in phase between pixels is expressed:

(Eq. 34.)

$$-\pi < \phi_C(x_k) - \phi_C(x_{k-1}) < \pi.$$

After adding  $\pi$ , and substituting for  $\phi_C(x_k)$ , the following expression is obtained:

(Eq. 35.)

$$0 < \phi_D(x_k) - \phi_C(x_{k-1}) + (2m + 1)\pi < 2\pi.$$

This relationship leads to the recurrence equation:

(Eq. 36.)

$$\phi_C(x_1) = \phi_D(x_1), \text{ and}$$

$$\phi_C(x_k) = \text{AMOD} [\phi_D(x_k) - \phi_C(x_{k-1}) + 201\pi, 2\pi] + \phi_C(x_{k-1}) - \pi.$$

AMOD is a FORTRAN function that gives the remainder when the first argument is divided by the second. The value 201 is an arbitrary large odd number, providing a required positive argument for AMOD.

### Enhancements to the Fourier-transform Method

In the years following the development of the Fourier-transform method by Takeda et al., several enhancements have been proposed. The procedure and the techniques of phase-unwrapping have been extended to two dimensions, thus enabling the Fourier-transform method to be applied to more problems. The accuracy of the method has been improved by the development of better techniques for carrier frequency determination. Finally, a correction for the problem of nonlinear film response has been proposed. These enhancements are discussed in the following sections.

## Extension to 2-D

The extension of the Fourier-transform method to two dimensions consists of two elements, extending the procedure itself, and extending the techniques of phase-unwrapping.

In regard to extending the Fourier-transform procedure, Takeda et al. [25] and Macy [27] chose repeated applications of the 1-D FFT, while Nugent [26] and Bone et al. [28] turned to the 2-D FFT. When the first approach is applied, the carrier frequency  $f_0$  is assumed to vary in only one direction. Steps 1) through 6) of the 1-D Fourier-transform procedure are modified for two dimensions as follows:

- 1) Eq. 14 is rewritten:

(Eq. 37.)

$$g(x,y) = a(x,y) + c(x,y) \exp(2\pi j f_0 x) + c^*(x,y) \exp(-2\pi j f_0 x),$$

where  $c(x,y) = 1/2 b(x,y) \exp [j\phi(x,y)]$ .

- 2) The 1-D FFT is computed for each column of data:

(Eq. 38.)

$$G(f,y) = A(f,y) + C(f-f_0,y) + C^*(f+f_0,y).$$

- 3) The spectrum  $C(f-f_0, y)$  is selected with a filter.
- 4)  $C(f-f_0, y)$  is translated to the origin. Through the translation property of the discrete Fourier transform, the result is  $C(f, y)$ .
- 5) The inverse 1-D FFT of  $C(f, y)$  is computed, to obtain  $c(x, y)$ .
- 6) The phase is calculated by taking the imaginary part of the complex log:

(Eq. 39.)

$\ln [c(x, y)] = \ln [1/2 b(x, y)] + j\phi(x, y)$ , and

$\phi(x, y) = \text{Im} \{ \ln [c(x, y)] \}$ ,

or via the arctangent function:

(Eq. 40.)

$\phi(x, y) = \arctan \{ \text{Im} [c(x, y)] / \text{Re} [c(x, y)] \}$ .

In contrast to the first approach, the more general case of a two-dimensional carrier frequency is allowed when the 2-D FFT is used to implement the 2-D Fourier-transform method:

(Eq. 41.)

$$g(x,y) = a(x,y) + b(x,y) \cos [2\pi(u_0x + v_0y) + \phi(x,y)],$$

where  $u_0$  and  $v_0$  give the carrier frequencies in the  $x$  and  $y$  directions, respectively. The use of the 2-D FFT permits better separation, and thus discrimination, among information components and unwanted components. [28] Error is thus reduced.

Steps 1) through 6) of the previous 2-D Fourier-transform procedure are now repeated, with notational changes to include 2-D spectra:

1) Eq. 41 is rewritten:

(Eq. 42.)

$$g(x,y) = a(x,y) + c(x,y) \exp[2\pi j(u_0x + v_0y)] + c^*(x,y) \exp[-2\pi j(u_0x + v_0y)],$$

where  $c(x,y) = 1/2 b(x,y) \exp [j\phi(x,y)]$ .

2) The 2-D FFT is computed:

(Eq. 43.)

$$G(u,v) = A(u,v) + C(u-u_0,v-v_0) + C^*(u+u_0,v+v_0),$$

where  $(u,v)$  gives the frequency of the 2-D Fourier spectra.

- 3) The spectrum  $C(u-u_0,v-v_0)$  is selected with a filter.
- 4)  $C(u-u_0,v-v_0)$  is translated to the origin, resulting in the spectrum  $C(u,v)$ .
- 5) The inverse 2-D FFT of  $C(u,v)$  is computed, to obtain  $c(x,y)$ .
- 6) Step 6) is identical to that in the previous 2-D Fourier-transform procedure. That is, either Eq. 39 or Eq. 40 is chosen to calculate the phase.

The second element of the extension of the Fourier-transform method to two dimensions is phase-unwrapping. The 1-D unwrapping schemes of Takeda et al. and Macy, discussed earlier, have 2-D analogs. Both proceed in a similar manner. The phase along every row is unwrapped with the 1-D unwrapping scheme. Since the phase of each row is given in reference to the first point in the row, this step does not provide phase relationships among the rows themselves. To connect the rows, the 1-D scheme is applied once more, along any column. With this additional information, the continuous phase can be corrected to refer to a single point in the 2-D array.

The 2-D phase-unwrapping technique of Takeda et al. [25] begins with the rewriting of Eq. 32:

(Eq. 44.)

$$\begin{aligned} \phi_o^x(x_1, y) &= 0, \\ \phi_o^x(x_k, y) &= \begin{cases} \phi_o^x(x_{k-1}, y) - 2\pi & \text{if } D(x_k, y) \geq \phi_{\text{jump}}, \\ \phi_o^x(x_{k-1}, y) + 2\pi & \text{if } D(x_k, y) \leq -\phi_{\text{jump}}, \\ \phi_o^x(x_{k-1}, y) & \text{otherwise, and} \end{cases} \\ \phi_c(x, y) &= \phi_D(x, y) + \phi_o(x, y). \end{aligned}$$

The superscript  $x$  on  $\phi_o$  indicates that the offset corrects only in the  $x$  direction. Where  $\phi_o$  appears without a superscript, the offset corrects in both the  $x$  and  $y$  directions. To obtain an expression for  $D(x_k, y)$ , the 1-D expression given by Eq. 31 is rewritten:

(Eq. 45.)

$$D(x_k, y) = \phi_D(x_k, y) - \phi_D(x_{k-1}, y).$$

Eq. 44 does not indicate how to progress from rows of  $x$  direction offsets to the 2-D offset,  $\phi_o(x, y)$ . To accomplish this, a  $y$  offset must be calculated, since the initial values of the offsets of all the rows were set with the expression  $\phi_o^x(x_1, y) = 0$ . The  $y$  offset is determined along the column  $x = x_L$ , where  $L$  is arbitrary. The initial value of the column offset is set with the expression  $\phi_o^y(x_L, y_1) = 0$ . An expression similar to the second statement in Eq. 44 is applied to obtain  $\phi_o^y(x_L, y_k)$ , for all  $k$ . The 2-D offset phase is then given by:

(Eq. 46.)

$$\phi_o(x,y) = \phi_o^x(x,y) - \phi_o^x(x_L,y) + \phi_o^y(x_L,y).$$

The first two terms in this expression give the difference in the offset phase between  $(x,y)$  and  $(x_L,y)$ . The last term gives the difference between  $(x_L,y)$  and  $(x_L,y_1)$ . So the sum gives the offset phase relative to the point  $(x_L,y_1)$ .

In the 2-D unwrapping scheme developed by Macy [27], Eq. 33 is rewritten as:

(Eq. 47.)

$$\phi_c^x(x,y_k) = \phi_D(x) + 2m_k\pi.$$

The 2-D continuous phase is then given by:

(Eq. 48.)

$$\phi_c(x,y_k) = \phi_c^x(x,y_k) + 2m_k\pi,$$

where the superscript on  $\phi_c$  indicates that the phase is continuous in the x direction only. Here  $m_k$  is the number of cycles added or subtracted from the phase at row k. To determine  $m_k$ , Eq. 48 is rewritten for an arbitrary column,  $x = x_L$ :



(Eq. 49.)

$$\phi_c(x_L, y_k) = \phi_c^*(x_L, y_k) - 2m_k\pi.$$

Again noting the condition that the maximum change in phase between adjacent pixels is  $\pi$ , the following expression is obtained:

(Eq. 50.)

$$-\pi < \phi_c(x_L, y_k) - \phi_c(x_L, y_{k-1}) < \pi.$$

After adding  $\pi$ , dividing by  $2\pi$ , and substituting for  $\phi_c(x_L, y_k)$  and  $\phi_c(x_L, y_{k-1})$ , the result is:

(Eq. 51.)

$$0 < [\phi_c^*(x_L, y_k) - \phi_c^*(x_L, y_{k-1})]/2\pi + 0.5 - m_k + m_{k-1} < 1.$$

This leads to the following recurrence relationship:

(Eq. 52.)

$m_1 = 0$ , and

$$m_k = \text{INT} ([\phi_c^*(x_L, y_k) - \phi_c^*(x_L, y_{k-1})]/2\pi + 0.5) + m_{k-1},$$

where INT is a FORTRAN function that truncates to take the integer part of the argument.

### More Accurate Determination of the Carrier Frequency

The extension of the Fourier-transform method to two dimensions is only one enhancement proposed in recent years. Another enhancement is an improved determination of the carrier frequency. The Fourier-transform method calls for a translation of the spectrum  $C(f-f_0)$ ,  $C(f-f_0,y)$ , or  $C(u-u_0,v-v_0)$  to the origin. The result is the spectrum  $C(f)$ ,  $C(f,y)$ , or  $C(u,v)$ , respectively. However, inaccuracies in this operation exist, due to the digitization of data. The intensity functions  $g(x)$  and  $g(x,y)$  are sampled, or digitized, at finite intervals. Transformed functions in the Fourier domain, then, are also digitized. As a result, convenient shifts of spectra are quantized or discrete. Thus it is unlikely that any of these discrete steps will permit spectra to be positioned precisely at the origin. [26] See Figure 8.

Since the error in the carrier frequency can lead to serious errors in calculating the phase  $\phi(x)$  or  $\phi(x,y)$ , Nugent and Bone et al. have proposed methods for more accurate determination of the carrier frequency. Nugent [26] noted that a positioning error of  $(u_E, v_E)$  will alter Steps 5) and 6) of the Fourier-transform methods. Instead of obtaining  $c(x,y)$  in Step 5) of the second 2-D method (see following Eq. 41), for example, the result is:

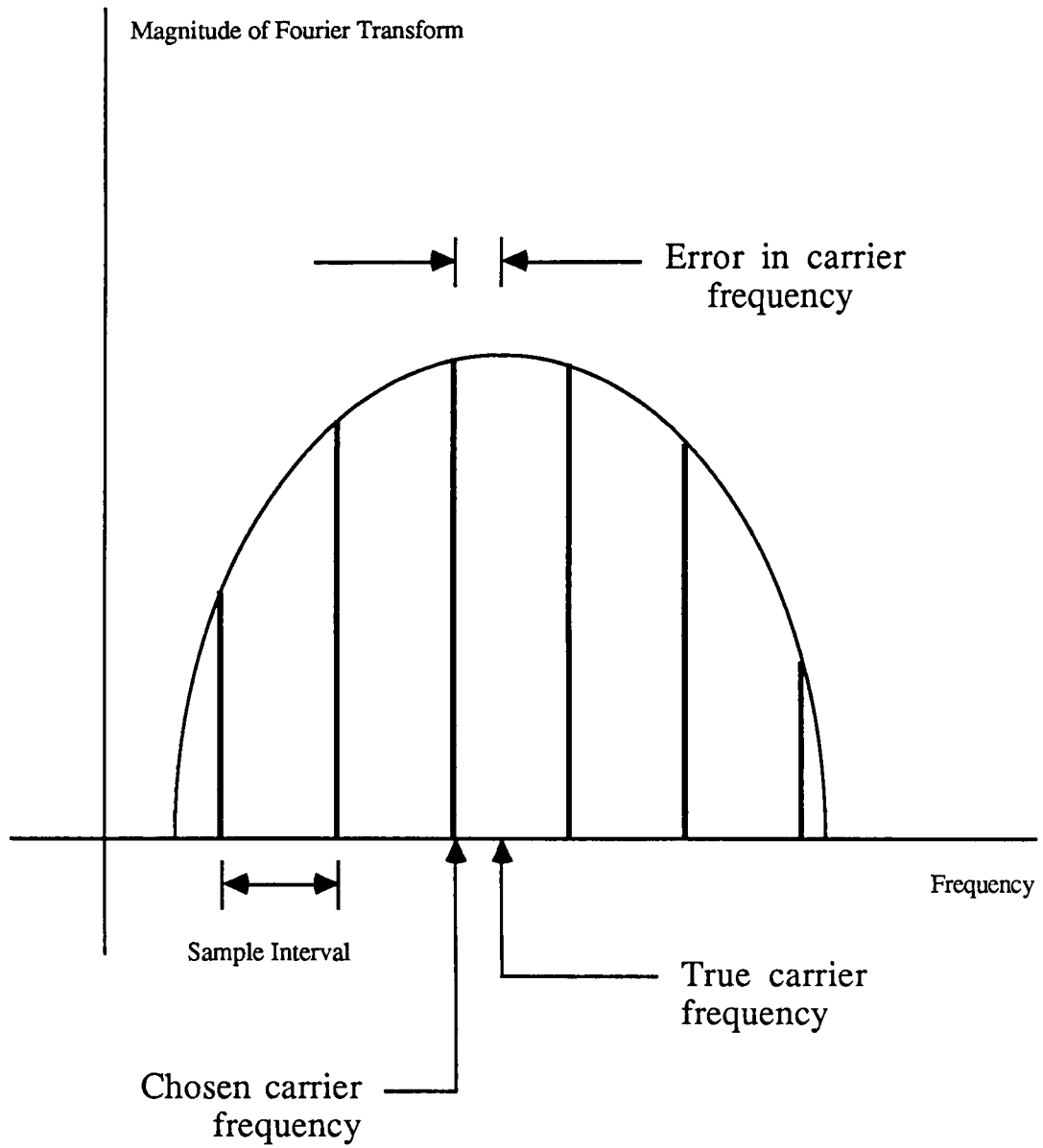


**Figure 8.** Digitization of data leading to an error in the carrier frequency.

(Eq. 53.)

$$c'(x,y) = \exp [-2\pi j(u_E x + v_E y)] c(x,y).$$

This expression seriously distorts the phase calculated in Step 6), as follows:

(Eq. 54.)

$$\phi'(x,y) = \phi(x,y) + 2\pi(u_E x + v_E y).$$

If the interferogram is arranged to show a region where phase does not vary, it is possible to detect if a phase modulation of the above form exists. If the spectrum  $C(u-u_0, v-v_0)$  has been translated incorrectly in the course of the Fourier-transform method, such a region will no longer be featureless. Nugent used this fact to develop a minimization procedure. The parameters  $u_E'$  and  $v_E'$  in the function:

(Eq. 55.)

$$c''(x,y) = \exp [2\pi j(u_E' x + v_E' y)] c'(x,y),$$

were adjusted to minimize modulation over regions that should have been featureless.

While Nugent relied on minimization for more accurate determination of the carrier frequency, Bone et al. took another approach. [28] They revised the

second 2-D Fourier-transform method (see following Eq. 41), neglecting translation of  $C(u-u_0, v-v_0)$  and substituting the following steps:

4) The inverse 2-D FFT of  $C(u-u_0, v-v_0)$  is computed, to obtain:

(Eq. 56.)

$$c_1(x,y) = c(x,y) \exp [2\pi j(u_0x + v_0y)], \text{ or}$$

$$c_1(x,y) = 1/2 b(x,y) \exp \{j[2\pi(u_0x + v_0y) + \phi(x,y)]\}.$$

5) The phase of this expression,  $\phi_1(x,y) = 2\pi(u_0x + v_0y) + \phi(x,y)$ , is calculated by taking the imaginary part of the complex log:

(Eq. 57.)

$$\ln [c_1(x,y)] = \ln [1/2 b(x,y)] + j[2\pi(u_0x + v_0y) + \phi(x,y)], \text{ and}$$

$$\phi_1(x,y) = \text{Im} \{ \ln [c_1(x,y)] \},$$

or via the arctangent function:

(Eq. 58.)

$$\phi_1(x,y) = \arctan \{ \text{Im} [c_1(x,y)] / \text{Re} [c_1(x,y)] \}.$$

6) The desired phase is then determined by direct subtraction:

(Eq. 59.)

$$\phi(x,y) = \phi_1(x,y) - 2\pi(u_0x + v_0y).$$

To determine  $u_0$  and  $v_0$ , which are needed in Step 6) of this new procedure, Bone et al., like Nugent, used a region of the interferogram devoid of phase information  $\phi(x,y)$ . Since  $\phi(x,y) = 0$  in such a region, Step 4) yields the expression  $1/2 b(x,y) \exp [2\pi j(u_0x + v_0y)]$ , with phase given by  $2\pi(u_0x + v_0y)$ . A least-squares fit was applied to this inclined plane, to obtain a good estimate of the carrier frequencies  $u_0$  and  $v_0$ .

#### Correction for Nonlinear Film Response

A final enhancement to the Fourier-transform method is the correction for nonlinear film response developed by Nugent. [26] If the photographic film used to record a fringe pattern has a nonlinear response function, the fringes will be distorted. The Fourier-transform method does not distinguish this fringe distortion from variations in the desired phase information, so phase errors will result.

Nonlinear film response adds another term to the equation for the intensity of a fringe pattern. [28] The revised equation, shown below in Eq. 60, can be compared with Eq. 41.

(Eq. 60.)

$$g(x,y) = a(x,y) + b(x,y) \cos [2\pi(u_0x + v_0y) + \phi(x,y)] \\ + h(x,y) \cos [4\pi(u_0x + v_0y) + \phi(x,y)].$$

In this equation  $h(x,y)$  gives the variation of the second harmonic term that represents the nonlinear response of the recording medium.  $h(x,y)$  depends on  $a(x,y)$ ,  $b(x,y)$ , and the response function of the recording system.

A typical nonlinear film response function, or characteristic curve, is given in Figure 9. Tone differences in the photographic subject translate to differences in the density of the emulsion layer on the photograph. The characteristic curve plots this density versus the log of the exposure, where the exposure equals the product of intensity and exposure time.

To investigate the effect of nonlinear film response, Nugent produced a synthetic interferogram distorted by a nonlinear characteristic curve. Application of the usual Fourier-transform method resulted in a distorted phase  $\phi(x,y)$ . To correct the distortion, the film was calibrated over a region of the interferogram devoid of phase information. In such a region, Eq. 60 can be rewritten:

(Eq. 61.)

$$g_1(x,y) = a(x,y) + b(x,y) \cos [2\pi(u_0x + v_0y)] + h(x,y) \cos [4\pi(u_0x + v_0y)].$$

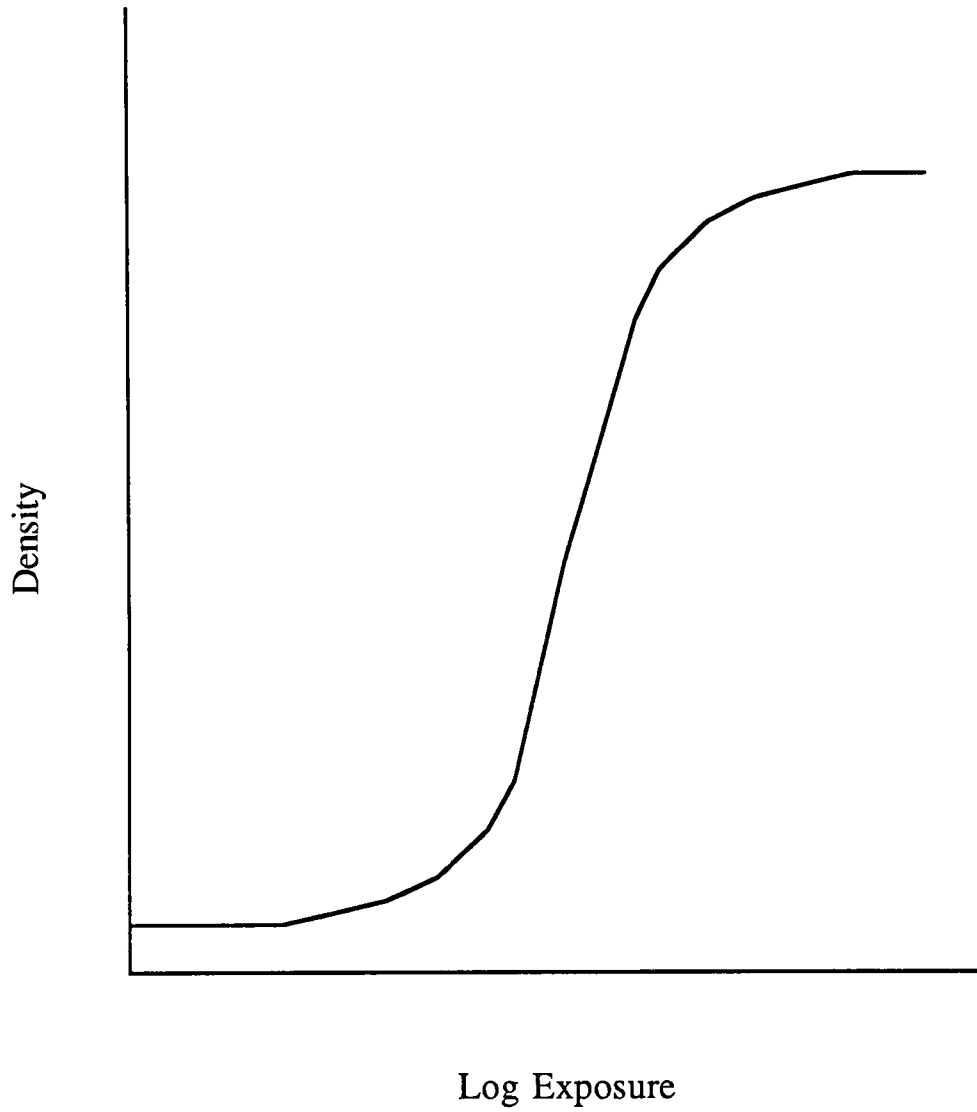


**Figure 9.** Typical characteristic curve, illustrating nonlinear film response.



The FFT of  $g_1(x,y)$  was computed, and frequencies other than those near the origin and those near the carrier frequency were filtered. The inverse transform produced a fringe pattern closely corresponding to the original:

(Eq. 62.)

$$g_2(x,y) = a(x,y) + b(x,y) \cos [2\pi(u_0x + v_0y)].$$

$g_1(x,y)$ , the distorted fringe pattern, and  $g_2(x,y)$ , the true fringe pattern emanating from the subject, were then compared to provide a film calibration curve.

Nugent applied this technique to the synthetic interferogram, and got a close match when comparing the resultant calibration curve with the characteristic curve used to produce the interferogram. The calibration curve was used to remap the intensity in the interferogram, thus correcting for nonlinear film response. The technique was applied once again for verification, and the revised calibration curve was found to be linear.

#### Other Versions of the Fourier-transform Method

Several other versions of the Fourier-transform method have been developed in recent years. In this section, an approximation to the method is described. A Fourier-transform method without tilt is also discussed.

## An Approximation to the Fourier-transform Method

Noting that the computation of the FFT is time-consuming, Mertz developed a three-sample complex convolution filter to approximate the Fourier-transform method. [29] In implementing the filter with electronic integrated circuits, he achieved an operation rate of 5 MHz, and made the process real time.

Mertz began by setting the carrier frequency to obtain three pixels per fringe. This established the 1-D fringe pattern:

(Eq. 63.)

$$g(x) = a(x) + b(x) \cos [2\pi x/3 + \phi(x)].$$

Three adjacent points were fit to the first three terms of the Fourier series. The three points and the Fourier series representation are given by:

(Eq. 64.)

$$g_{k-1}(x) = a(x) + b(x) \cos [\phi(x) - 2\pi/3],$$

$$g_k(x) = a(x) + b(x) \cos [\phi(x)],$$

$$g_{k+1}(x) = a(x) + b(x) \cos [\phi(x) + 2\pi/3], \text{ and}$$

$$g(x) = d_0 + d_1 \cos (2\pi x/3) + e_1 \sin (2\pi x/3).$$

Since  $a(x)$ ,  $b(x)$ , and  $\phi(x)$  vary slowly over one fringe cycle, they were treated as constants in calculating the Fourier coefficients  $d_1$  and  $e_1$ . [27] The result was:

(Eq. 65.)

$$d_1 = b(x) \cos \phi(x), \text{ and}$$

$$e_1 = - b(x) \sin \phi(x).$$

Then  $\phi(x)$  was computed:

(Eq. 66.)

$$\phi(x) = - \arctan (e_1 / d_1).$$

The quantity  $(e_1 / d_1)$  was actually evaluated via:

(Eq. 67.)

$$(e_1 / d_1) = [- (3/4)^{1/2} g(x_{k-1}) + (3/4)^{1/2} g(x_{k+1})] / [- 1/2 g(x_{k-1}) + g(x_k) - 1/2 g(x_{k+1})].$$

However, Mertz found that  $d_1$  and  $e_1$  could be written in the form of a three-sample convolution filter with complex coefficients:

(Eq. 68.)

$$z = d_1 + je_1$$

$$z = g(x_{k-1}) \exp (-2\pi j/3) + g(x_k) \exp (0j) + g(x_{k+1}) \exp (2\pi j/3).$$

In other words,  $d_1 = \text{Re } z$ , and  $e_1 = \text{Im } z$ . The filter was applied to the fringe data, yielding the phase:

(Eq. 69.)

$$\phi(x_e) = - \arctan (\text{Im } z / \text{Re } z).$$

The phase error for this procedure was calculated for a matrix of values of phase and spatial frequency. Since the procedure is an approximation, it did not perform as well as the Fourier-transform method. However, for frequencies near the assumed spatial frequency, the phase error was found to be less than the resolution of the instrumentation.

#### A Fourier-transform Method without Tilt

Kreis developed a version of the Fourier-transform method similar to that of Takeda et al., but asserted that a tilted wavefront is not needed. [30] A carrier frequency is not introduced, so translation of Fourier spectra to the origin is unnecessary. The procedure begins with the fringe pattern often analyzed by intensity techniques, Eq. 17. The equation is rewritten here in 1-D notation:

(Eq. 70.)

$$g(x) = a(x) + b(x) \cos [\phi(x)].$$

The Kreis method then proceeds as discussed below:

- 1) Euler's formula is used to rewrite the intensity equation:

(Eq. 71.)

$$g(x) = a(x) + c(x) + c^*(x),$$

where  $c(x) = \frac{1}{2} b(x) \exp [j\phi(x)]$ .

- 2) The 1-D FFT is computed:

(Eq. 72.)

$$G(f) = A(f) + C(f) + C^*(f).$$

- 3) If the background intensity  $a(x)$  varies slowly in comparison with the fringe spacing, it is possible to isolate  $C(f)$  with a notch filter.
- 4) The inverse FFT of  $C(f)$  is computed, to obtain  $c(x)$ .
- 5) The phase is computed as before, via Eq. 28 or Eq. 29.

Since a tilted wavefront is not required in the Kreis method, the method can be applied to the contour interferograms often analyzed by intensity techniques. However, the accuracy of the method has not been established. Unlike the conventional Fourier-transform method, the Kreis method does not separate spurious components from information components before filtering. This undoubtedly affects performance.

### Evaluation of the Fourier-transform Method

The Fourier-transform method has been evaluated in a variety of ways. Its response to a complicated phase has been quantified, as has its response to random noise. The performance of the method has been compared with that of intensity techniques and other phase techniques.

#### Response to Complicated Phase

In the Fourier-transform method it is assumed that  $\phi(x)$  varies slowly in comparison to the carrier frequency  $f_0$ . This requirement was not quantified, so Green et al. measured how complicated the phase function can become before the method breaks down. [31]

Green et al. synthesized a fringe pattern of the form given by Eq. 25. The phase  $\phi(x)$  was formed by adding 100 sine functions, with frequencies determined by a random number generator having zero mean and standard deviation  $\sigma_p$ . A measure of the complexity of the phase, as compared with the carrier frequency, was defined:

(Eq. 73.)

$$C_p = \sigma_p / f_0.$$

The quantity  $C_p$  was then varied, and the response of the Fourier-transform method to increasingly complicated phase functions was noted. The method was found to break down when  $C_p$  approached the value 0.31. A good reconstruction of the phase was obtained when the variation due to the phase function remained below 30% of the variation introduced by the carrier frequency.

(Alternatively, the effect of phase variations on the Fourier-transform method might be approached by checking Carson's rule for phase modulated signals. Carson's rule relates transmission bandwidth to maximum phase deviation; see standard communications texts.)

#### Ideal Response of the Fourier-transform Method

Even in the absence of random noise, the Fourier-transform method will not produce a perfect reconstruction of the phase. [31] Because  $C(f-f_0)$  and  $C^*(f+f_0)$  are often not bandlimited, their spectral sidelobes overlap with  $A(f)$  and with each other. In isolating the spectrum  $C(f-f_0)$ , some information is lost through truncation. The remaining information is also corrupted because the tail of  $C^*(f+f_0)$  extends beyond the origin, thus modifying the spectrum  $C(f-f_0)$ . See Figure 10. All of this affects the reconstruction of the phase. Assuming proper filtering in the Fourier domain, however, the dominant source of error in the Fourier-transform method is random noise. [28]

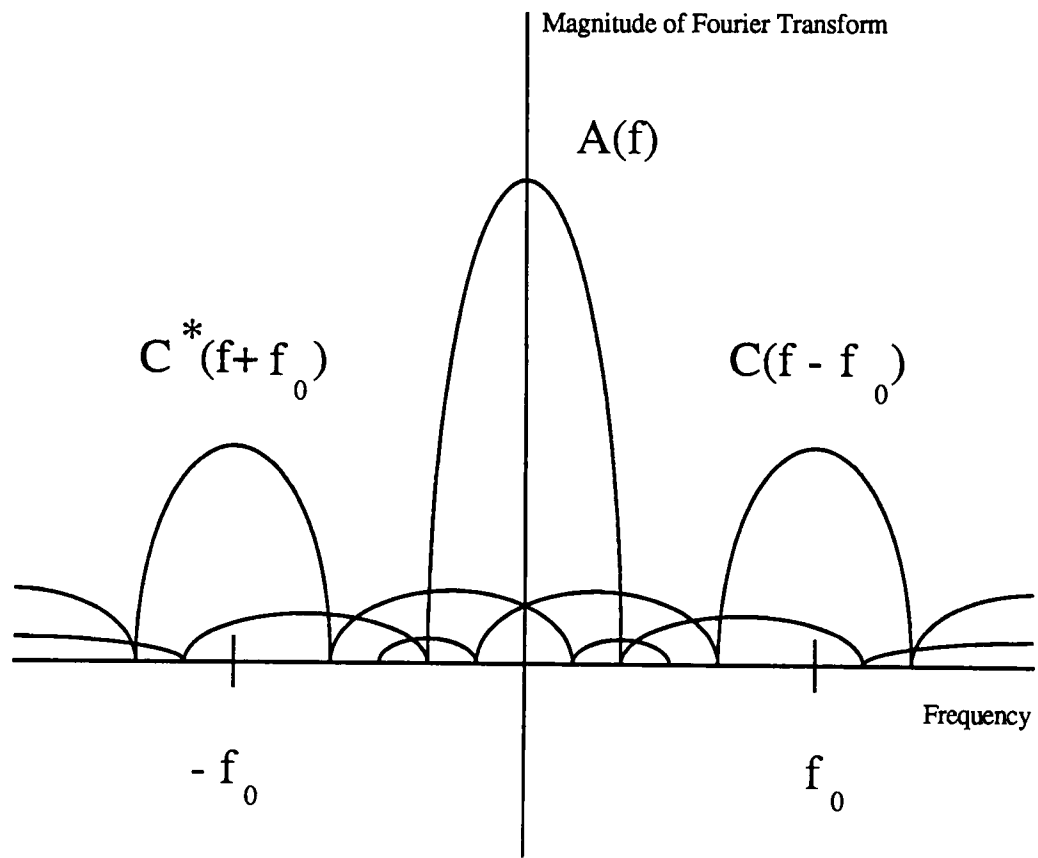


Figure 10. Overlap of spectra that are not bandlimited.



## Response to Random Noise

Macy demonstrated that error due to random noise exceeds the error induced by the Fourier-transform method itself. [27] Phase maps were calculated for synthesized interferograms at time intervals one minute apart. Phase variation due to random noise was found to have a standard deviation of 1/15 to 1/30 wave. (Takeda et al. found standard deviation of 1/30 wave in a similar experiment. [25]) In separate tests, Macy found the Fourier-transform method to have a standard deviation of 1/50 wave. Thus the accuracy of the method is usually limited by random noise, not by the method itself.

Bone et al. conducted experiments to quantify the effect of random noise on the Fourier-transform method. [28] An interferogram was synthesized to include a random noise component having a standard deviation of 12% of the average variation in fringe visibility. The error in the resulting phase distribution was less than 1% of the maximum phase variation.

Green et al. measured how great random noise can become before the Fourier-transform method breaks down. [31] A fringe pattern of the following form was synthesized:

(Eq. 74.)

$$g(x) = a(x) + b(x) \cos [2\pi f_0 x + \phi(x)] + n(x).$$

Here  $n(x)$  represents the effect of signal-independent random additive noise. The noise distribution was generated with a Gaussian random number generator having zero mean and standard deviation  $\sigma_N$ . A signal-to-noise ratio was defined:

(Eq. 75.)

$$S_N = 1/\sigma_N.$$

The quantity  $S_N$  was varied to determine the tolerance of the Fourier-transform method to increasing levels of random noise. For  $S_N = 1.8$ , the method broke down. Due to the presence of noise, phase jumps were distorted beyond the ability of the phase-unwrapping scheme to detect them. The Fourier-transform method produced reasonable reconstructions for values of  $S_N$  greater than 2.

#### Comparison to Intensity Techniques

Part of the evaluation of the Fourier-transform method includes a comparison of its performance with that of the intensity techniques. Macy synthesized an interferogram, then analyzed it with the Fourier-transform method, sinusoidal fitting, and sinusoidal fitting followed by smoothing. [27] The standard deviation of the computed phase from the known phase was given in waves, for several fringe spacings:

Method	Standard Deviation	
	3 pixels/fringe	6 pixels/fringe
Fourier-transform	0.0150	0.0175
Smoothed fit	0.0200	0.0275
Sinusoid fitting	0.0225	0.0650

By these criteria, the performance of the Fourier-transform method was clearly superior.

Macy also compared the performance of the Fourier-transform method with that of the Zygo Mark III system, which fits Zernike polynomials to fringes to determine phase maps. Although standard deviation data were not given, the phase maps agreed well. Contour plots showed that the number of fringes predicted by the methods varied no more than two over the viewing area, which was an average 56 centimeters in diameter. The two methods computed the phase to within 1/5 wave of each other.

In a review of fringe pattern analysis techniques, Hesselink noted that intensity techniques are the least accurate because only fringe extrema are used: "In general, elaborate and semiautomated techniques are required to obtain phase measurements at maxima and minima with similar accuracy as those achievable with transform techniques." Hesselink prefers the Fourier-transform method over intensity techniques whenever enough fringes, about four to six, are available.

[23]

### Comparison to Other Phase Techniques

When the Fourier-transform method is compared to the phase-stepping technique, its advantages are less clear. When accuracy is considered, Hesselink maintains that phase-stepping is superior to the Fourier-transform method. [23] However, Takeda et al. note that phase-stepping requires more than one fringe pattern. Moreover, the moving components used in phase-stepping must be positioned with great precision. Since the Fourier-transform method does not require such equipment, it excels in ease of use. [25]

## CHAPTER 4

### METHODS

In this project the Fourier-transform method was used to analyze the phase and concentration changes that took place during controlled solidification of ammonium chloride-water solution. Images depicting the solidification process were acquired with the optical techniques of interferometry and holographic interferometry, then translated to digital format. This chapter discusses the experimental methods employed in the areas of solidification, interferometry, holographic interferometry, and image translation. The FORTRAN programs written to implement the Fourier-transform method are explained, and their application to a particular solidification run is documented.

This chapter then describes investigations of the Fourier-transform method itself. The consistency of results produced by the Fourier-transform method was determined, and the performance of the method was compared with that of intensity methods. The effect of the technique of base phase subtraction was measured. Finally, the method was applied to holographic interferometry.

#### Solidification

To prepare  $\text{NH}_4\text{Cl-H}_2\text{O}$  solution for solidification experiments, quantities of  $\text{NH}_4\text{Cl}$  and  $\text{H}_2\text{O}$  were measured with a laboratory scale and combined in a 125 milliliter plastic bottle. The  $\text{NH}_4\text{Cl}$  used was catalog number A649-500, while the

deionized, filtered H<sub>2</sub>O was catalog number W2-4, both from Fisher Scientific. The solution was heated to 55 °C, then shaken to dissolve the NH<sub>4</sub>Cl. Two solution concentrations were used in this project: 28 wt% NH<sub>4</sub>Cl and 28.5 wt% NH<sub>4</sub>Cl.

The cuvette used to contain the NH<sub>4</sub>Cl-H<sub>2</sub>O solution was manufactured by Spectrocell and is depicted in Figure 11 and Figure 12. Composed of optical quality quartz, the cuvette has walls of thickness two millimeters, and inner dimensions 25 by 16 by 8 millimeters. A fill tube is located on the front wall of the cuvette.

To fill the cuvette, a syringe with spinal needle was extended with a 20 cm length of wire wrap. Heated solution was loaded into the syringe, and the flexible wire wrap was inserted through the fill tube into the body of the cuvette. The solution was carefully injected into the cuvette such that any air bubbles were left in the fill tube, not in the cuvette. The fill tube was then covered with a rubber cap.

The solidification assembly for the cuvette is shown in Figure 13 and Figure 14. The cuvette was sandwiched between thin copper plates that house thermocouples in slots. See Figure 15. During the course of solidification experiments, these thermocouples sensed the temperature at the top and bottom of the cuvette. Thermoelectric devices (TEDs) provided heating and cooling in response to a computer control program, while copper blocks acted as heat sinks for the assembly. To increase thermal conductivity, all adjoining surfaces were coated with a high temperature conductive paste, Omega Omegatherm 201.

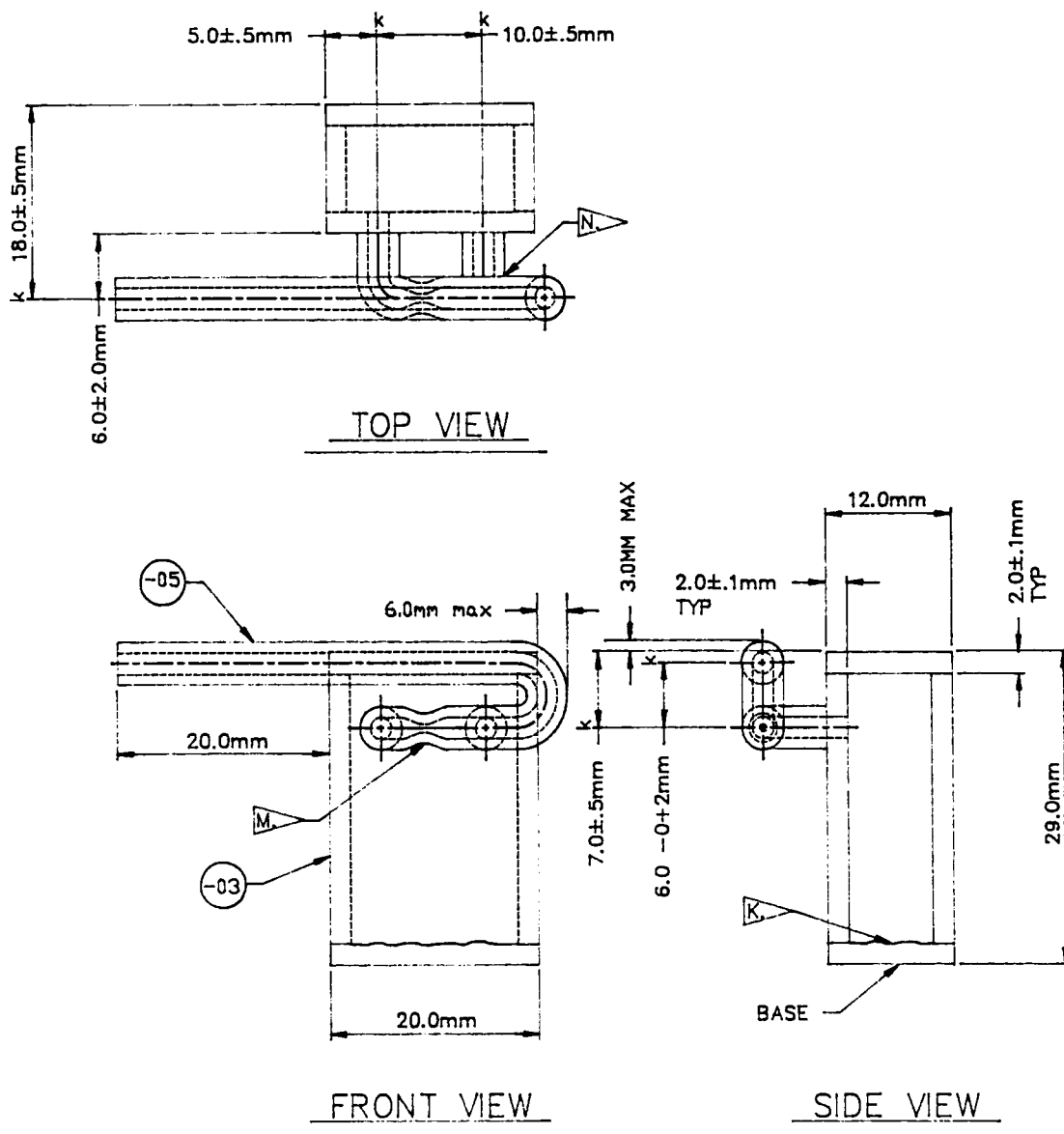


Figure 11. Scale drawing of the quartz cuvette (Part 1, schematic).

NOTES:

OPTICAL QUALITY QUARTZ PLATE SPECIFICATIONS:

- A. FIGURE, MAX: LAMDA OVER 8
- B. IRREGULARITY, MAX: LAMDA OVER 20
- C. COSMETIC & SURFACE QUALITY: 80-50 SCRATCH & DIG
- D. FLATNESS: 3 LAMDA PER 25 mm OVER CLEAR APERTURE AT 546nm
- E. PARALLELISM:
  1. PARALLEL TO WITHIN 5 ARC-MINUTES BETWEEN INSIDE AND OUTSIDE OF OPTICAL SURFACE (2mm THICKNESS)
  2. PARALLEL TO WITHIN 5 ARC-MINUTES BETWEEN DIFFERENT OPTICAL SURFACES
- F. PERPENDICULARITY: EACH OPTICAL SURFACE PERPENDICULAR TO BASE WITHIN 5 ARC-MINUTES
- G. EDGE/BEVEL: FINE GRIND OR FLAME POLISH
- H. STRIATIONS: STRIATIONS SHALL BE IMMEASURABLE AT VISIBLE WAVE LENGTHS
- I. DIMENSIONS (OUTSIDE):
  - LONGITUDINAL: 29±1.27mm
  - RADIAL: 20±0.762 mm
  - TRANSVERSE: 12±0.762mm
  - WEDGE: 30±5 ARC-MINUTES
  - BEVEL: 45°, (D+2)/200°NOMINAL
- J. THE HEATING AND COOLING SURFACES ARE 20MM X 12MM. THE OPTICAL PATH IS THROUGH THE 29mm x 20mm SURFACES.
- K. FROSTED INSIDE SURFACE OF THE BASE OF THE CUVETTE FOR UNIFORM NUCLEATION.
- L. GENERAL CONSTRUCTION SHALL ADHERE TO SPECIFICATION REQUIRED FOR COMMERCIAL QUALITY SPECTROSCOPY CELLS.
- M. FILL TUBE CONTRACTION DIAMETER SHALL BE .7±.15 mm.
- N. FUSED JOINT.

Tubing Specifications: Quartz Tubing

CAST-01 REV1

AS REQD	-05	TUBING	4.0±.1mm OD x 2.0±.1mm ID				
AS REQD	-03	PLATE	2.0±.1mm THK				
QTY.	PART NO.	PART NAME	DESCRIPTION				
BILL OF MATERIAL							
TOLERANCES UNLESS OTHERWISE SPECIFIED		THE UNIVERSITY OF TENNESSEE SPACE INSTITUTE TULLAHOMA, TENNESSEE 37388					
ANGULAR		CAST CUVETTE					
LINEAR DIM. IN							
FRACTIONS							
TENTHS							
HUNDREDTHS							
THOUSANDTHS							
SHOP STANDARDS <input type="checkbox"/>		SCALE	NAME	DATE	APPRD.	NAME	DATE
		3 : 1	DRAWN: T RIDDLE	9-29-88			
		CONTRACT NUMBER	CHECKED:				
		NAS8-37292					
		PROJECT NO.	SIZE	DRAWING NO.	REV.	SHEET	
		R02-434502	C	CAST-01	1	1	
						OF 1	

Figure 12. Scale drawing of the quartz cuvette (Part 2, specifications).



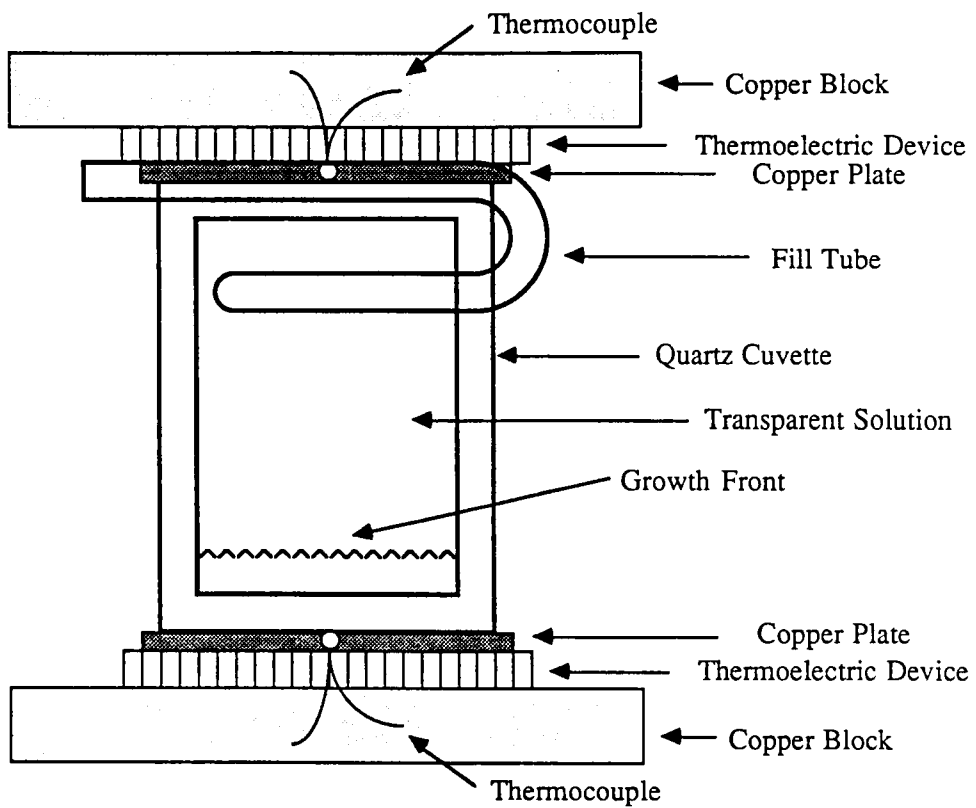
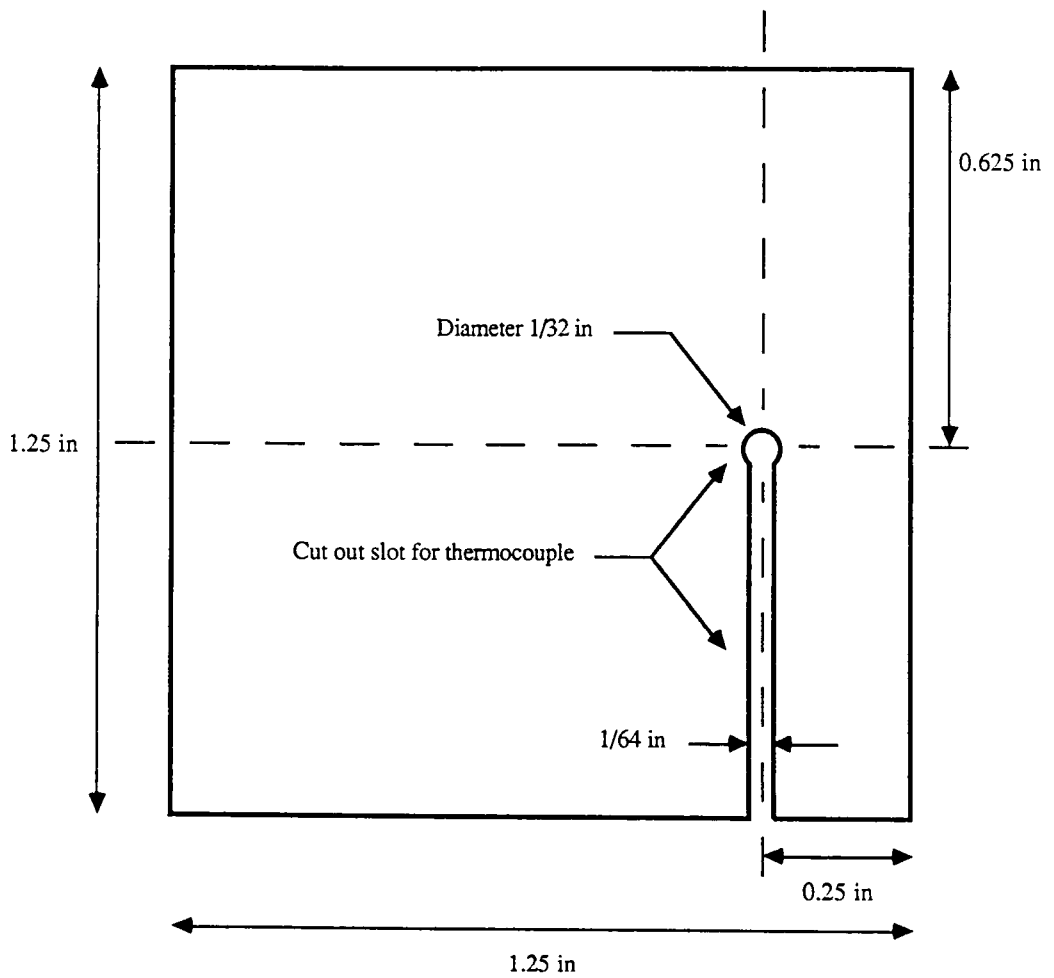


Figure 13. The cuvette assembly. Adapted from [12].





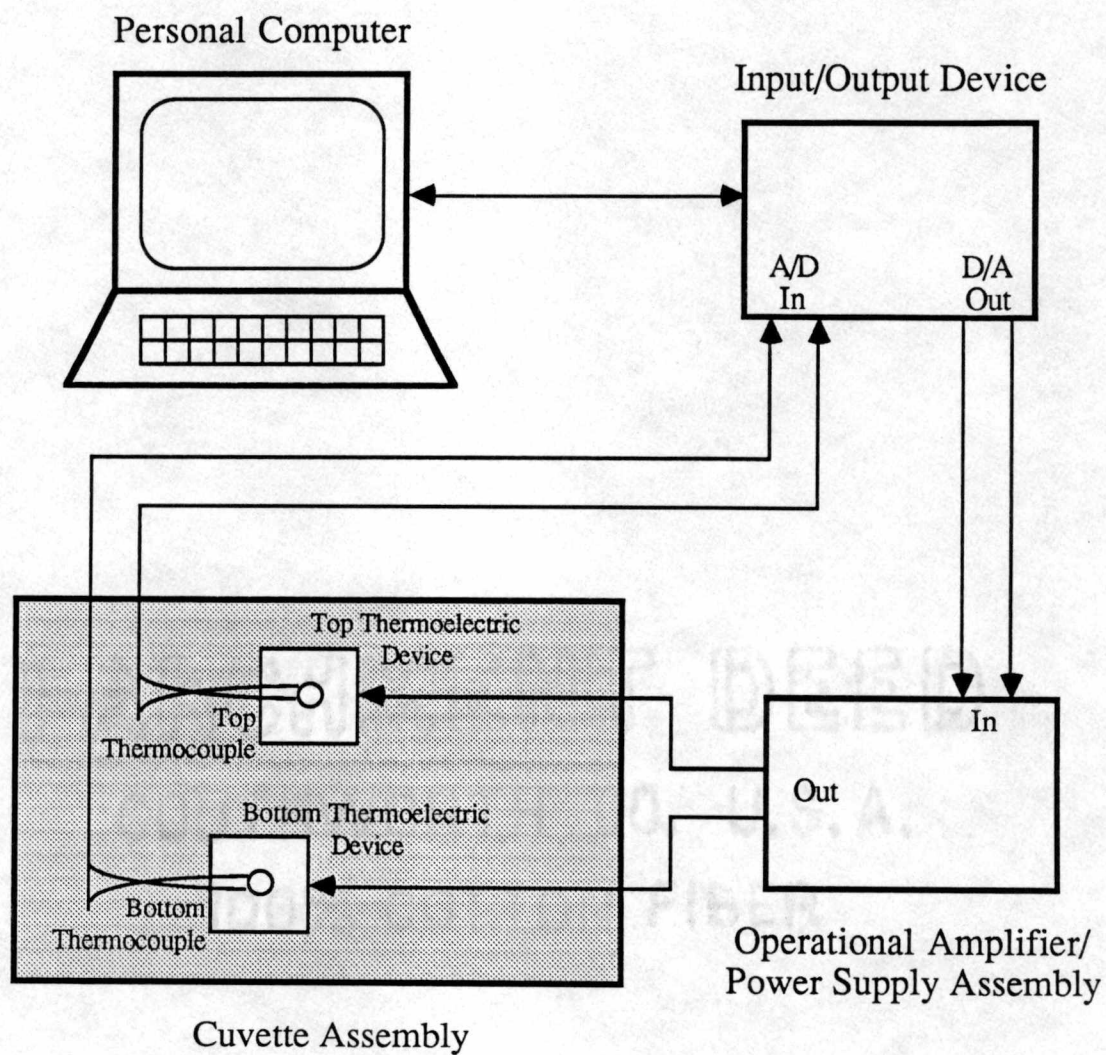
Material: Copper  $2/100$  in thickness

Figure 15. Scale drawing of the copper plate slotted for a thermocouple.

Temperature control and measurement for the solidification experiments were accomplished with the control system shown in Figure 16. A personal computer executed a BASIC program to control and record temperatures at the top and bottom of the cuvette. An input/output device, manufactured by Keithley, acquired temperature data from the thermocouples and passed this information to the computer. The computer then calculated voltages that should be applied to the thermoelectric devices to correct the temperatures. This information was routed through the input/output device, amplified by the op amp assembly, and passed onto the thermoelectric devices, which responded to achieve the desired temperatures.

The solidification assembly and control system have been described previously. For more information, see Gray [12] and Hopkins [2]. The equipment list for the control system is given in Appendix 2.

All solidification experiments proceeded in the same general way, as follows. A temperature gradient was applied to the cuvette by setting the top TED to be warmer than the bottom TED. This temperature gradient was held for a specified length of time, to allow the solid-liquid region at the bottom of the cuvette to approach equilibrium. At the end of the hold time, the temperatures of both TEDs were lowered at a specified cooling rate. As solidification proceeded, changes in the refractive index of the  $\text{NH}_4\text{Cl-H}_2\text{O}$  solution were observed with the techniques of interferometry and holography. Later discussion of the experiments gives the specifics regarding parameters set by the control system: initial top and bottom temperatures, gradient hold time, and cooling rate.



**Figure 16.** The solidification control system. Adapted from [12].

## Interferometry

Mach-Zehnder interferometry was used to acquire images for analysis by the Fourier-transform method. The solidification assembly was placed within the interferometer shown in Figure 17. In this system, a collimated laser beam was split into an object beam and a reference beam by beam splitter B1. As the solidification experiment proceeded, light passing through the cuvette underwent a phase shift due to temperature and concentration changes within the solution. Beam splitter B2 recombined this object beam with the undisturbed reference beam, producing an interference pattern at the lens. An area about seven millimeters high was magnified and imaged onto the camera. The entire interferometer was mounted on an optical table with a pneumatic vibration isolation system. The equipment list for the interferometer is given in Appendix 2.

Along the height of the cuvette, the intensity pattern at the camera was given by the general expression:

(Eq. 76.)

$$g(y) = a(y) + b(y) \cos [\phi_r(y) + \phi_o(y)],$$

where  $\phi_r(y)$  is the phase of the reference beam and  $\phi_o(y)$  is the phase of the object beam.

The following procedure was used to produce the interferograms analyzed later by the Fourier-transform method. Before mounting the cuvette in the

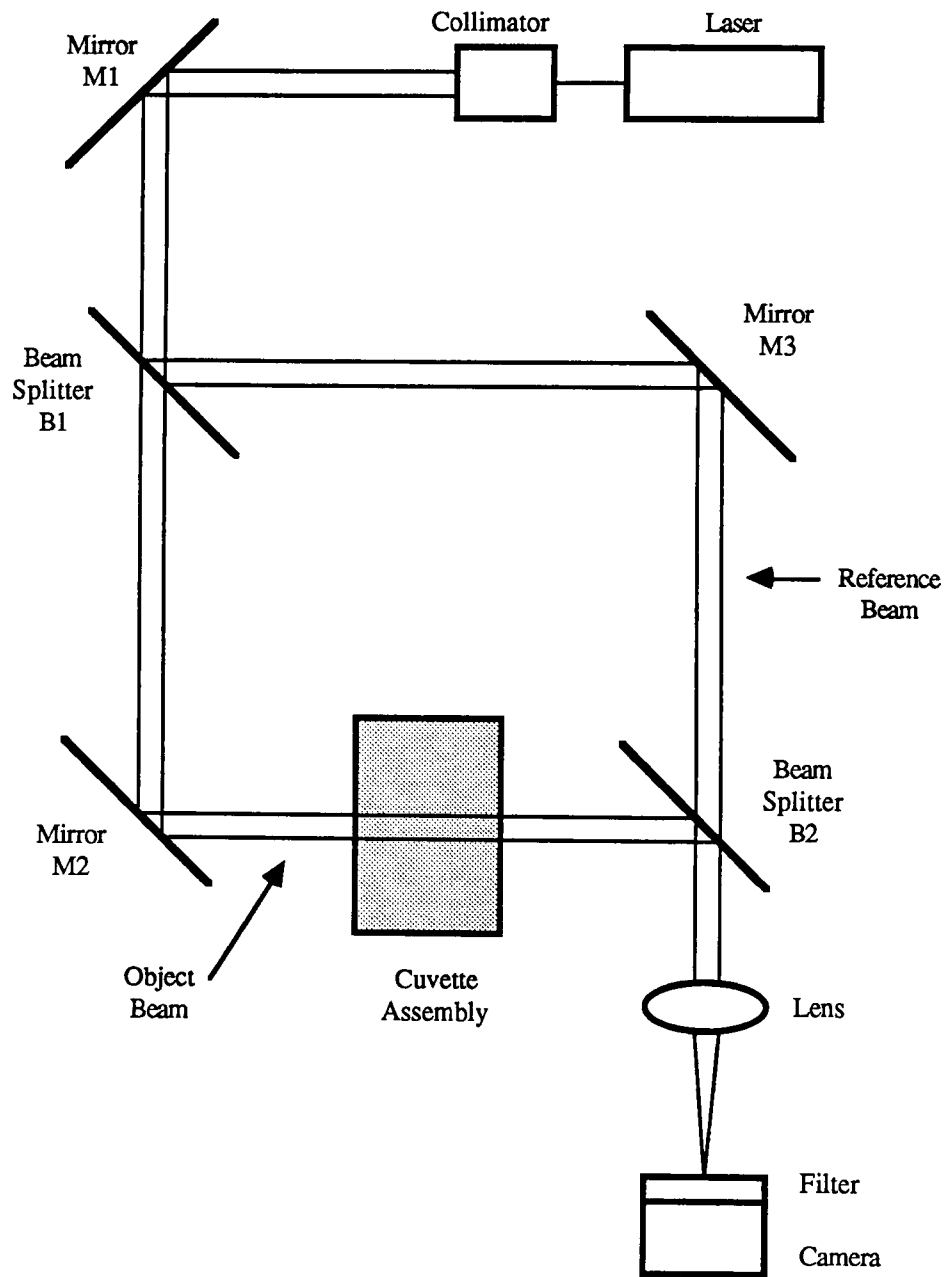


Figure 17. Optics system for interferometry.

solidification assembly, the interferometer was nulled, that is, the object beam and the reference beam were adjusted until no fringes were present. The reference mirror, mirror M3 in Figure 17, was then deflected to create horizontal, finely spaced tilt fringes. The tilt fringes appeared as a pattern of bright and dark bands with uniform spacing. These fringes contained the carrier frequency information used in the Fourier-transform method, so the image is referred to as the carrier image. With  $\phi_R(y) = \phi_C(y)$ , where  $\phi_C(y)$  is the linear phase of the carrier image, and  $\phi_O(y) = 0$ , the intensity pattern at the camera was:

(Eq. 77.)

$$g_C(y) = a(y) + b(y) \cos [\phi_C(y)].$$

The cuvette was then filled with solution, placed in the solidification assembly, and allowed to sit for one hour. During that time the solution did not nucleate, that is, it was completely liquid. At the end of the hour it was assumed that the solution was at a uniform temperature. Thus any phase shift detected by the interferometer was due to imperfections in the quartz cuvette walls, not to changes in concentration or temperature. The resulting image is referred to as the base image. With  $\phi_R(y) = \phi_C(y)$ , and  $\phi_O(y) = \phi_B(y)$ , where  $\phi_B(y)$  was the phase change due to the cuvette walls, the intensity pattern was:

(Eq. 78.)

$$g_B(y) = a(y) + b(y) \cos [\phi_B(y) + \phi_C(y)].$$



Next the solidification control system was used to lower the TED temperatures to approximately 0 °C, and the solution then nucleated. Over the course of several days, the control system was operated to grow and smooth the crystal interface. The solidification experiments for this project were then conducted, as discussed previously. During the course of a solidification run,  $\phi_R(y) = \phi_C(y)$ , and  $\phi_O(y) = \phi_E(y) + \phi_B(y)$ , where  $\phi_E(y)$  was the phase change due to the experiment. The intensity pattern recorded at the camera for an experimental image was then:

(Eq. 79.)

$$g_E(y) = a(y) + b(y) \cos [\phi_E(y) + \phi_B(y) + \phi_C(y)].$$

### Holographic Interferometry

Holographic interferometry was also used to acquire images for analysis by the Fourier-transform method. Procedures for recording and reconstructing holograms are outlined below.

#### Recording of Holograms

A portable version of the control system discussed earlier was used to conduct solidification experiments in the Holographic Ground System (HGS) at NASA Marshall Space Flight Center in Huntsville, Alabama. A solidification assembly was installed within the HGS optics system, as depicted in Figure 18. Unlike photography, which records only the amplitude of incident light,

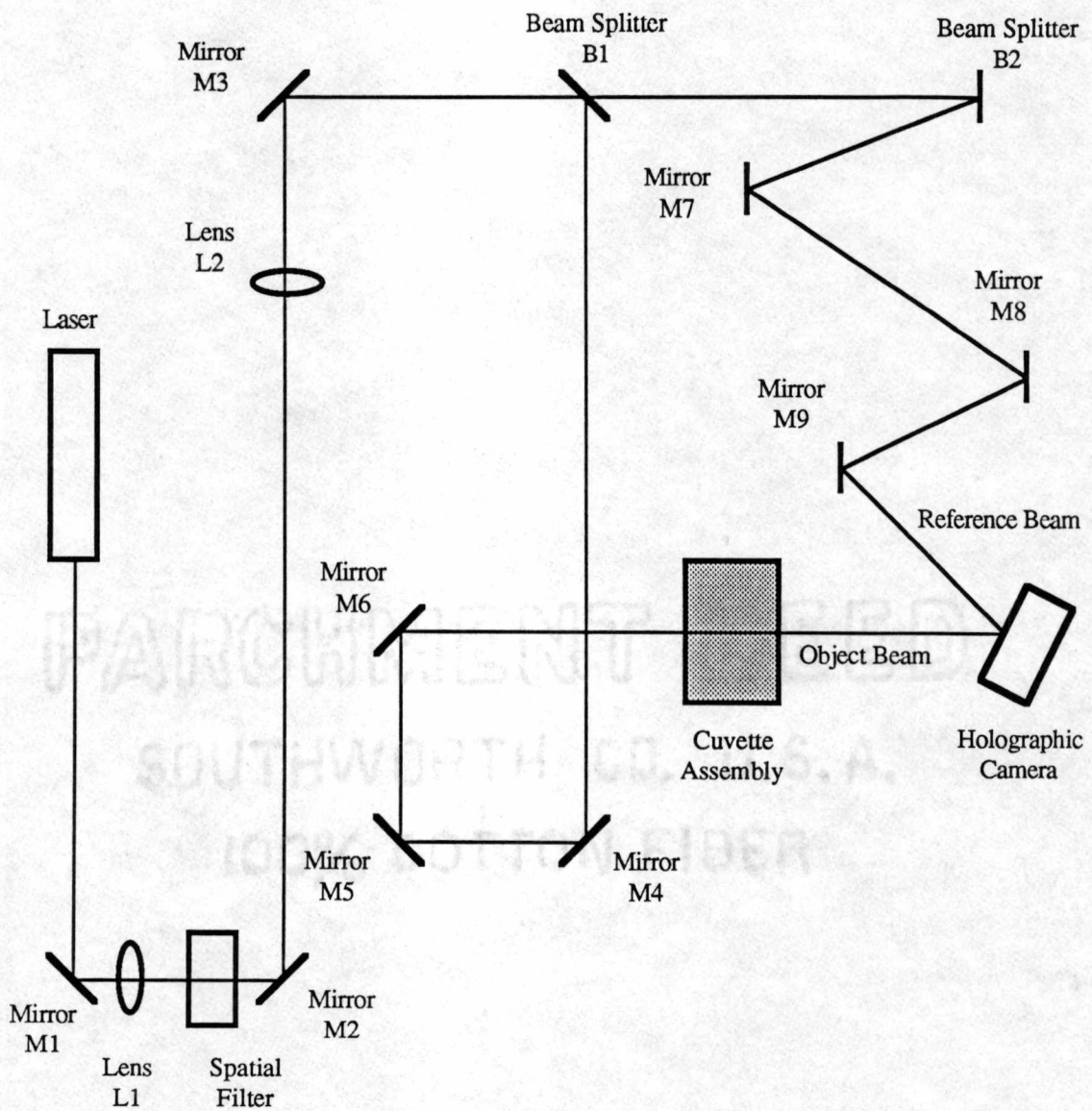


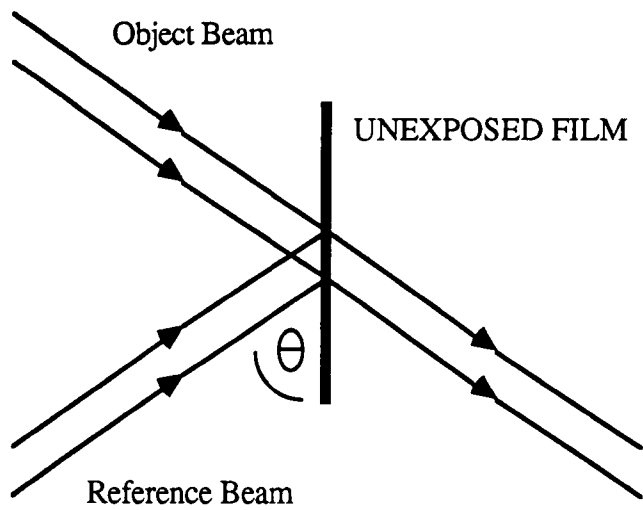
**Figure 18.** Optics system for holography at the Holographic Ground System. Adapted from [16].

holography records both amplitude and phase. Light passing through the cuvette underwent a phase shift, and when it was combined with the reference beam, interference resulted, creating a diffraction pattern at the holographic camera. The camera recorded the diffraction pattern, or hologram, on 70 millimeter high speed holographic film, Kodak's SO-253 with ESTAR base. As opposed to glass plate holograms, SO-253 is a flexible acetate film. Holograms were exposed for 50 milliseconds, and were developed with Kodak D-19, per the manufacturer's instructions.

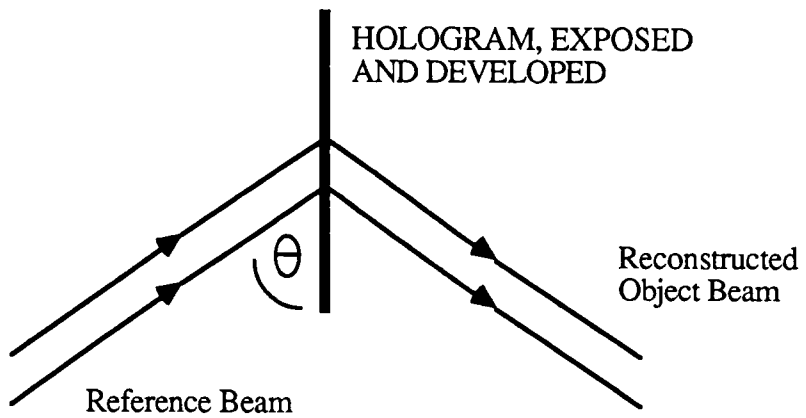
### Reconstruction of Holograms

Holographic reconstruction is a process in which a beam of light with the same amplitude and phase as the original object beam is produced. To achieve this, a beam duplicating the original reference beam is passed through the hologram. The angle at which the reference beam strikes the hologram must be the same as when the hologram was recorded. See Figure 19. The hologram then acts as a diffraction grating, deflecting rays of the reference beam to reproduce the original object beam.

An optical system that performs both reconstruction and Mach-Zehnder interferometry was designed; this holographic interferometry system is shown in Figure 20. (The term holographic interferometry encompasses several techniques, e.g. real time holographic interferometry, double exposure holography, etc. [32] In this project the term holographic interferometry refers to the type of system shown in Figure 20, holographic interferometry with a single hologram.) The



## RECORDING A HOLOGRAM



## RECONSTRUCTING A HOLOGRAM

Figure 19. Recording and reconstructing a hologram.

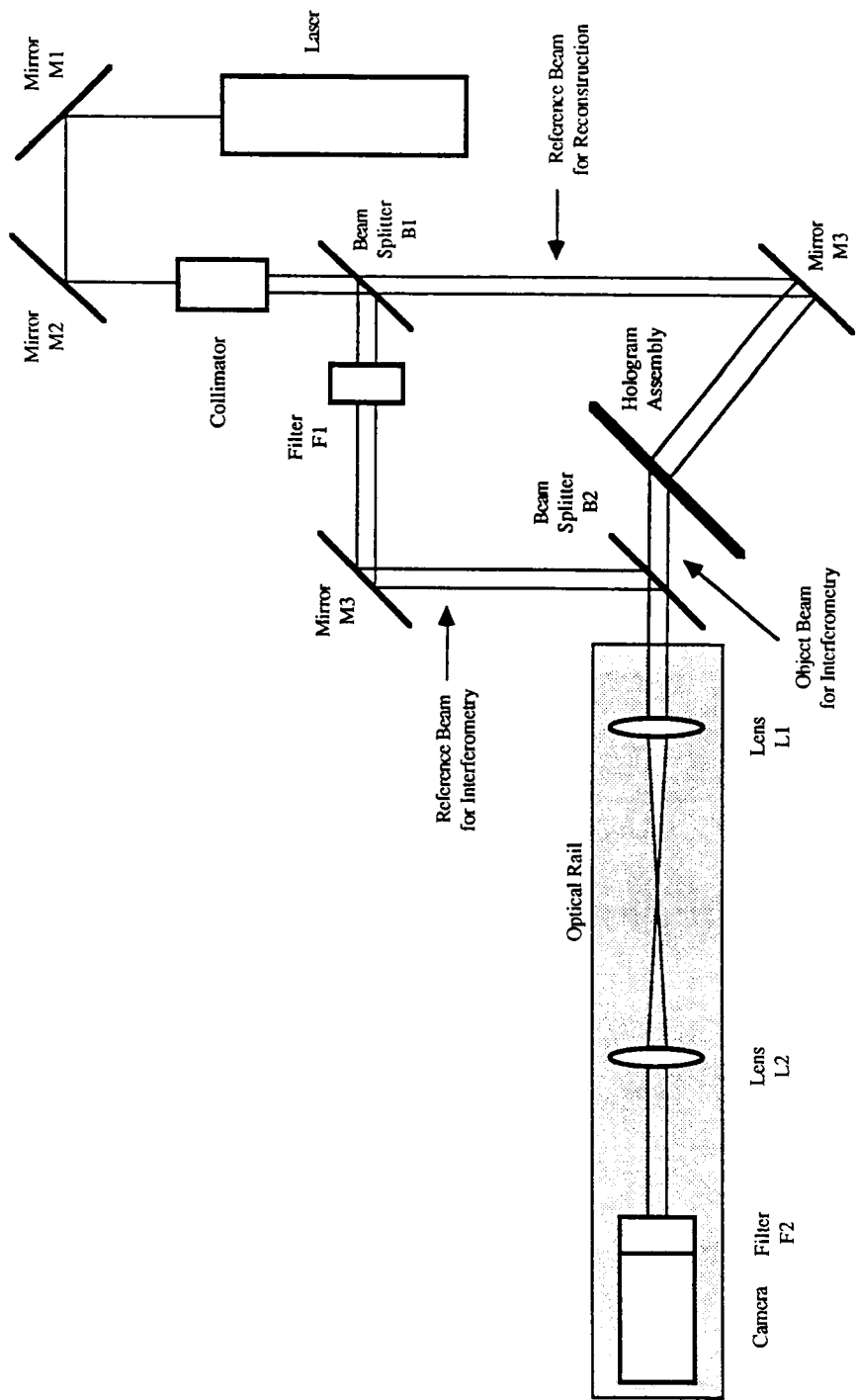
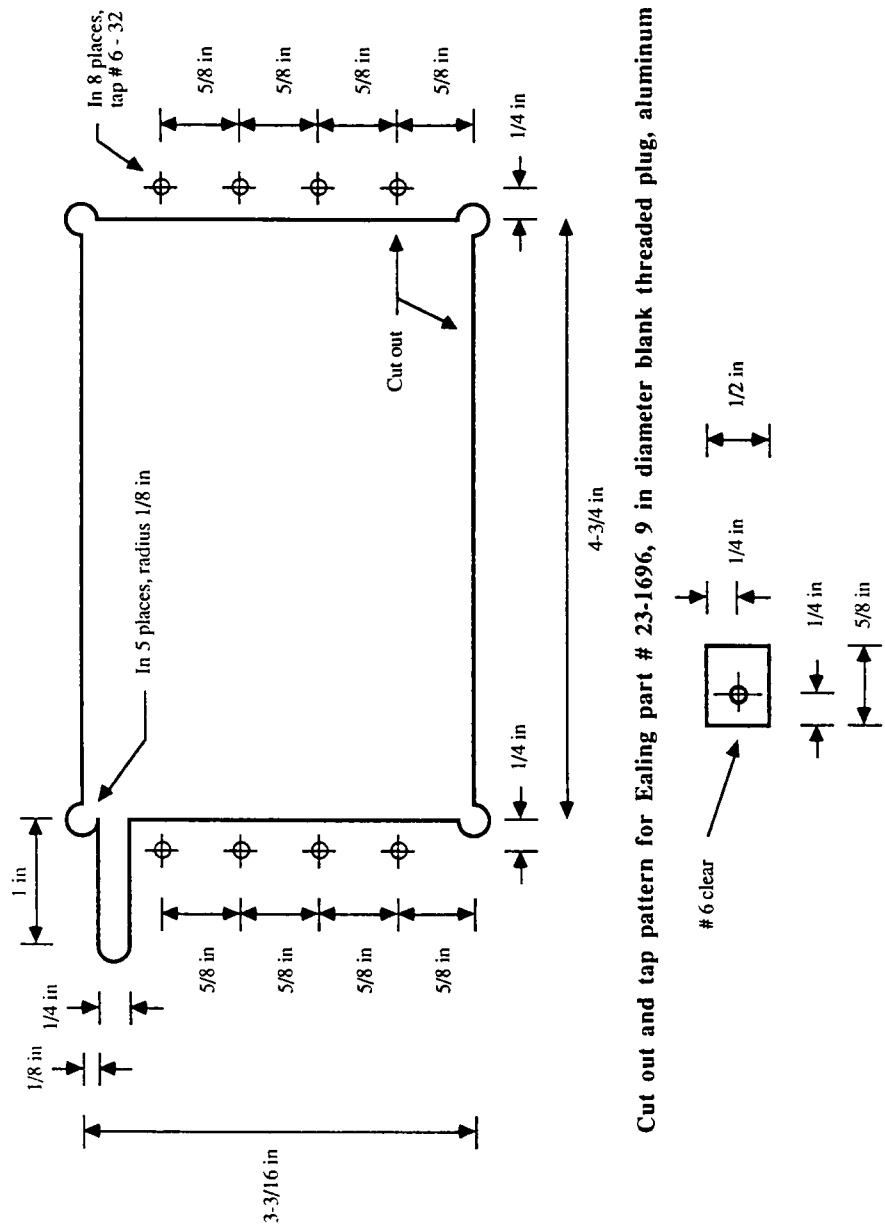


Figure 20. Optics system for holographic interferometry.

hologram assembly, which consisted of a glass window mounted in an angle bracket, was positioned via a tilt table and a rotation stage. Specifications for mounting the window are given in Figure 21. It was necessary to reposition some of the optical components during the holographic alignment process. Rather than bolting these components to the optical table, they were mounted on a rail, which could be moved easily. The optical table was equipped with a pneumatic vibration isolation system.

In order to mount a hologram, a trough was etched into the glass window and connected to a vacuum pump. See Figure 22. Upon activation of the pump, the hologram was held firmly in place via suction. To assure proper alignment of the hologram, the procedure in Figure 23 was followed, with the reference beam for interferometry blocked. The beam emanating from the hologram became the object beam for interferometry. The reference beam was unblocked, and neutral density filters were used to match its intensity to that of the object beam. The reference beam was then combined with the object beam by beam splitter B2. See Figure 20. The resulting interference pattern was magnified via the optical rail lenses, and an area about five millimeters high was imaged onto the camera. The equipment list for the holographic interferometry system is given in Appendix 2.

Interferograms for analysis by the Fourier-transform method were produced as follows. The hologram of interest was mounted and aligned as discussed above. The camera was then positioned to show an open air region outside the cuvette, and the interferometer was nulled. It was not possible to null the



Cut out and tap pattern for Ealing part # 23-1696, 9 in diameter blank threaded plug, aluminum

Clamp for mounting optical window in above, material aluminum thickness 1/8 in

Figure 21. Scale drawing of the mount for the optical window.

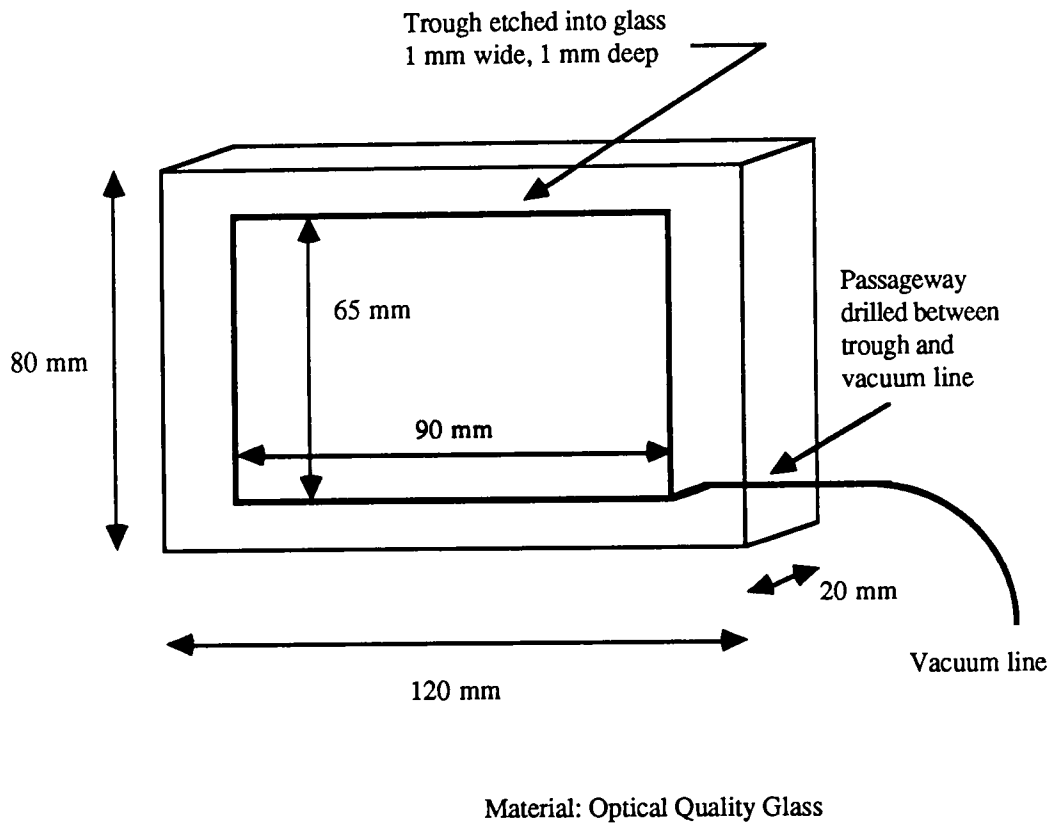
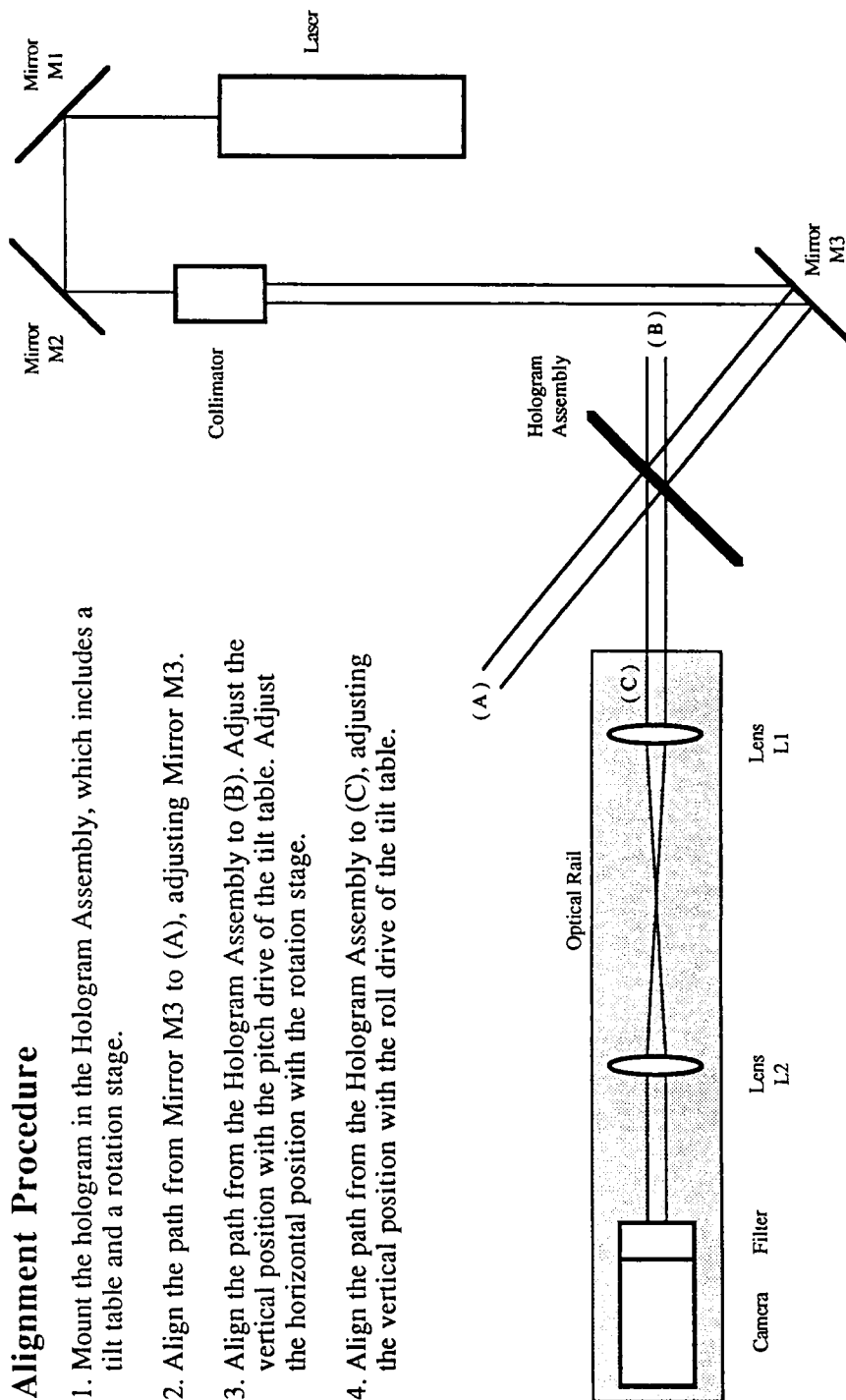


Figure 22. Optical window etched for a vacuum line.





### Alignment Procedure

1. Mount the hologram in the Hologram Assembly, which includes a tilt table and a rotation stage.
2. Align the path from Mirror M3 to (A), adjusting Mirror M3.
3. Align the path from the Hologram Assembly to (B). Adjust the vertical position with the pitch drive of the tilt table. Adjust the horizontal position with the rotation stage.
4. Align the path from the Hologram Assembly to (C), adjusting the vertical position with the roll drive of the tilt table.

Figure 23. Alignment procedure for holographic reconstruction.

interferometer without the hologram in place, since it was the hologram that created the object beam. The reference mirror, Mirror M3 in Figure 20, was deflected to create horizontal tilt fringes. The resultant image, the carrier image, was recorded. With  $\phi_r(y) = \phi_c(y)$  and  $\phi_o(y) = 0$ , the intensity pattern at the camera was:

$$g_c(y) = a(y) + b(y) \cos [\phi_c(y)].$$

As previously discussed,  $\phi_r(y)$  was the phase of the reference beam,  $\phi_c(y)$  the phase of the carrier image, and  $\phi_o(y)$  the phase of the object beam.

The camera was then panned to focus on the interior of the cuvette, where the hologram had recorded the solidification taking place. With  $\phi_r(y) = \phi_c(y)$ , and  $\phi_o(y) = \phi_E(y) + \phi_B(y)$ , the intensity pattern at the camera was:

$$g_E(y) = a(y) + b(y) \cos [\phi_E(y) + \phi_B(y) + \phi_c(y)].$$

In this expression,  $\phi_E(y)$  was the phase change due to the solidification experiment, and  $\phi_B(y)$  was the base phase, the phase change due to the cuvette walls. Unlike the case discussed in the Interferometry section, it was not possible to isolate the base phase because a hologram depicting  $\text{NH}_4\text{Cl-H}_2\text{O}$  solution at uniform temperature and concentration was not available.

## Image Translation

Images created in the interferometry and holographic interferometry systems above were recorded with a videocassette recorder (VCR) on VHS format videotape. The videotape was carried by hand to another VCR attached to an image processing system. The image processor ran Data Translation's DT-IRIS software on a personal computer. A frame grabber was used to digitize selected video frames to 512 by 512 pixels. The image processor offered additional features used in this project: pixel location via a mouse and mouse pad, image zooming, and contrast enhancement.

## Fourier-transform Method to Measure Concentration

### Overview

FORTTRAN programs were written to analyze the solidification images digitized by the image processor. The Fourier-transform method was used to decode phase information from the intensity patterns in the images. Phase was then converted to a concentration profile.

The programs analyzed intensity data along a single column in the image. This 1-D approach was chosen for several reasons. Assuming a smooth and flat interface, the concentration profiles were expected to be similar across the width of the cuvette; that is, the data analyzed was 1-D in nature. The 1-D analysis could be run quickly on the personal computer available, whereas a 2-D approach would have required additional memory for array processing. Also, the 1-D

approach was easier to program than a 2-D implementation. In this initial attempt with the Fourier-transform method, it was thought best to implement in one dimension first, perhaps extending to two dimensions in the future.

The analysis was broken up into several programs so that results could be inspected before proceeding to the next part of the procedure. In addition, this approach allowed pieces of the analysis process to be applied to other problems. For example, determining the phase of an image need not always be followed by determining its concentration. The individual programs were chained together by data files, named with the suffix ".DAT."

Input to the programs was the digitized image to be analyzed, but additional information was supplied interactively. Some of this information, such as pixel location of the interface, was obtained at the image processor. Other required inputs, such as frequency cutoffs, were determined through inspection of output plots. All output plot files were named with the suffix ".PLT."

The flowchart in Figure 24 and Figure 25 illustrates the relationships among the individual programs. Program GET\_COL saves a selected column of the image to be analyzed. Program AUTO1 produces a Fourier plot so the user can determine cutoff frequencies, while program AUTO2 filters the Fourier data to obtain the phase of the image. Program CONCEN1 converts phase to index of refraction, then program CONCEN2 subtracts temperature effects from the index of refraction, yielding a concentration profile.

Program AUTO2 requires information about the carrier phase,  $\phi_c(y)$ . An image column containing carrier fringes is acquired with program GET\_COL,

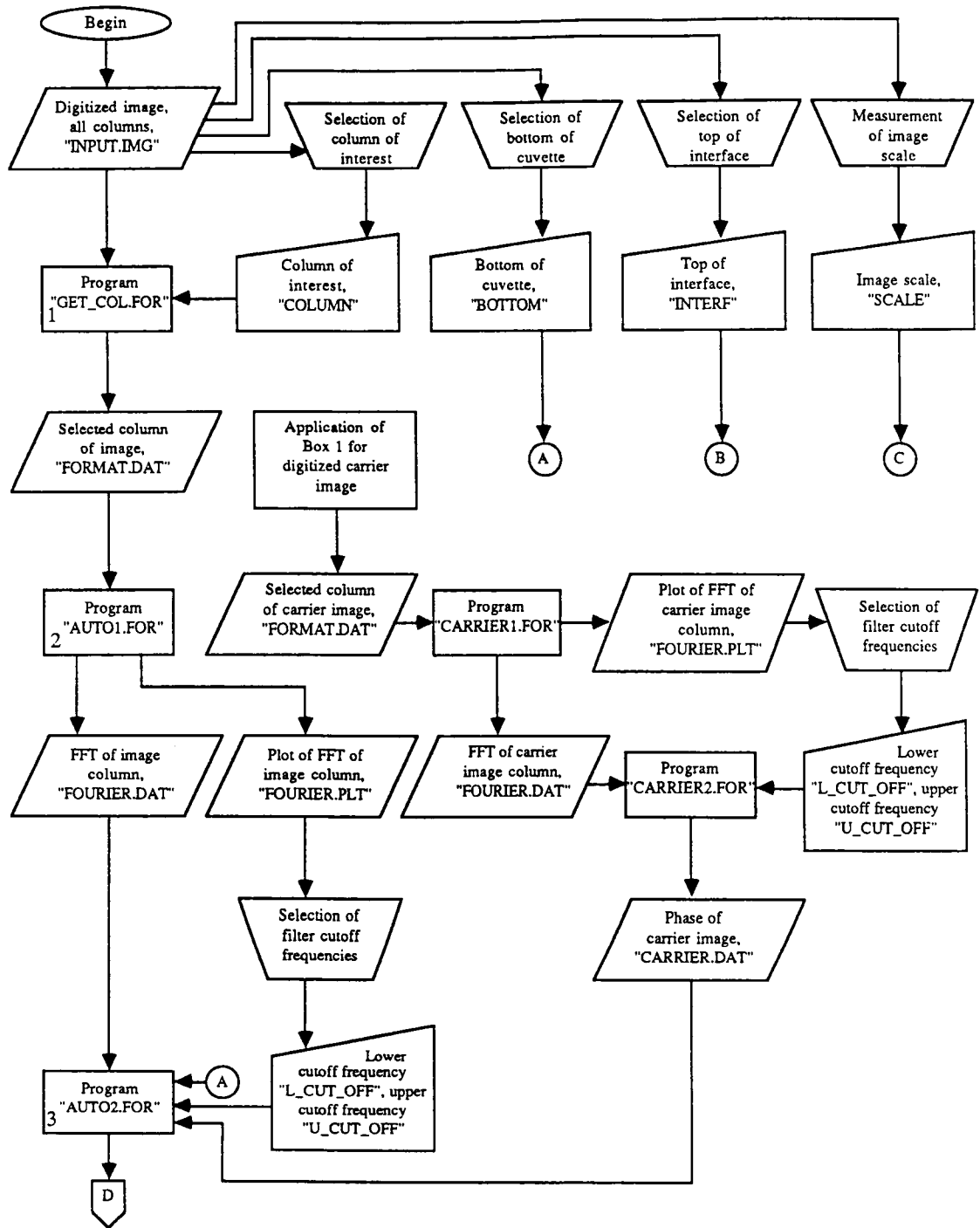


Figure 24. Flowchart for FORTRAN programs (Part 1).

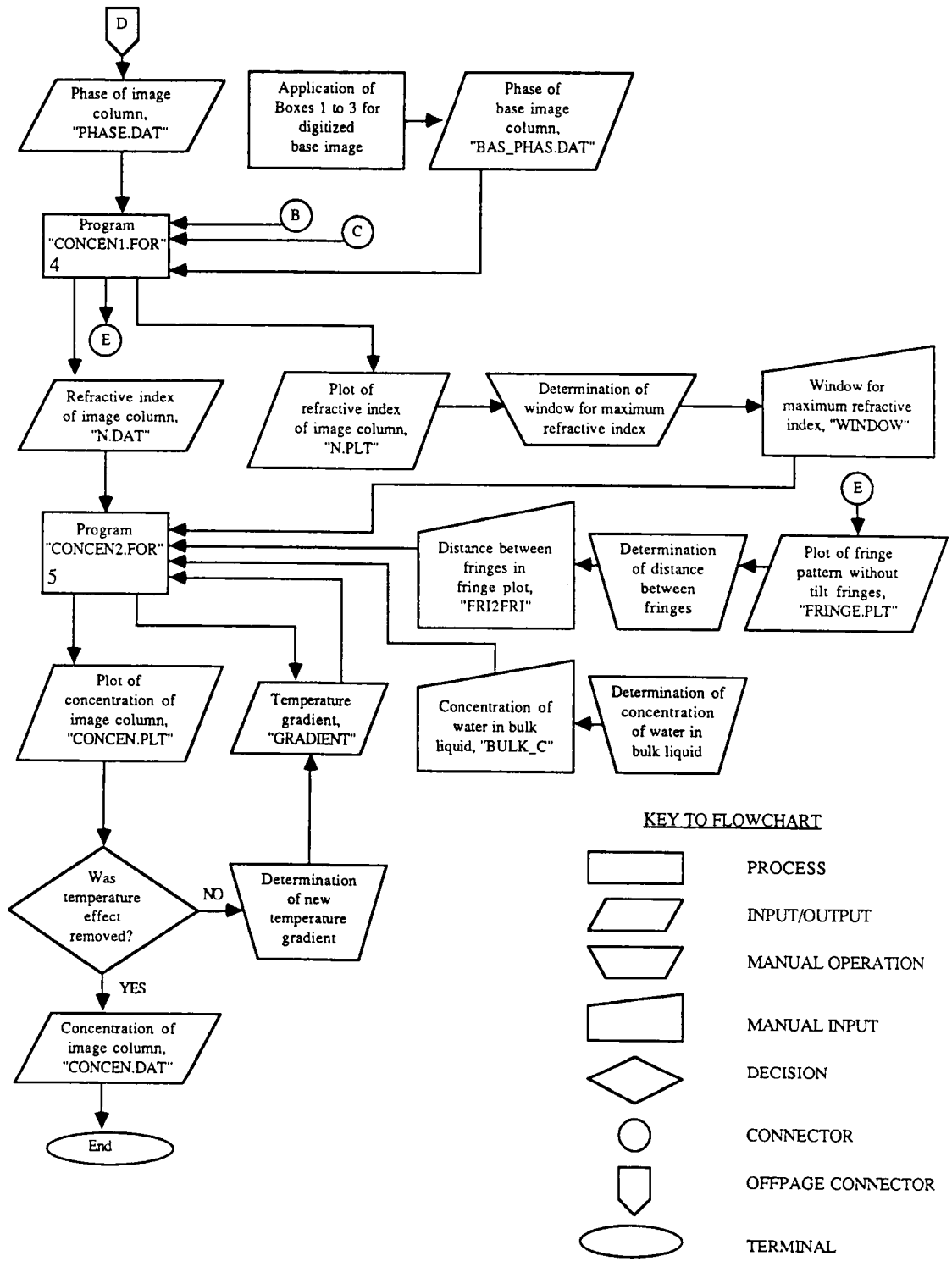


Figure 25. Flowchart for FORTRAN programs (Part 2).

then analyzed with programs CARRIER1 and CARRIER2. Program CARRIER1 is similar to AUTO1: it produces a Fourier plot so the user can determine cutoff frequencies. Program CARRIER2 is similar to program AUTO2 in that it filters the Fourier data to obtain the phase of the image. The phase information is written to file CARRIER.DAT, then accessed by program AUTO2.

Program CONCEN1 requires information about the base phase,  $\phi_B(y)$ . The base phase image column is acquired with program GET\_COL, then analyzed as usual with programs AUTO1 and AUTO2. The user renames the phase output file "BAS\_PHAS.DAT." Program CONCEN1 then accesses the file to incorporate base phase information into the analysis procedure.

The complete analysis process for a particular run is outlined below, including the programs executed and the user operations performed. Figures are included to illustrate the procedure. Program listings, as well as lists of user inputs, file inputs, and file outputs, are given in Appendices 3 through 9.

#### Complete Analysis for Run 64 at 45 Seconds

Run 64 was conducted as discussed earlier in the Solidification and Interferometry sections. A solution of 28 wt%  $\text{NH}_4\text{Cl}$  in  $\text{H}_2\text{O}$  was used. The top temperature during the gradient hold was 56.5 °C, and the bottom temperature was 19 °C. At the end of a one hour gradient hold, the interface height was 0.30 millimeters. The cooling rate was 2 °C/minute, and the time selected for analysis was 45 seconds after cooling began.

- 1) Perform user operations for all images.

Before any programs were executed, specific features in each image were identified at the image processor. Figure 26 shows slices of the images analyzed for this run: the carrier image, the base image, and the experimental image. The mouse and mouse pad were used to locate the column of interest for all three images. For the base image and the experimental image, the pixel location at the bottom of the cuvette was also noted. For the experimental image, the pixel location at the interface was recorded.

An image scale for this run was determined. Before the run took place, a ruler with 0.4 millimeter graduations was placed in the object plane and videotaped. The image was digitized, and the pixel-to-pixel distance between graduations was noted. In this way a scale giving pixels per millimeter was calculated.

Several techniques were used to increase the accuracy of feature location. Due to the presence of fringes in the interferometric images, identification of the cuvette bottom and the interface was difficult. For this reason, images containing only the object beam were used to locate these features. Contrast enhancement was applied to improve the appearance of edges, while image zooming permitted very close examination of the features. In addition, all feature locations taken with the mouse were checked against those suggested by intensity plots of the same region.

The image processor numbered rows and columns from zero to 511. For greater ease in array processing, however, the FORTRAN programs were written



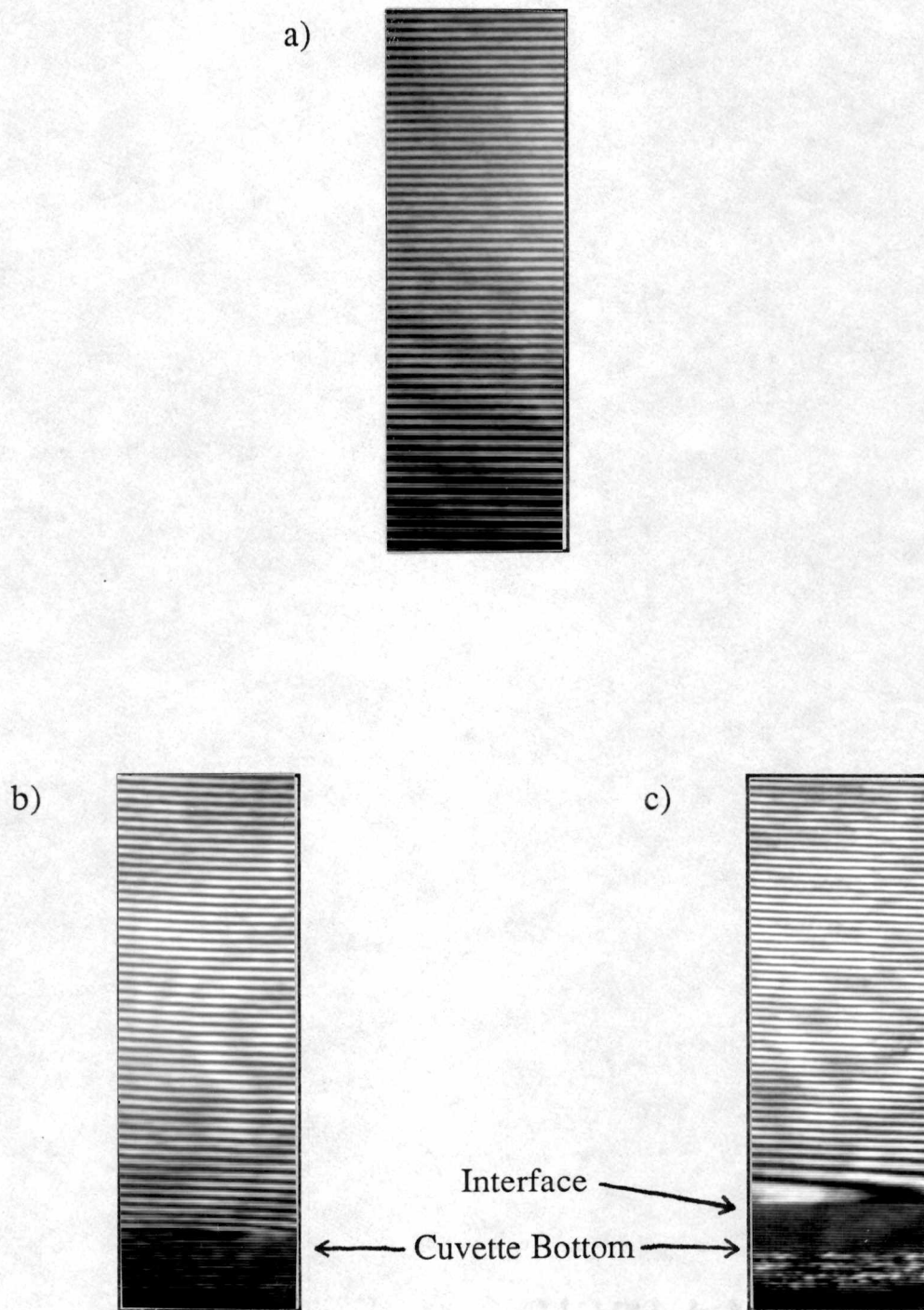


**Figure 26.** Slices of the images analyzed. a) The carrier image. b) The base image. c) The experimental image for Run 64 at 45 seconds.

to use values from one to 512. For this reason, the locations that were recorded for the column, the cuvette bottom, and the interface were one greater than the values given by the mouse. Incrementing the mouse values in this way provided the correct conversion between the two numbering systems.

The camera and solidification assembly were not disturbed during the time the images for this run were recorded. For this reason, the same column, 155, was used for all three images. The bottom of the cuvette was located at pixel 401, and the interface was located at pixel 379. (Pixel locations with lower numbers appear nearer to the top of the image.) These values were supplied interactively when the analysis programs prompted.

2) Execute program GET\_COL for the carrier image.

Program GET\_COL read the image to be analyzed, which was written by the image processor to a binary data file. Program GET\_COL then saved a specified column, so that the intensity value of each pixel in the column was available for following programs.

3) Execute program CARRIER1 for the carrier image.

Program CARRIER1 first produced a plot of the intensity of the carrier image,  $g_c(y)$ , given previously in Eq. 77. See Figure 27. The intensity plot illustrates the unwanted irradiance variations  $a(y)$  and  $b(y)$ . [25] Variation in background intensity,  $a(y)$ , can be seen by noting that the average intensity is brighter in the center of the image. Variation in fringe visibility,  $b(y)$ , can be

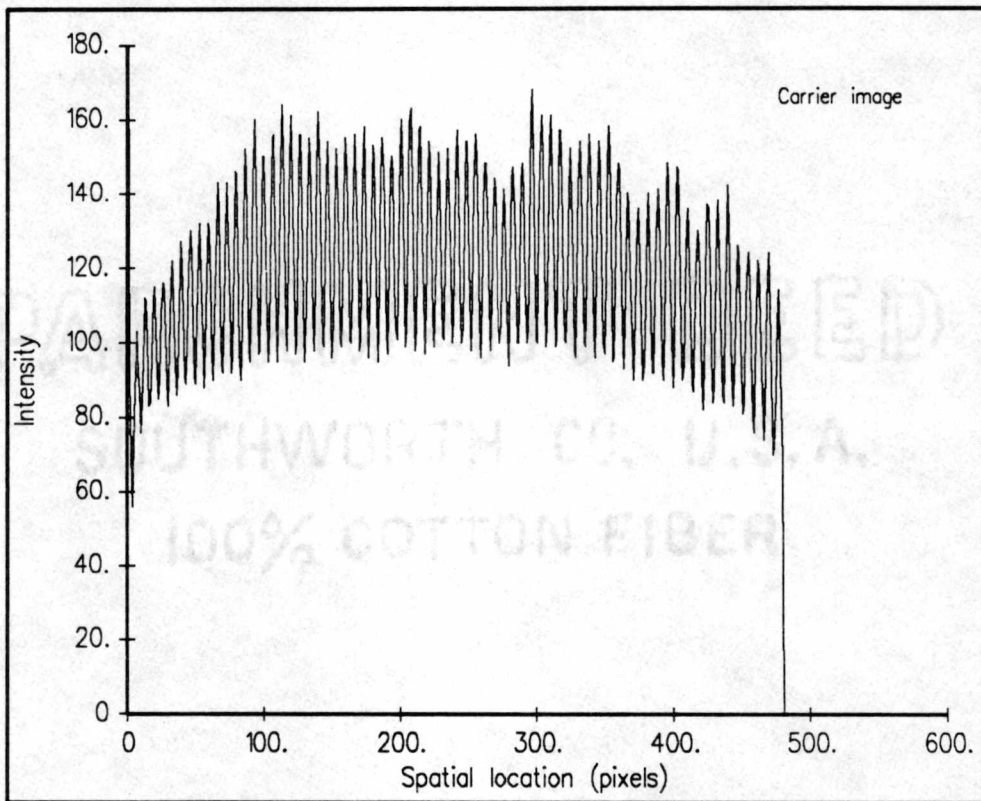


**Figure 27.** Intensity for the carrier image,  $g_c(y)$  vs.  $y$ .

seen in that individual fringes vary in brightness. The Fourier-transform method separates phase from the irradiance variations.

(Notes regarding plots: Spatial domain plots are given versus spatial location ( $y$ ), while Fourier domain plots are given versus spatial frequency ( $f$ ). For those plots given in units of pixels, pixel one marks the top of the image, and pixel 512 the bottom.)

Next, program CARRIER1 produced a plot of the image's 1-D Fourier transform,  $G_c(f)$ . In Figure 28 the trimodal nature of the Fourier transform is easily seen. With reference to Eq. 27, the spectrum  $C(f-f_0)$  has a distinct peak away from the origin. In this plot the peak is located near pixel 90.

(Notes regarding Fourier plots: The discrete Fourier transform has period  $N$ ; [33] here  $N = 512$ . Fourier plots often range from  $-N/2$  to  $+N/2$ , as in Figure 6, but it is also common to plot from the origin to  $N$ , as is done in the Fourier plots given in this work. A consequence of the property of conjugate symmetry of the discrete Fourier transform is that Fourier magnitude plots are symmetric. [33] The Fourier plots in this work show symmetry about the point 257.)

4) Perform user operations for the carrier image.

The Fourier plot produced by program CARRIER1 was inspected, and cutoff frequencies for a lowpass filter were chosen. The cutoff frequencies for the carrier image were 64 and 85.

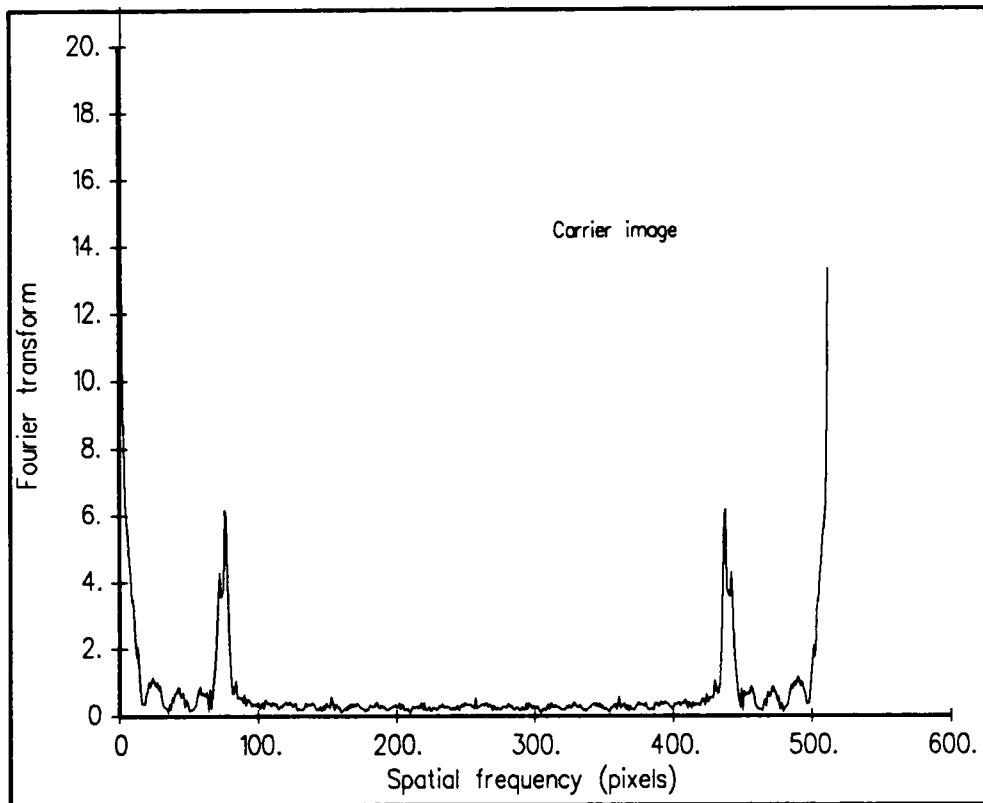


**Figure 28.** Fourier transform for the carrier image,  $G_c(f)$  vs.  $f$ .

5) Execute program CARRIER2 for the carrier image.

The main goal of program CARRIER2 was to apply the Fourier-transform method to determine the carrier phase,  $\phi_c(y)$ , from  $g_c(y)$ , the carrier image. See Eq. 77. The basis of the program was a 1-D version of the method proposed by Bone et al. [28] (See the discussion following Eq. 56.) The Fourier domain filtering required for the method was conducted as follows.

Program CARRIER2 used the cutoff frequencies determined in Step 4) to prepare an ideal lowpass filter,  $I(f)$ , shown in Figure 29. The cutoffs for the ideal lowpass filter were 502 and 12. The ideal lowpass filter was centered at the Fourier domain origin, located at pixel 1. Because the sharp edges in an ideal lowpass filter lead to ringing in the data filtered, [33] the ideal lowpass filter was modified with a Hanning window. In addition to eliminating ringing, this filter design method also eliminated wraparound error in that the Fourier transform of the modified filter was finite in extent.

Modification began by computing the inverse Fourier transform of the ideal lowpass filter,  $i(y)$ , shown in Figure 30. Much of the information regarding the ideal lowpass filter was contained within the first two sidelobes of this plot. The Hanning window was thus designed to extend to this location,  $K = \text{pixel } 68$ . The Hanning window was computed via:

(Eq. 80.)

$$h(y) = 0.5 + 0.5 \cos [\pi y / (K + 1)], \text{ with } |y| < K,$$

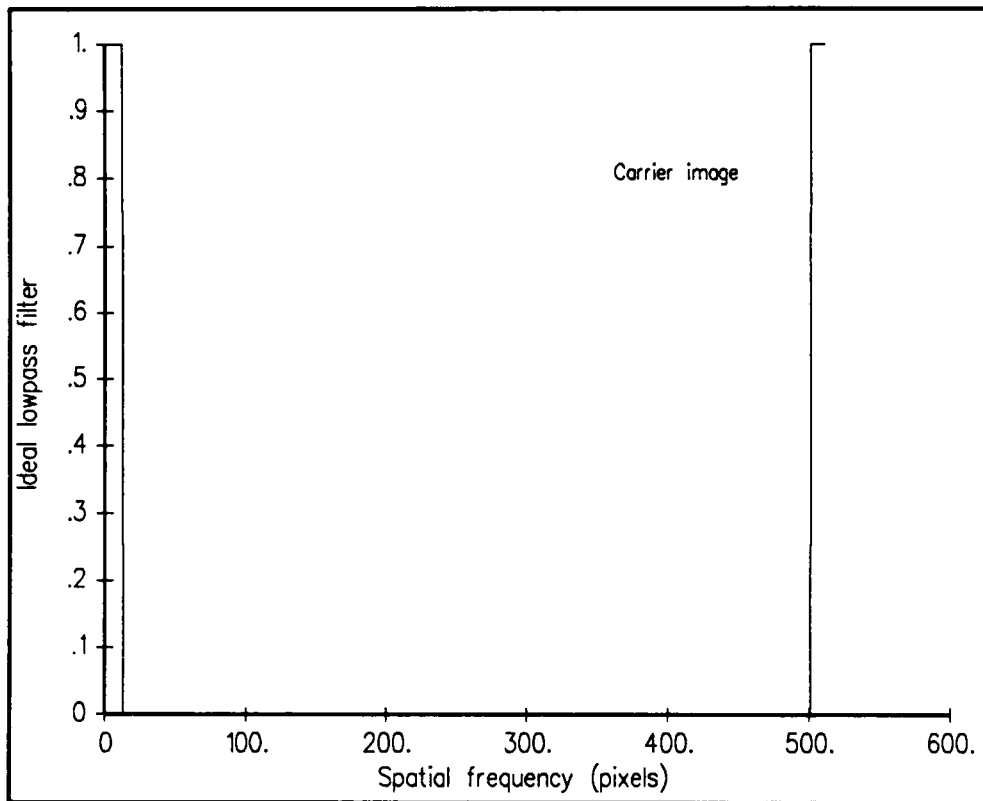
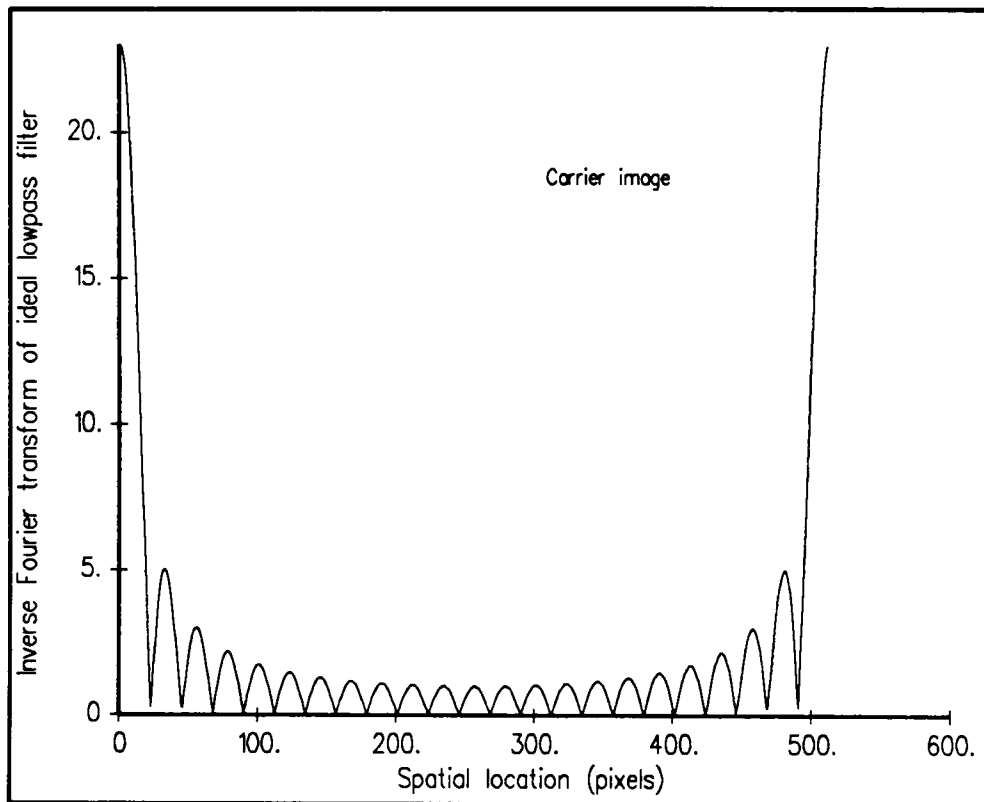


Figure 29. Ideal lowpass filter for the carrier image,  $I(f)$  vs.  $f$ .



**Figure 30.** Inverse Fourier transform of ideal lowpass filter, for the carrier image,  $i(y)$  vs.  $y$ .



and is shown in Figure 31. The inverse Fourier transform of the ideal lowpass filter was then multiplied by the Hanning window, to obtain:

(Eq. 81.)

$$j(y) = i(y)h(y),$$

as shown in Figure 32. Finally, the Fourier transform was applied to yield a modified filter with a gradual dropoff,  $J(f)$ . See Figure 33.

Since all of the filter design steps were conducted at the origin,  $J(f)$  was moved to the location of the passband originally specified by the user, then multiplied by the image's Fourier transform. See Figure 34. In comparing this figure with Figure 28, it can be seen that  $C(f-f_0)$  was filtered. The Fourier domain filtering process was then complete.

The next task for program CARRIER2 was to compute the inverse Fourier transform of  $C(f-f_0)$ , and to calculate the carrier phase with a 1-D form of Eq. 57. In Figure 35 the phase varies over a  $2\pi$  range, from  $-\pi$  to  $\pi$ . A 1-D version of Macy's recurrence procedure was then used to unwrap the phase. [27] (See Eq. 36.) The result is given in Figure 36. The phase of the carrier image was written to file "CARRIER.DAT," for later use in Steps 9) and 13).

The carrier phase was linear, taking the form:

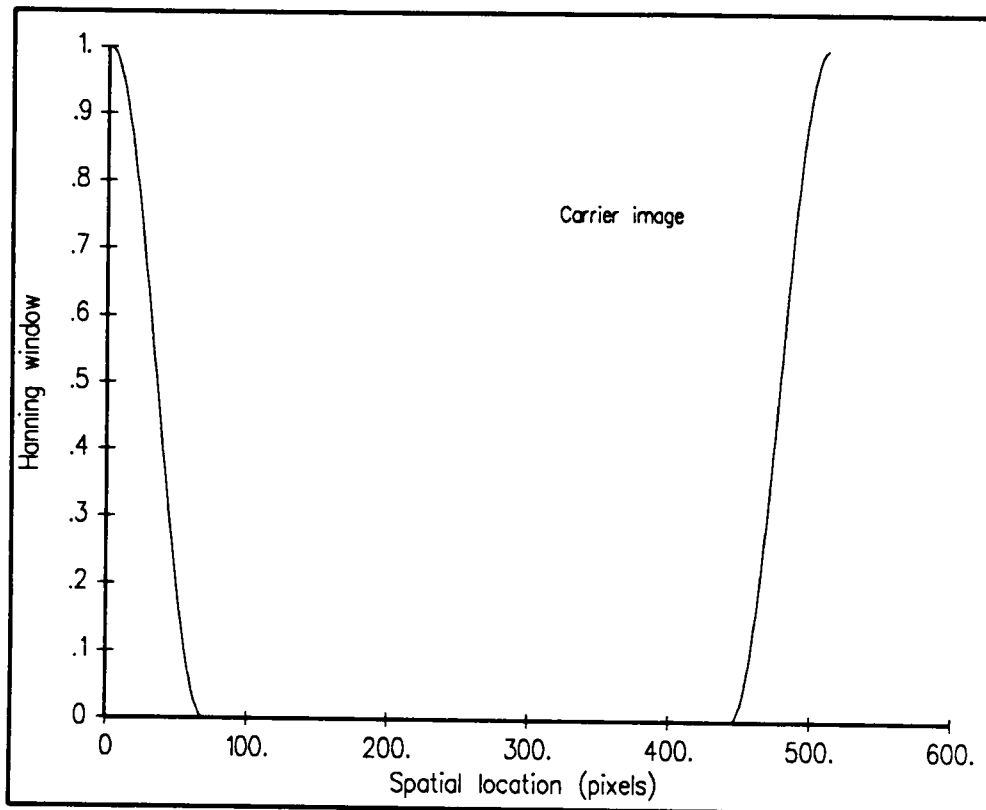


**Figure 31.** Hanning window for the carrier image,  $h(y)$  vs.  $y$ .

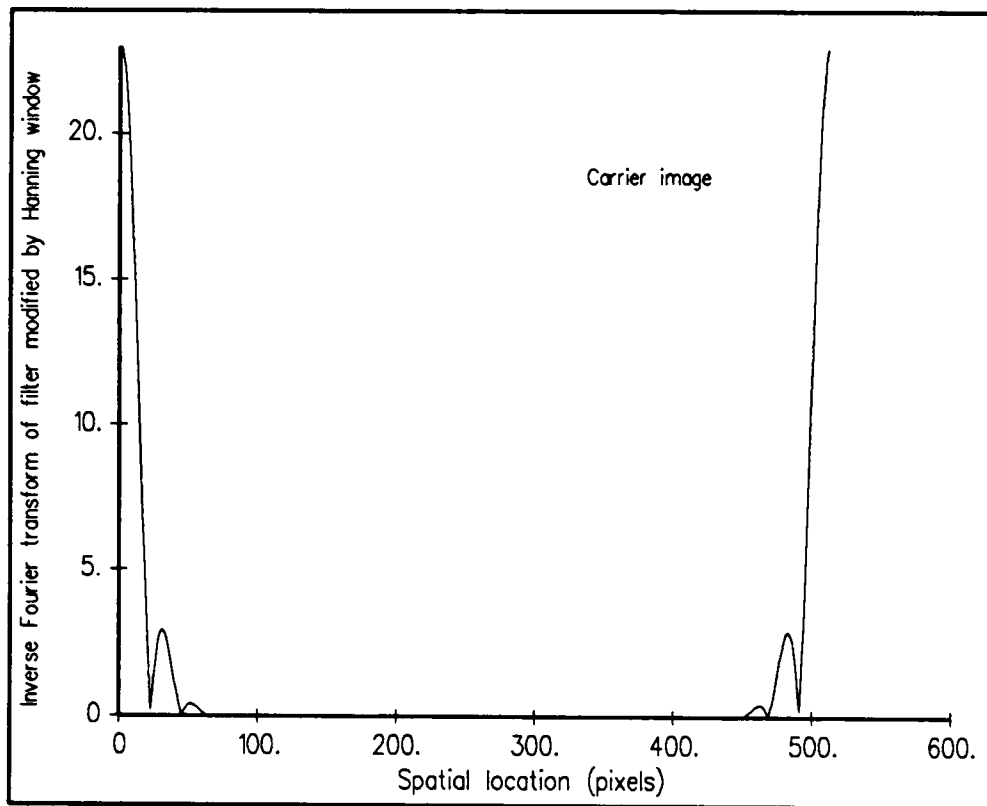


Figure 32. Inverse Fourier transform of filter modified by Hanning window, for carrier image,  $j(y)$  vs.  $y$ .

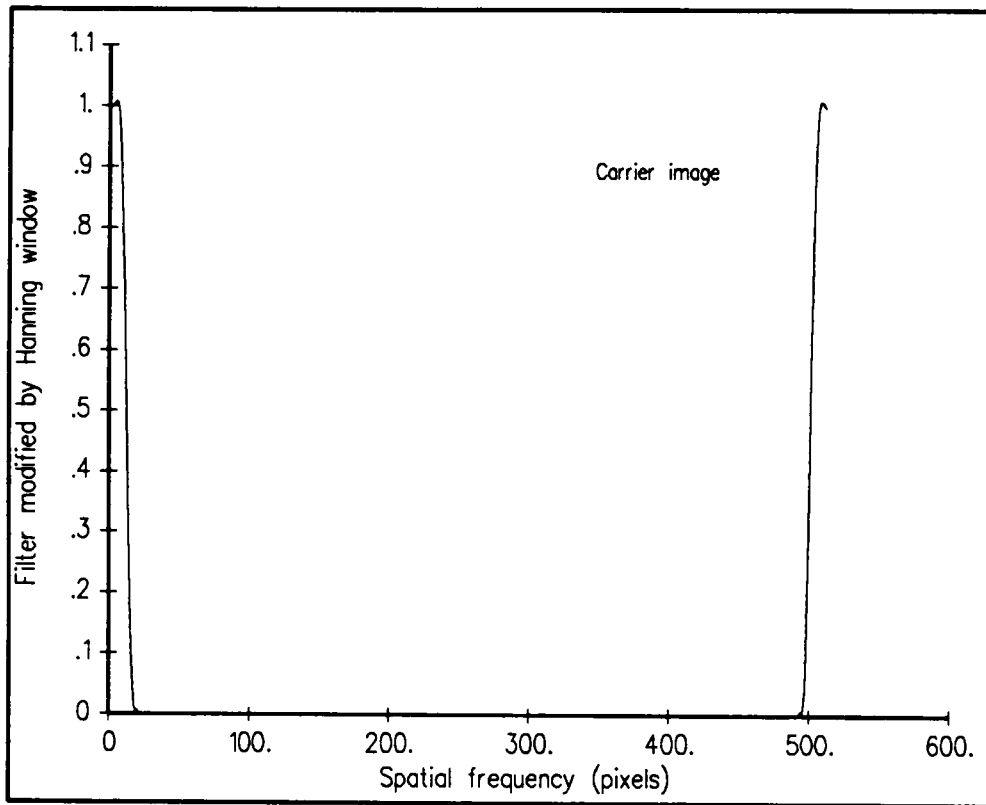


Figure 33. Filter modified by Hanning window, for the carrier image,  $J(f)$  vs.  $f$ .

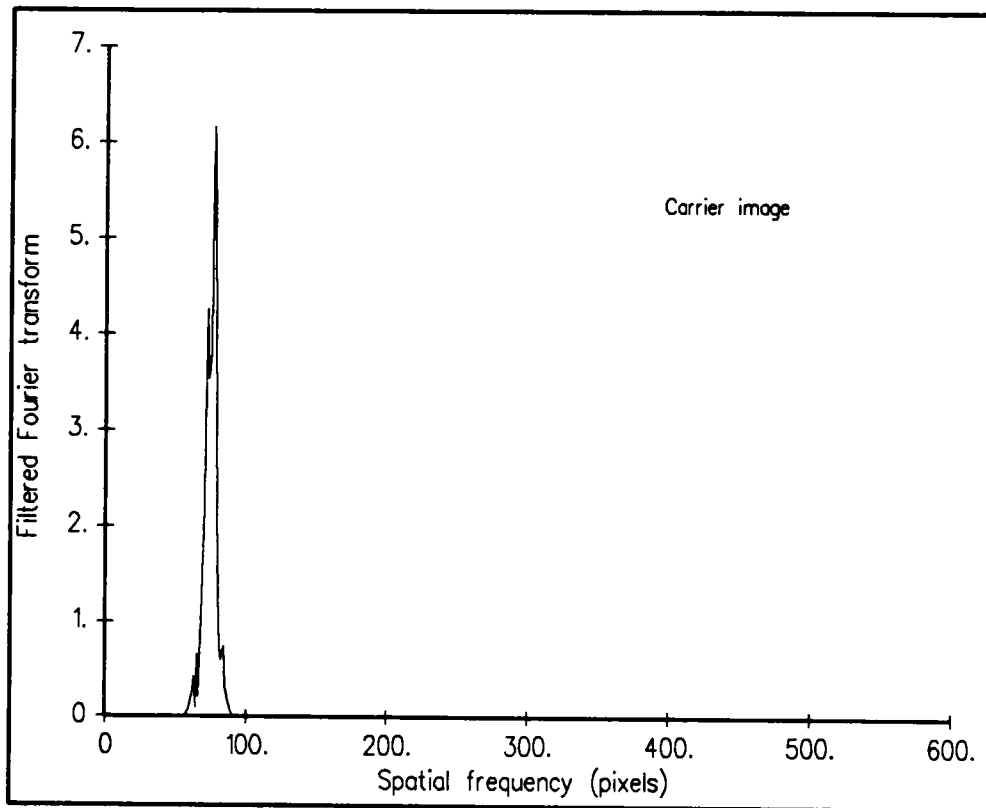
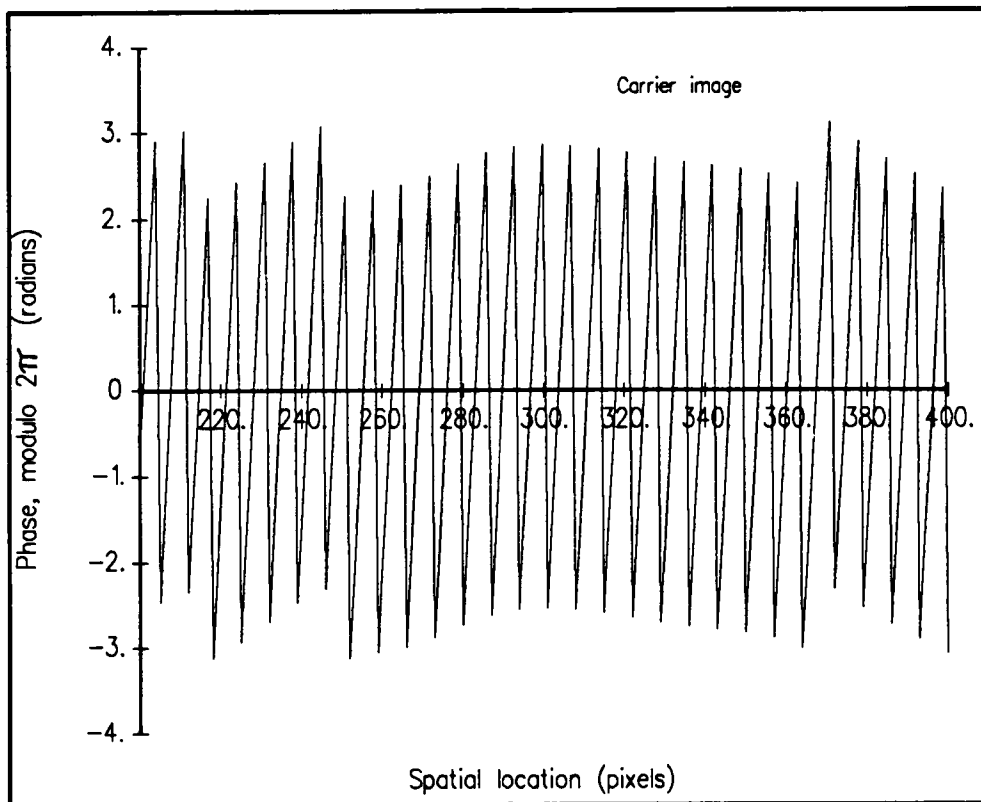


Figure 34. Filtered Fourier transform for the carrier image,  $C(f-f_0)$  vs.  $f$ .



**Figure 35.** Phase, modulo  $2\pi$ , for the carrier image,  $\phi_c(y)$  vs.  $y$ .

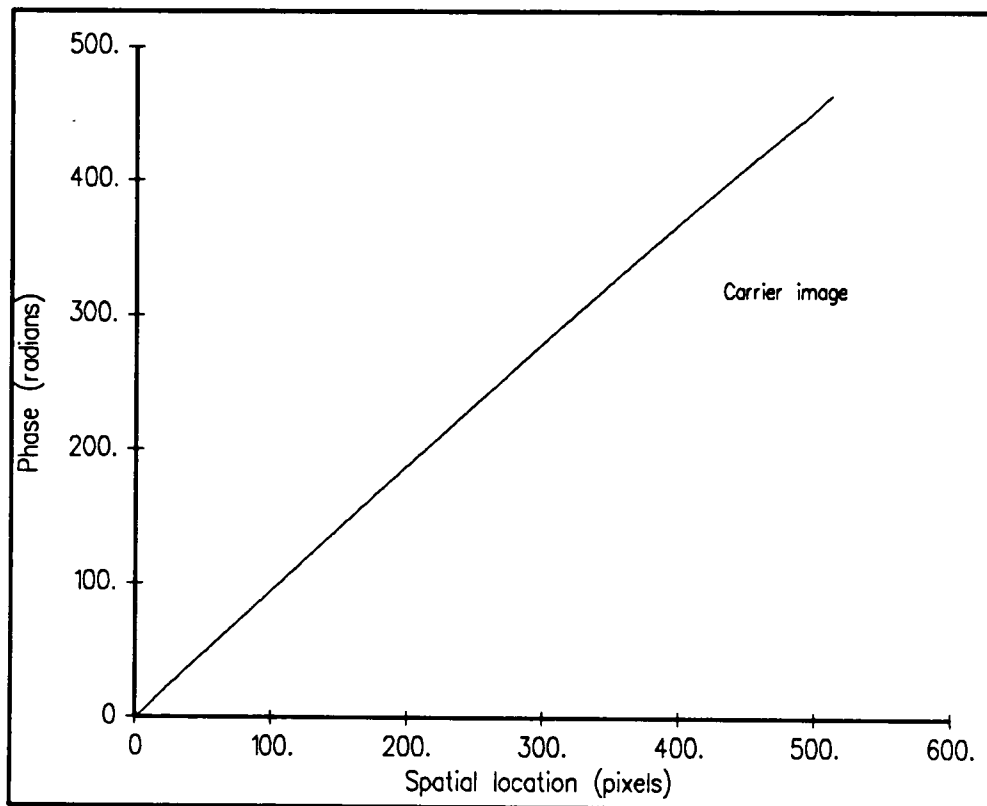


Figure 36. Phase for the carrier image,  $\phi_c(y)$  vs.  $y$ .

(Eq. 82.)

$$\phi_c(y) = 2\pi f_0 y,$$

where  $f_0$  is the carrier frequency. Program CARRIER2 concluded by applying a least squares fit to the carrier phase, to obtain an estimate of the carrier frequency  $f_0$ . The carrier frequency for this run was 74.24.

6) Execute program GET\_COL for the base image.

Program GET\_COL was applied to the base image. See Step 2) for further explanation.

7) Execute program AUTO1 for the base image.

Program AUTO1 is identical to CARRIER1, so the discussion in Step 3) is applicable. The intensity plot for the base image,  $g_B(y)$ , is given in Figure 37. See Eq. 78. The figure shows that carrier fringes are present in the cuvette. Less regular patterns below pixel 401, the location of the cuvette bottom, represent opaque features such as the mounting base.

The Fourier plot for the base image,  $G_B(f)$ , is shown in Figure 38.

8) Perform user operations for the base image.



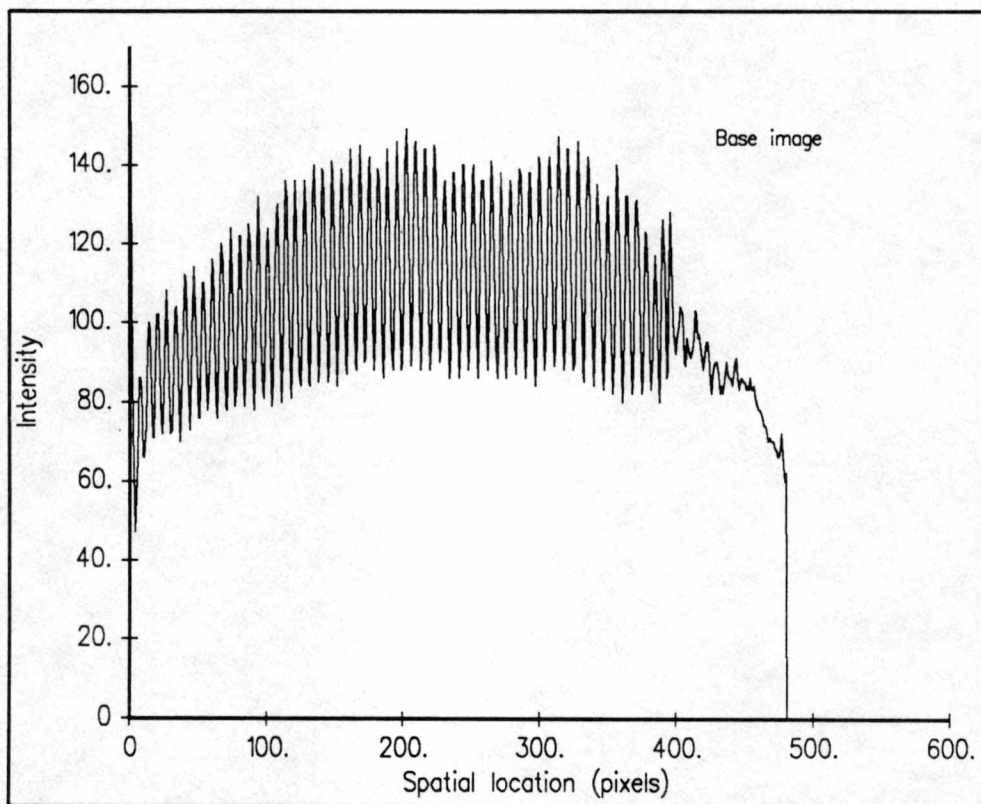
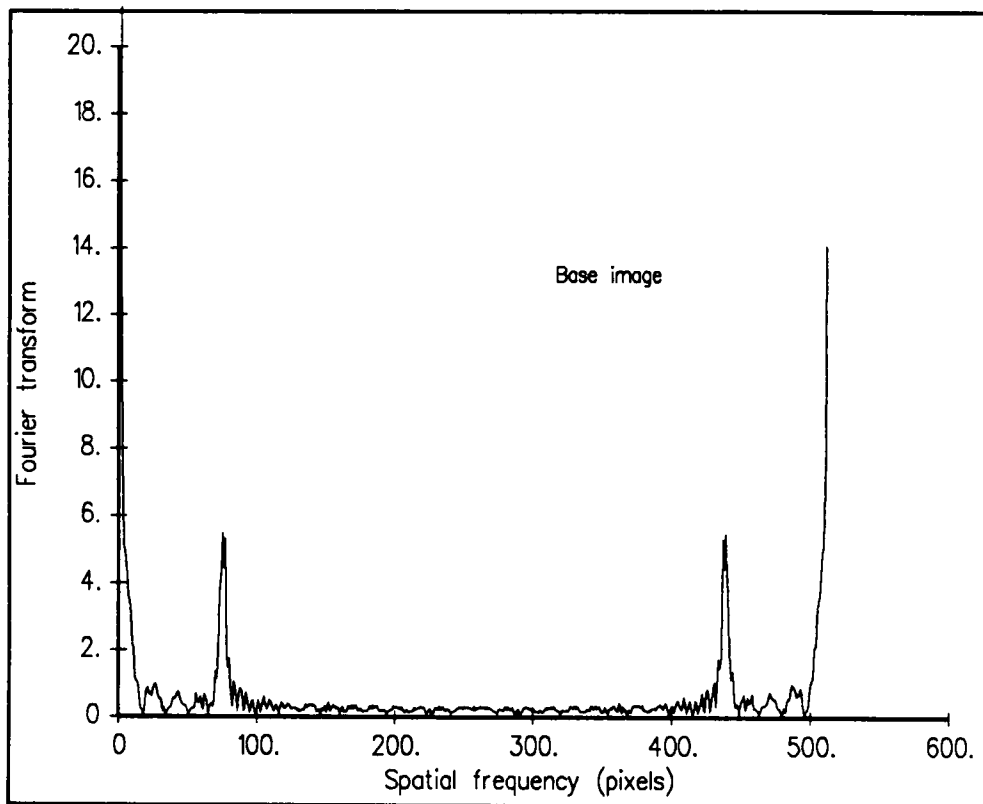


Figure 37. Intensity for the base image,  $g_B(y)$  vs.  $y$ .



**Figure 38.** Fourier transform for the base image,  $G_B(f)$  vs.  $f$ .

As in Step 4), cutoff frequencies were determined, this time for the Fourier plot of the base image. The cutoff frequencies for the base image were 65 and 86.

9) Execute program AUTO2 for the base image.

The main goal of this execution of program AUTO2 was to apply the Fourier-transform method to determine the base phase,  $\phi_B(y)$ , from  $g_B(y)$ , the base image. See Eq. 78. Since program AUTO2 is similar to program CARRIER2, much of the discussion in Step 5) is applicable. Plots of the ideal lowpass filter, its inverse Fourier transform, the Hanning window, the product of the Hanning window and the ideal lowpass filter, the modified filter, and the filtered image are given in Figure 39 through Figure 44. The cutoff frequencies for the ideal lowpass filter were 502 and 12. For the Hanning window,  $K = 68$ .

The phase [ $\phi_B(y) + \phi_C(y)$ ] was determined and unwrapped, then the carrier phase  $\phi_C(y)$ , calculated earlier in Step 3), was subtracted. The base phase,  $\phi_B(y)$ , is shown in Figure 45. Since the bottom of the cuvette was located at pixel 401, the phase plot below that point (at higher pixel values) is irrelevant. The phase plot above that point indicates that the cuvette wall deformed slightly at its juncture with the cuvette bottom, or that inhomogeneities were present in the quartz.

The phase of the base image was written to file "PHASE.DAT," then renamed "BAS\_PHAS.DAT" for later use in Step 14).

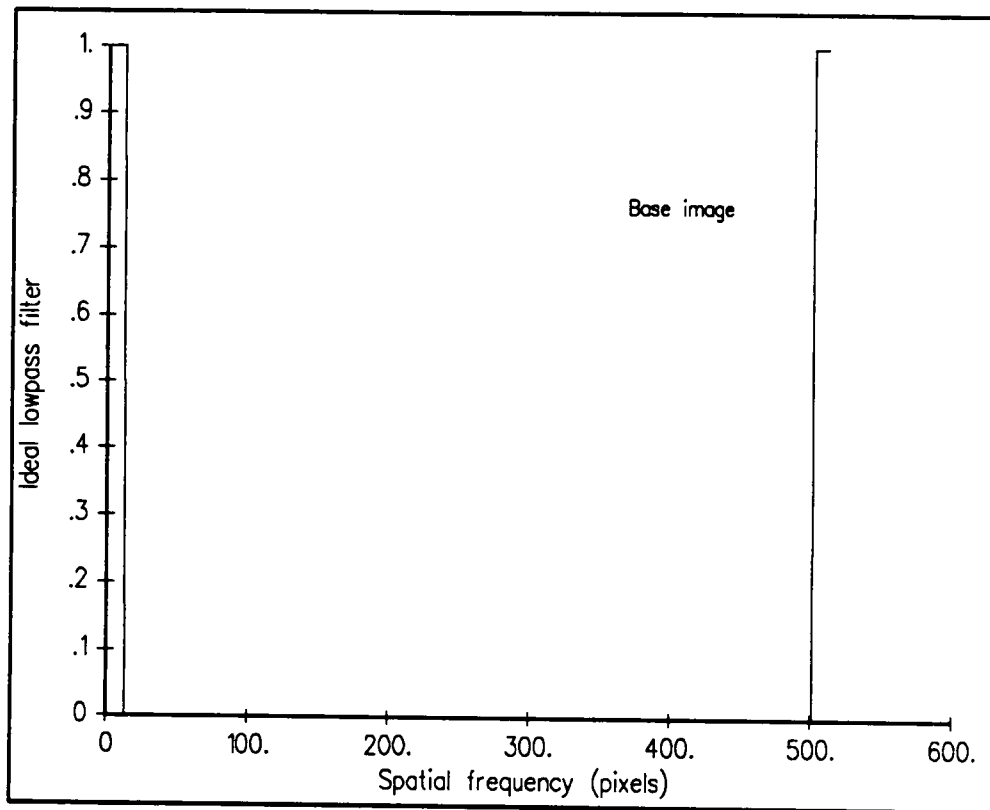
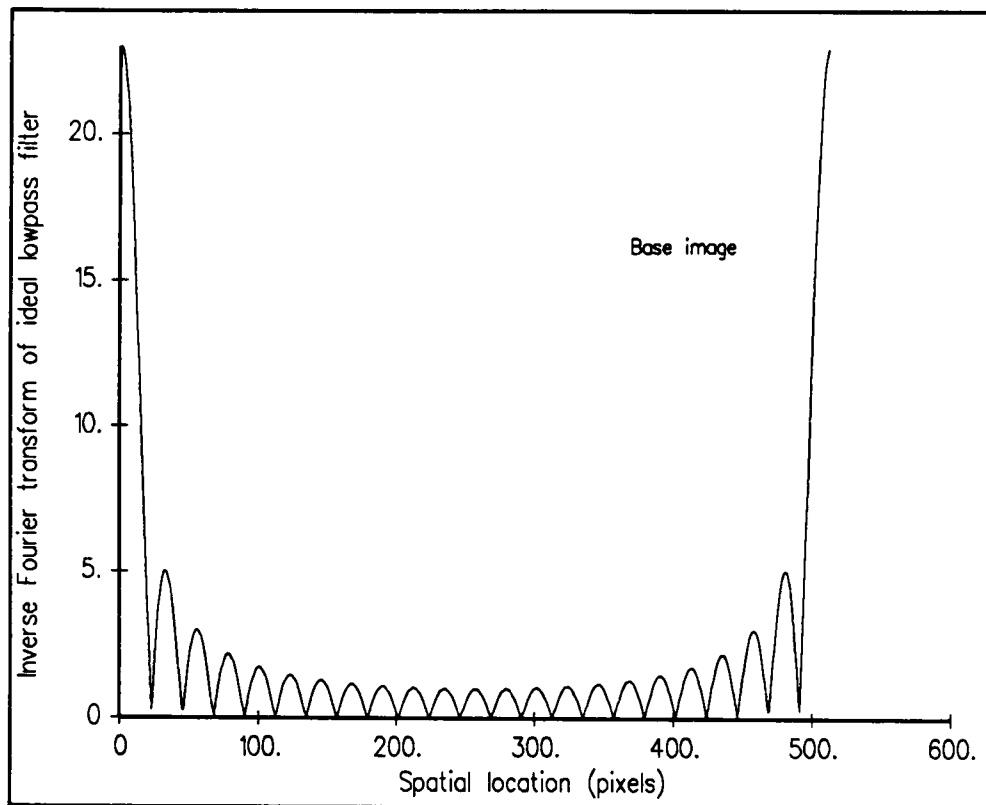


Figure 39. Ideal lowpass filter for the base image,  $I(f)$  vs.  $f$ .



**Figure 40.** Inverse Fourier transform of ideal lowpass filter, for the base image,  $i(y)$  vs.  $y$ .

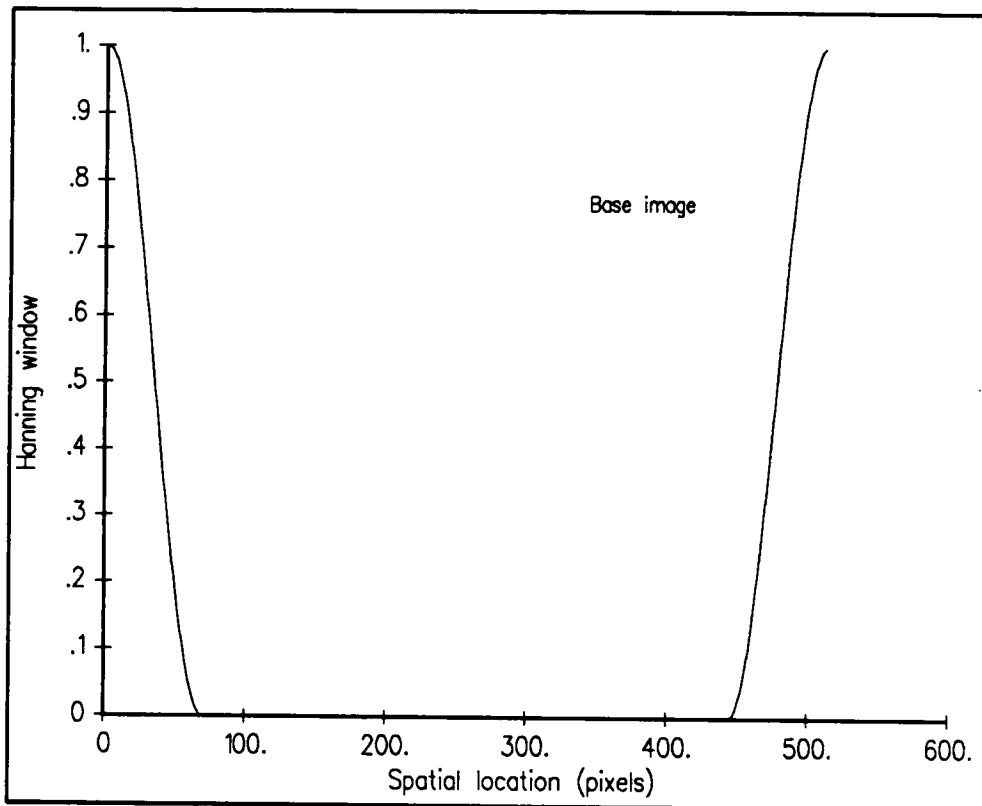
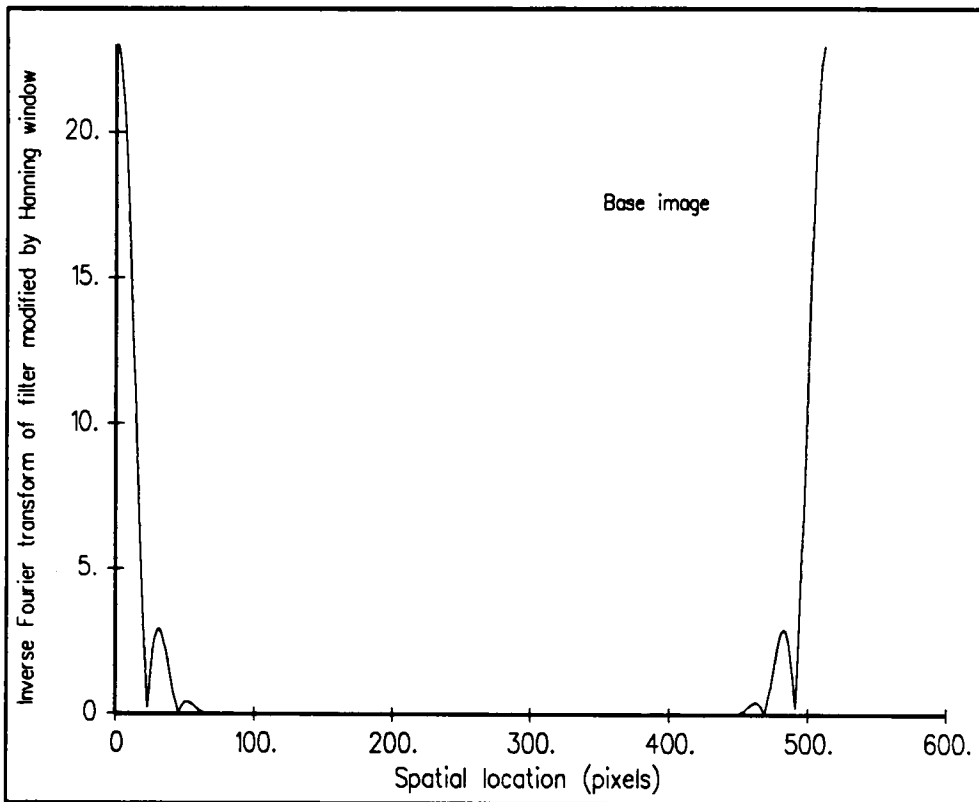


Figure 41. Hanning window for the base image,  $h(y)$  vs.  $y$ .



**Figure 42.** Inverse Fourier transform of filter modified by Hanning window, for the base image,  $j(y)$  vs.  $y$ .

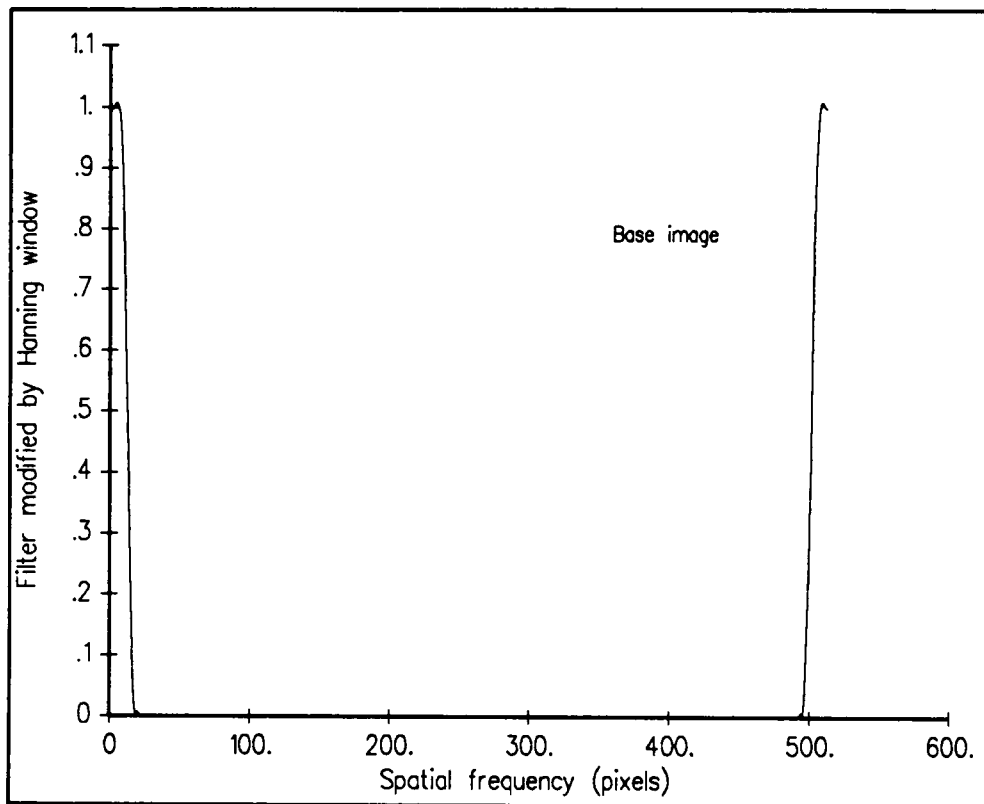


Figure 43. Filter modified by Hanning window, for the base image,  $J(f)$  vs.  $f$ .



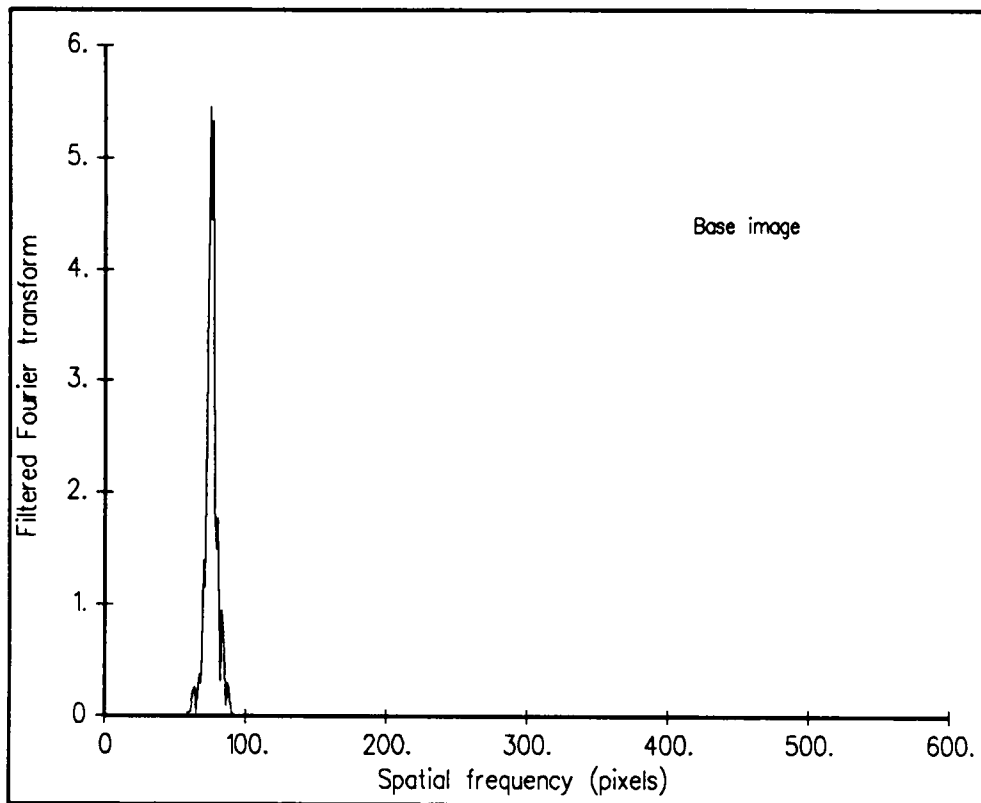


Figure 44. Filtered Fourier transform for the base image,  $C(f-f_0)$  vs.  $f$ .

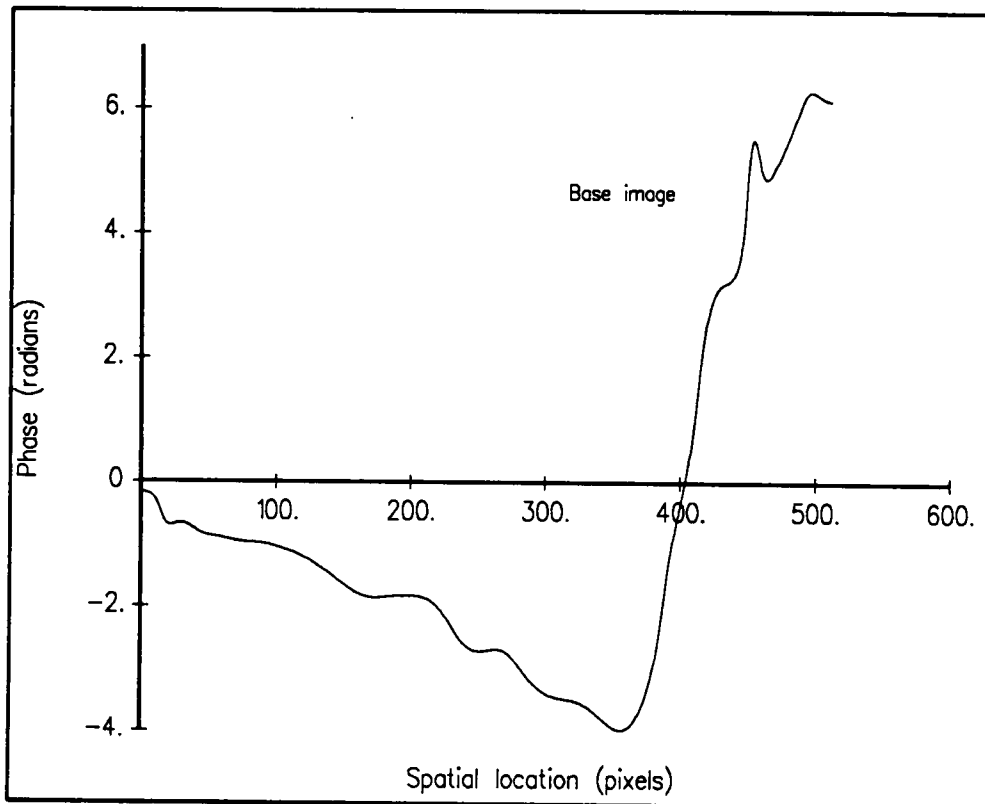


Figure 45. Phase for the base image,  $\phi_B(y)$  vs.  $y$ .

10) Execute program GET\_COL for the experimental image.

Program GET\_COL was applied to the experimental image. See Step 2) for further explanation.

11) Execute program AUTO1 for the experimental image.

Program AUTO1 is identical to CARRIER1, so the discussion in Step 3) is applicable. The intensity plot for the experimental image,  $g_E(y)$ , is given in Figure 46. See Eq. 79. Widely spaced fringes above the interface, which was located at pixel 379, indicate that solidification was proceeding. Patterns below pixel 379 represent opaque features, such as the mushy zone and cuvette bottom.

The Fourier plot for the experimental image,  $G_E(f)$ , is shown in Figure 47.

12) Perform user operations for the experimental image.

As in Step 4), cutoff frequencies were determined, this time for the Fourier plot of the experimental image. The cutoff frequencies were 32 and 99.

13) Execute program AUTO2 for the experimental image.

The main goal of this second execution of program AUTO2 was to apply the Fourier-transform method to determine the phase  $[\phi_E(y) + \phi_B(y)]$  from  $g_E(y)$ , the experimental image. See Eq. 79. Since program AUTO2 is an analog to program CARRIER2, much of the discussion in Step 5) is applicable. Plots of the ideal lowpass filter, its inverse Fourier transform, the Hanning window, the product of the Hanning window and the ideal lowpass filter, the modified filter,

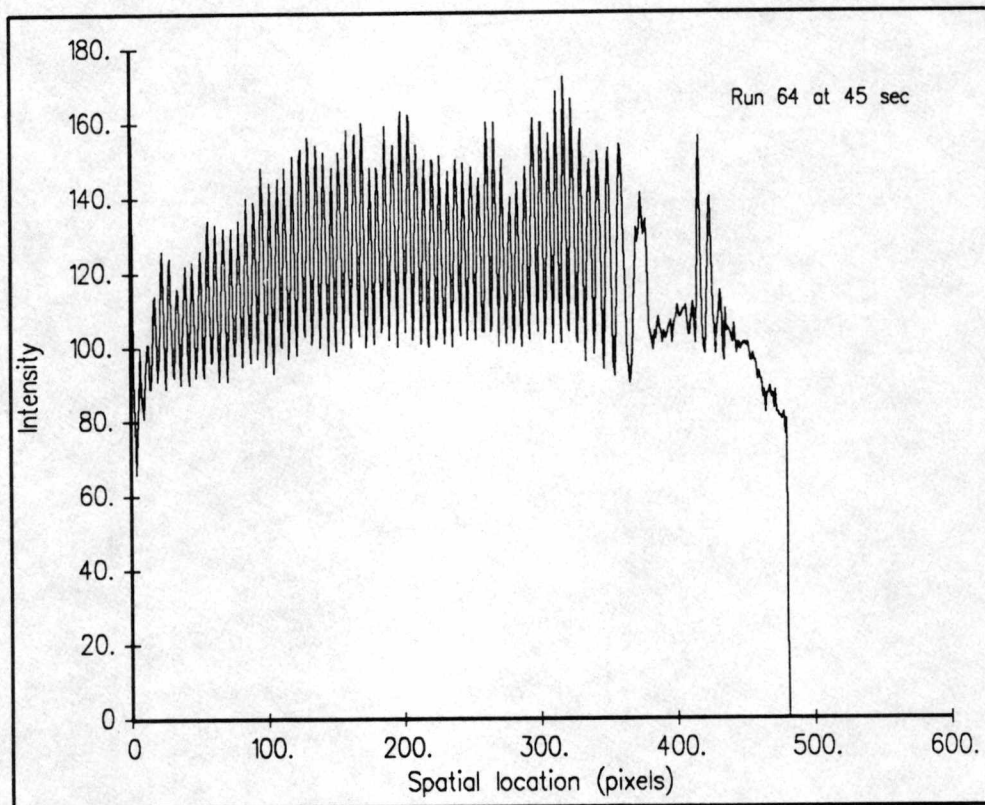


Figure 46. Intensity for the experimental image,  $g_E(y)$  vs.  $y$ .

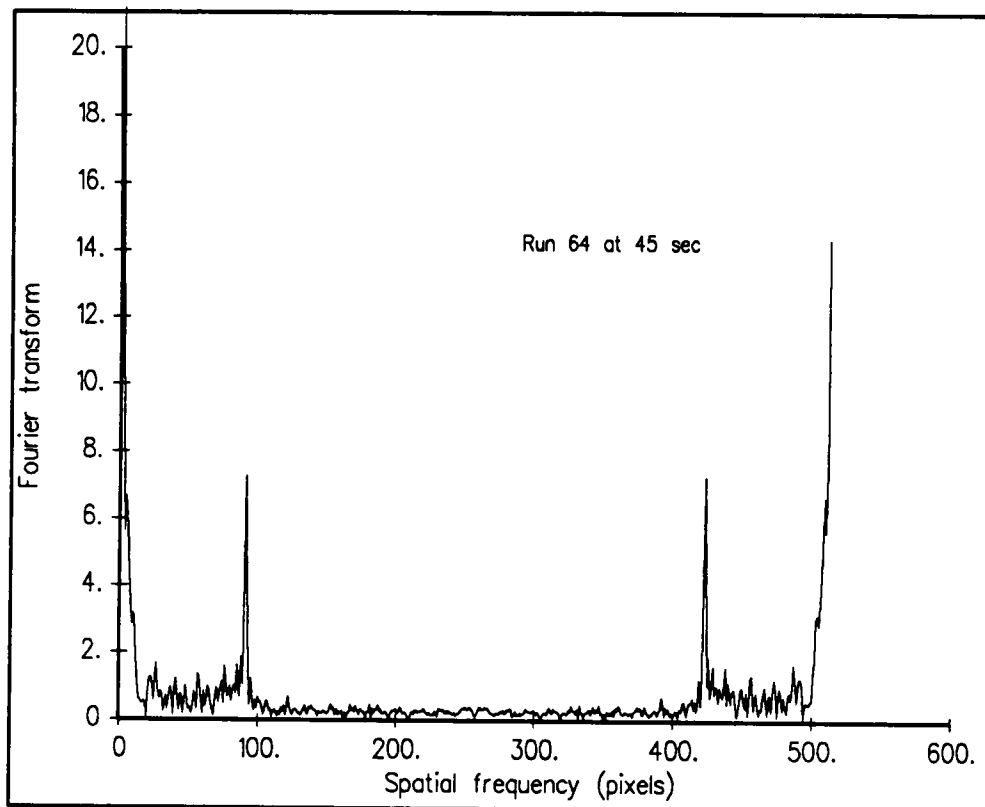


Figure 47. Fourier transform for the experimental image,  $G_E(f)$  vs.  $f$ .

and the filtered image are given in Figure 48 through Figure 53. The cutoff frequencies for the ideal lowpass filter were 479 and 35. For the Hanning window,  $K = 23$ .

The phase  $[\phi_E(y) + \phi_B(y) + \phi_C(y)]$  was determined and unwrapped, then the carrier phase  $\phi_C(y)$ , calculated earlier in Step 3), was subtracted. The phase  $[\phi_E(y) + \phi_B(y)]$  is shown in Figure 54. Since the interface was located at pixel 379, the phase plot below that point (at higher pixel values) is irrelevant. The smooth linear graph in the top of the cuvette indicates the zone where only the temperature gradient contributes to phase changes. The phase plot then has an inflection point. The graph to the right of the inflection point represents phase changes due to the combined effect of temperature and concentration changes. The combined effects of a temperature gradient and a diffusion gradient were discussed earlier with reference to density; see Figure 2.

14) Execute program CONCEN1 for the experimental image.

The main goal of program CONCEN1 was to convert the experimental phase  $\phi_E(y)$  to a refractive index field  $n(y)$ . First the base phase,  $\phi_B(y)$ , was subtracted from  $[\phi_E(y) + \phi_B(y)]$  to obtain  $\phi_E(y)$ , the experimental phase. The base phase was calculated in Step 9), while the phase  $[\phi_E(y) + \phi_B(y)]$  was calculated in Step 13). Takeda et al. suggested the phase subtraction technique; to correct error, interferometer aberrations were subtracted from measurement data. [25] The experimental phase is plotted versus distance from the interface in Figure 55.

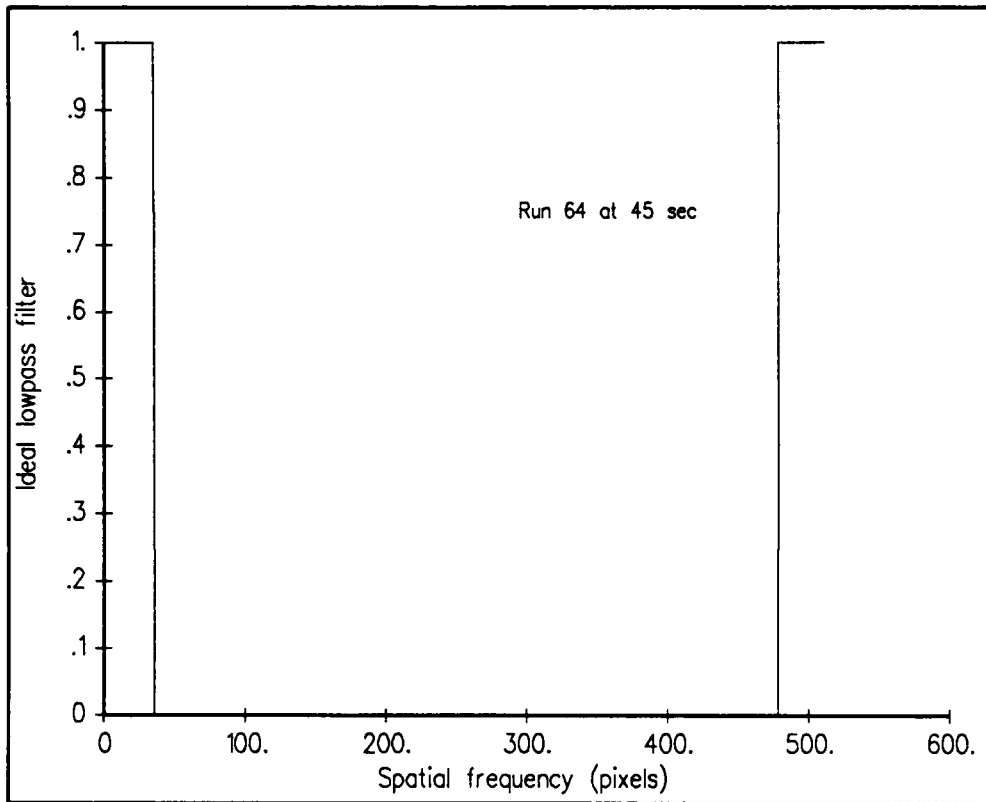
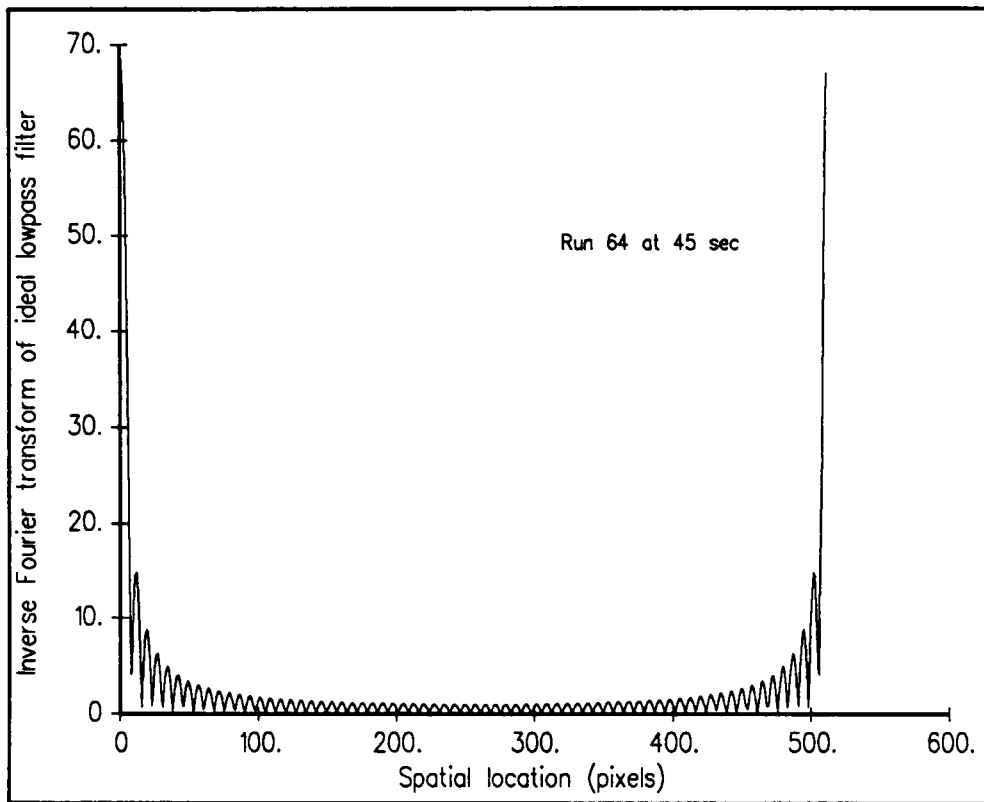


Figure 48. Ideal lowpass filter for the experimental image,  $I(f)$  vs.  $f$ .



**Figure 49.** Inverse Fourier transform of ideal lowpass filter, for the experimental image,  $i(y)$  vs.  $y$ .



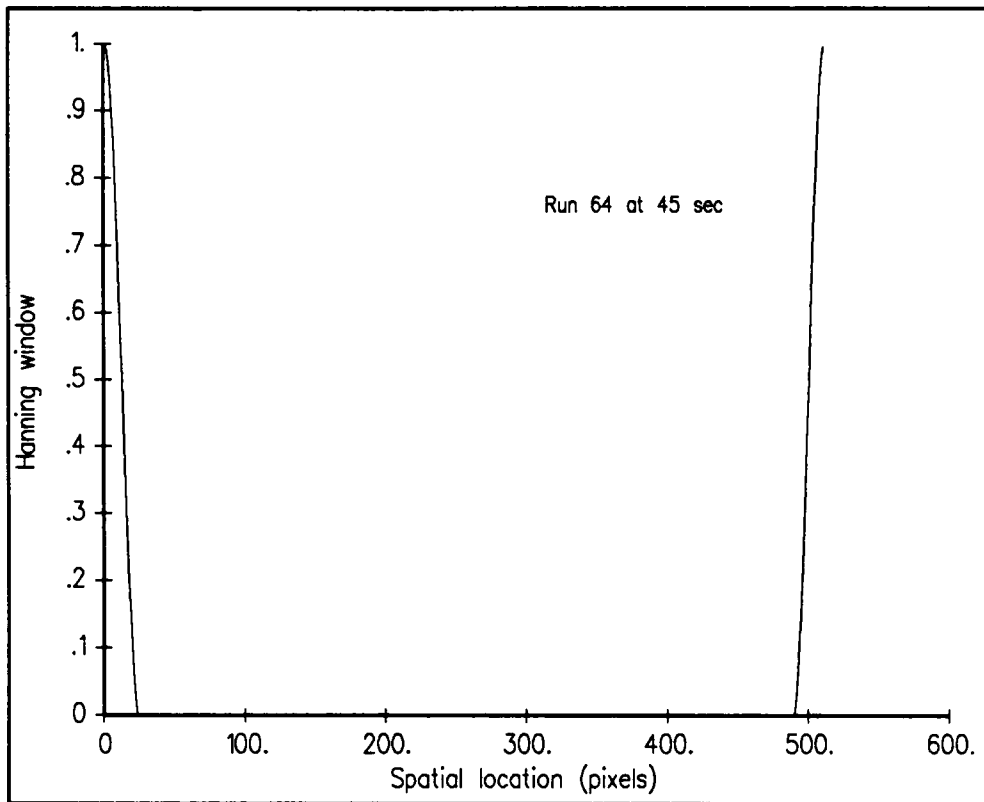
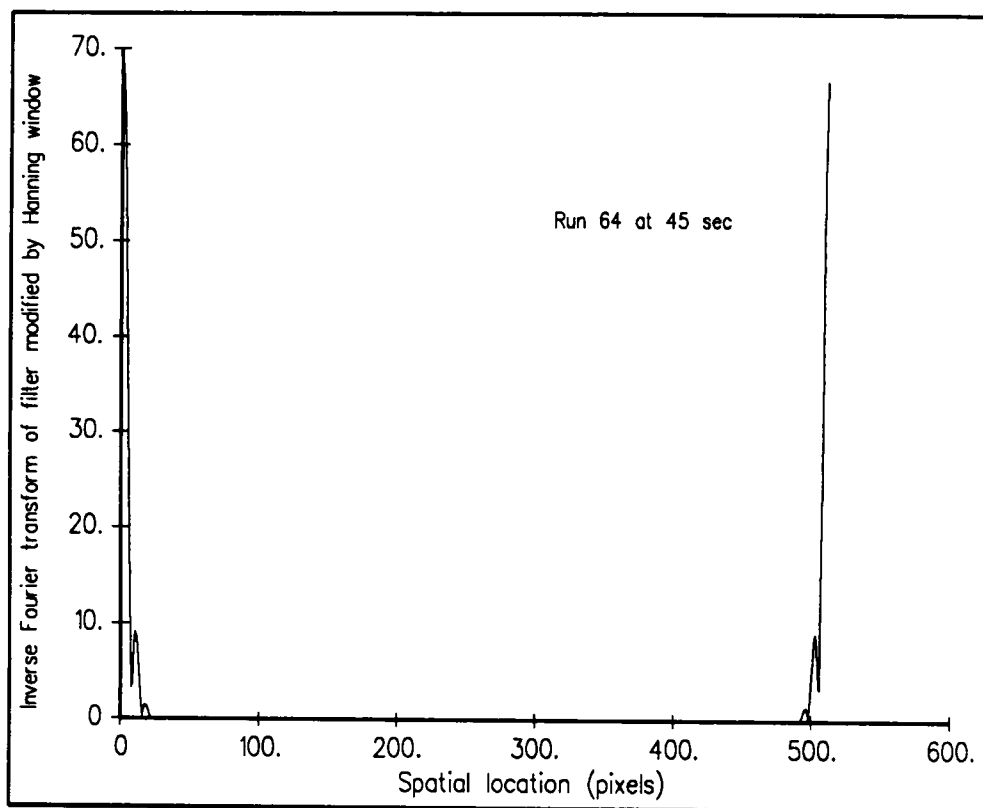


Figure 50. Hanning window for the experimental image,  $h(y)$  vs.  $y$ .



**Figure 51.** Inverse Fourier transform of filter modified by Hanning window, for the experimental image,  $j(y)$  vs.  $y$ .

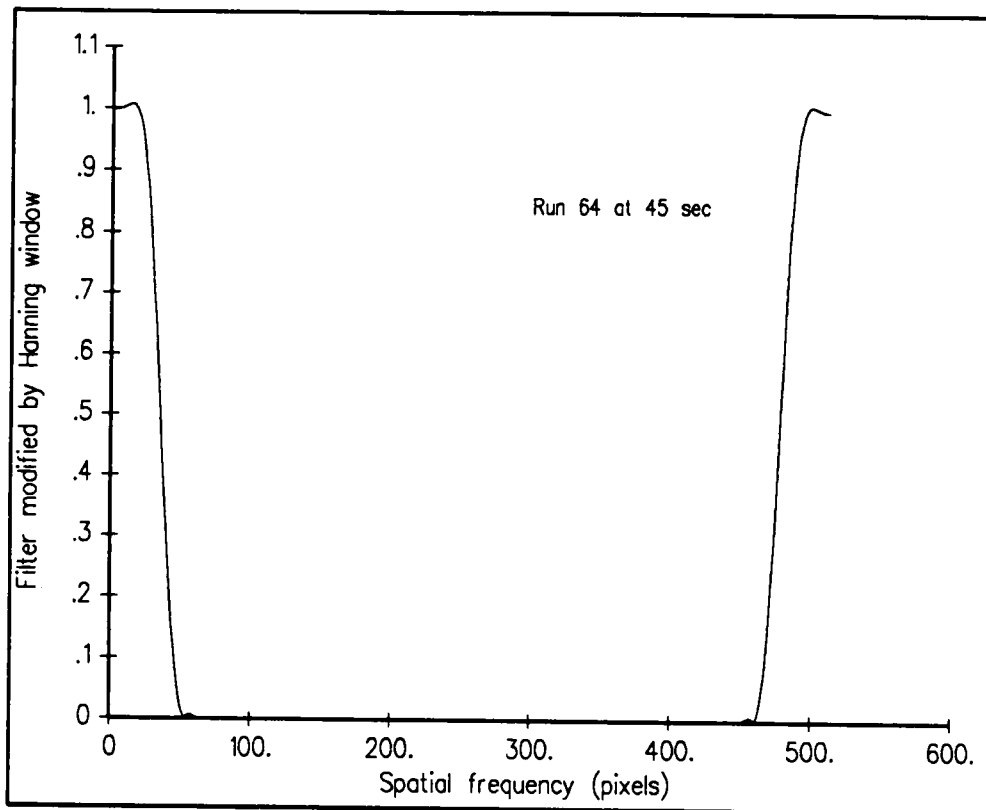


Figure 52. Filter modified by Hanning window, for the experimental image,  $J(f)$  vs.  $f$ .

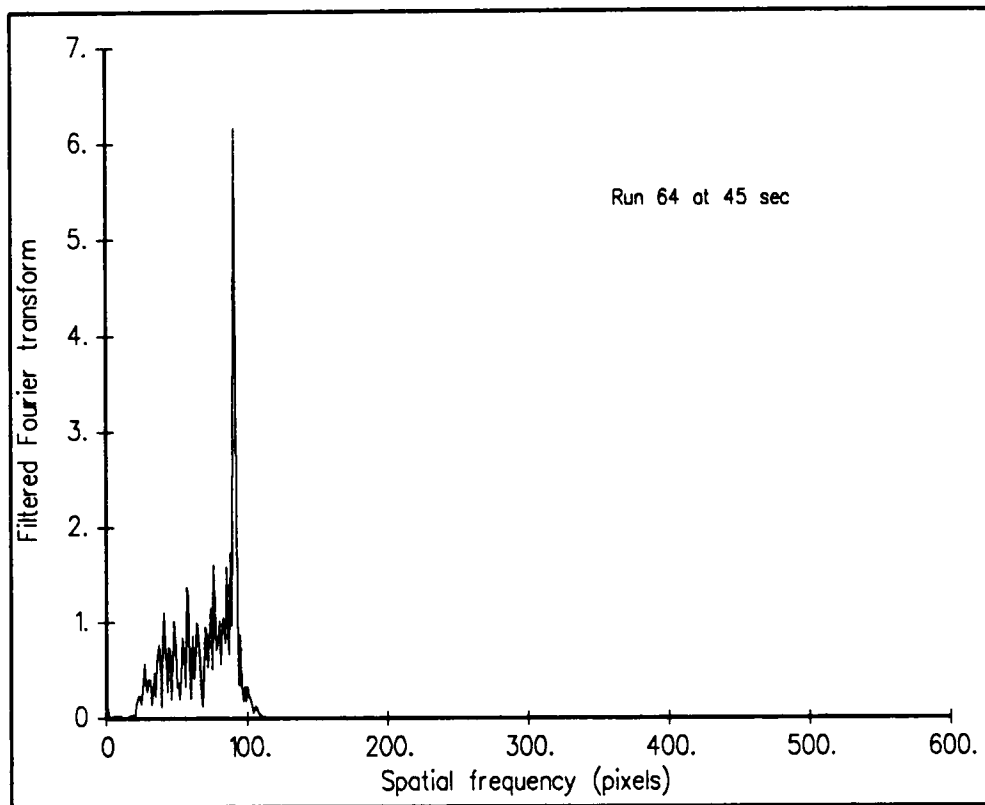
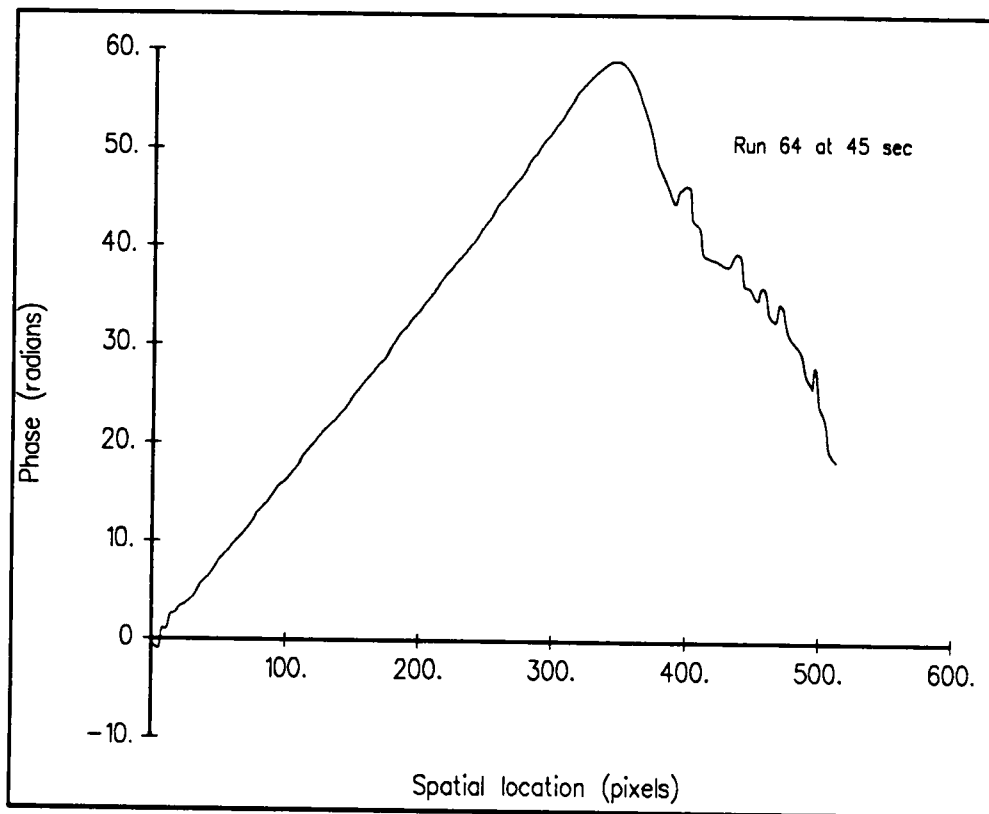


Figure 53. Filtered Fourier transform for the experimental image,  $C(f-f_0)$  vs.  $f$ .



**Figure 54.** Phase for the experimental image,  $[\phi_E(y) + \phi_B(y)]$  vs.  $y$ .

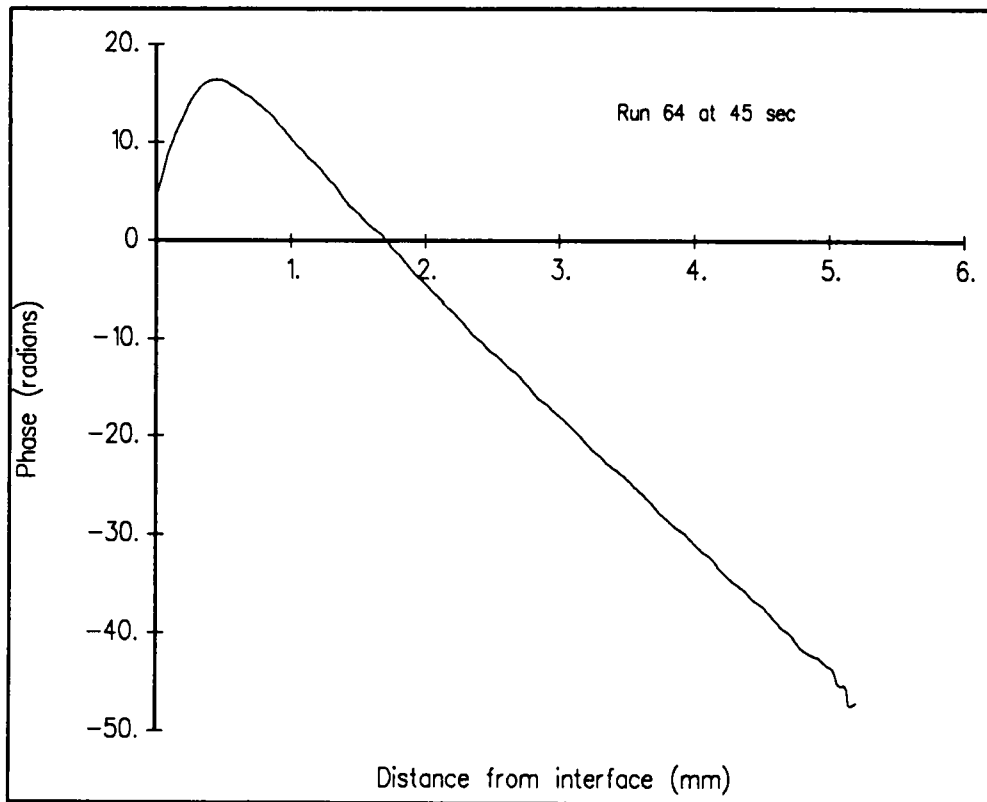


Figure 55. Phase,  $\phi_E(y)$  vs.  $y$ .

As noted earlier, the experimental image was a fringe pattern with intensity:

$$g_E(y) = a(y) + b(y) \cos [\phi_E(y) + \phi_B(y) + \phi_C(y)].$$

During application of the Fourier-transform method,  $a(y)$  and  $b(y)$  were filtered, then the base phase and the carrier phase were subtracted, leaving only the experimental phase,  $\phi_E(y)$ . Program CONCEN1 calculated the intensity:

(Eq. 83.)

$$p(y) = \cos \phi_E(y),$$

Since the effects of  $a(y)$ ,  $b(y)$ ,  $\phi_B(y)$ , and  $\phi_C(y)$  were removed,  $p(y)$  is an enhanced version of the fringe pattern that would be observed if tilt fringes had not been induced. [30] It can be compared with a fringe pattern produced via conventional interferometry. Figure 56 shows the enhanced fringe pattern for this run. Closely spaced fringes can be seen near the solidifying interface. The null layer, which can be located by finding the widest fringe, [3] is observed about 0.5 millimeters from the interface. Regularly spaced fringes in the upper portion of the cuvette indicate the effects of the linear temperature gradient.

Program CONCEN1 then calculated the relative refractive index field:

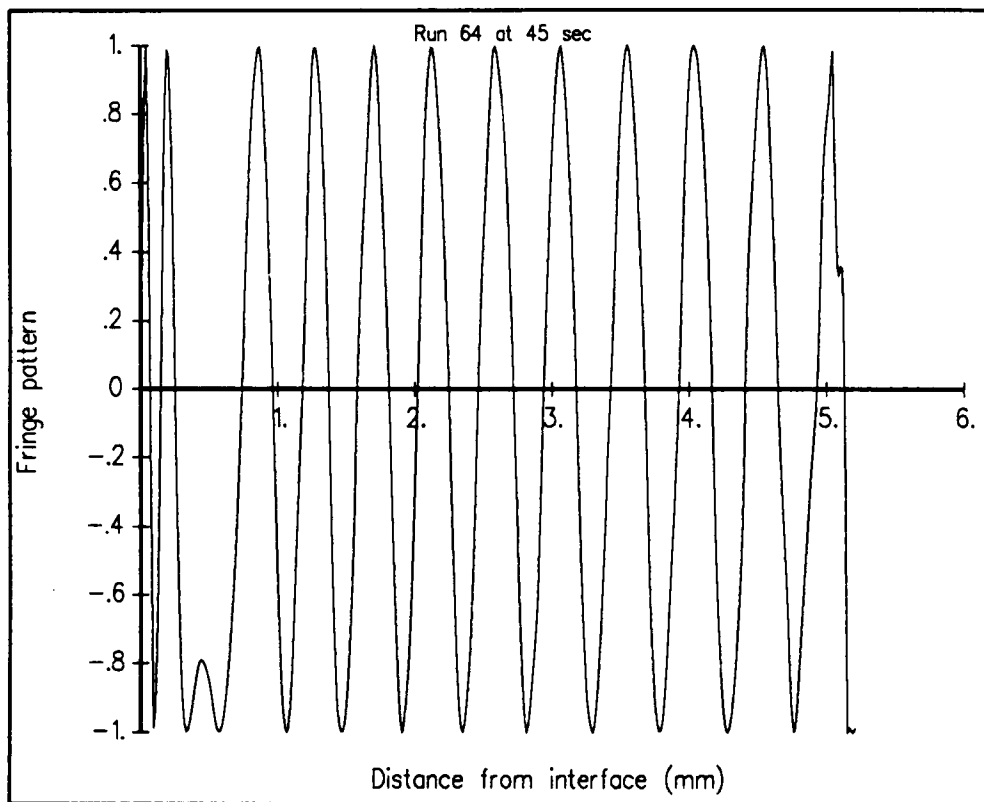


Figure 56. Fringe pattern,  $p(y)$  vs.  $y$ .



(Eq. 84.)

$$n(y) = \lambda \phi_E(y) / 2\pi d,$$

which is shown in Figure 57.

15) Perform user operations for the experimental image.

The distance between fringes around 2 millimeters from the interface was determined from the fringe pattern plot produced in Step 14), for later use in Step 16). For this run the distance was 30 pixels.

The plot of refractive index produced in Step 14) was inspected to obtain a window within which the maximum refractive index occurs. This information is used in Step 16); for this run the window was 2 millimeters.

16) Execute program CONCEN2 for the experimental image.

The main goal of program CONCEN2 was to obtain a concentration profile by removing the effects of temperature from the refractive index field calculated in Step 14). The methods used here were adapted from earlier formulations. [2] [3]

The index of refraction is a function of both temperature and concentration, as shown by expressing Eq. 10 in the form:

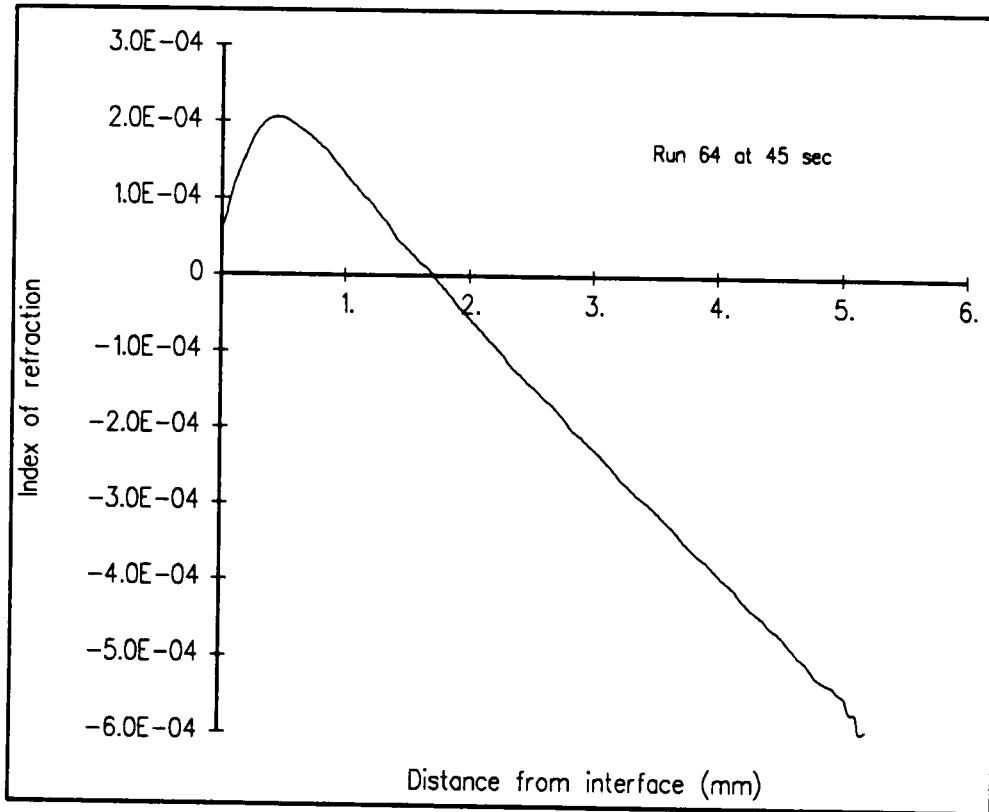


Figure 57. Index of refraction,  $n(y)$  vs.  $y$ .

(Eq. 85.)

$$n(T,C) = n_0 + n_T T + n_C C.$$

In this formulation  $n_0 = 1.3419$ ,  $n_T = -1.73 \times 10^{-4}$ , and  $n_C = 1.63 \times 10^{-3}$ . Taking the differential of Eq. 85 yields:

(Eq. 86.)

$$dn = n_T dT + n_C dC.$$

Integration over a change in C and T ( $C_1$  to  $C_2$ ,  $T_1$  to  $T_2$ ) gives:

(Eq. 87.)

$$n_2 - n_1 = n_T(T_2 - T_1) + n_C(C_2 - C_1).$$

Substituting a general change ( $\Delta n = n_2 - n_1$ ,  $\Delta T = T_2 - T_1$ ,  $\Delta C = C_2 - C_1$ ) then yields:

(Eq. 88.)

$$\Delta n = n_T \Delta T + n_C \Delta C.$$

In this project the temperature field in the cuvette was assumed to be linear:

(Eq. 89.)

$$T = T_0 + Gy,$$

where  $G$  is the linear temperature gradient. After taking the differential, integrating over a change in  $y$ , and substituting  $\Delta y = y_2 - y_1$  and  $\Delta T = T_2 - T_1$ , the result is:

(Eq. 90.)

$$\Delta T = G \Delta y.$$

Upon substituting Eq. 90 into Eq. 88, the following expression is obtained:

(Eq. 91.)

$$\Delta n = n_T G \Delta y + n_C \Delta C.$$

To isolate the field of point-to-point concentration changes in this expression, all of the other variables must be known. The point-to-point refractive index changes,  $\Delta n$ , were calculated in Step 14), the point-to-point changes in height,  $\Delta y$ , are known, and the constants  $n_T$  and  $n_C$  were given above. The only unknown, the temperature gradient, was calculated as discussed below.

In the bulk liquid the concentration is constant, so program CONCEN2 used the fringe spacing there to recommend a temperature gradient. Since  $\Delta C = 0$  in the bulk liquid, Eq. 91 there becomes  $\Delta n = n_T G \Delta y$ . Solving for the

gradient and converting refractive index to phase via Eq. 84 yields the expression:

(Eq. 92.)

$$G = \lambda \Delta \phi / 2\pi dn_T \Delta y.$$

$\Delta y$  was determined by identifying the distance between fringes in Step 15). The corresponding phase change is  $\Delta \phi = 2\pi$ , and substituting this into Eq. 92 gives the temperature gradient:

(Eq. 93.)

$$G = \lambda / dn_T \Delta y.$$

In summary, program CONCEN2 used Eq. 93 to recommend a temperature gradient  $G$ . Eq. 91 was then used to subtract temperature effects and calculate concentration. The recommended temperature gradient for this run was 11.05 °C/cm. Program CONCEN2 plotted concentration with reference to the bulk concentration, which was supplied interactively. The bulk concentration for this run was 72.0 wt%.

Program CONCEN2 requested information regarding the window selected in Step 15). Although this input was not used in any direct calculations, it served as a programming flag. In cases of noisy image data, it is possible for the

refractive index data to have several inflection points. The window flag insured that program CONCEN2 looked at the first refractive index inflection point in its calculations.

17) Iterate further with program CONCEN2 for experimental image.

Although program CONCEN2 recommended a temperature gradient in Step 16), it was corrected by executing the program several more times. The recommended gradient was adjusted by 0.1 °C/cm for each execution. This iteration process was halted when the exponential tail of the concentration plot was flat at 3 millimeters away from the interface.

The final temperature gradient was 10.65 °C/cm. A refractive index plot with temperature effects subtracted is given in Figure 58. The concentration plot is shown in Figure 59. The tip concentration for this run was 72.16 wt%.

Steps 1) through 17) typically took less than an hour to complete.

### 1-D Processing

In order to assess the Fourier-transform method for measuring concentration during solidification, several sets of results were studied. As noted earlier, a 1-D approach was chosen because concentration profiles across the width of the cuvette were expected to be similar. To verify this, the analyses for five adjacent columns were compared.

Run 49 was conducted as discussed earlier in the Solidification and Interferometry sections. A solution of 28 wt% NH<sub>4</sub>Cl in H<sub>2</sub>O was used in this

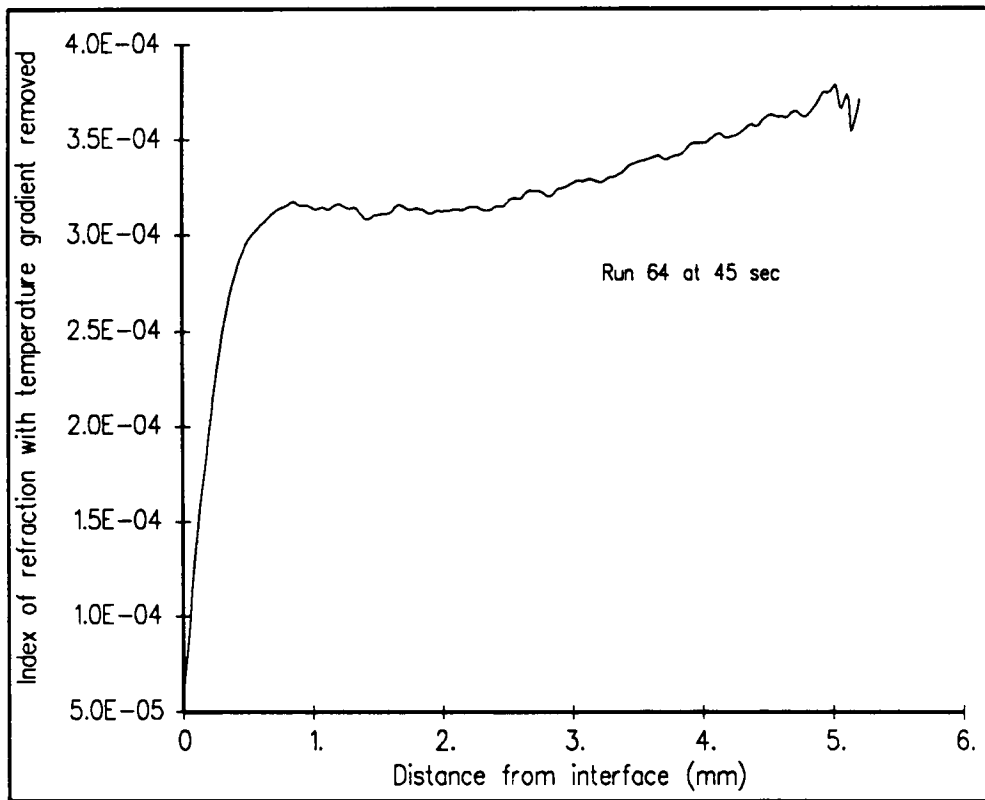


Figure 58. Index of refraction with temperature gradient removed,  $n(y)$  vs.  $y$ .

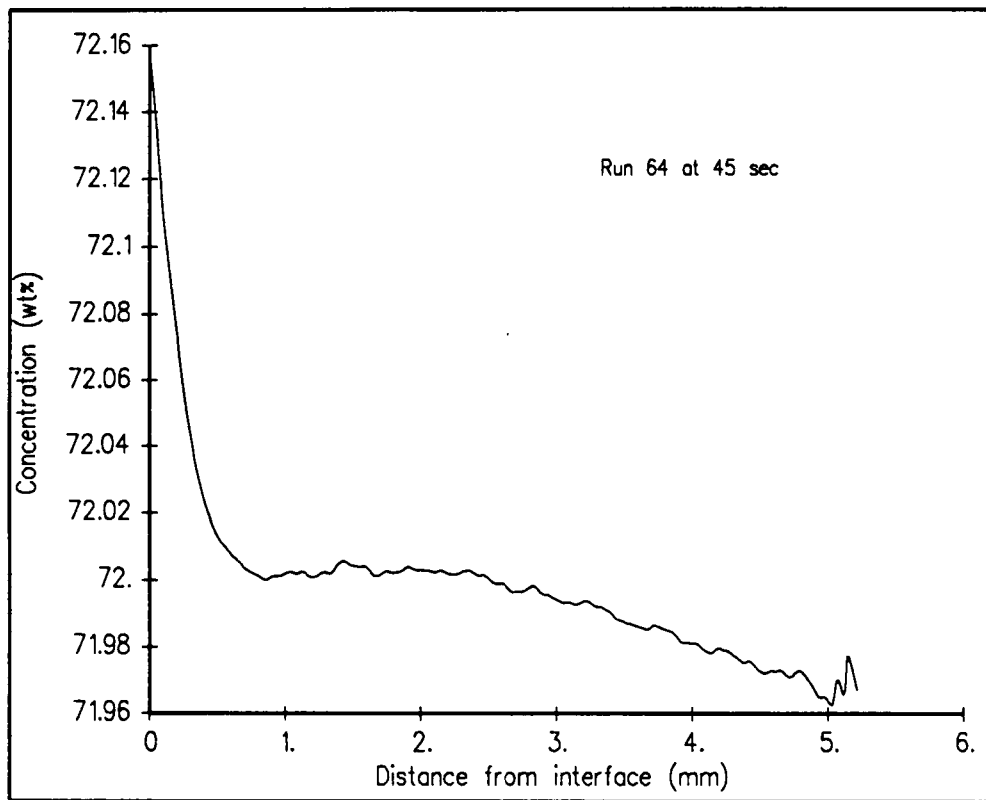


Figure 59. Concentration,  $C(y)$  vs.  $y$ .



run. The top temperature during the gradient hold was 58.5 °C, and the bottom temperature was 21 °C. At the end of a three hour gradient hold, the interface height was 0.17 millimeters for all five columns. The cooling rate was 2 °C/minute, and the time selected for analysis was 30 seconds after cooling began.

The Fourier-transform method was applied as discussed for Run 64, for each of image columns 66, 67, 68, 69, and 70. A carrier phase and a base phase were determined for each individual column. Locations of the cuvette bottom and interface were found to be identical for all five columns, as were the cutoff frequencies.

#### Consistency

To demonstrate that the Fourier-transform method gives consistent results from run to run, the analyses for four runs with similar experimental conditions were compared. Runs 47 through 50 were conducted as outlined in the Solidification and Interferometry sections. A solution of 28 wt% NH<sub>4</sub>Cl in H<sub>2</sub>O was used. During the gradient hold the top temperature was 58.5 °C, while the bottom temperature was 21 °C. Gradient hold times for the four runs varied from 2.75 hours to 3 hours. At the end of the gradient hold, the interface heights ranged from 0.11 millimeters to 0.17 millimeters. The cooling rate for all four runs was 2 °C/minute.

Images at 30 seconds, 55 seconds, and 75 seconds after cooling began were processed as discussed for Run 64. The column analyzed varied from run to run.

### Comparison with Intensity Methods

In order to compare the Fourier-transform method with an outside standard, analyses of four runs were compared with intensity methods applied to a similar solidification run.

#### Fourier-transform Method

Runs 61, 62, 64, and 65 were conducted as discussed earlier in the Solidification and Interferometry sections. A solution of 28 wt%  $\text{NH}_4\text{Cl}$  in  $\text{H}_2\text{O}$  was used for these runs. The gradient hold varied from 45 minutes to 75 minutes; the top temperature during the hold was 56.5 °C, while the bottom temperature was 19 °C. At the end of the gradient hold, interface heights varied from 0.30 millimeters to 0.32 millimeters. The cooling rate was 2 °C/minute. The Fourier-transform method was applied in the usual way, to images acquired 45 seconds and 75 seconds after cooling began. The same column number was analyzed for each of the four runs.

#### Intensity Method with Spline Fit

Runs 61, 62, 64, and 65 were patterned after a similar experiment described by Hopkins in 1989. [2] The same solidification control system was used in that earlier work. Hopkins used a cuvette dimensionally identical to the one used in this project, but it was filled through a hole in the top wall, not through a fill tube. He used a solution of 28 wt%  $\text{NH}_4\text{Cl}$  in  $\text{H}_2\text{O}$ . The gradient

was held for 39 minutes; the top temperature was 58.5 °C, while the bottom temperature was 21 °C. The cooling rate was 2 °C/minute.

The top and bottom temperatures for Runs 61, 62, 64, and 65 differ from those listed above. For this project it was necessary to lower the bottom temperature in order to achieve an initial interface height similar to 0.33 millimeters, the value reported by Hopkins. It was assumed that differences in thermocouple calibration or room temperature led to the discrepancies in the relationship between temperature and interface height.

Hopkins applied an intensity method to analyze fringe patterns produced by conventional interferometry (tilt fringes were not present). Fringe spacings were determined with a VICOM image processor, via a cursor, then converted to a phase field. The position of the null layer indicated where phase had an inflection point. The average of the fringe spacings in the bulk liquid was used to extend the phase profile in that region. Phase was then converted to refractive index, which was fit to a spline. The temperature gradient was subtracted to yield a concentration plot.

Hopkins analyzed solidification images at 45 seconds, 75 seconds, and 105 seconds after cooling began. Since convective breakdown occurred around 80 seconds for Runs 61, 62, 64, and 65, no Fourier-transform analysis was attempted at 105 seconds.

### Intensity Method with Exponential Curve Fit

Recent solidification work incorporated several changes to the intensity method described above. [3] In the new procedure, actual fringe spacings in the bulk, not an average, were noted. Fringe spacings were converted to phase, then phase to refractive index. The temperature gradient was subtracted to yield a concentration profile. An exponential fit was then applied to the data.

Accordingly, the revised method was applied to the runs Hopkins conducted. It was not possible to analyze the same images, since the actual image files were not available. However, frames were selected for analysis from videotapes of these runs, and were judged to be close in time to the original images. It was uncertain which column had been analyzed with the earlier intensity method, therefore column 255, the center of the image, was analyzed with the revised intensity method.

Neither intensity method employed the equivalent of the subtraction of the base phase used in the Fourier-transform method.

### Base Phase Subtraction

As discussed earlier in the Interferometry section, irregularities in the quartz cuvette walls may introduce the phase change  $\phi_B(y)$ . If this phase change was not subtracted, the programs would have incorrectly assumed that the phase change was due to the solidification experiment. Assuming the cuvette was well made, however,  $\phi_B(y)$  was not expected to be extremely significant. It was

anticipated that most of the phase changes detected by the programs would be due to the solidification experiment, not the optics.

To assess the effect of the base phase, Run 48 was analyzed with and without base phase subtraction, at times of 30 seconds, 55 seconds, and 75 seconds after cooling began. Run 48 was conducted as described in the Consistency section.

#### Application: Holographic Interferometry

As mentioned in Chapter 1, the Fourier-transform method will be used to process holograms from an upcoming microgravity flight experiment. Since HGS holograms are similar to the type of holograms expected from the flight, one was analyzed via the Fourier-transform method.

The hologram was taken during a solidification experiment, conducted as described in the Solidification section. The cuvette contained a solution of 28.5 wt%  $\text{NH}_4\text{Cl}$  in  $\text{H}_2\text{O}$ . The top temperature during the gradient hold was 55.5 °C, and the bottom temperature was 25.5 °C. After a 38 minute gradient hold, the interface height was 0.37 millimeters. The cooling rate was 0.15 °C/minute. The hologram selected for analysis was taken 6 minutes and 37 seconds after cooling began. It was reconstructed in the holographic interferometry system discussed earlier.

The Fourier-transform method was applied to the hologram as discussed for Run 64, but there were several changes. Base phase subtraction was not applied because a base phase image was not available; thus Steps 6) through 9)

were omitted. To obtain an image scale, the camera was panned along the entire height of the cuvette, which was of known dimension. Pixel measurements were taken from the recorded images, and a scale giving pixels per millimeter was calculated. In the interferometry work, columns selected from the carrier image and the experimental image lined up physically. This was not possible with holographic interferometry, however, since the camera was repositioned after recording the carrier image. As discussed earlier, it was necessary to acquire the carrier image by panning the camera to an open air region outside the cuvette.

The hologram selected for Fourier-transform analysis was also reconstructed in a conventional holographic interferometer, without the addition of horizontal tilt fringes. That is, the interferometer was nulled, then the interference pattern created by the combination of the object and reference beams was recorded. This image was analyzed with the intensity method with exponential curve fit discussed earlier. In this way the Fourier-transform method was again compared with an intensity method. The column selected for analysis was located in the same area of the cuvette as the column processed with the Fourier-transform method.

## CHAPTER 5

### RESULTS

This chapter details the results obtained in assessing the Fourier-transform method, then closes with a discussion of problems and a summary of results. Raw data for all the analyses considered here are listed in Appendix 10.

#### 1-D Processing

Phase and concentration for the five adjacent columns analyzed are given in Figure 60 and Figure 61. The carrier frequencies for the five columns varied from 74.21 to 74.22. The temperature gradients, which were applied interactively in the analysis programs, ranged from 9.77 °C/cm to 9.87 °C/cm. Tip concentrations for the five columns showed good agreement, varying from 72.122 wt% to 72.125 wt%.

#### Consistency

Phase and concentration for four similar solidification runs are given in Figure 62 and Figure 63. Each phase curve has a unique y-axis intercept. When phase profiles at the same time are compared, it is therefore more pertinent to compare the shapes of the phase curves, rather than the phase values themselves. The shapes of the phase curves for each selected time are similar.

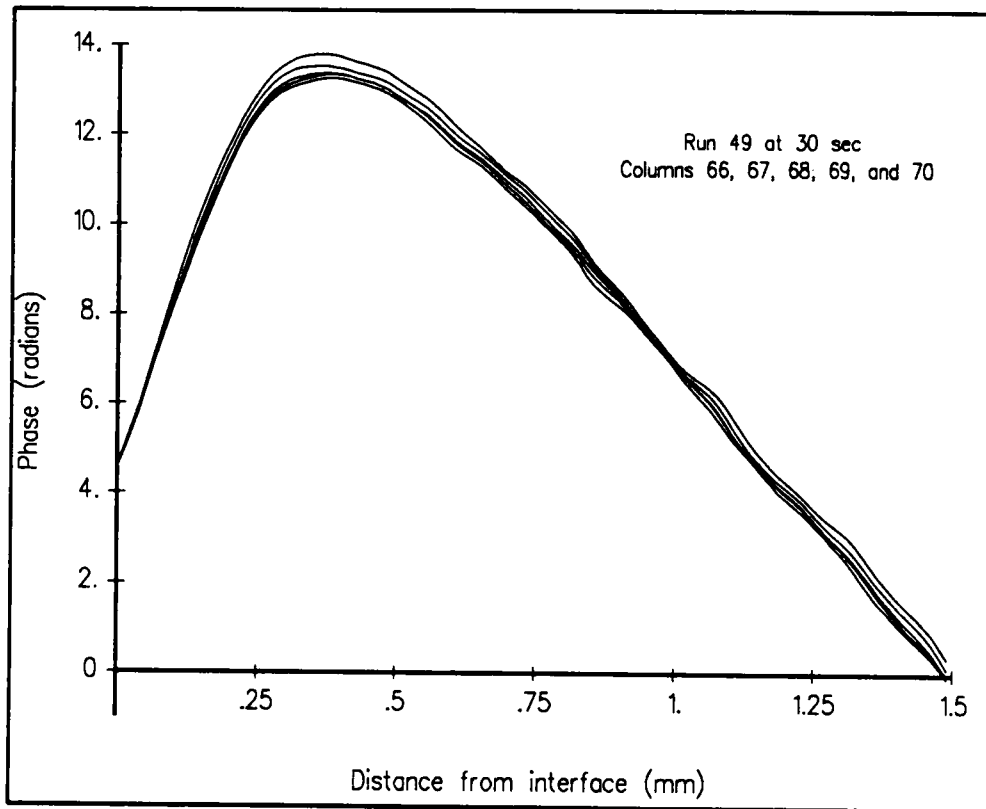


Figure 60. Phase plot for adjacent columns.



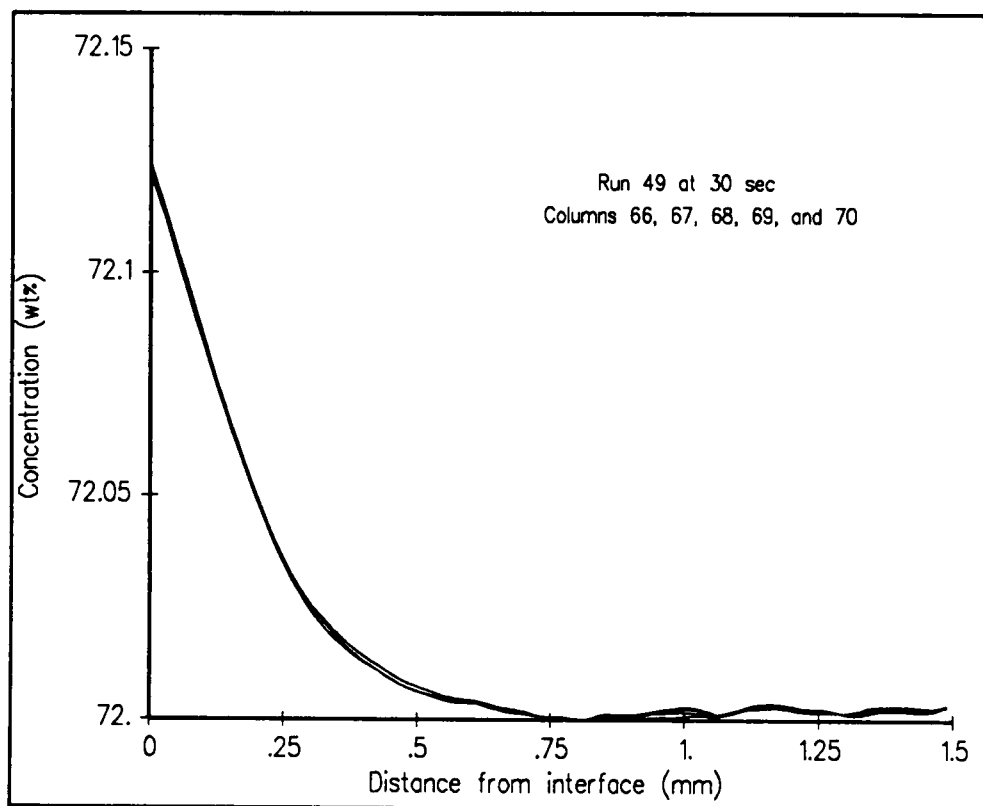


Figure 61. Concentration plot for adjacent columns.

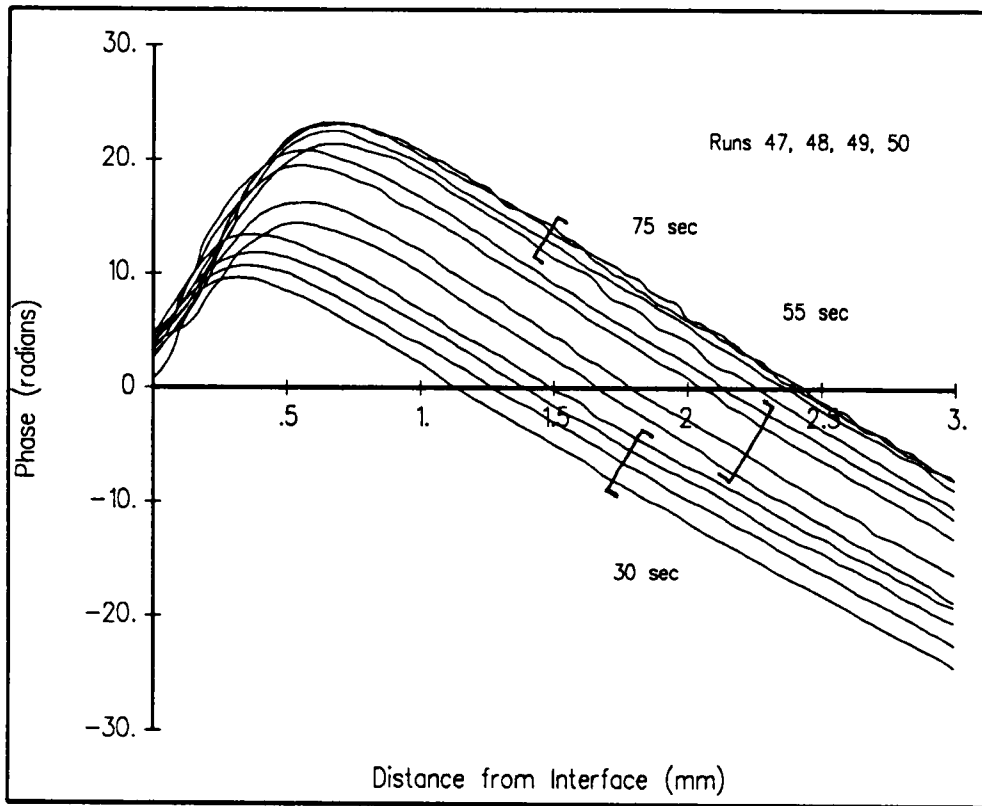


Figure 62. Phase plot for consistency check.

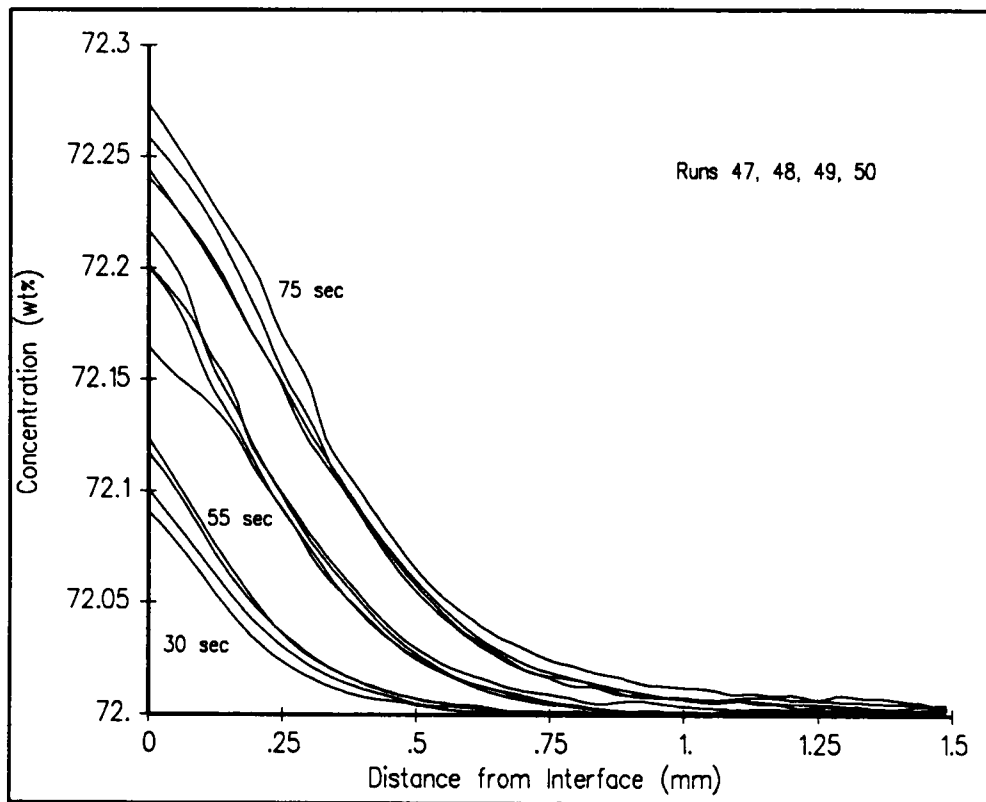


Figure 63. Concentration plot for consistency check.

At 30 seconds the tip concentration varied from 72.09 wt% to 72.12 wt%, at 55 seconds from 72.17 wt% to 72.22 wt%, and at 75 seconds from 72.24 wt% to 72.27 wt%. Concentration values show better agreement further from the interface. For each selected time, the concentration values beyond 0.25 millimeters from the interface agreed within 0.02 wt%.

The 0.05 wt% variation in the tip concentration at 55 seconds is fairly significant in that the total concentration variation over the time period studied was 0.18 wt%. However, it was difficult to create identical experimental conditions in these solidification runs. For example, the initial interface height varied by 0.06 millimeters. Moreover, tip concentration variations of this magnitude have been reported previously. Tip concentrations varied by 0.06 wt% at a cooling rate of 1 °C/minute, and by 0.10 wt% at cooling rate 3 °C/minute.

[3]

The temperature gradient ranged from 9.77 °C/cm to 9.97 °C/cm at 30 seconds, from 10.56 °C/cm to 10.79 °C/cm at 55 seconds, and from 10.99 °C/cm to 11.34 °C/cm at 75 seconds. As discussed in Chapter 4, program CONCEN2 recommended a temperature gradient, which was then adjusted with additional iterations of the program. The temperature gradient used was an average 0.3 °C/cm higher than the recommended gradient.

#### Comparison with Intensity Methods

Photographs of Run 64 at 45 seconds and 75 seconds are compared with the images analyzed with the intensity methods, in Figure 64. (The image scales

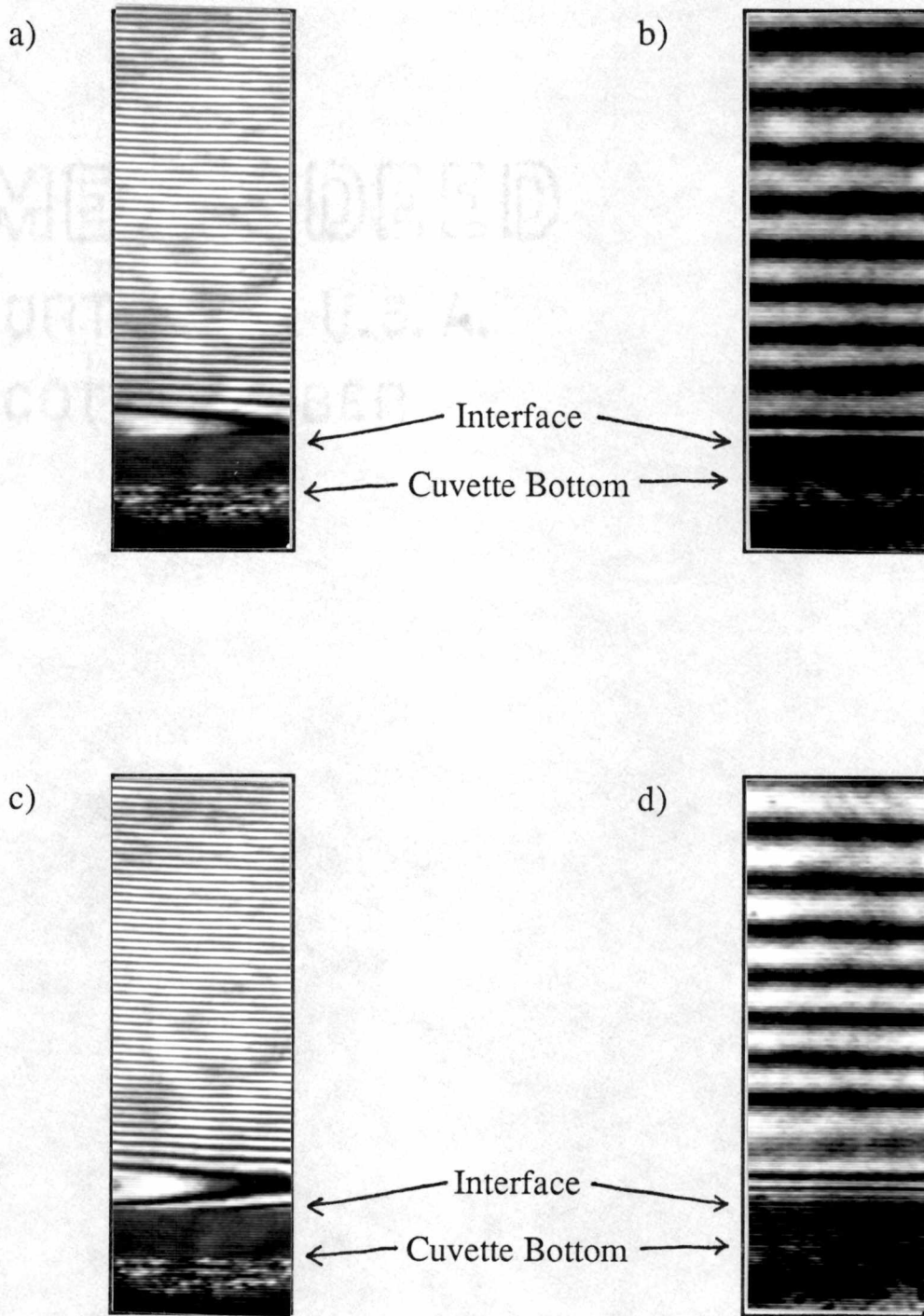


**Figure 64.** a) Fourier-transform method at 45 sec. b) Intensity method at 45 sec. c) Fourier-transform method at 75 sec. d) Intensity method at 75 sec.

for the two sets of photographs are slightly different: 72.5 pixels/millimeter for the Fourier-transform method versus 75.6 pixels/millimeter for the intensity methods.) The tilt fringes used in the Fourier-transform method produced the closely spaced fringes evident in the photographs on the left side of the figure.

Comparisons of the Fourier-transform method, the intensity method with spline fit, and the intensity method with exponential curve fit are given in the concentration plots in Figure 65 and Figure 66. At 45 seconds the Fourier-transform method gave tip concentrations varying from 72.16 wt% to 72.18 wt%. For the intensity method with spline fit, the tip concentration was 72.11 wt%, and the intensity method with exponential curve fit yielded a value of 72.15 wt%. At 75 seconds the comparison was: a range of 72.22 wt% to 72.26 wt% for the Fourier-transform method, 72.23 wt% for the intensity method with spline fit, and 72.26 wt% for the intensity method with exponential curve fit. In general the intensity methods gave concentration profiles that dropped off more quickly than those produced with the Fourier-transform method.

For the Fourier-transform method the temperature gradients varied from 10.65 °C/cm to 11.15 °C/cm at 45 seconds, and from 11.33 °C/cm to 12.04 °C/cm at 75 seconds. For the intensity method with exponential fit, the temperature gradient was 11.4 °C/cm at both 45 seconds and 75 seconds. The temperature gradient for the intensity method with spline fit was approximately 11.0 °C/cm.

The error of the intensity method with exponential fit has been estimated to be 0.04 wt%. [3] The concentration curve produced by this method was compared with the average of the curves produced by the Fourier-transform

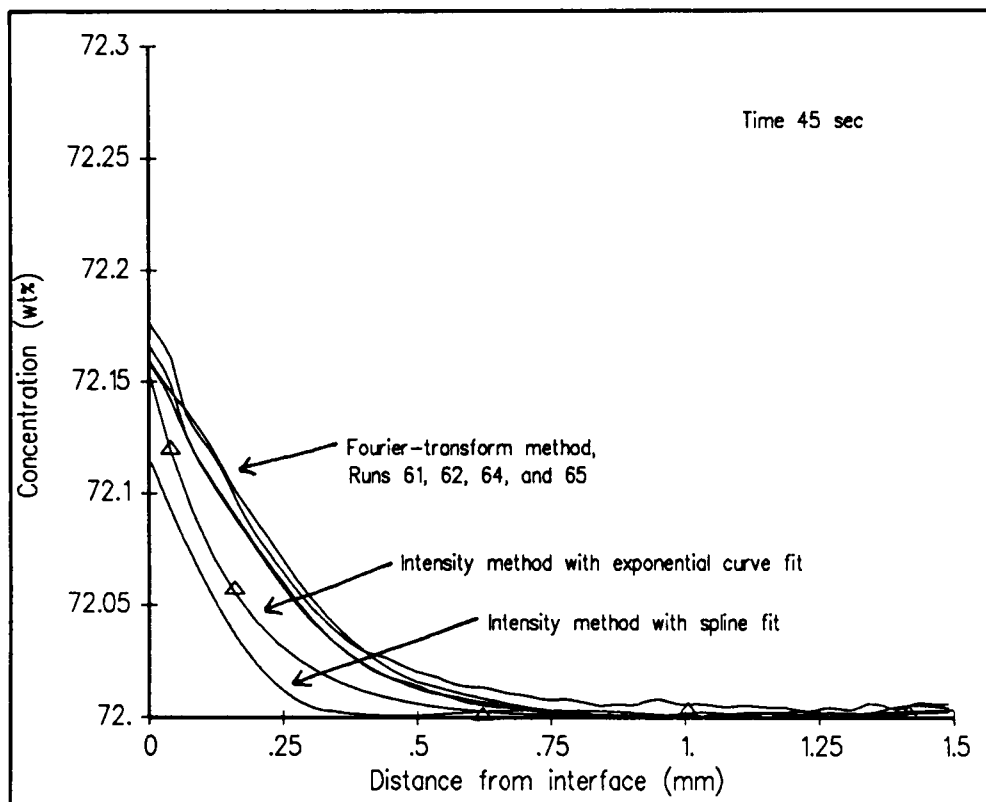


Figure 65. Concentration plot at 45 seconds, comparing three analytical methods.

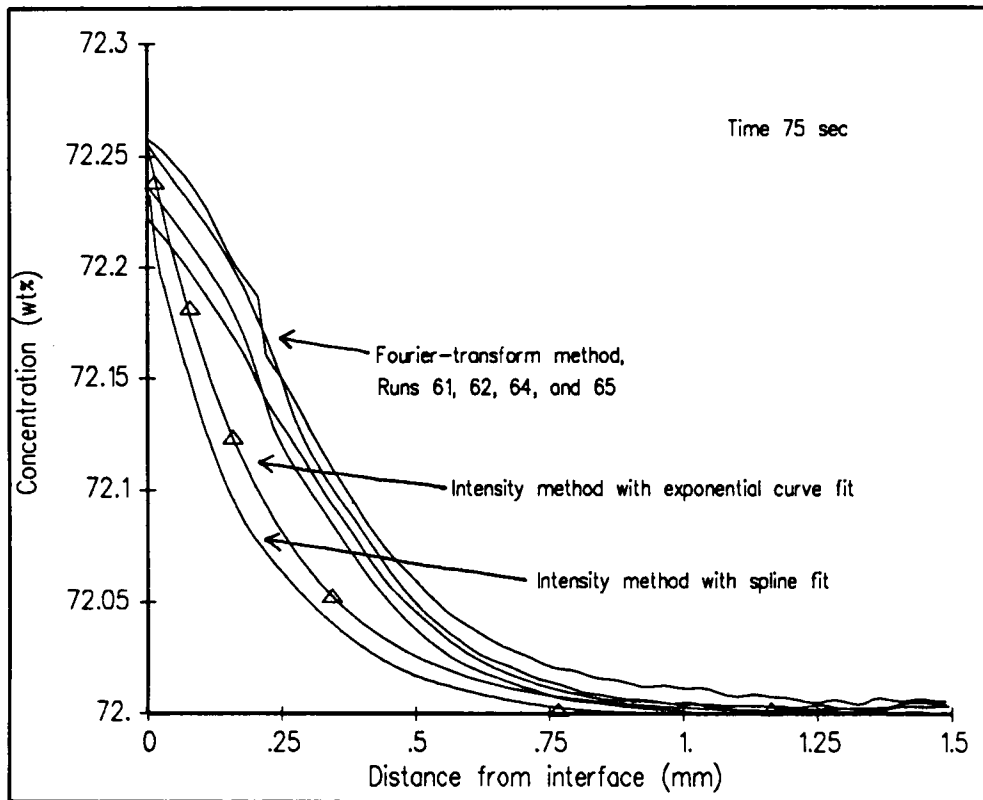


Figure 66. Concentration plot at 75 seconds, comparing three analytical methods.



method, at both 45 seconds and 75 seconds, to determine if the two curves agreed within the error of the exponential fit method. Within 0.16 millimeters of the interface, the values produced by the Fourier-transform method fell within 0.04 wt% of the intensity method values. Values for the two methods agreed within 0.01 wt% far away from the interface, around 0.62 millimeters at 45 seconds and 0.77 millimeters at 75 seconds. In the middle range, 0.16 millimeters to 0.62 millimeters at 45 seconds, and 0.16 millimeters to 0.77 millimeters at 75 seconds, the values matched within 0.07 wt%.

Unlike the intensity methods, the Fourier-transform method uses in its calculations the intensity of each pixel in the image column. The intensity methods rely on interpolation to obtain a complete concentration field. For example, at 45 seconds the intensity method with exponential fit used five data points over a distance of 1.5 millimeters. Over the same distance the Fourier-transform method used 109 data points.

The runs analyzed via the Fourier-transform method provide additional data regarding consistency of the method. For both times analyzed, the tip concentrations fell within a 0.04 wt% range, as compared with a 0.05 wt% range for the runs discussed in the Consistency section. This smaller concentration range could be related to the smaller range of initial interface heights: 0.30 millimeters to 0.32 millimeters, as compared with 0.11 millimeters to 0.17 millimeters for the Consistency runs.

The concentration curves for these runs show a smaller range earlier in the run; this trend also appeared in the Consistency runs. For example, the range

at 45 seconds was 0.03 wt%; for the Consistency runs a 0.03 wt% range was obtained at 30 seconds.

### Base Phase Subtraction

A plot of the base phase is given in Figure 67. As noted earlier, the cuvette wall deformed slightly at its juncture with the cuvette bottom.

Phase plots produced with and without base phase subtraction are shown in Figure 68. Since it is difficult to compare phase in this format, fringe patterns calculated with and without base phase subtraction are given in Figure 69 through Figure 71. As discussed earlier, the fringe pattern is obtained by taking the cosine of the phase. See Eq. 83. Significant differences in phase are observed in the region within 1.5 millimeters of the solidifying interface.

Concentration plots calculated with and without base phase subtraction are shown in Figure 72. For each time analyzed, subtraction of the base phase yielded a tip concentration 0.01 wt% higher than without base phase subtraction. Values of concentration further from the interface were similar for the two procedures.

It was noted that the temperature gradient for the base phase subtraction analyses was an average 0.71 °C/cm higher than the temperature gradient for the analyses without base phase subtraction. The comparison was as follows:

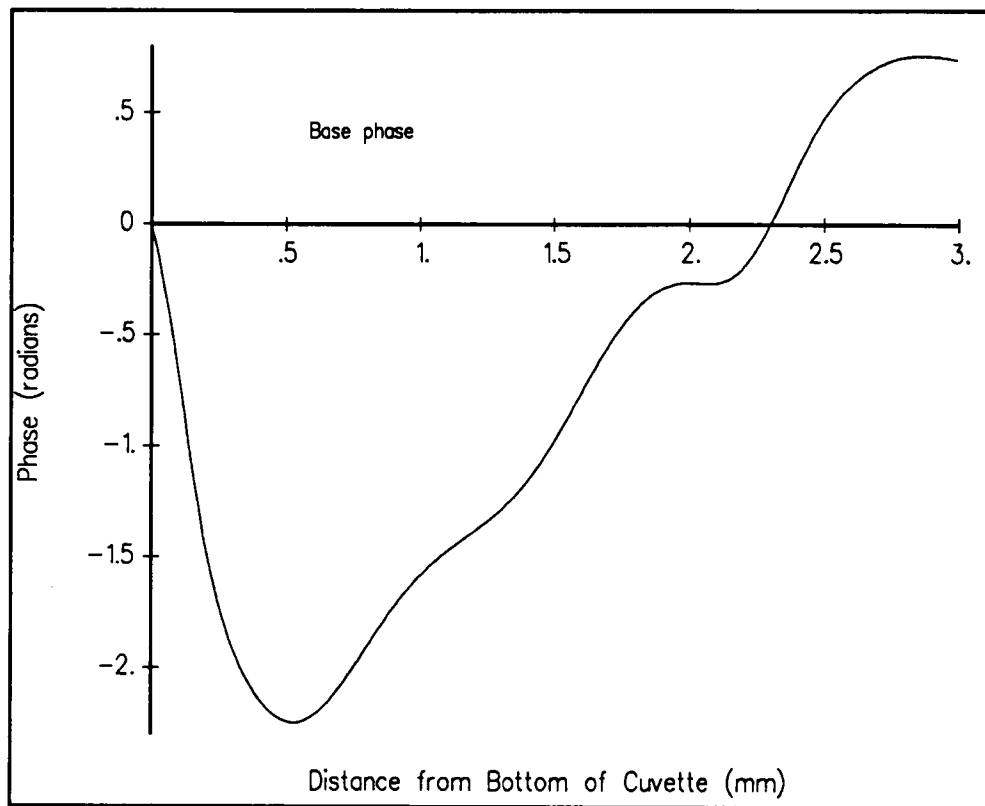


Figure 67. The base phase.

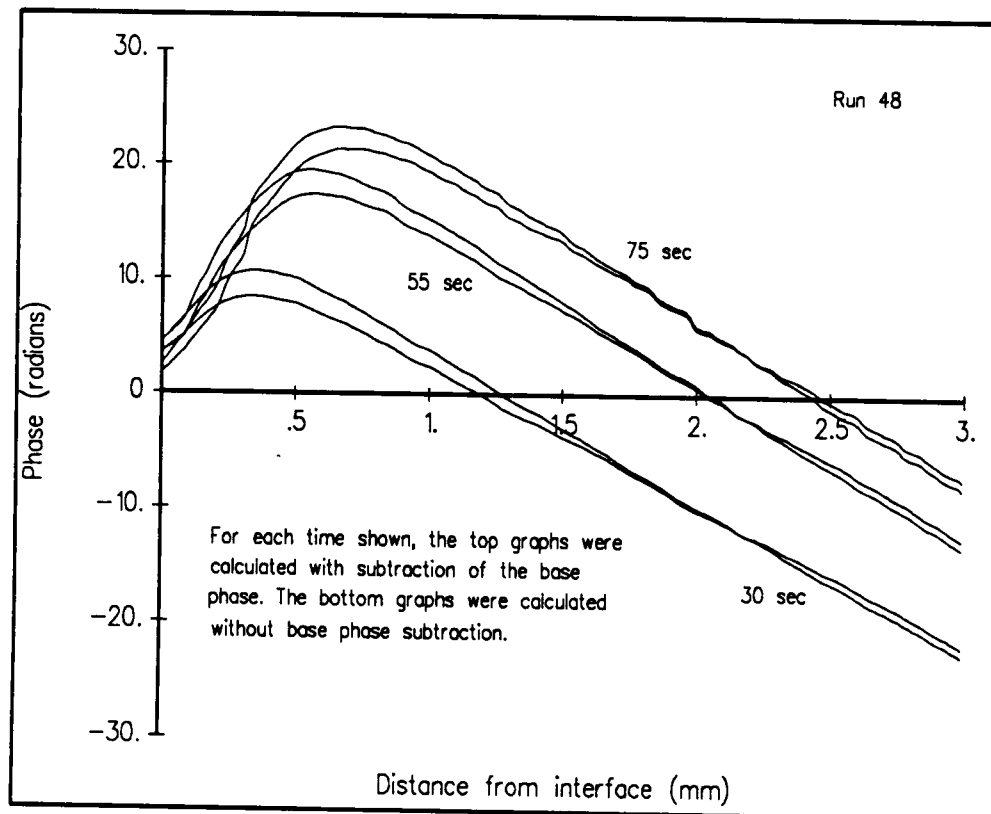
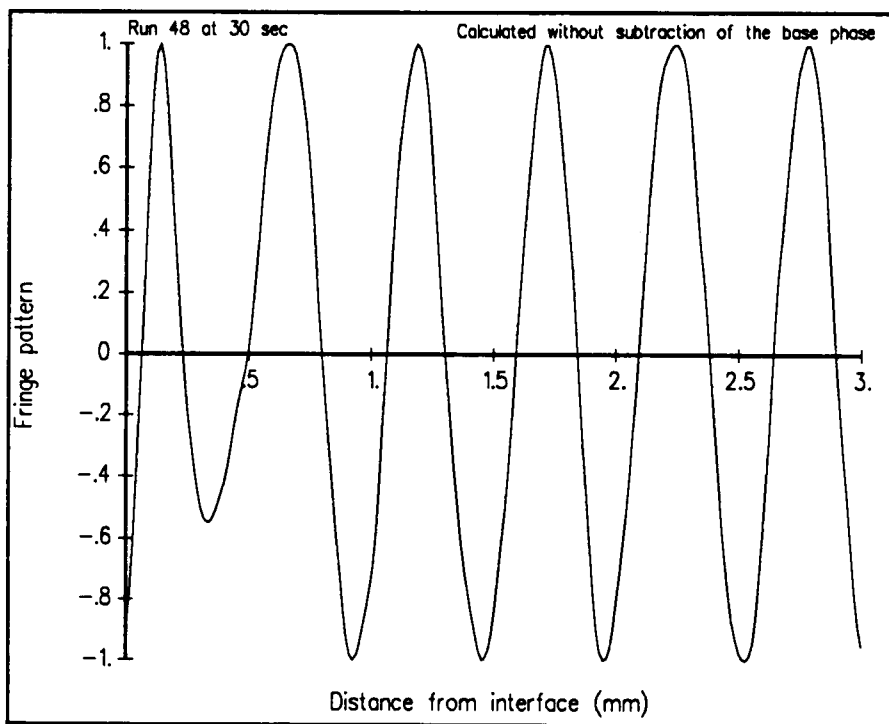
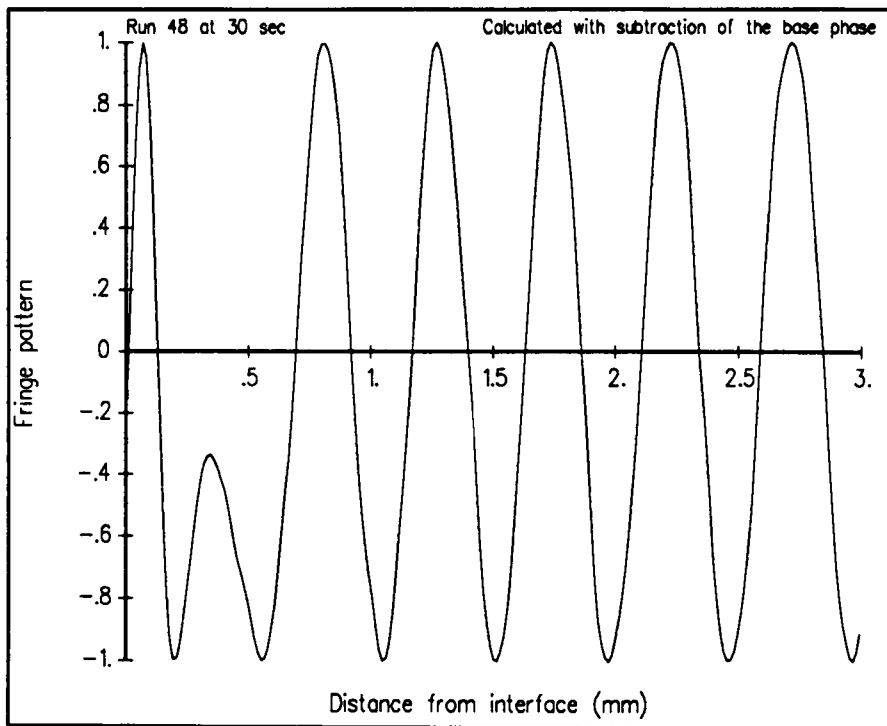
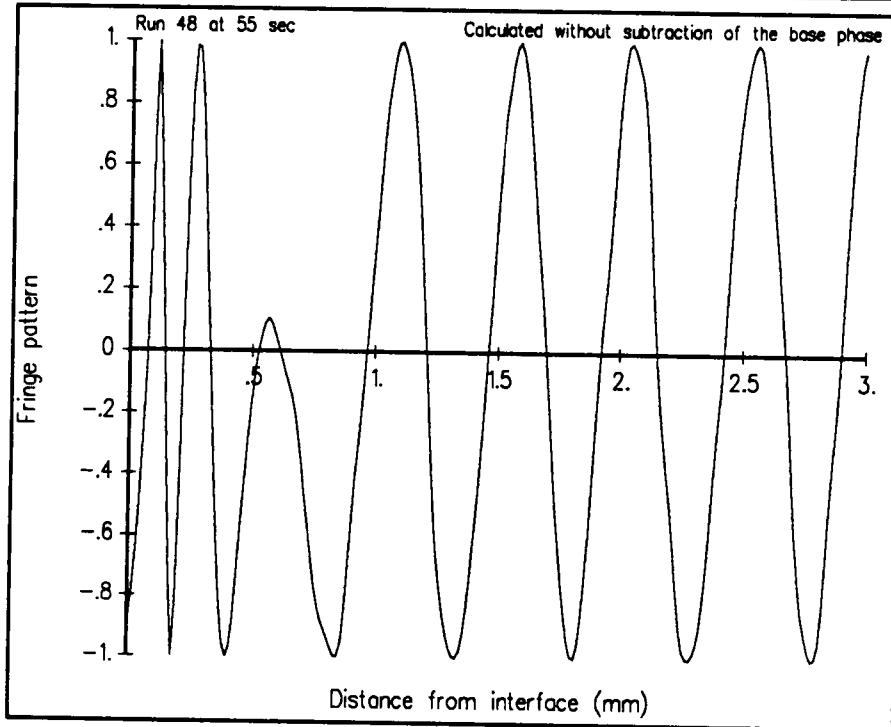
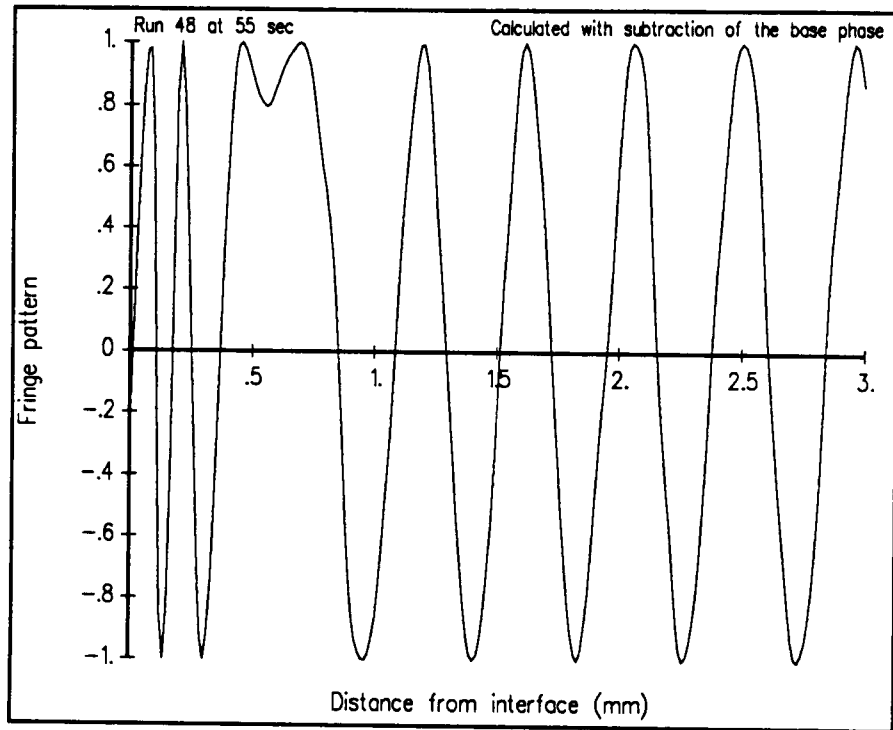


Figure 68. Phase plots produced with and without base phase subtraction.



**Figure 69.** Comparison of fringe patterns at 30 seconds, with and without base phase subtraction.



**Figure 70.** Comparison of fringe patterns at 55 seconds, with and without base phase subtraction.

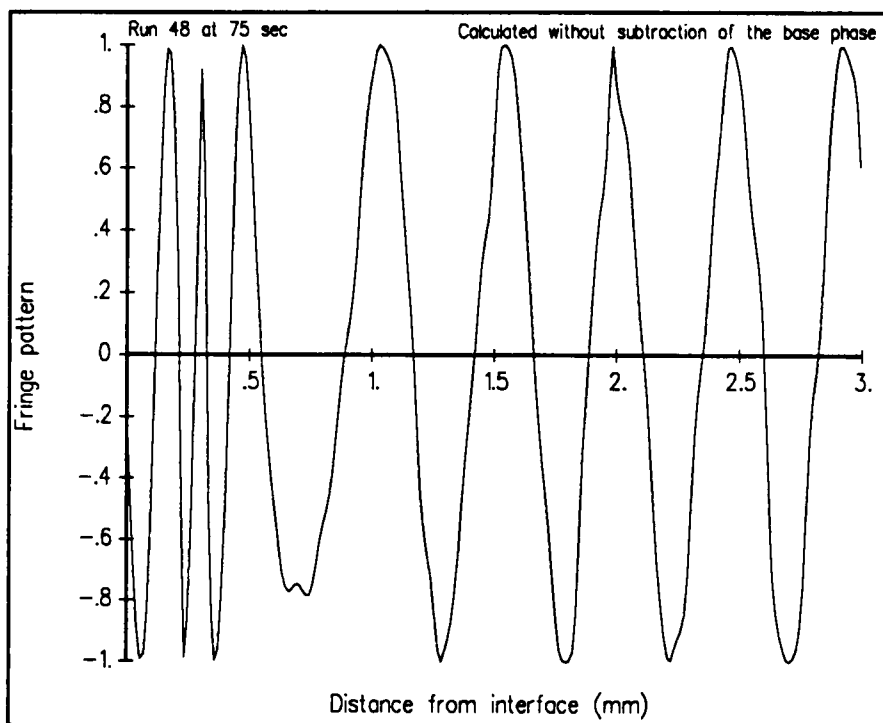
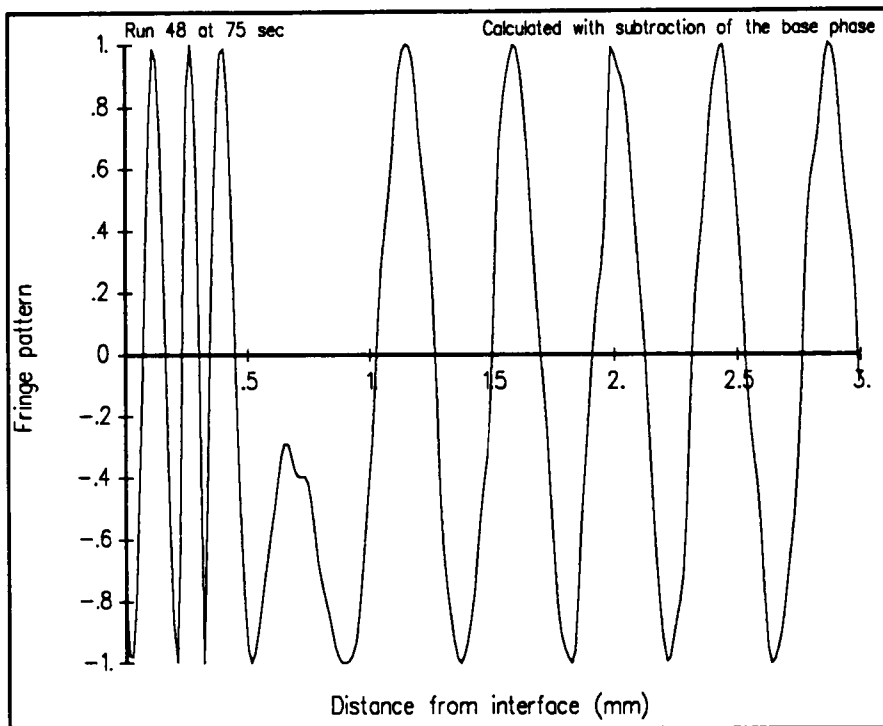


**Figure 71.** Comparison of fringe patterns at 75 seconds, with and without base phase subtraction.

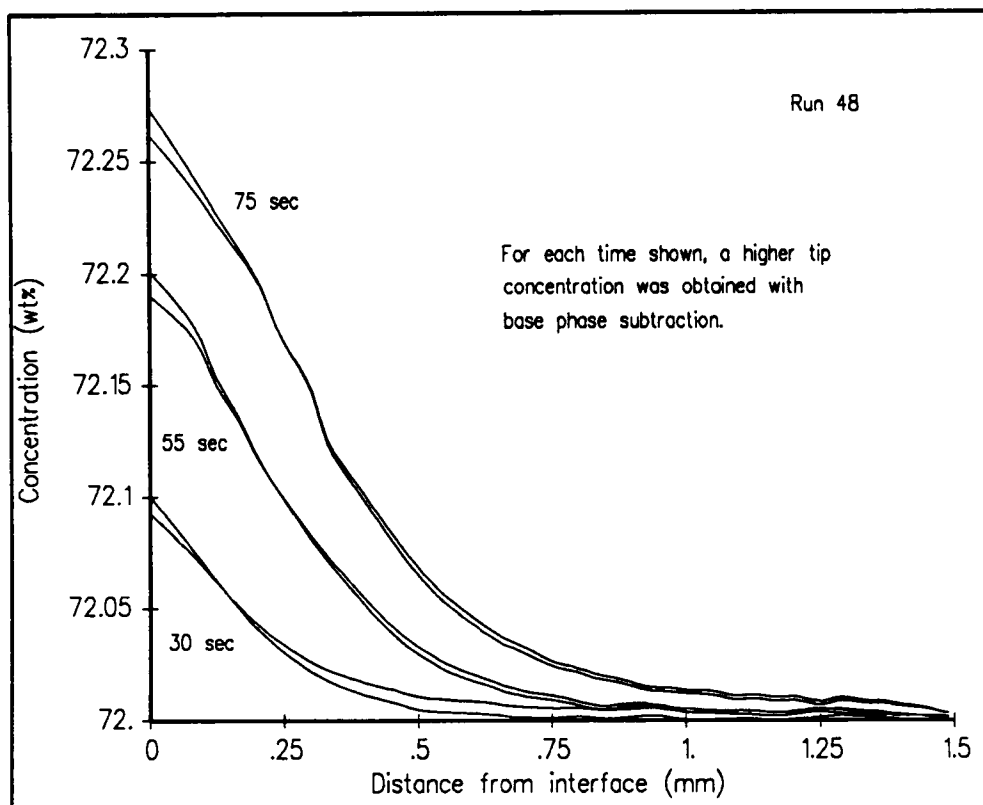


**Figure 72.** Concentration plots produced with and without base phase subtraction.



### Temperature Gradient

Time	With Base Phase Subtraction	Without
30 seconds	9.87 °C/cm	9.22 °C/cm
55 seconds	10.79 °C/cm	10.05 °C/cm
75 seconds	11.34 °C/cm	10.59 °C/cm

Apparently, subtraction of a decreased linear temperature gradient acted to remove the base phase from runs in which base phase subtraction was not performed. This may be due to the fact that a large portion of the base phase is nearly linear, as shown in Figure 67. As discussed in Chapter 4, the temperature gradient was selected in a systematic way: it was adjusted until the exponential tail of the concentration plot was flat at 3 millimeters away from the interface. Thus the application of the temperature gradient should not be viewed as a "fudge factor" for correction of the situation where the base phase was not subtracted.

The base phase and the temperature gradient are related because the base phase is a component of the phase distribution in the upper portion of the cuvette. The temperature gradient is selected by observing this phase distribution. It should therefore be possible to determine the effects of a given base phase profile on the selected temperature gradient. Since only a single base phase pattern was used in this project, such a correlation was not defined.

### Application: Holographic Interferometry

The phase plot produced during the analysis of an HGS hologram is given in Figure 73. Although the shape of the phase curve is similar to that produced in the interferometry runs, the phase output is noisy. The pattern closely approximates one produced by Green et al., in which signal-independent random additive noise was introduced in a simulation. [31]

Figure 74 gives the corresponding concentration plot, which is also noisy. The tip concentration was 71.70 wt%. The previous section suggests that the true value may be slightly higher, since base phase subtraction could not be applied. The concentration curve dropped less quickly than those produced for the interferometry runs; the use of different solidification parameters undoubtedly contributed to this effect.

The same temperature gradient, 16.25 °C/cm, was applied in both the Fourier-transform method and the intensity method. The intensity method yielded a slightly higher tip concentration, 71.71 wt%. See Figure 75. The Fourier-transform method produced a concentration curve that dropped more quickly than the intensity method.

### Discussion of Problems

#### Fringe Visibility in Holographic Interferometry

The noisy phase plot produced with holographic interferometry (see Figure 73) was the best encountered after reconstructing many holograms taken

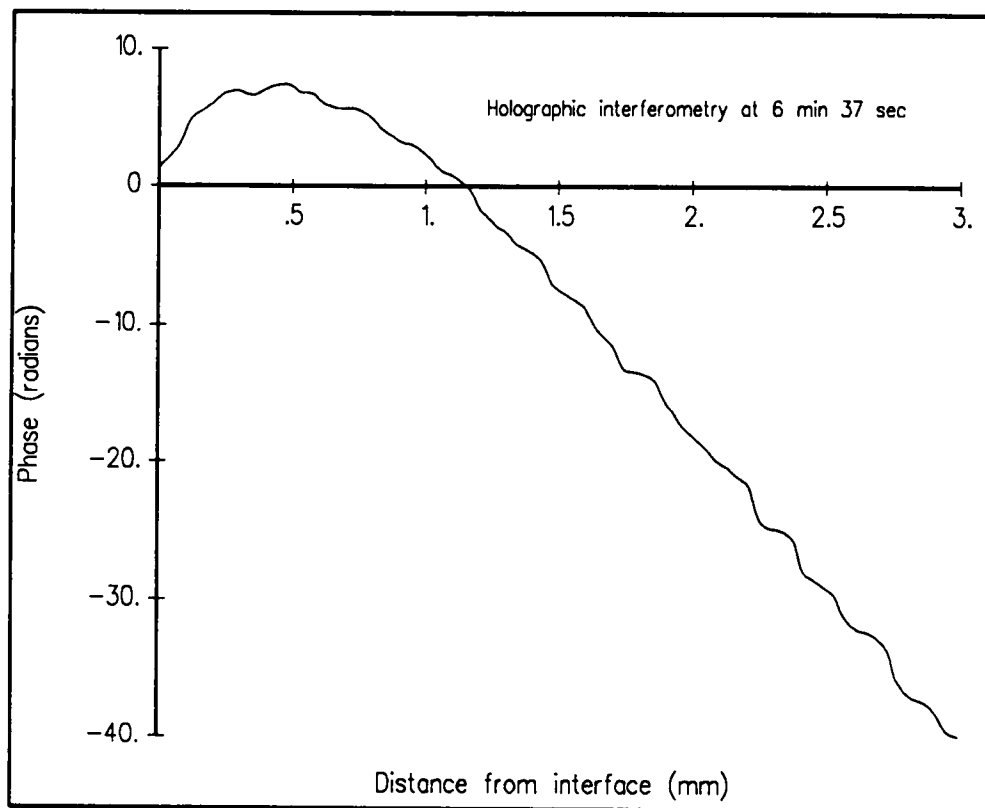
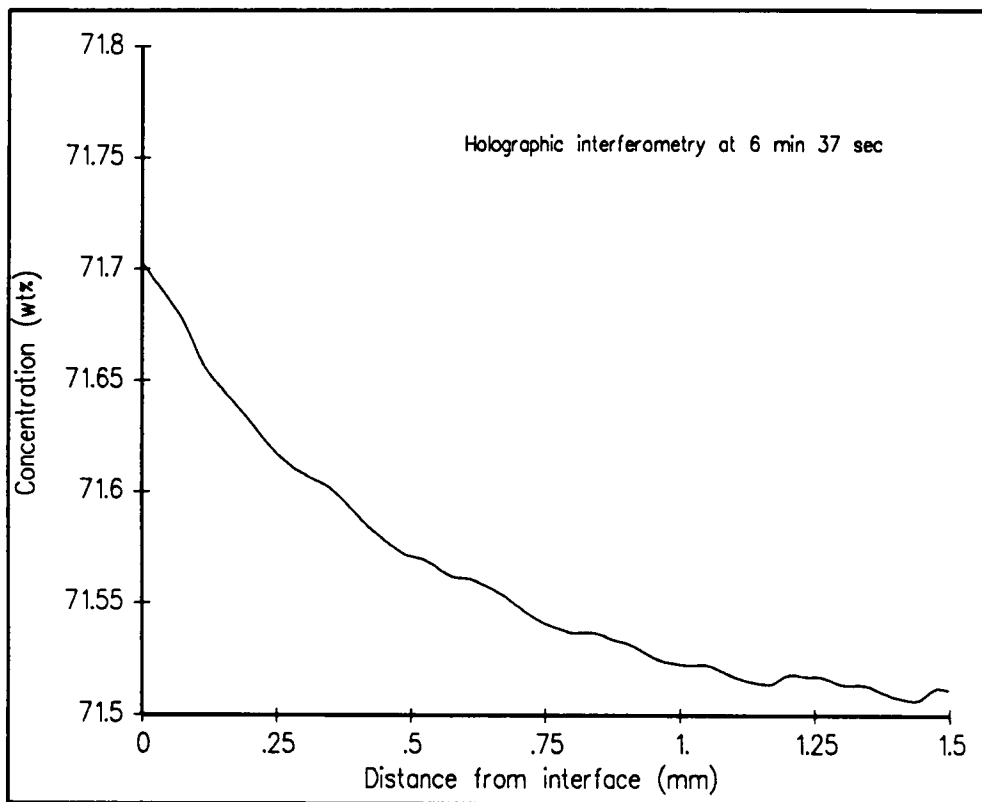
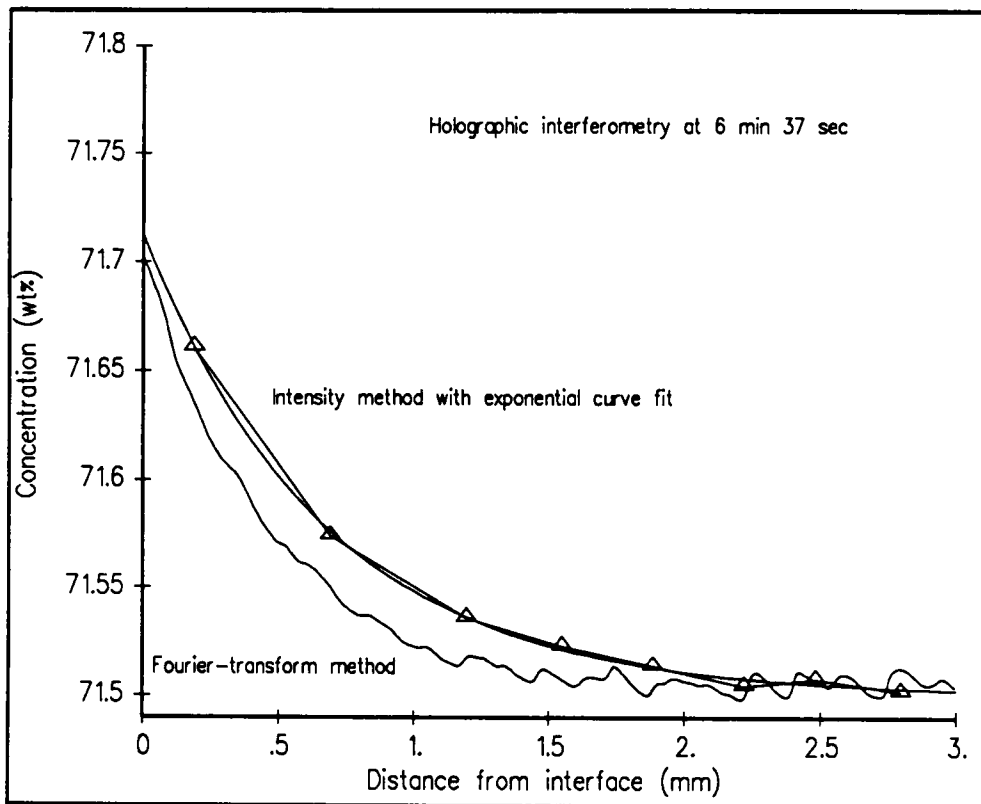


Figure 73. Phase plot for holographic interferometry.



**Figure 74.** Concentration plot for holographic interferometry.



**Figure 75.** Concentration plot for holographic interferometry, comparing Fourier-transform analysis with an intensity method.

during a variety of solidification runs. The reference beam used in reconstruction did not duplicate exactly the reference beam used in recording the holograms. The holograms themselves were not the highest quality. Both of these factors, among others, contributed to poor fringe visibility, which increased the noise in reconstructed images.

Poor fringe visibility was especially troublesome when carrier fringes, the basis of the Fourier-transform method, were introduced. The method requires finely spaced fringes for isolation of spectral components, yet fringe visibility worsened when additional fringes were induced. Resolution of the faint variations of intensity by the camera was not possible beyond carrier frequency 61.05, the value used in this project. Higher carrier frequency values led to phase distributions which were too noisy to unwrap correctly.

To partially alleviate the effects of poor fringe visibility, special attention was paid to vibration isolation. Also, neutral density filters were used to match the intensities of the object and reference beams as closely as possible.

### Spectral Overlap

As discussed in Chapter 3, the fact that  $C(f - f_0)$  is not bandlimited causes its spectral sidelobes to overlap with other spectral components in the Fourier transform of an image. See Figure 10. In this project, spectral overlap became apparent when the low-frequency cutoffs for Fourier domain filters were chosen. In several analyses a range of cutoff frequencies was attempted before a reasonable phase profile was produced.

Setting a higher carrier frequency via the introduction of more carrier fringes would help to reduce the effects of spectral overlap. As explained earlier, this was not possible for holographic interferometry because of the corresponding decrease in fringe visibility. The carrier frequency could have been set slightly higher for interferometry, but the limited resolution of the camera was a concern.

Sufficient experience with the data led to increased success in choosing the low-frequency cutoff. Selecting a cutoff that was too low led to a noisy phase plot and a distorted fringe pattern. Phase plots did not take the expected form when a cutoff that was too high was selected. The cutoff selection was more critical when processing images acquired later in the run.

### Overall Results

A 1-D implementation of the Fourier-transform method was acceptable for calculating concentration changes that developed during solidification of  $\text{NH}_4\text{Cl}$ . Analysis of a single column of intensity values gave an accurate picture of the phase and concentration changes which occurred in that section of the cuvette. Tip concentrations for five adjacent columns varied no more than 0.003 wt%.

When the analyses of runs conducted under similar conditions were compared, the Fourier-transform method was found to produce concentration plots of consistent shape and value. For example, tip concentrations agreed within 0.05 wt%.

When the Fourier-transform method was compared with an intensity method with exponential fit, the concentration curves agreed within 0.07 wt%,

with a tighter match at the interface. This is an acceptable tolerance given that solidification conditions could not be duplicated exactly. In addition, the Fourier-transform method and the intensity method are very different techniques; thus an exact match should not be expected. For example, the intensity method neglected base phase subtraction, did not filter the irradiance variations  $a(y)$  and  $b(y)$ , and used outside information to determine the location of an inflection point in the density. Manual fringe location required in the intensity method is a subjective activity, prone to operator error.

The technique of base phase subtraction was found to have an effect on concentration plots, particularly at the interface. In this project it was noted that application of a decreased temperature gradient partially compensated for situations in which the base phase could not be subtracted. In general applications, the effectiveness of this technique would depend on the particular base phase pattern.

The Fourier-transform method was successfully applied in the area of holographic interferometry. However, poor fringe visibility led to considerable noise in the resultant concentration profiles.

The performances of the Fourier-transform method and the intensity method with exponential fit were compared for images produced via interferometry and holographic interferometry, with conflicting results. For the interferometry runs, the Fourier-transform method yielded a concentration curve that dropped less quickly than the results produced with the intensity method. For holographic interferometry the opposite occurred: the Fourier-transform method



produced a concentration plot that dropped more quickly than the intensity method. In evaluating these results, the attributes of the techniques of interferometry and holographic interferometry should be considered. Holographic interferometry provided an excellent platform for comparison in that the same hologram, thus the same run conditions, was used for both methods. However, conventional interferometry produced images with less noise.

## CHAPTER 6

### CONCLUSIONS

#### Discussion

In conclusion, a 1-D version of the Fourier-transform method has been shown to perform well in a specific application, determination of the phase changes produced in the diffusion layer of a solidifying metal model material. Phase plots calculated by the method took the expected form. Since phase can be related to concentration, the Fourier-transform method is an excellent tool for determining concentration profiles. When applied to analyze solidification runs conducted under similar experimental conditions, the method produced concentration profiles that agreed within 0.05 wt%.

The images analyzed in this project were obtained with the laser optical techniques of interferometry and holographic interferometry. However, the Fourier-transform method can be applied to a wide variety of fringe patterns. Although the method developed here was used to study an ammonium chloride-water system, it should also be useful to researchers working with other transparent metal models. Preliminary work indicates that the Fourier-transform method permits concentration measurements to be taken much earlier than other analysis methods, as soon as five seconds after cooling begins.

The Fourier-transform method is more sensitive and accurate than intensity methods. Unlike intensity methods, the Fourier-transform method uses all of the

intensity information in an image and produces a continuous phase profile. Phase variations of less than  $2\pi$  can be detected with the Fourier-transform method. Outside information is not required to determine an inflection point in phase, and unwanted irradiance variations are filtered, improving accuracy. Because it relies less on a human operator, the Fourier-transform method is less subjective than intensity methods.

Since the Fourier-transform method developed in this project included the improved determination of the carrier frequency suggested by Bone et al., [28] significant errors due to digitization of the data were eliminated. In addition, the technique of base phase subtraction reduced erroneous phase contributions caused by optical aberrations. The method used in this project is highly automated, which will be of particular advantage when it is used to analyze hundreds of holograms from an upcoming flight experiment.

One limitation of this work was due to the fact that interferometry is a line-of-sight technique, thus phase and concentration measurements were averaged over the optical path. For images obtained with holographic interferometry, the performance of the Fourier-transform method was also limited in that base phase subtraction could not be performed. In addition these images showed significant noise. Images obtained with (non-holographic) interferometry had good fringe visibility, so noise was not a problem. Another limitation in this project was the frequency domain filtering operation. Because spectral overlap exists, the truncation that is part of this operation introduced some amount of corruption

into the filtered data. The largest errors in filtering probably occurred at the solid-liquid interface, due to the sharp transition there between opaque features and fringes.

### Recommendations

Several topics for future study are suggested by this project. A more complete comparison between the intensity method discussed previously and the Fourier-transform method is warranted. If the effects of noise can be lessened, holographic interferometry would be an excellent platform for such a study. The same hologram would be reconstructed as required by the two methods, with the advantage that the reconstructions would show identical solidification conditions. Another option would be to test the performance of the two methods with a computer model, which would simulate concentration, phase, and intensity fields for analysis.

The performance of the Fourier-transform method would be enhanced if data acquisition techniques were improved. For example, improved magnification optics could be incorporated into the interferometers.

In this project a 1-D version of the Fourier-transform method was implemented; a logical followup to this study would be an extension to two dimensions. Several of the other decisions made in implementing the Fourier-transform method merit additional consideration. For example, an ideal lowpass filter modified by a Hanning window was used in Fourier domain processing. Other windowing schemes could be investigated, or an optimal filter could be

designed. The carrier frequency was determined as suggested by Bone et al.; [28] the increased accuracy over the Takeda et al. method [25] could be measured. Macy's recurrence relationship for phase-unwrapping was chosen for this project. [27] The performance of this method could be compared with the many other phase-unwrapping algorithms found in the literature.

As discussed in Chapter 3, a Fourier-transform method without tilt fringes has been proposed. [30] If accurate, the method has the advantage of direct applicability to the contour interferograms usually analyzed by intensity methods. The utility of the method could be gauged by comparison with the conventional Fourier-transform method or with intensity methods.

## **LIST OF REFERENCES**

- [1] M.H. McCay and T.D. McCay, "Experimental measurement of solutal layers in unidirectional solidification," *Journal of Thermophysics and Heat Transfer*, v. 2, n. 3, pp. 197-202, July 1988.
- [2] J.A. Hopkins, "Experimental study of convective instability of the diffusion layer produced during directional solidification of a metal model material," M.S. Thesis, University of Tennessee, Knoxville, August 1989.
- [3] J.A. Hopkins, T.D. McCay, and M.H. McCay, "Interferometric measurements of a dendritic growth front solutal diffusion layer," Paper #91-1334, Proceedings of the 26th AIAA Thermophysics Conference, Honolulu, Hawaii, June 24-26, 1991.
- [4] M.H. McCay, Principal Investigator, Rudy Ruff, Technical Officer, Casting and Solidification Technology, Fluid Experiment System, International Microgravity Laboratory I, NASA Marshall Space Flight Center.
- [5] R.F. Pierret, *Advanced Semiconductor Fundamentals*, Addison-Wesley, Reading, Massachusetts, 1987.
- [6] M.C. Flemings, *Solidification Processing*, McGraw-Hill, New York, 1974.
- [7] T.D. McCay, M.H. McCay, and J.A. Hopkins, "Thermal and solutal conditions at the tips of a directional dendritic growth front," Paper 91-1333, Proceedings of the 26th AIAA Thermophysics Conference, Honolulu, Hawaii, June 24-26, 1991.
- [8] S.V. Patankar, *Numerical Heat Transfer and Fluid Flow*, Hemisphere Publishing, New York, 1980.
- [9] M.H. McCay, T.D. McCay, and L.M. Smith, "Solidification studies using a confocal optical signal processor," *Applied Optics*, v. 29, n. 5, pp. 699-703, 10 February 1990.
- [10] S.A. Lowry, "A numerical model of convective effects in diffusion dominated directional solidification of a metal analogue ( $\text{NH}_4\text{Cl}-\text{H}_2\text{O}$ ) at one gravity and microgravity," Ph.D. Dissertation, University of Tennessee, Knoxville, May 1991.
- [11] M.H. Johnston and R.B. Owen, "Optical observations of unidirectional solidification in microgravity," *Metallurgical Transactions*, v. 14A, pp. 2163-2167, October 1983.
- [12] P.A. Gray, "Experimental study of convective breakdown during solidification of a metal model material," M.S. Thesis, University of Tennessee, Knoxville, May 1989.
- [13] T.D. McCay, M.H. McCay, and P.A. Gray, "Experimental observation of convective breakdown during directional solidification," *Physical Review Letters*, v. 62, n. 17, pp. 2060-2063, 24 April 1989.
- [14] T.D. McCay, M.H. McCay, S.A. Lowry, and L.M. Smith, "Convective instabilities during directional solidification," *Journal of Thermophysics and Heat Transfer*, v. 3, n. 3, pp. 345-350, July 1989.
- [15] M.S. Christenson and F.P. Incropera, "Solidification of an aqueous ammonium chloride solution in a rectangular cavity - I. Experimental study," *International Journal of Heat and Mass Transfer*, v. 32, n. 1, pp. 47-68, 1989.
- [16] W.K. Witherow, "Reconstruction techniques of holograms from Spacelab 3," *Applied Optics*, v. 26, n. 12, pp. 2465-2473, 15 June 1987.

- [17] R.B. Owen, R.L. Kroes, and W.K. Witherow, "Results and further experiments using Spacelab holography," *Optics Letters*, v. 11, n. 7, pp. 407-409, July 1988.
- [18] H. Tan, J.D. Trolinger, and D. Modarress, "An automated holographic interferometry data reduction system," *SPIE*, v. 693, pp. 161-165, 1986.
- [19] H.-D. Yoo, W.R. Wilcox, R. Lal, and J.D. Trolinger, "Modelling the growth of triglycine sulphate crystals in Spacelab 3," *Journal of Crystal Growth*, n. 92, pp. 101-117, 1988.
- [20] R.B. Lal, J.D. Trolinger, W.R. Wilcox, and R.L. Kroes, "Holographic flow field analysis in Spacelab-3 crystal growth experiments," *SPIE*, v. 788, pp. 62-72, May 1987.
- [21] R.L. Kroes and D. Reiss, "Properties of TGS aqueous solution for crystal growth," *Journal of Crystal Growth*, n. 69, pp. 414-420, 1984.
- [22] G.T. Reid, "Automatic fringe pattern analysis: a review," *Optics and Lasers in Engineering*, v. 7, n. 1, pp. 37-68, 1986/87.
- [23] L. Hesselink, "Digital image processing in flow visualization," *Annual Review of Fluid Mechanics*, v. 20, pp. 421-485, 1988.
- [24] K.H. Womack, "Interferometric phase measurements using spatial synchronous detection," *Optical Engineering*, v. 23, n. 4, pp. 391-395, July/August 1984.
- [25] M. Takeda, H. Ina, and S. Kobayashi, "Fourier-transform method of fringe-pattern analysis for computer-based topography and interferometry," *Journal of the Optical Society of America*, v. 72, n. 1, pp. 156-160, January 1982.
- [26] K.A. Nugent, "Interferogram analysis using an accurate fully automatic algorithm," *Applied Optics*, v. 24, n. 18, pp. 3101-3105, 15 September 1985.
- [27] W.W. Macy, "Two-dimensional fringe-pattern analysis," *Applied Optics*, v. 22, n. 23, pp. 3898-3901, 1 December 1983.
- [28] D.J. Bone, H.-A. Bachor, and R.J. Sandeman, "Fringe pattern analysis using a 2-D Fourier transform," *Applied Optics*, v. 25, n. 10, pp. 1653-1660, 15 May 1986.
- [29] L. Mertz, "Real-time fringe-pattern analysis," *Applied Optics*, v. 22, n. 10, pp. 1535-1539, 15 May 1983.
- [30] T. Kreis, "Digital holographic interference-phase measurement using the Fourier-transform method," *Journal of the Optical Society of America A*, v. 3, n. 6, pp. 847-855, June 1986.
- [31] R.J. Green, J.G. Walker, and D.W. Robinson, "Investigation of the Fourier-transform method of fringe pattern analysis," *Optics and Lasers in Engineering*, v. 8, n. 1, pp. 29-44, 1988.
- [32] J.D. Trolinger, "Particle and flow field holography: a critical survey," *SPIE Proceedings*, v. 532, pp. 40-62, 1985.
- [33] R.C. Gonzalez and P. Wintz, *Digital Image Processing*, Addison-Wesley, Reading, Massachusetts, 1987.



## **APPENDICES**

**APPENDIX 1**

**THE DISCRETE FOURIER TRANSFORM**

A Fourier transform pair gives the relationship between a spatial function and its spatial frequency transform. The 1-D and 2-D discrete Fourier transform pairs are given by:

(Eq. 94.)

$$F(u) = 1/N \sum_{x=0}^{N-1} f(x) \exp (-j2\pi ux/N),$$

for  $u = 0, 1, \dots, N-1,$

(Eq. 95.)

$$f(x) = \sum_{u=0}^{N-1} F(u) \exp (j2\pi ux/N),$$

for  $x = 0, 1, \dots, N-1,$

(Eq. 96.)

$$F(u,v) = 1/N \sum_{x=0}^{N-1} \sum_{y=0}^{N-1} f(x,y) \exp [-j2\pi(ux + vy)/N],$$

for  $u, v = 0, 1, \dots, N-1,$  and

(Eq. 97.)

$$f(x,y) = 1/N \sum_{u=0}^{N-1} \sum_{v=0}^{N-1} F(u,v) \exp [j2\pi(ux + vy)/N],$$

for  $x, y = 0, 1, \dots, N-1,$

where  $f(x)$  and  $f(x,y)$  are sequences of discrete samples of continuous, spatial domain functions.  $F(u)$  and  $F(u,v)$  are the Fourier domain transforms of  $f(x)$  and  $f(x,y)$ , respectively.  $f(x)$  and  $F(u)$  are each composed of  $N$  elements.  $f(x,y)$  and  $F(u,v)$  are square arrays composed of  $N$  by  $N$  elements.

The fast Fourier transform (FFT) is an algorithm for computing the discrete Fourier transform. By decomposing the summation in Eq. 94 or Eq. 95, the 1-D transforms, the FFT reduces the number of complex multiply and add operations from the order of  $N^2$  to the order of  $N \log_2 N$ . [33] 2-D transforms are computed with successive applications of the 1-D FFT.

The translation properties of the 1-D and 2-D discrete Fourier transforms are given by:

(Eq. 98.)

$$f(x) \exp(j2\pi u_0 x/N) \longleftrightarrow F(u - u_0),$$

(Eq. 99.)

$$f(x - x_0) \longleftrightarrow F(u) \exp(-j2\pi u x_0/N),$$

(Eq. 100.)

$$f(x,y) \exp[j2\pi(u_0 x + v_0 y)/N] \longleftrightarrow F(u - u_0, v - v_0),$$

(Eq. 101.)

$$f(x - x_0, y - y_0) \longleftrightarrow F(u,v) \exp[-j2\pi(u x_0 + v y_0)/N].$$

Multiplying a spatial domain function by the given exponential expression shifts its Fourier domain spectrum. Multiplying a Fourier domain spectrum by the given exponential expression shifts the corresponding spatial domain function.

**APPENDIX 2**

**EQUIPMENT LISTS**

## CONTROL SYSTEM FOR SOLIDIFICATION

See Figure 16

### Computer

Personal Computer - IBM PC-XT

Interface Card - Keithley

### Input/Output Device

Data Acquisition System - Keithley 570

Thermocouple Card - Keithley AIM7

### Operational Amplifier/Power Supply Assembly

2 Operational Amplifiers - Burr Brown OPA 512 SM

2 DC Power Supplies - Condor F15-15.0

### Cuvette Assembly - see Figure 13

Quartz Cuvette with Expansion Tube - Spectrocell - see Figure 11 and Figure 12

Chromel-Alumel (K) Thermocouple Wire - Omega TT-K-36

2 Copper Plates Slotted for Thermocouples - see Figure 15

2 Thermoelectric Devices (TED) - Melcore CP1.4-71-045L

2 Copper Heat Sinks - see Figure 14

4 Aluminum Angles - see Figure 14

## OPTICS SYSTEM FOR INTERFEROMETRY

See Figure 17

### Laser

Helium-Neon Laser - Aerotech LL25P

2 Adjustable Radius Chucks - Newport AC-3

2 Support Posts - Newport VPH-2

2 Sliding Bases - Newport B-2A

2 Adjustable Mounting Bases - Newport AMB-2

### Collimator

Collimating Lens - Spectra-Physics 336

Adjustable Radius Chuck - Newport AC-3

Support Post - Newport VPH-2

Sliding Base - Newport B-2A

Adjustable Mounting Base - Newport AMB-2

### Mirror M1

Mirror, 75 mm diameter - Melles Griot 02 MFG 021

Support Post - Newport VPH-3

Sliding Base - Newport B-2A

Adjustable Mounting Base - Newport AMB-2

### Beam Splitter B1

Beam Splitter - Ealing 24-5043

Filter Holder - Oriel 12650

Support Post - Newport VPH-3

Sliding Base - Newport B-2A

Adjustable Mounting Base - Newport AMB-2

### Mirror M2

Mirror, 100 mm diameter - Melles Griot 02 MFG 023

Rod Mounted Kinematic Mirror Mount - Newport 625

Objective Mount - Newport MM-2A

2 Translation Stages - Newport TSX-1A

### Mirror M3

Mirror, 100 mm diameter - Melles Griot 02 MFG 023

Rod Mounted Kinematic Mirror Mount - Newport 625

### Cuvette Assembly

Laboratory Jack - Newport 270

Low Profile Translation Stage - Newport 440

### Beam Splitter B2

Same as Beam Splitter B1



### Lens

Lens, 120 mm focal length, 50 mm diameter - Ealing 42-1727

Adjustable Radius Chuck - Newport AC-2

Support Post - Newport VPH-3

Sliding Base - Newport B-2A

Adjustable Mounting Base - Newport AMB-2

### Filter

Neutral Density Filter Set - Newport FS-3

Filter Holder - Newport FH-1

Support Post - Newport VPH-2

Base Clamp - Newport BC-1

### Camera

CCTV Camera - Hitachi

Optical Rail - Newport URL-36

Mounting Platform - Newport 38

2 Tie Down Clamps - Newport CL-4

## OPTICS SYSTEM FOR HOLOGRAPHIC INTERFEROMETRY

See Figure 20

### Laser

Helium-Neon Laser - Spectra-Physics 127-35

2 Aluminum Mounting Brackets, 200 mm height - custom

### Mirror M1

Mirror, 50 mm diameter - Melles Griot 02 MFG 019

Rod Mounted Kinematic Mirror Mount - Newport 625A-2

Magnetic Base - Newport 150

### Mirror M2

Same as Mirror M1

### Collimator

Spatial Filter - Melles Griot 09 LSF 011

Laser Collimator, 50 mm - Melles Griot 09 LCM 013

Collet-Type Post Holder - Melles Griot 07 PCL 001

Translation Stage - Newport TSX-1A

Laboratory Jack - Newport 280

### Beam Splitter B1

Cube Beam Splitter, 50.8 mm - Melles Griot 03 BSD 018

Beam Splitter Table - Melles Griot 07 TTA 003

2 Laboratory Jacks - Newport 270

### Filter F1

Neutral Density Filter Set - Newport FS-3

Filter Holder - Newport FH-1

Base Clamp - Newport BC-1

Support Post - Newport VPH-6

Sliding Base - Newport B-2A

### Mirror M3

Mirror, 75 mm diameter - Melles Griot 02 MFG 021

Rod Mounted Kinematic Mirror Mount - Newport 625A-4

Magnetic Base - Newport 150

### Mirror M4

Mirror, 50 mm diameter - Melles Griot 02 MFG 019

Rod Mounted Kinematic Mirror Mount - Newport 625

Low Profile Translation Stage - Newport 430

### Hologram Assembly

Optical Window etched for vacuum line, dimensions 80 mm x 120 mm x 20 mm

- see Figure 22

Blank Threaded Plug, 9 in. diameter - Ealing 23-1696 - Custom cut out and tap

pattern - see Figure 21

8 Aluminum Clamps - see Figure 21

Angle Bracket, 9 in. diameter - Ealing 23-1720

Tilt Table - Aerotech ATT185-5

Manual Rotary Stage - Aerotech MR150

Motor with vacuum lines - Gast 0521-V19

### Beam Splitter B2

Same as Beam Splitter B1

### Optical Rail

2 Optical Rails - Newport URL-36

2 Tie Down Clamps - Newport CL-4 with Ex-2.5

2 Sliding Bases - Newport B-2A

### Lens L1

Bi-convex Lens, 500 mm focal length, 63 mm diameter - Ealing 42-2121

Lens Holder - Melles Griot 07 LHF 025

Support Post - Newport VPH-6

Sliding Base - Newport B-2

Lens L2

Same as Lens L1

Filter F2

Neutral Density Filter Set - Newport FS-3

Filter Holder - Newport FH-1

Base Clamp - Newport BC-1

Support Post - Newport VPH-2

Sliding Base - Newport B-2A

Camera

Camera - Burle TC651E

Support Post - Newport VPH-3

Adjustable Mounting Base - Newport AMB-2

Laboratory Jack - Newport 270

2 Low Profile Translation Stages - Newport 440

**APPENDIX 3**

**PROGRAM GET\_COL**

## PROGRAM GET\_COL

User inputs: Column of interest, "COLUMN"

File inputs: Digitized image containing all columns, "INPUT.IMG"

File outputs: Selected column of image, "FORMAT.DAT"

```

cccccccccccccccccccccccccccccccccccccccccccccccccccccccccccc
c
c Mary E. Magnani
c 26 June 1991
c
cccccccccccccccccccccccccccccccccccccccccccccccccccccccccccc
c
c File list:
c
c FORMAT.DAT   Output, formatted image file
c INPUT.IMG   Input, binary image file from IRIS
c
cccccccccccccccccccccccccccccccccccccccccccccccccccccccccccc
c
c This program reads a binary data file that was saved
c in the image processing package IRIS, and saves a
c given column.
c
cccccccccccccccccccccccccccccccccccccccccccccccccccccccccccc
c
c Variable list:
c
c COLUMN      Column to save
c IMAGE(J,K)  Input data, entire image
c MAX_X       Number of columns
c MAX_Y       Number of rows
c OUT(K)      Output data, one column
c
cccccccccccccccccccccccccccccccccccccccccccccccccccccccccccc

```

```

PROGRAM GET_COL

```

```

c   Declare variables.

c   Pixels are stored in 8 bits.
INTEGER*1 IMAGE
INTEGER COLUMN,MAX_X,MAX_Y,OUT

c   Define parameters.

PARAMETER (MAX_X=512,MAX_Y=512)

c   Dimension arrays.

DIMENSION IMAGE(MAX_X,MAX_Y)
DIMENSION OUT(MAX_Y)

c   Open input and output files.

OPEN (3,FILE='INPUT.IMG',ACCESS='SEQUENTIAL',
+     FORM='BINARY')
REWIND 3
OPEN (4,FILE='FORMAT.DAT',STATUS='NEW')

c   Read pixels from data file. The first row contains
c   header information.

PRINT*
PRINT*,'Reading file named INPUT.IMG ...'
READ (3) (IMAGE(J,1),J=1,512)
DO 10 K=1,512

```



```

    READ (3) (IMAGE(J,K),J=1,512)
10  CONTINUE
    CLOSE (3)

c   Write pixels to output file.
    PRINT*
    PRINT*,'Enter column of interest:'
    READ*,COLUMN
    DO 15 K=1,512
      OUT(K)=IMAGE(COLUMN,K)
15  CONTINUE
    DO 17 K=1,512
      IF (OUT(K).LT.0) OUT(K)=256+OUT(K)
17  CONTINUE
    WRITE (4,22) (OUT(K),K=1,512)
    CLOSE (4)
    PRINT*
    PRINT*,'Output file is named FORMAT.DAT.'
    PRINT*

c   Format statements.

22  FORMAT (8I6)

    STOP
    END

```

**APPENDIX 4**

**PROGRAM CARRIER1**

## PROGRAM CARRIER1

User inputs: None

File inputs: Selected column of image, "FORMAT.DAT"

File outputs: Plot of intensity of image column, "INTENSIT.PLT"

FFT of image column, "FOURIER.DAT"

Plot of FFT of image column, "FOURIER.PLT"

```

cccccccccccccccccccccccccccccccccccccccccccccccccccccccccccc
c
c Mary E. Magnani
c 26 June 1991
c
cccccccccccccccccccccccccccccccccccccccccccccccccccccccccccc
c
c File list:
c
c FORMAT.DAT      Input: formatted image file
c FOURIER.DAT     Output: Fourier transform data
c FOURIER.PLT     Output: plot of Fourier transform
c                 magnitude
c INTENSIT.PLT    Output: plot of image intensity
c
cccccccccccccccccccccccccccccccccccccccccccccccccccccccccccc
c
c This program, CARRIER1, is the first part of a two-
c part programming package to determine the carrier
c frequency. This first part produces a plot from
c which the user can determine cutoff frequencies.
c
cccccccccccccccccccccccccccccccccccccccccccccccccccccccccccc
c
c Variable list:
c
c C_IMAGE(K)      An image column in complex form
c IMAGE(K)        An image column in integer form
c MAX_MAG         Maximum magnitude
c MAX_Y           Number of rows
c MIN_MAG         Minimum magnitude
c POWER_2         Power to which two is raised
c R_IMAGE(K)      An image column in real form
c
cccccccccccccccccccccccccccccccccccccccccccccccccccccccccccc

```

PROGRAM CARRIER1

```

c   Declare variables.

COMPLEX C_IMAGE
INTEGER IMAGE,MAX_Y,POWER_2
REAL MIN_MAG,MAX_MAG,R_IMAGE

c   Define parameters.

PARAMETER (MAX_Y=512)
PARAMETER (POWER_2=9)

c   Dimension arrays.

DIMENSION C_IMAGE(MAX_Y)
DIMENSION IMAGE(MAX_Y)
DIMENSION R_IMAGE(MAX_Y)

c   Read image column data from file.

PRINT*
PRINT*,'Reading the image file named'
PRINT*,'FORMAT.DAT ...'

```

```

CALL READ_COL(IMAGE,MAX_Y)
c Translate column from integer to real format.
CALL INT2REAL(IMAGE,R_IMAGE,MAX_Y)
c Prepare plot file of pixel intensities.
CALL PLOT(R_IMAGE,MAX_Y,10)
PRINT*
PRINT*, 'Plot of pixel intensities is named'
PRINT*, 'INTENSIT.PLT.'
c Translate column from integer to complex format.
CALL INT2COMPL(IMAGE,C_IMAGE,MAX_Y)
c Take 1-D Fourier transform.
CALL FFT_1D(C_IMAGE,POWER_2)
c Prepare output file of FFT results.
CALL WRITE_COL (C_IMAGE,MAX_Y)
PRINT*
PRINT*, 'Fourier transform data are stored'
PRINT*, 'in file FOURIER.DAT.'
c Determine magnitude of column data.
CALL MAG(C_IMAGE,R_IMAGE,MAX_Y,MIN_MAG,MAX_MAG)
c Prepare plot file.
CALL PLOT(R_IMAGE,MAX_Y,15)
PRINT*
PRINT*, 'Plot of Fourier transform is named'
PRINT*, 'FOURIER.PLT.'
PRINT*

STOP
END

```

```

cccccccccccccccccccccccccccccccccccccccccccccccccccccccccccc

```

```

c
c This subroutine reads an image column from a file
c named FORMAT.DAT to the array IMAGE.

```

```

cccccccccccccccccccccccccccccccccccccccccccccccccccccccccccc

```

```

c
c Variable list:

```

```

c
c IMAGE(K)           An image column in integer form
c MAX_Y             Maximum value of NY
c NY                Number of rows

```

```

cccccccccccccccccccccccccccccccccccccccccccccccccccccccccccc

```

```

SUBROUTINE READ_COL(IMAGE,NY)

```

```

c Declare variables.

```

```

    INTEGER IMAGE,MAX_Y,NY

c   Define parameters.

    PARAMETER (MAX_Y=512)

c   Dimension arrays.

    DIMENSION IMAGE(MAX_Y)

c   Open input file.

    OPEN (3,FILE='FORMAT.DAT',STATUS='OLD')

c   Read pixels into array IMAGE.

    READ (3,190) (IMAGE(K),K=1,NY)
    CLOSE(3)

c   Format statements.

190  FORMAT (8I6)

    RETURN
    END

cccccccccccccccccccccccccccccccccccccccccccccccccccccccccccc
c
c This subroutine translates an image column from
c integer to real format.
c
cccccccccccccccccccccccccccccccccccccccccccccccccccccccccccc
c
c Variable list:
c
c IMAGE(K)           An image column in integer form
c MAX_Y             Maximum value of NY
c NY                Number of rows
c R_IMAGE(K)        An image column in real form
c
cccccccccccccccccccccccccccccccccccccccccccccccccccccccccccc

    SUBROUTINE INT2REAL(IMAGE,R_IMAGE,NY)

c   Declare variables.

    INTEGER IMAGE,MAX_Y,NY
    REAL R_IMAGE

c   Define parameters.

    PARAMETER (MAX_Y=512)

c   Dimension arrays.

    DIMENSION IMAGE(MAX_Y)
    DIMENSION R_IMAGE(MAX_Y)

c   Set up real form of IMAGE.

    DO 520 K=1,NY

```

```
      R_IMAGE(K)=IMAGE(K)
520  CONTINUE
```

```
      RETURN
      END
```

```
cccccccccccccccccccccccccccccccccccccccccccccccccccccccccccc
```

```
c
c This subroutine prepares a plot file.
```

```
cccccccccccccccccccccccccccccccccccccccccccccccccccccccccccc
```

```
c
c Variable list:
```

```
c
c FILE_NUM      A file number
c INDEX(K)      X-axis for graphs
c MAX_Y         Maximum value of NY
c NY            Number of rows
c R_IMAGE(K)    An image column in real form
```

```
cccccccccccccccccccccccccccccccccccccccccccccccccccccccccccc
```

```
      SUBROUTINE PLOT(R_IMAGE,NY,FILE_NUM)
```

```
c   Declare variables.
```

```
      INTEGER FILE_NUM,MAX_Y,NY
      REAL INDEX,R_IMAGE
```

```
c   Define parameters.
```

```
      PARAMETER (MAX_Y=512)
```

```
c   Dimension arrays.
```

```
      DIMENSION INDEX(MAX_Y)
      DIMENSION R_IMAGE(MAX_Y)
```

```
c   Open output file.
```

```
      IF (FILE_NUM.EQ.10) THEN
        OPEN (FILE_NUM,FILE='INTENSIT.PLT',STATUS='NEW')
      ELSEIF (FILE_NUM.EQ.15) THEN
        OPEN (FILE_NUM,FILE='FOURIER.PLT',STATUS='NEW')
      ENDIF
```

```
c   Prepare x-axis for graph.
```

```
      DO 620 K=1,MAX_Y
        INDEX(K)=K
620  CONTINUE
```

```
c   Write pixels to file.
```

```
      WRITE (FILE_NUM,690) NY
      DO 630 K=1,MAX_Y
        WRITE(FILE_NUM,691) INDEX(K),R_IMAGE(K)
630  CONTINUE
      CLOSE(FILE_NUM)
```

```
c   Format statements.
```

```
690 FORMAT (I4)
691 FORMAT (F6.1,E15.8)
```

```
RETURN
END
```

```
cccccccccccccccccccccccccccccccccccccccccccccccccccccccccccc
c
c This subroutine translates an image column from
c integer to complex format.
c
cccccccccccccccccccccccccccccccccccccccccccccccccccccccccccc
c
c Variable list:
c
c C_IMAGE(K)      An image column in complex form
c IMAGE(K)        An image column in integer form
c MAX_Y           Maximum value of NY
c NY              Number of rows
c
cccccccccccccccccccccccccccccccccccccccccccccccccccccccccccc
```

```
SUBROUTINE INT2COMPL(IMAGE,C_IMAGE,NY)
```

```
c Declare variables.
```

```
COMPLEX C_IMAGE
INTEGER IMAGE,MAX_Y,NY
```

```
c Define parameters.
```

```
PARAMETER (MAX_Y=512)
```

```
c Dimension arrays.
```

```
DIMENSION C_IMAGE(MAX_Y)
DIMENSION IMAGE(MAX_Y)
```

```
c Set up complex form of IMAGE.
```

```
DO 570 K=1,NY
  C_IMAGE(K)=CMPLX(FLOAT(IMAGE(K)),0.0)
570 CONTINUE
```

```
RETURN
END
```

```
cccccccccccccccccccccccccccccccccccccccccccccccccccccccccccc
c
c This subroutine computes a 1-D FFT by successive
c doubling. C_IMAGE must be complex.
c
c Adapted from R.C. Gonzales and P. Wintz, Digital
c Image Processing, Addison-Wesley, Reading,
c Massachusetts, 1987, p.108.
c
cccccccccccccccccccccccccccccccccccccccccccccccccccccccccccc
c
c Variable list:
c
```



c C\_IMAGE(K)      An image column in complex form  
 c EXPON            Exponential expression in FFT  
 c HALF\_N\_LEV      Half of N\_LEVEL  
 c MAX\_Y            Number of rows  
 c N                Number of elements in 1-D FFT  
 c N\_LEVEL         N at a certain level in 1-D FFT  
 c PI                The constant pi  
 c POWER\_2         Power to which two is raised  
 c TEMPn            Temporary variables  
 c U                Frequency coordinate

c  
 ccc

SUBROUTINE FFT\_1D(C\_IMAGE,POWER\_2)

c    Declare variables.

COMPLEX C\_IMAGE,EXPON,TEMP,U  
 INTEGER HALF\_N\_LEV,MAX\_Y,N,N\_LEVEL,POWER\_2  
 REAL PI

c    Define parameters.

PARAMETER (MAX\_Y=512)  
 PARAMETER (PI=3.141592654)

c    Dimension arrays.

DIMENSION C\_IMAGE(MAX\_Y)

c    Determine N, the number of pixels.

N=2\*\*POWER\_2

c    Reorder the input data.

J=1  
 DO 330 I=1,N-1  
   IF (I.LT.J) THEN  
 c      Switch pixels I and J.  
     TEMP=C\_IMAGE(J)  
     C\_IMAGE(J)=C\_IMAGE(I)  
     C\_IMAGE(I)=TEMP  
   ENDIF  
   K=N/2  
 320   CONTINUE  
   IF (K.LT.J) THEN  
     J=J-K  
     K=K/2  
     GO TO 320  
   ENDIF  
   J=J+K  
 330   CONTINUE

c    Perform successive doubling calculations.

c    For each level.

DO 350 L=1,POWER\_2  
   N\_LEVEL=2\*\*L  
   HALF\_N\_LEV=N\_LEVEL/2  
   U=(1.0,0.0)

```

      EXPON=CMPLX(COS(PI/HALF_N_LEV),
+      -SIN(PI/HALF_N_LEV))
      DO 345 J=1,HALF_N_LEV
      DO 340 I=J,N,N_LEVEL
      I2=I+HALF_N_LEV
      TEMP=C_IMAGE(I2)*U
      C_IMAGE(I2)=C_IMAGE(I)-TEMP
      C_IMAGE(I)=C_IMAGE(I)+TEMP
340      CONTINUE
      U=U*EXPON
345      CONTINUE
350      CONTINUE

c      Normalize result.
      DO 360 I=1,N
      C_IMAGE(I)=C_IMAGE(I)/FLOAT(N)
360      CONTINUE

      RETURN
      END

```

```

cccccccccccccccccccccccccccccccccccccccccccccccccccccccccccc
c
c This subroutine writes an image column from an array
c C_IMAGE to a file named FOURIER.DAT.
c
cccccccccccccccccccccccccccccccccccccccccccccccccccccccccccc
c
c Variable list:
c
c C_IMAGE(K) An image column in complex form
c MAX_Y      Maximum value of NY
c NY         Number of rows
c
cccccccccccccccccccccccccccccccccccccccccccccccccccccccccccc

```

```

      SUBROUTINE WRITE_COL(C_IMAGE,NY)

```

```

c      Declare variables.

      COMPLEX C_IMAGE
      INTEGER MAX_Y,NY

c      Define parameters.

      PARAMETER (MAX_Y=512)

c      Dimension arrays.

      DIMENSION C_IMAGE(MAX_Y)

c      Open output file.

      OPEN (4,FILE='FOURIER.DAT',STATUS='NEW')

c      Write pixels to file.

      WRITE (4,291) (C_IMAGE(K),K=1,NY)
      CLOSE(4)

c      Format statements.

```

291 FORMAT (1X,E15.8,E15.8)

RETURN  
END

cc

c  
c This subroutine finds the magnitude of an image  
c column.

cc

c  
c Variable list:  
c  
c C\_IMAGE(K) An image column in complex form  
c MAX\_MAG Maximum magnitude  
c MAX\_Y Maximum value of NY  
c MIN\_MAG Minimum magnitude  
c NY Number of rows  
c R\_IMAGE(K) An image column in real form  
c

cc

SUBROUTINE MAG(C\_IMAGE,R\_IMAGE,NY,MIN\_MAG,MAX\_MAG)

c Declare variables.

COMPLEX C\_IMAGE  
INTEGER MAX\_Y,NY  
REAL MIN\_MAG,MAX\_MAG,R\_IMAGE

c Define parameters.

PARAMETER (MAX\_Y=512)

c Dimension arrays.

DIMENSION C\_IMAGE(MAX\_Y)  
DIMENSION R\_IMAGE(MAX\_Y)

c Keep track of maximum and minimum magnitudes.

MAX\_MAG=0.0  
MIN\_MAG=1.0E10

DO 910 K=1,NY  
R\_IMAGE(K)=ABS(C\_IMAGE(K))  
IF (R\_IMAGE(K).GT.MAX\_MAG) MAX\_MAG=R\_IMAGE(K)  
IF (R\_IMAGE(K).LT.MIN\_MAG) MIN\_MAG=R\_IMAGE(K)

910 CONTINUE

RETURN  
END

**APPENDIX 5**

**PROGRAM CARRIER2**

## PROGRAM CARRIER2

User inputs: Lower cutoff frequency, "L\_CUT\_OFF"

Upper cutoff frequency, "U\_CUT\_OFF"

File inputs: FFT of image column, "FOURIER.DAT"

File outputs: Plot of ideal lowpass filter, "ILPF.PLT"

Plot of inverse FFT of ideal lowpass filter, "INV\_ILPF. PLT"

Plot of Hanning window, "HANNING.PLT"

Plot of inverse FFT of filter modified by Hanning window,  
"INV\_FIL.PLT"

Plot of filter modified by Hanning window, "FILTER.PLT"

Plot of filtered image column, "FIL\_DATA.PLT"

Plot of phase of carrier image column, "PHAS\_2PI.PLT"

Plot of continuous phase of carrier image column, "C\_PHASE.PLT"

Continuous phase of carrier image column, "CARRIER.DAT"

cc

c  
c Mary E. Magnani  
c 26 June 1991

c  
cc

c  
c File list:

c  
c CARRIER.DAT     Output: Carrier phase data (spatial)  
c C\_PHASE.PLT     Output: Plot of continuous phase  
c                   (spatial)  
c FIL\_DATA.PLT     Output: Plot of filtered FFT data  
c                   (Fourier)  
c FILTER.PLT       Output: Plot of filter modified by  
c                   Hanning window (Fourier)  
c FOURIER.DAT     Input: Fourier transform data  
c                   (Fourier)  
c ILPF.PLT         Output: Plot of ideal lowpass  
c                   filter (Fourier)  
c INV\_ILPF.PLT     Output: Plot of ideal lowpass  
c                   filter (spatial)  
c INV\_FIL.PLT     Output: Plot of filter modified by  
c                   Hanning window (spatial)  
c HANNING.PLT     Output: Plot of Hanning window  
c                   (spatial)  
c PHAS\_2PI.PLT     Output: Plot of carrier phase, modulo  
c                   2\*pi (spatial)

c  
cc

c  
c This program, CARRIER2, is the second part of a two-  
c part programming package that determines the carrier  
c frequency. This second program filters a column of  
c Fourier transform data to obtain phase. A least  
c squares fit is then applied to obtain the carrier  
c frequency. Before executing this program, the user  
c executes program CARRIER1 to determine filter cutoff  
c frequencies. The phase of the carrier image,  
c CARRIER.DAT, is an input to the program AUTO2.

c  
cc

c  
c Variable list:

c  
c A                y = A+Bx given by least-squares fit  
c B                y = A+Bx given by least-squares fit  
c CARRIER        Carrier frequency  
c C\_IMAGE(K)     An image column in complex form  
c C\_PHASE(K)     Continuous phase  
c DATA(K)        Data for least-squares fit  
c DUMMY           Dummy variable  
c FILTER(K)       An ideal lowpass filter  
c FILT\_IM(K)     A filtered image  
c FIL\_WIN(K)     Filter modified by a window  
c FIT\_PTS         Number of points in least-squares fit  
c HALF\_PASS      Half of the extent of passband  
c INDEX           Index for least-squares fit  
c L\_CUT\_OFF      Lower cutoff frequency for filter  
c MAX\_MAG         Maximum magnitude  
c MAX\_Y           Number of rows

c MIDPT Midpoint of passband  
 c MIN\_MAG Minimum magnitude  
 c PHASE(K) Phase  
 c PI The constant pi  
 c PIX\_LOC Pixel location at end of filter's  
 c second side lobe  
 c POWER\_2 Power to which two is raised  
 c R\_IMAGE(K) An image column in real form  
 c SHFT\_FIL(K) Shifted version of FIL\_WIN(K)  
 c TEMP Temporary variable  
 c U\_CUT\_OFF Upper cutoff frequency for filter  
 c WIDTH Width of window  
 c WINDOW(K) Hanning window

c  
 ccc

PROGRAM CARRIER2

c Declare variables.

```

COMPLEX C_IMAGE,FILTER,FILT_IM,FIL_WIN
COMPLEX SHFT_FIL,WINDOW
INTEGER FIT_PTS,HALF_PASS,L_CUT_OFF,MAX_Y
INTEGER MIDPT,PIX_LOC,POWER_2,TEMP
INTEGER U_CUT_OFF,WIDTH
REAL A,B,CARRIER,C_PHASE,DATA,DUMMY
REAL INDEX,MAX_MAG,MIN_MAG
REAL PHASE,R_IMAGE
  
```

c Define parameters.

```

PARAMETER (FIT_PTS=479)
PARAMETER (MAX_Y=512)
PARAMETER (PI=3.141592654)
PARAMETER (POWER_2=9)
  
```

c Dimension arrays.

```

DIMENSION C_IMAGE(MAX_Y)
DIMENSION C_PHASE(MAX_Y)
DIMENSION DATA(MAX_Y)
DIMENSION FILTER(MAX_Y)
DIMENSION FILT_IM(MAX_Y)
DIMENSION FIL_WIN(MAX_Y)
DIMENSION INDEX(FIT_PTS)
DIMENSION PHASE(MAX_Y)
DIMENSION R_IMAGE(MAX_Y)
DIMENSION SHFT_FIL(MAX_Y)
DIMENSION WINDOW(MAX_Y)
  
```

c Read input data.

```
CALL READ_COL(C_IMAGE,MAX_Y)
```

c Apply ideal lowpass filter with window.

c Obtain cutoff frequencies and prepare ideal  
 c lowpass filter with user-specified cutoffs.  
 c The user enters frequencies determined by  
 c executing program CARRIER1.

35 CONTINUE

```

PRINT*
PRINT*, 'Enter the lower cutoff frequency:'
READ*, L_CUT_OFF
PRINT*, 'Enter the upper cutoff frequency:'
READ*, U_CUT_OFF

c   If the cutoff frequencies were switched,
c   correct the situation.

IF (L_CUT_OFF.GT.U_CUT_OFF) THEN
  TEMP=L_CUT_OFF
  L_CUT_OFF=U_CUT_OFF
  U_CUT_OFF=TEMP
ENDIF

c   Find the midpoint of the passband, and
c   half its extent.

MIDPT=(U_CUT_OFF+L_CUT_OFF)/2
HALF_PASS=U_CUT_OFF-MIDPT

c   Prepare an ideal lowpass filter, located
c   at the origin.
CALL ILPF(FILTER,HALF_PASS,MAX_Y)
c   Prepare plot file, taking image magnitude first.
CALL MAG(FILTER,R_IMAGE,MAX_Y,MIN_MAG,MAX_MAG)
CALL PLOT(R_IMAGE,MAX_Y,11)
PRINT*
PRINT*, 'Plot of the ideal lowpass filter'
PRINT*, 'is named ILPF.PLT.'

c   Modify ideal lowpass filter with a window.
c   Take inverse Fourier transform of ideal
c   lowpass filter.

CALL INV_FFT_1D(FILTER,POWER_2)
c   Prepare plot file, taking image magnitude
c   first.
CALL MAG(FILTER,R_IMAGE,MAX_Y,MIN_MAG,MAX_MAG)
CALL PLOT(R_IMAGE,MAX_Y,13)
PRINT*
PRINT*, 'Plot of the inverse Fourier'
PRINT*, 'transform of the ideal lowpass'
PRINT*, 'filter is named INV_ILPF.PLT.'

c   Find the pixel location where the second
c   side lobe of the inverse Fourier transform
c   of the ideal lowpass filter ends.
CALL SECOND(FILTER,PIX_LOC,MAX_Y)

c   Determine window size.
WIDTH=2*PIX_LOC+1
PRINT*
PRINT 40, WIDTH
40  FORMAT (1X, 'The window size is ', I3, '.')

c   Prepare window.
CALL HANNING(WINDOW,WIDTH,MAX_Y)
c   Prepare plot file, taking image magnitude
c   first.
CALL MAG(WINDOW,R_IMAGE,MAX_Y,MIN_MAG,MAX_MAG)

```



```

CALL PLOT(R_IMAGE,MAX_Y,14)
PRINT*
PRINT*,'Plot of the Hanning window is'
PRINT*,'named HANNING.PLT.'

c   Multiply ideal lowpass filter and window to
c   form new filter.
CALL MULT(FIL_WIN,FILTER,WINDOW,MAX_Y)
c   Prepare plot file, taking image magnitude
c   first.
CALL MAG(FIL_WIN,R_IMAGE,MAX_Y,MIN_MAG,
+      MAX_MAG)
CALL PLOT(R_IMAGE,MAX_Y,15)
PRINT*
PRINT*,'Plot of the inverse Fourier'
PRINT*,'transform of the filter modified by'
PRINT*,'the Hanning window is named'
PRINT*,'INV_FIL.PLT.'

c   Take the Fourier transform to get final
c   filter.
CALL FFT_1D(FIL_WIN,POWER_2)
c   Prepare plot file, taking image magnitude
c   first.
CALL MAG(FIL_WIN,R_IMAGE,MAX_Y,MIN_MAG,
+      MAX_MAG)
CALL PLOT(R_IMAGE,MAX_Y,16)
PRINT*
PRINT*,'Plot of the filter modified by the'
PRINT*,'Hanning window is named FILTER.PLT.'

c   The final filter is located at the origin.
c   So shift it up to MIDPT, the midpoint of
c   the actual passband.

CALL FREQ_SHIFT(FIL_WIN,SHFT_FIL,MAX_Y,MIDPT)

c   To filter the image, multiply the image
c   and the filter.
CALL MULT(FILT_IM,C_IMAGE,SHFT_FIL,MAX_Y)
c   Prepare plot file, taking image magnitude first.
CALL MAG(FILT_IM,R_IMAGE,MAX_Y,MIN_MAG,MAX_MAG)
CALL PLOT(R_IMAGE,MAX_Y,12)
PRINT*
PRINT*,'Plot of the filtered data is named'
PRINT*,'FIL_DATA.PLT.'

c   Take the inverse 1-D Fourier transform.
CALL INV_FFT_1D(FILT_IM,POWER_2)

c   Determine phase.
DO 45 K=1,MAX_Y
  PHASE(K)=AIMAG(CLOG(FILT_IM(K)))
c   Another option.
c   PHASE(K)=ATAN2(AIMAG(FILT_IM(K)),
+     REAL(FILT_IM(K)))
45 CONTINUE
c   Prepare plot file.
CALL PLOT(PHASE,MAX_Y,18)
PRINT*
PRINT*,'Plot of the phase is named PHAS_2PI.PLT.'

```

```

c   Apply phase continuation.
CALL PHASE_CONT(C_PHASE,PHASE,MAX_Y)
c   Prepare plot file.
CALL PLOT(C_PHASE,MAX_Y,19)
PRINT*
PRINT*,'Plot of the continuous phase is '
PRINT*,'named C_PHASE.PLT.'

c   Prepare output file.
CALL WRITE_COL(C_PHASE,MAX_Y)
PRINT*
PRINT*,'Phase data are stored in file'
PRINT*,'CARRIER.DAT.'

c   The continuous phase is of the form
c    $2*PI*CARRIER*K$ . Do a least squares fit
c   to get CARRIER.

c   Prepare data points for least-squares fit.
c   Exclude first data point, as the image
c   processor gives a faulty value for its
c   intensity. Exclude data points greater than
c   FIT_PTS+1, as the image processor does not
c   extend to this region.
DO 60 K=1,FIT_PTS
  DATA(K)=C_PHASE(K+1)
60  CONTINUE

c   Prepare index for least-squares fit.
DO 65 K=1,FIT_PTS
  INDEX(K)=K
65  CONTINUE

c   Calculate least-squares fit.
CALL FIT(INDEX,DATA,FIT_PTS,DUMMY,0,A,B)
CARRIER=B*MAX_Y/(2*PI)
PRINT*
PRINT*,'The carrier frequency is',CARRIER
PRINT*

STOP
END

```

```

cccccccccccccccccccccccccccccccccccccccccccccccccccccccccccc
c
c This subroutine reads an image column from a file to
c the array C_IMAGE.
c
cccccccccccccccccccccccccccccccccccccccccccccccccccccccccccc
c
c Variable list:
c
c C_IMAGE(K)      An image column in complex form
c MAX_Y          Maximum value of NY
c NY             Number of rows
c
cccccccccccccccccccccccccccccccccccccccccccccccccccccccccccc

```

```

SUBROUTINE READ_COL(C_IMAGE,NY)

```

```

c   Declare variables.

      COMPLEX C_IMAGE
      INTEGER MAX_Y,NY

c   Define parameters.

      PARAMETER (MAX_Y=512)

c   Dimension arrays.

      DIMENSION C_IMAGE(MAX_Y)

c   Open input file.

      OPEN (3,FILE='FOURIER.DAT',STATUS='OLD')

c   Read pixels into array C_IMAGE.

      READ (3,190) (C_IMAGE(K),K=1,NY)
      CLOSE(3)

c   Format statements.

190  FORMAT (1X,E15.8,E15.8)

      RETURN
      END

```

```

cccccccccccccccccccccccccccccccccccccccccccccccccccccccccccc

```

```

      SUBROUTINE MAG(C_IMAGE,R_IMAGE,NY,MIN_MAG,MAX_MAG)

```

See Appendix 4.

```

cccccccccccccccccccccccccccccccccccccccccccccccccccccccccccc

```

```

cccccccccccccccccccccccccccccccccccccccccccccccccccccccccccc

```

```

c
c   This subroutine prepares a plot file.
c
cccccccccccccccccccccccccccccccccccccccccccccccccccccccccccc

```

```

c   Variable list:
c
c   FILE_NUM      A file number
c   INDEX(K)      X-axis for graphs
c   MAX_Y         Maximum value of NY
c   NY            Number of rows
c   R_IMAGE(K)    An image column in real form
c
cccccccccccccccccccccccccccccccccccccccccccccccccccccccccccc

```

```

      SUBROUTINE PLOT(R_IMAGE,NY,FILE_NUM)

```

```

c   Declare variables.

      INTEGER FILE_NUM,MAX_Y,NY
      REAL INDEX,R_IMAGE

c   Define parameters.

```

PARAMETER (MAX\_Y=512)

c Dimension arrays.

```
DIMENSION INDEX(MAX_Y)
DIMENSION R_IMAGE(MAX_Y)
```

c Open output file.

```
IF (FILE_NUM.EQ.11) THEN
  OPEN (FILE_NUM,FILE='ILPF.PLT',STATUS='NEW')
ELSEIF (FILE_NUM.EQ.12) THEN
  OPEN (FILE_NUM,FILE='FIL_DATA.PLT',STATUS='NEW')
ELSEIF (FILE_NUM.EQ.13) THEN
  OPEN (FILE_NUM,FILE='INV_ILPF.PLT',STATUS='NEW')
ELSEIF (FILE_NUM.EQ.14) THEN
  OPEN (FILE_NUM,FILE='HANNING.PLT',STATUS='NEW')
ELSEIF (FILE_NUM.EQ.15) THEN
  OPEN (FILE_NUM,FILE='INV_FIL.PLT',STATUS='NEW')
ELSEIF (FILE_NUM.EQ.16) THEN
  OPEN (FILE_NUM,FILE='FILTER.PLT',STATUS='NEW')
ELSEIF (FILE_NUM.EQ.18) THEN
  OPEN (FILE_NUM,FILE='PHAS_2PI.PLT',STATUS='NEW')
ELSEIF (FILE_NUM.EQ.19) THEN
  OPEN (FILE_NUM,FILE='C_PHASE.PLT',STATUS='NEW')
ENDIF
```

c Prepare x-axis for graph.

```
DO 620 K=1,MAX_Y
  INDEX(K)=K
```

620 CONTINUE

c Write pixels to file.

```
WRITE (FILE_NUM,690) NY
DO 630 K=1,MAX_Y
  WRITE(FILE_NUM,691) INDEX(K),R_IMAGE(K)
```

630 CONTINUE

```
CLOSE(FILE_NUM)
```

c Format statements.

690 FORMAT (I4)

691 FORMAT (F6.1,E15.8)

```
RETURN
END
```

cc

c

c This subroutine prepares an ideal lowpass filter with  
c user-specified cutoff frequencies. The filter exists  
c in the frequency domain.

c

cc

c

c Variable list:

c

c FILTER(K)           An ideal lowpass filter

```

c HALF_PASS      Half of the extent of passband
c MAX_Y          Maximum value of NY
c NY             Number of rows
c
cccccccccccccccccccccccccccccccccccccccccccccccccccccccccccc

```

```

SUBROUTINE ILPF(FILTER,HALF_PASS,NY)

```

```

c Declare variables.

```

```

COMPLEX FILTER
INTEGER HALF_PASS,MAX_Y,NY

```

```

c Define parameters.

```

```

PARAMETER (MAX_Y=512)

```

```

c Dimension arrays.

```

```

DIMENSION FILTER(MAX_Y)

```

```

c The ideal lowpass filter has a value of one in
c the frequency range specified by HALF_PASS.

```

```

DO 310 K=1,HALF_PASS+1
  FILTER(K)=(1.0,0.0)
310 CONTINUE
DO 320 K=HALF_PASS+2,NY-HALF_PASS
  FILTER(K)=(0.0,0.0)
320 CONTINUE
DO 330 K=NY-HALF_PASS+1,NY
  FILTER(K)=(1.0,0.0)
330 CONTINUE

```

```

RETURN
END

```

```

cccccccccccccccccccccccccccccccccccccccccccccccccccccccccccc
c
c This subroutine multiplies two complex images.
c
cccccccccccccccccccccccccccccccccccccccccccccccccccccccccccc

```

```

c Variable list:

```

```

c IN1(K),IN2(K)  Input images to be multiplied
c NY             Number of rows
c MAX_Y          Maximum value of NY
c OUT(K)         Result of multiplication
c

```

```

cccccccccccccccccccccccccccccccccccccccccccccccccccccccccccc

```

```

SUBROUTINE MULT(OUT,IN1,IN2,NY)

```

```

c Declare variables.

```

```

COMPLEX IN1,IN2,OUT
INTEGER MAX_Y,NY

```

```

c Define parameters.

```

PARAMETER (MAX\_Y=512)

c Dimension arrays.

DIMENSION IN1(MAX\_Y)  
DIMENSION IN2(MAX\_Y)  
DIMENSION OUT(MAX\_Y)

DO 3140 K=1,NY  
OUT(K)=IN1(K)\*IN2(K)  
3140 CONTINUE

RETURN  
END

cc

c  
c This subroutine computes an inverse 1-D FFT by  
c successive doubling. C\_IMAGE must be complex.

c  
c Adapted from R.C. Gonzales and P. Wintz, Digital  
c Image Processing, Addison-Wesley, Reading,  
c Massachusetts, 1987, p. 108.

c  
cc

c  
c Variable list:

c  
c C\_IMAGE(K)      An image column in complex form  
c EXPON            Exponential expression in FFT  
c HALF\_N\_LEV      Half of N\_LEVEL  
c MAX\_Y            Number of rows  
c N                Number of elements in 1-D FFT  
c N\_LEVEL         N at a certain level in 1-D FFT  
c PI               The constant pi  
c POWER\_2         Power to which two is raised  
c TEMPn            Temporary variables  
c U                Frequency coordinate

c  
cc

SUBROUTINE INV\_FFT\_1D(C\_IMAGE,POWER\_2)

c Declare variables.

COMPLEX C\_IMAGE,EXPON,TEMP,U  
INTEGER HALF\_N\_LEV,MAX\_Y,N,N\_LEVEL,POWER\_2  
REAL PI

c Define parameters.

PARAMETER (MAX\_Y=512)  
PARAMETER (PI=3.141592654)

c Dimension arrays.

DIMENSION C\_IMAGE(MAX\_Y)

c Determine N, the number of pixels.

N=2\*\*POWER\_2

c Reorder the input data.

```
J=1
DO 1330 I=1,N-1
  IF (I.LT.J) THEN
c    Switch pixels I and J.
    TEMP=C_IMAGE(J)
    C_IMAGE(J)=C_IMAGE(I)
    C_IMAGE(I)=TEMP
  ENDIF
  K=N/2
1320  CONTINUE
  IF (K.LT.J) THEN
    J=J-K
    K=K/2
    GO TO 1320
  ENDIF
  J=J+K
1330  CONTINUE
```

c Perform successive doubling calculations.

```
c For each level.
DO 1350 L=1,POWER_2
  N_LEVEL=2**L
  HALF_N_LEV=N_LEVEL/2
  U=(1.0,0.0)
  EXPON=CMPLX(COS(PI/HALF_N_LEV),
+    SIN(PI/HALF_N_LEV))
  DO 1345 J=1,HALF_N_LEV
    DO 1340 I=J,N,N_LEVEL
      I2=I+HALF_N_LEV
      TEMP=C_IMAGE(I2)*U
      C_IMAGE(I2)=C_IMAGE(I)-TEMP
      C_IMAGE(I)=C_IMAGE(I)+TEMP
1340    CONTINUE
      U=U*EXPON
1345    CONTINUE
1350  CONTINUE
```

```
RETURN
END
```

cc

c  
c This subroutine finds the pixel location where the  
c second side lobe of the inverse Fourier transform of  
c the ideal lowpass filter ends.

c  
cc

c  
c Variable list:  
c  
c C\_IMAGE(K)        An image column in complex form  
c MAX\_MAG         Maximum magnitude  
c MAX\_Y            Number of rows  
c MIN\_MAG         Minimum magnitude  
c NY               Number of rows  
c PIX\_LOC          Pixel location at end of filter's  
c                   second side lobe

c R\_IMAGE(K)      An image column in real form  
 c TEMP            Temporary variable  
 c  
 ccc

SUBROUTINE SECOND(C\_IMAGE,PIX\_LOC,NY)

c    Declare variables.

COMPLEX C\_IMAGE  
 INTEGER MAX\_Y,NY,PIX\_LOC  
 REAL MAX\_MAG,MIN\_MAG,R\_IMAGE,TEMP

c    Define parameters.

PARAMETER (MAX\_Y=512)

c    Dimension arrays.

DIMENSION C\_IMAGE(MAX\_Y)  
 DIMENSION R\_IMAGE(MAX\_Y)

c    Determine magnitude of column data.

CALL MAG(C\_IMAGE,R\_IMAGE,NY,MIN\_MAG,MAX\_MAG)

c    The end of the second side lobe occurs at  
 c    R\_IMAGE's third minimum.

K=0

c    First minimum.

630 CONTINUE

K=K+1

TEMP=R\_IMAGE(K)-R\_IMAGE(K+1)

IF (TEMP.GT.0) GOTO 630

c    First maximum.

640 CONTINUE

K=K+1

TEMP=R\_IMAGE(K)-R\_IMAGE(K+1)

IF (TEMP.LT.0) GOTO 640

c    Second minimum.

650 CONTINUE

K=K+1

TEMP=R\_IMAGE(K)-R\_IMAGE(K+1)

IF (TEMP.GT.0) GOTO 650

c    Second maximum.

660 CONTINUE

K=K+1

TEMP=R\_IMAGE(K)-R\_IMAGE(K+1)

IF (TEMP.LT.0) GOTO 660

c    Third minimum.

670 CONTINUE

K=K+1

TEMP=R\_IMAGE(K)-R\_IMAGE(K+1)

IF (TEMP.GT.0) GOTO 670

PIX\_LOC=K



```
RETURN
END
```

```
cccccccccccccccccccccccccccccccccccccccccccccccccccccccccccc
c
c This subroutine prepares a Hanning window for a
c user-specified window width. The window exists in the
c spatial domain. It is centered about pixel 1.
c
cccccccccccccccccccccccccccccccccccccccccccccccccccccccccccc
c
c Variable list:
c
c C_IMAGE(K)      An image column in complex form
c MAX_Y           Number of rows
c NY              Number of rows
c PI              The constant pi
c RANGE           The extent of window, measured
c                 from center to edge
c TEMP            Temporary variable
c WIDTH           Width of window
c
cccccccccccccccccccccccccccccccccccccccccccccccccccccccccccc
```

```
      SUBROUTINE HANNING(C_IMAGE,WIDTH,NY)
```

```
c   Declare variables.
```

```
      COMPLEX C_IMAGE
      INTEGER MAX_Y,NY,RANGE,WIDTH
      REAL PI,TEMP
```

```
c   Define parameters.
```

```
      PARAMETER (MAX_Y=512)
      PARAMETER (PI=3.141592654)
```

```
c   Dimension arrays.
```

```
      DIMENSION C_IMAGE(MAX_Y)
```

```
c   Calculate the range of window, as measured
c   from the center.
      RANGE=(WIDTH-1)/2
```

```
c   Form Hanning window, centered about pixel 1.
```

```
      DO 740 K=1,RANGE
          TEMP=PI*FLOAT(K-1)/FLOAT(RANGE+1)
          TEMP=0.5 + 0.5*COS(TEMP)
          C_IMAGE(K)=CMPLX(TEMP,0.0)
740   CONTINUE
      DO 750 K=RANGE+1,NY-RANGE
          C_IMAGE(K)=(0.0,0.0)
750   CONTINUE
      DO 760 K=NY-RANGE+1,NY
          C_IMAGE(K)=C_IMAGE(-K+NY+2)
760   CONTINUE
```

```
      RETURN
      END
```

cc

c  
c This subroutine computes a 1-D FFT by successive  
c doubling. C\_IMAGE must be complex.

c  
c Adapted from R.C. Gonzales and P. Wintz, Digital  
c Image Processing, Addison-Wesley, Reading,  
c Massachusetts, 1987, p. 108.

cc

c  
c Variable list:

c  
c C\_IMAGE(K)      An image column in complex form  
c EXPON            Exponential expression in FFT  
c HALF\_N\_LEV      Half of N\_LEVEL  
c MAX\_Y            Number of rows  
c N                Number of elements in 1-D FFT  
c N\_LEVEL         N at a certain level in 1-D FFT  
c PI               The constant pi  
c POWER\_2         Power to which two is raised  
c TEMPn            Temporary variables  
c U                Frequency coordinate

cc

SUBROUTINE FFT\_1D(C\_IMAGE,POWER\_2)

c    Declare variables.

COMPLEX C\_IMAGE,EXPON,TEMP,U  
INTEGER HALF\_N\_LEV,MAX\_Y,N,N\_LEVEL,POWER\_2  
REAL PI

c    Define parameters.

PARAMETER (MAX\_Y=512)  
PARAMETER (PI=3.141592654)

c    Dimension arrays.

DIMENSION C\_IMAGE(MAX\_Y)

c    Determine N, the number of pixels.

N=2\*\*POWER\_2

c    Reorder the input data.

J=1  
DO 330 I=1,N-1  
  IF (I.LT.J) THEN  
c      Switch pixels I and J.  
    TEMP=C\_IMAGE(J)  
    C\_IMAGE(J)=C\_IMAGE(I)  
    C\_IMAGE(I)=TEMP  
  ENDIF  
  K=N/2  
330 CONTINUE  
  IF (K.LT.J) THEN  
    J=J-K

```

        K=K/2
        GO TO 320
    ENDIF
    J=J+K
330 CONTINUE

c Perform successive doubling calculations.

c For each level.
DO 350 L=1,POWER_2
    N_LEVEL=2**L
    HALF_N_LEV=N_LEVEL/2
    U=(1.0,0.0)
    EXPON=CMPLX(COS(PI/HALF_N_LEV),
+             -SIN(PI/HALF_N_LEV))
    DO 345 J=1,HALF_N_LEV
        DO 340 I=J,N_LEVEL
            I2=I+HALF_N_LEV
            TEMP=C_IMAGE(I2)*U
            C_IMAGE(I2)=C_IMAGE(I)-TEMP
            C_IMAGE(I)=C_IMAGE(I)+TEMP
340 CONTINUE
            U=U*EXPON
345 CONTINUE
350 CONTINUE

c Normalize result.
DO 360 I=1,N
    C_IMAGE(I)=C_IMAGE(I)/FLOAT(N)
360 CONTINUE

RETURN
END

cccccccccccccccccccccccccccccccccccccccccccccccccccccccccccc
c
c This subroutine shifts an image that is centered at
c the origin by a frequency equal to the SHFT_FRE.
c The indices of the input image, C_IMAGE, are simply
c renumbered to produce the output image, SHIFT_IM.
c Example: If SHFT_FRE=20, then the value in C_IMAGE(1)
c will be placed in SHIFT_IM(20), C_IMAGE(2) will be
c placed in SHIFT_IM(21), and C_IMAGE(512) will be
c placed in SHIFT_IM(19).
c
cccccccccccccccccccccccccccccccccccccccccccccccccccccccccccc
c
c Variable list:
c
c C_IMAGE(K)      An image column in complex form
c MAX_Y          Maximum value of NY
c NEW_IND        A new index
c NY             Number of rows
c SHFT_FRE       Distance to shift
c SHIFT_IM(K)    Shifted version of C_IMAGE
c
cccccccccccccccccccccccccccccccccccccccccccccccccccccccccccc

SUBROUTINE FREQ_SHIFT(C_IMAGE,SHIFT_IM,NY,
+                   SHFT_FRE)

```

```

c   Declare variables.

COMPLEX C_IMAGE,SHIFT_IM
INTEGER MAX_Y,NEW_IND,NY,SHFT_FRE

c   Define parameters.

PARAMETER (MAX_Y=512)

c   Dimension arrays.

DIMENSION C_IMAGE(MAX_Y)
DIMENSION SHIFT_IM(MAX_Y)

c   Renumber the indices of C_IMAGE to obtain the
c   shifted image, SHIFT_IM.

DO 200 K=1,NY
  NEW_IND=MOD(K + SHFT_FRE + NY - 1, NY)
  IF (NEW_IND.EQ.0) NEW_IND=NY
  SHIFT_IM(NEW_IND)=C_IMAGE(K)
200 CONTINUE

RETURN
END

```

```

cccccccccccccccccccccccccccccccccccccccccccccccccccccccccccc

```

```

c
c This subroutine calculates the continuous phase
c C_PHASE from PHASE. PHASE varies from -pi to pi.
c
c Adapted from W.W. Macy, "Two-dimensional fringe-
c pattern analysis," Applied Optics, v. 22, n. 23, pp.
c 3898-3901, 1 December 1983.

```

```

cccccccccccccccccccccccccccccccccccccccccccccccccccccccccccc

```

```

c Variable list:
c
c C_PHASE(K)      Continuous phase
c MAX_Y           Maximum value of NY
c NY              Number of rows
c PHASE(K)        Phase
c PI              The constant pi

```

```

cccccccccccccccccccccccccccccccccccccccccccccccccccccccccccc

```

```

SUBROUTINE PHASE_CONT(C_PHASE,PHASE,NY)

```

```

c   Declare variables.

REAL C_PHASE,PHASE,PI
INTEGER MAX_Y,NY

c   Define parameters.

PARAMETER (MAX_Y=512)
PARAMETER (PI=3.141592654)

c   Dimension arrays.

```

```

DIMENSION C_PHASE(MAX_Y)
DIMENSION PHASE(MAX_Y)

c Use recurrence relationship to obtain
c continuous phase.
C_PHASE(1)=PHASE(1)
DO 880 K=2,NY
  C_PHASE(K)=AMOD(PHASE(K)-C_PHASE(K-1)
+                +201*PI,2*PI) + C_PHASE(K-1) - PI
880 CONTINUE

RETURN
END

```

```

cccccccccccccccccccccccccccccccccccccccccccccccccccccccccccc
c
c This subroutine writes an image column from an array
c R_IMAGE to a to a file named CARRIER.DAT.
c
cccccccccccccccccccccccccccccccccccccccccccccccccccccccccccc
c
c Variable list:
c
c R_IMAGE(K)      An image column in real form
c MAX_Y           Maximum value of NY
c NY              Number of rows
c
cccccccccccccccccccccccccccccccccccccccccccccccccccccccccccc

```

SUBROUTINE WRITE\_COL(R\_IMAGE,NY)

```

c Declare variables.

INTEGER MAX_Y,NY
REAL R_IMAGE

c Define parameters.

PARAMETER (MAX_Y=512)

c Dimension arrays.

DIMENSION R_IMAGE(MAX_Y)

c Open output file.

OPEN (4,FILE='CARRIER.DAT',STATUS='NEW')

c Write pixels to file.

WRITE (4,291) (R_IMAGE(K),K=1,NY)
CLOSE(4)

c Format statements.

291 FORMAT (1X,E15.8)

RETURN
END

```

```

cccccccccccccccccccccccccccccccccccccccccccccccccccccccccccc
c
c Given a set of NDATA points X(I), Y(I) with
c standard deviations SIG(I), fit them to a straight
c line  $Y = AX + B$  by minimizing chi-squared. Returned
c are A and B. If MWT=0 on input, then the standard
c deviations are assumed to be unavailable.
c
c Adapted from W.H. Press et al., Numerical Recipes:
c The Art of Scientific Computing, Cambridge University
c Press, Cambridge, 1986, pp. 508-509.
c
cccccccccccccccccccccccccccccccccccccccccccccccccccccccccccc

```

```

SUBROUTINE FIT(X,Y,NDATA,SIG,MWT,A,B)

DIMENSION X(NDATA),Y(NDATA),SIG(NDATA)
c Initialize sums to zero.
SX=0.
SY=0.
ST2=0.
B=0.
IF(MWT.NE.0) THEN
c Accumulate sums ...
SS=0.
DO 11 I=1,NDATA
c ... with weights
WT=1./((SIG(I)**2)
SS=SS+WT
SX=SX+X(I)*WT
SY=SY+Y(I)*WT
11 CONTINUE
ELSE
DO 12 I=1,NDATA
c ... or without weights.
SX=SX+X(I)
SY=SY+Y(I)
12 CONTINUE
SS=FLOAT(NDATA)
ENDIF
SXOSS=SX/SS
IF(MWT.NE.0) THEN
DO 13 I=1,NDATA
T=(X(I)-SXOSS)/SIG(I)
ST2=ST2+T*T
B=B+T*Y(I)/SIG(I)
13 CONTINUE
ELSE
DO 14 I=1,NDATA
T=X(I)-SXOSS
ST2=ST2+T*T
B=B+T*Y(I)
14 CONTINUE
ENDIF
c Solve for A and B.
B=B/ST2
A=(SY-SX*B)/SS

RETURN
END

```

**APPENDIX 6**

**PROGRAM AUTO1**

## PROGRAM AUTO1

User inputs: None

File inputs: Selected column of image, "FORMAT.DAT"

File outputs: FFT of image column, "FOURIER.DAT"

Plot of FFT of image column, "FOURIER.PLT"

Plot of intensity of image column, "INTENSIT.PLT"



```

cccccccccccccccccccccccccccccccccccccccccccccccccccccccccccc
c
c Mary E. Magnani
c 26 June 1991
c
cccccccccccccccccccccccccccccccccccccccccccccccccccccccccccc
c
c File list:
c
c FORMAT.DAT      Input: formatted image file
c FOURIER.DAT     Output: Fourier transform data
c FOURIER.PLT     Output: plot of Fourier transform
c                 magnitude
c INTENSIT.PLT    Output: plot of image intensity
c
cccccccccccccccccccccccccccccccccccccccccccccccccccccccccccc
c
c This program, AUTO1, is the first part of a two-part
c programming package that calculates the phase of an
c image. This first program produces a plot from which
c the user can determine cutoff frequencies.
c
cccccccccccccccccccccccccccccccccccccccccccccccccccccccccccc
c
c Variable list:
c
c C_IMAGE(K)      An image column in complex form
c IMAGE(K)        An image column in integer form
c MAX_MAG         Maximum magnitude
c MAX_Y           Number of rows
c MIN_MAG         Minimum magnitude
c POWER_2         Power to which two is raised
c R_IMAGE(K)      An image column in real form
c
cccccccccccccccccccccccccccccccccccccccccccccccccccccccccccc

```

PROGRAM AUTO1

```

c   Declare variables.

COMPLEX C_IMAGE
INTEGER IMAGE,MAX_Y,POWER_2
REAL MAX_MAG,MIN_MAG,R_IMAGE

c   Define parameters.

PARAMETER (MAX_Y=512)
PARAMETER (POWER_2=9)

c   Dimension arrays.

DIMENSION C_IMAGE(MAX_Y)
DIMENSION IMAGE(MAX_Y)
DIMENSION R_IMAGE(MAX_Y)

c   Read image column data from file.

PRINT*
PRINT*, 'Reading the image file named'
PRINT*, 'FORMAT.DAT ...'

```

```

CALL READ_COL(IMAGE,MAX_Y)
c Translate column from integer to real format.
CALL INT2REAL(IMAGE,R_IMAGE,MAX_Y)
c Prepare plot file of pixel intensities.
CALL PLOT(R_IMAGE,MAX_Y,10)
PRINT*
PRINT*, 'Plot of pixel intensities is named'
PRINT*, 'INTENSIT.PLT.'
c Translate column from integer to complex
c format.
CALL INT2COMPL(IMAGE,C_IMAGE,MAX_Y)
c Take 1-D Fourier transform.
CALL FFT_1D(C_IMAGE,POWER_2)
c Prepare output file of FFT results.
CALL WRITE_COL(C_IMAGE,MAX_Y)
PRINT*
PRINT*, 'Fourier transform data are stored'
PRINT*, 'in file FOURIER.DAT.'
c Determine magnitude of column data.
CALL MAG(C_IMAGE,R_IMAGE,MAX_Y,MIN_MAG,MAX_MAG)
c Prepare plot file.
CALL PLOT(R_IMAGE,MAX_Y,15)
PRINT*
PRINT*, 'Plot of Fourier transform is named'
PRINT*, 'FOURIER.PLT.'
PRINT*

STOP
END

```

```

cccccccccccccccccccccccccccccccccccccccccccccccccccccccccccc

```

```

SUBROUTINE READ_COL(IMAGE,NY)

```

See Appendix 4.

```

cccccccccccccccccccccccccccccccccccccccccccccccccccccccccccc

```

```

cccccccccccccccccccccccccccccccccccccccccccccccccccccccccccc

```

```

SUBROUTINE INT2REAL(IMAGE,R_IMAGE,NY)

```

See Appendix 4.

```

cccccccccccccccccccccccccccccccccccccccccccccccccccccccccccc

```

cc

SUBROUTINE PLOT(R\_IMAGE,NY,FILE\_NUM)

See Appendix 4.

cc

cc

SUBROUTINE INT2COMPL(IMAGE,C\_IMAGE,NY)

See Appendix 4.

cc

cc

SUBROUTINE FFT\_1D(C\_IMAGE,POWER\_2)

See Appendix 4.

cc

cc

SUBROUTINE WRITE\_COL(C\_IMAGE,NY)

See Appendix 4.

cc

cc

SUBROUTINE MAG(C\_IMAGE,R\_IMAGE,NY,MIN\_MAG,MAX\_MAG)

See Appendix 4.

cc

**APPENDIX 7**

**PROGRAM AUTO2**

## PROGRAM AUTO2

User inputs: Pixel location of bottom of cuvette, "BOTTOM"

Lower cutoff frequency, "L\_CUT\_OFF"

Upper cutoff frequency, "U\_CUT\_OFF"

File inputs: FFT of image column, "FOURIER.DAT"

Continuous phase of carrier image, "CARRIER.DAT"

File outputs: Plot of ideal lowpass filter, "ILPF.PLT"

Plot of inverse FFT of ideal lowpass filter, "INV\_ILPF. PLT"

Plot of Hanning window, "HANNING.PLT"

Plot of inverse FFT of filter modified by Hanning window,  
"INV\_FIL.PLT"

Plot of filter modified by Hanning window, "FILTER.PLT"

Plot of filtered image column, "FIL\_DATA.PLT"

Plot of continuous phase of image column, "C\_PHASE.PLT"

Continuous phase of image column, "PHASE.DAT"

cc

c  
c Mary E. Magnani  
c 26 June 1991

cc

c  
c File list:

c  
c CARRIER.DAT Input: Carrier phase data (spatial)  
c C\_PHASE.PLT Output: Plot of continuous phase  
c (spatial)  
c FIL\_DATA.PLT Output: Plot of shifted, filtered  
c FFT data (Fourier)  
c FILTER.PLT Output: Plot of filter modified by  
c Hanning window (Fourier)  
c FOURIER.DAT Input: Fourier transform data  
c (Fourier)  
c ILPF.PLT Output: Plot of ideal lowpass  
c filter (Fourier)  
c INV\_ILPF.PLT Output: Plot of ideal lowpass  
c filter (spatial)  
c INV\_FIL.PLT Output: Plot of filter modified by  
c Hanning window (spatial)  
c HANNING.PLT Output: Plot of Hanning window  
c (spatial)  
c PHASE.DAT Output: Phase data (spatial)

cc

c  
c This program, AUTO2, is the second part of a two-part  
c programming package that calculates the phase of an  
c image. This second program filters a column of  
c Fourier transform data to obtain phase. Before  
c executing this program, the user executes program  
c AUTO1 to determine filter cutoff frequencies.

cc

c  
c Variable list:

c  
c BOTTOM Pixel location marking cuvette bottom  
c CARRIER(K) Carrier frequency  
c C\_IMAGE(K) An image column in complex form  
c C\_PHASE(K) Continuous phase  
c FILTER(K) An ideal lowpass filter  
c FILT\_IM(K) A filtered image  
c FIL\_WIN(K) Filter modified by a window  
c HALF\_PASS Half of the extent of passband  
c L\_CUT\_OFF Lower cutoff frequency for filter  
c MAX\_MAG Maximum magnitude  
c MAX\_Y Number of rows  
c MIDPT Midpoint of passband  
c MIN\_MAG Minimum magnitude  
c PHASE(K) Phase  
c PHAS\_IM(K) Phase from which phase is  
c calculated  
c PI The constant pi  
c PIX\_LOC Pixel location at end of filter's  
c second side lobe  
c POWER\_2 Power to which two is raised

c R\_IMAGE(K) An image column in real form  
 c SHFT\_FIL(K) Shifted version of FILTER(K) or  
 c FIL\_WIN(K)  
 c TEMPn Temporary variables  
 c U\_CUT\_OFF Upper cutoff frequency for filter  
 c WIDTH Width of window  
 c WINDOW(K) Hanning window  
 c  
 ccc

PROGRAM AUTO2

c Declare variables.

```
COMPLEX C_IMAGE,FILTER,FILT_IM,FIL_WIN
COMPLEX SHFT_FIL,WINDOW
INTEGER BOTTOM,HALF_PASS,L_CUT_OFF,MAX_Y
INTEGER MIDPT,PIX_LOC,POWER_2,TEMP1
INTEGER U_CUT_OFF,WIDTH
REAL CARRIER,C_PHASE,MAX_MAG,MIN_MAG
REAL PHASE,PI,R_IMAGE
```

c Define parameters.

```
PARAMETER (MAX_Y=512)
PARAMETER (PI=3.141592654)
PARAMETER (POWER_2=9)
```

c Dimension arrays.

```
DIMENSION CARRIER(MAX_Y)
DIMENSION C_IMAGE(MAX_Y)
DIMENSION C_PHASE(MAX_Y)
DIMENSION FILTER(MAX_Y)
DIMENSION FILT_IM(MAX_Y)
DIMENSION FIL_WIN(MAX_Y)
DIMENSION PHASE(MAX_Y)
DIMENSION R_IMAGE(MAX_Y)
DIMENSION SHFT_FIL(MAX_Y)
DIMENSION WINDOW(MAX_Y)
```

c Read input data.

```
CALL READ_COL(C_IMAGE,MAX_Y)
```

c Obtain pixel location marking cuvette bottom.

```
PRINT*
PRINT*, 'Enter the pixel location of the'
PRINT*, 'bottom of the cuvette:'
READ*, BOTTOM
```

c Apply ideal lowpass filter with window.

```
c Obtain cutoff frequencies and prepare ideal
c lowpass filter with user-specified cutoffs.
c The user enters frequencies determined by
c executing program AUTO1.
35 CONTINUE
PRINT*
PRINT*, 'Enter the lower cutoff frequency:'
READ*, L_CUT_OFF
```

```

PRINT*, 'Enter the upper cutoff frequency:'
READ*, U_CUT_OFF

c   If the cutoff frequencies were switched,
c   correct the situation.

IF (L_CUT_OFF.GT.U_CUT_OFF) THEN
  TEMP1=L_CUT_OFF
  L_CUT_OFF=U_CUT_OFF
  U_CUT_OFF=TEMP1
ENDIF

c   Find the midpoint of the passband, and
c   half its extent.
MIDPT=(U_CUT_OFF+L_CUT_OFF)/2
HALF_PASS=U_CUT_OFF-MIDPT

c   Prepare an ideal lowpass filter,
c   located at the origin.
CALL ILPF(FILTER,HALF_PASS,MAX_Y)
c   Prepare plot file, taking image magnitude first.
CALL MAG(FILTER,R_IMAGE,MAX_Y,MIN_MAG,MAX_MAG)
CALL PLOT(R_IMAGE,MAX_Y,11)
PRINT*
PRINT*, 'Plot of the ideal lowpass filter'
PRINT*, 'is named ILPF.PLT.'

c   Modify ideal lowpass filter with a window.
c   Take inverse Fourier transform of ideal
c   lowpass filter.

CALL INV_FFT_1D(FILTER,POWER_2)
c   Prepare plot file, taking image magnitude
c   first.
CALL MAG(FILTER,R_IMAGE,MAX_Y,MIN_MAG,MAX_MAG)
CALL PLOT(R_IMAGE,MAX_Y,13)
PRINT*
PRINT*, 'Plot of the inverse Fourier'
PRINT*, 'transform of the ideal lowpass'
PRINT*, 'filter is named INV_ILPF.PLT.'

c   Find the pixel location where the second
c   side lobe of the inverse Fourier transform
c   of the ideal lowpass filter ends.
CALL SECOND(FILTER,PIX_LOC,MAX_Y)

c   Determine window size.
WIDTH=2*PIX_LOC+1
PRINT*
PRINT 40, WIDTH
40  FORMAT (1X, 'The window size is ', I3, '.')

c   Prepare window.
CALL HANNING(WINDOW,WIDTH,MAX_Y)
c   Prepare plot file, taking image magnitude
c   first.
CALL MAG(WINDOW,R_IMAGE,MAX_Y,MIN_MAG,MAX_MAG)
CALL PLOT(R_IMAGE,MAX_Y,14)
PRINT*
PRINT*, 'Plot of the Hanning window is'
PRINT*, 'named HANNING.PLT.'

```



```

c      Multiply ideal lowpass filter and window to
c      form new filter.
c      CALL MULT(FIL_WIN,FILTER,WINDOW,MAX_Y)
c      Prepare plot file, taking image magnitude
c      first.
c      CALL MAG(FIL_WIN,R_IMAGE,MAX_Y,MIN_MAG,
+       MAX_MAG)
c      CALL PLOT(R_IMAGE,MAX_Y,15)
c      PRINT*
c      PRINT*,'Plot of the inverse Fourier'
c      PRINT*,'transform of the filter modified by'
c      PRINT*,'the Hanning window is named'
c      PRINT*,'INV_FIL.PLT.'

c      Take the Fourier transform to get final
c      filter.
c      CALL FFT_1D(FIL_WIN,POWER_2)
c      Prepare plot file, taking image magnitude
c      first.
c      CALL MAG(FIL_WIN,R_IMAGE,MAX_Y,MIN_MAG,
+       MAX_MAG)
c      CALL PLOT(R_IMAGE,MAX_Y,16)
c      PRINT*
c      PRINT*,'Plot of the filter modified by the'
c      PRINT*,'Hanning window is named FILTER.PLT.'

c      The final filter is located at the origin. So
c      shift it up to MIDPT, the midpoint of the
c      actual passband.

c      CALL FREQ_SHIFT(FIL_WIN,SHFT_FIL,MAX_Y,MIDPT)

c      To filter the image, multiply the image
c      and the filter.
c      CALL MULT(FILT_IM,C_IMAGE,SHFT_FIL,MAX_Y)
c      Prepare plot file, taking image magnitude first.
c      CALL MAG(FILT_IM,R_IMAGE,MAX_Y,MIN_MAG,MAX_MAG)
c      CALL PLOT(R_IMAGE,MAX_Y,12)
c      PRINT*
c      PRINT*,'Plot of the filtered data is named'
c      PRINT*,'FIL_DATA.PLT.'

c      Take the inverse 1-D Fourier transform.
c      CALL INV_FFT_1D(FILT_IM,POWER_2)

c      Determine phase.
c      DO 45 K=1,MAX_Y
c          PHASE(K)=AIMAG(CLOG(FILT_IM(K)))
c      Another option.
c      PHASE(K)=ATAN2(AIMAG(FILT_IM(K)),
c      + REAL(FILT_IM(K)))
45  CONTINUE

c      Apply phase continuation.
c      CALL PHASE_CONT(C_PHASE,PHASE,MAX_Y)

c      Read and subtract carrier phase.
c      PRINT*
c      PRINT*,'Reading the file named CARRIER.DAT ...'
c      CALL READ_REAL(CARRIER,MAX_Y)

```

```

DO 50 K=1,MAX_Y
  C_PHASE(K)=C_PHASE(K)-CARRIER(K)
50 CONTINUE

```

```

c Prepare plot file.
CALL PLOT(C_PHASE,MAX_Y,19)
PRINT*
PRINT*,'Plot of the continuous phase is '
PRINT*,'named C_PHASE.PLT.'

```

```

c Prepare output file.
CALL WRITE_COL(C_PHASE,MAX_Y,BOTTOM)
PRINT*
PRINT*,'Phase data are stored in file'
PRINT*,'PHASE.DAT.'
PRINT*

```

```

STOP
END

```

cc

```

SUBROUTINE READ_COL(C_IMAGE,NY)

```

See Appendix 5.

cc

cc

```

SUBROUTINE ILPF(FILTER,HALF_PASS,NY)

```

See Appendix 5.

cc

cc

```

SUBROUTINE MAG(C_IMAGE,R_IMAGE,NY,MIN_MAG,MAX_MAG)

```

See Appendix 4.

cc

cc

```

c
c This subroutine prepares a plot file.

```

cc

```

c
c Variable list:

```

- c FILE\_NUM A file number
- c INDEX(K) X-axis for graphs
- c MAX\_Y Maximum value of NY
- c NY Number of rows
- c R\_IMAGE(K) An image column in real form

cc

```

SUBROUTINE PLOT(R_IMAGE,NY,FILE_NUM)

```

c Declare variables.

```
INTEGER FILE_NUM,MAX_Y,NY  
REAL INDEX,R_IMAGE
```

c Define parameters.

```
PARAMETER (MAX_Y=512)
```

c Dimension arrays.

```
DIMENSION INDEX(MAX_Y)  
DIMENSION R_IMAGE(MAX_Y)
```

c Open output file.

```
IF (FILE_NUM.EQ.11) THEN  
  OPEN (FILE_NUM,FILE='ILPF.PLT',STATUS='NEW')  
ELSEIF (FILE_NUM.EQ.12) THEN  
  OPEN (FILE_NUM,FILE='FIL_DATA.PLT',STATUS='NEW')  
ELSEIF (FILE_NUM.EQ.13) THEN  
  OPEN (FILE_NUM,FILE='INV_ILPF.PLT',STATUS='NEW')  
ELSEIF (FILE_NUM.EQ.14) THEN  
  OPEN (FILE_NUM,FILE='HANNING.PLT',STATUS='NEW')  
ELSEIF (FILE_NUM.EQ.15) THEN  
  OPEN (FILE_NUM,FILE='INV_FIL.PLT',STATUS='NEW')  
ELSEIF (FILE_NUM.EQ.16) THEN  
  OPEN (FILE_NUM,FILE='FILTER.PLT',STATUS='NEW')  
ELSEIF (FILE_NUM.EQ.19) THEN  
  OPEN (FILE_NUM,FILE='C_PHASE.PLT',STATUS='NEW')  
ENDIF
```

c Prepare x-axis for graph.

```
DO 620 K=1,MAX_Y  
  INDEX(K)=K  
620 CONTINUE
```

c Write pixels to file.

```
WRITE (FILE_NUM,690) NY  
DO 630 K=1,MAX_Y  
  WRITE(FILE_NUM,691) INDEX(K),R_IMAGE(K)  
630 CONTINUE  
CLOSE(FILE_NUM)
```

c Format statements.

```
690 FORMAT (I4)  
691 FORMAT (F6.1,E15.8)
```

```
RETURN  
END
```

```
cccccccccccccccccccccccccccccccccccccccccccccccccccccccccccc
```

```
SUBROUTINE FREQ_SHIFT(C_IMAGE,SHIFT_IM,NY,SHFT_FRE)
```

See Appendix 5.

```
cccccccccccccccccccccccccccccccccccccccccccccccccccccccccccc
```

cc

SUBROUTINE MULT(OUT,IN1,IN2,NY)

See Appendix 5.

cc

cc

SUBROUTINE INV\_FFT\_1D(C\_IMAGE,POWER\_2)

See Appendix 5.

cc

cc

SUBROUTINE SECOND(C\_IMAGE,PIX\_LOC,NY)

See Appendix 5.

cc

cc

SUBROUTINE HANNING(C\_IMAGE,WIDTH,NY)

See Appendix 5.

cc

cc

SUBROUTINE FFT\_1D(C\_IMAGE,POWER\_2)

See Appendix 5.

cc

cc

c

c This subroutine reads a real image column from a  
c file to the array R\_IMAGE.

c

cc

c

c Variable list:

c

c MAX\_Y       Maximum value of NY

c NY           Number of rows

c REAL(K)     An image column in real form

c

cc

SUBROUTINE READ\_REAL(R\_IMAGE,NY)

c    Declare variables.

INTEGER MAX\_Y,NY

```

REAL R_IMAGE

c Define parameters.

PARAMETER (MAX_Y=512)

c Dimension arrays.

DIMENSION R_IMAGE(MAX_Y)

c Open input file.

OPEN (9,FILE='CARRIER.DAT',STATUS='OLD')

c Read pixels into array R_IMAGE.

READ (9,190) (R_IMAGE(K),K=1,NY)
CLOSE(9)

c Format statements.

190 FORMAT (1X,E15.8)

RETURN
END

cccccccccccccccccccccccccccccccccccccccccccccccccccccccccccc

SUBROUTINE PHASE_CONT(C_PHASE,PHASE,NY)

See Appendix 5.

cccccccccccccccccccccccccccccccccccccccccccccccccccccccccccc

cccccccccccccccccccccccccccccccccccccccccccccccccccccccccccc
c
c This subroutine writes an image column from an array
c R_IMAGE to a to a file named PHASE.DAT. The variable
c BOTTOM is also written.
c
cccccccccccccccccccccccccccccccccccccccccccccccccccccccccccc
c
c Variable list:
c
c BOTTOM Pixel location marking cuvette bottom
c R_IMAGE(K) An image column in real form
c MAX_Y Maximum value of NY
c NY Number of rows
c
cccccccccccccccccccccccccccccccccccccccccccccccccccccccccccc

SUBROUTINE WRITE_COL(R_IMAGE,NY,BOTTOM)

c Declare variables.

INTEGER BOTTOM,MAX_Y,NY
REAL R_IMAGE

c Define parameters.

PARAMETER (MAX_Y=512)

```

```
c   Dimension arrays.
    DIMENSION R_IMAGE(MAX_Y)

c   Open output file.
    OPEN (4,FILE='PHASE.DAT',STATUS='NEW')

c   Write pixels to file.
    WRITE (4,290) BOTTOM
    WRITE (4,291) (R_IMAGE(K),K=1,NY)
    CLOSE(4)

c   Format statements.
290  FORMAT (I4)
291  FORMAT (1X,E15.8)

    RETURN
    END
```

**APPENDIX 8**

**PROGRAM CONCEN1**

## PROGRAM CONCEN1

User inputs: Pixel location of top of interface, "INTERF"

Image scale, "SCALE"

File inputs: Continuous phase of image column, "PHASE.DAT"

Continuous phase of baseline image column, "BAS\_PHAS.DAT"

File outputs: Plot of phase of image column after base phase subtraction,

"PHASE.PLT"

Plot of fringe pattern without tilt fringes, "FRINGE.PLT"

Plot of refractive index of image column, "N.PLT"

Refractive index of image column, "N.DAT"



cc

c  
c Mary E. Magnani  
c 26 June 1991  
c

cc

c  
c File list:

c  
c BAS\_PHAS.DAT Input: Base phase data  
c FRINGE.PLT Output: Plot of fringes without  
c carrier (spatial)  
c N.DAT Output: Index of refraction data  
c N.PLT Output: Plot of index of refraction  
c PHASE.DAT Input: Experimental phase data  
c PHASE.PLT Output: Plot of phase after base  
c phase subtraction  
c

cc

c  
c This program, CONCEN1, is the first part of a two-  
c part programming package that calculates concentration  
c from phase. This first program subtracts a base phase  
c from an experimental phase, then converts the result  
c to index of refraction.

c  
cc

c  
c Variable list:

c  
c BAS\_PHA(K) Base phase  
c BOTTOM Pixel location marking cuvette bottom  
c EXP\_PHA(K) Experimental phase  
c FRINGE(K) Fringe pattern without effect of  
c tilt fringes  
c INTERF Pixel location marking top of  
c interface  
c MAX\_Y Number of rows  
c N(K) Index of refraction  
c PHASE(K) Phase resulting from subtracting  
c BAS\_PHAS from EXP\_PHAS  
c PI The constant pi  
c RESPONSE A response to program question  
c SCALE Image scale, number of pixels in  
c one millimeter  
c WAVELEN Wavelength of Helium-Neon laser  
c WIDTH Width of cuvette  
c Y(K) Distance from growth front  
c

cc

PROGRAM CONCEN1

c Declare variables.

INTEGER BOTTOM,INTERF,MAX\_Y,RESPONSE  
REAL BAS\_PHAS,EXP\_PHAS,FRINGE,N,PHASE,PI,SCALE  
REAL WAVELEN,WIDTH,Y

c Define parameters.  
c Units, where applicable, in meters.

```

PARAMETER (MAX_Y=512)
PARAMETER (PI=3.141592654)
PARAMETER (WAVELEN=6328E-10)
PARAMETER (WIDTH=0.008)

c   Dimension arrays.

DIMENSION BAS_PHAS(MAX_Y)
DIMENSION EXP_PHAS(MAX_Y)
DIMENSION FRINGE(MAX_Y)
DIMENSION PHASE(MAX_Y)
DIMENSION N(MAX_Y)
DIMENSION Y(MAX_Y)

c   Determine if a base phase will be used.

10  CONTINUE
    PRINT*
    PRINT*, 'To subtract a base phase,'
    PRINT*, 'enter 1.'
    PRINT*, 'Enter 2 otherwise.'
    READ*, RESPONSE

c   If a base phase will be used, read it.
    IF (RESPONSE.EQ.1) THEN
        PRINT*
        PRINT*, 'Reading the file named BAS_PHAS.DAT...'
        CALL READ_COL(BAS_PHAS,9,MAX_Y,BOTTOM)
    ELSEIF (RESPONSE.EQ.2) THEN
        CONTINUE
    ELSE
        PRINT*
        PRINT*, 'Incorrect response, try again.'
        GOTO 10
    ENDIF

c   Read experimental phase.

    PRINT*
    PRINT*, 'Reading the file named PHASE.DAT ...'
    CALL READ_COL(EXP_PHAS,10,MAX_Y,BOTTOM)

c   Obtain pixel location marking top of interface.
    PRINT*
    PRINT*, 'Enter the pixel location of the'
    PRINT*, 'top of the interface:'
    READ*, INTERF

c   Obtain image scale.
    PRINT*
    PRINT*, 'Enter image scale. How many pixels'
    PRINT*, 'in a millimeter?'
    READ*, SCALE

c   Compute distance from interface for each pixel,
c   in meters.

    DO 70 K=1,INTERF
        Y(K)=0.001*(INTERF-K)/SCALE
70  CONTINUE

```

c Shift the experimental phase so that zero  
c phase corresponds to the cuvette bottom.

```
CALL PHAS_SHFT(EXP_PHAS,BOTTOM,MAX_Y)
```

c If a base phase is being used, shift it so  
c that zero phase corresponds to the cuvette  
c bottom. Then subtract the base phase from the  
c experimental phase.

```
IF (RESPONSE.EQ.1) THEN
  CALL PHAS_SHFT(BAS_PHAS,BOTTOM,MAX_Y)
  DO 50 K=1,MAX_Y
    PHASE(K)=EXP_PHAS(K)-BAS_PHAS(K)
50  CONTINUE
  ELSE
    DO 55 K=1,MAX_Y
      PHASE(K)=EXP_PHAS(K)
55  CONTINUE
  ENDIF
```

c Prepare plot file.  
CALL PLT\_F\_INT(Y,PHASE,INTERF,9)  
PRINT\*  
PRINT\*,'Plot of the phase is named'  
PRINT\*,'PHASE.PLT.'

c Determine fringe pattern without tilt fringes.  
DO 57 K=1,MAX\_Y  
FRINGE(K)=COS(PHASE(K))  
57 CONTINUE

c Prepare plot file.  
CALL PLT\_F\_INT(Y,FRINGE,INTERF,10)  
PRINT\*  
PRINT\*,'Plot of the fringe pattern without'  
PRINT\*,'tilt fringes is named FRINGE.PLT.'

c Convert the phase to index of refraction.  
DO 60 K=1,INTERF  
N(K)=WAVELEN\*PHASE(K)/(2\*PI\*WIDTH)  
60 CONTINUE

c Prepare plot file.  
CALL PLT\_F\_INT(Y,N,INTERF,11)  
PRINT\*  
PRINT\*,'Plot of index of refraction is named'  
PRINT\*,'N.PLT.'

c Prepare output file.  
CALL WRITE\_COL(Y,N,INTERF,SCALE)  
PRINT\*  
PRINT\*,'Index of refraction data are stored'  
PRINT\*,'in file N.DAT.'  
PRINT\*

```
STOP
END
```

```

cccccccccccccccccccccccccccccccccccccccccccccccccccccccccccc
c
c This subroutine reads an image column from a file to
c the array R_IMAGE. The variable BOTTOM is also read.
c
cccccccccccccccccccccccccccccccccccccccccccccccccccccccccccc
c
c Variable list:
c
c BOTTOM      Pixel location marking cuvette bottom
c FILE_NUM    File number
c MAX_Y       Maximum value of NY
c NY          Number of rows
c R_IMAGE(K)  An image column in real form
c
cccccccccccccccccccccccccccccccccccccccccccccccccccccccccccc

```

```

SUBROUTINE READ_COL(R_IMAGE,FILE_NUM,NY,BOTTOM)

```

```

c Declare variables.

INTEGER BOTTOM,FILE_NUM,MAX_Y,NY
REAL R_IMAGE

c Define parameters.

PARAMETER (MAX_Y=512)

c Dimension arrays.

DIMENSION R_IMAGE(MAX_Y)

c Open input file.

IF (FILE_NUM.EQ.9) THEN
  OPEN (FILE_NUM,FILE='BAS_PHAS.DAT',
+      STATUS='OLD')
ELSEIF (FILE_NUM.EQ.10) THEN
  OPEN (FILE_NUM,FILE='PHASE.DAT',
+      STATUS='OLD')
ENDIF

c Read pixels into array R_IMAGE.

READ (FILE_NUM,189) BOTTOM
READ (FILE_NUM,190) (R_IMAGE(K),K=1,NY)
CLOSE(FILE_NUM)

c Format statements.

189 FORMAT (I4)
190 FORMAT (1X,E15.8)

RETURN
END

```

```

cccccccccccccccccccccccccccccccccccccccccccccccccccccccccccc
c
c This subroutine adds a constant to R_IMAGE, the input
c phase, such that zero phase corresponds to the bottom
c of the cuvette.

```

```

c
cccccccccccccccccccccccccccccccccccccccccccccccccccccccccccc
c
c Variable list:
c
c BOTTOM      Pixel location marking cuvette bottom
c MAX_Y      Maximum value of NY
c NY         Number of rows
c PHAS_BOT   Phase value at the bottom of cuvette
c R_IMAGE(K) An image column in real form
c
cccccccccccccccccccccccccccccccccccccccccccccccccccccccccccc

```

```

      SUBROUTINE PHAS_SHFT(R_IMAGE,BOTTOM,NY)

```

```

c   Declare variables.

      INTEGER BOTTOM,MAX_Y,NY
      REAL PHAS_BOT,R_IMAGE

c   Define parameters.

      PARAMETER (MAX_Y=512)

c   Dimension arrays.

      DIMENSION R_IMAGE(MAX_Y)

c   Make zero phase correspond to the bottom of
c   the cuvette.
      PHAS_BOT=R_IMAGE(BOTTOM)
      DO 200 K=1,NY
        R_IMAGE(K)=R_IMAGE(K)-PHAS_BOT
200  CONTINUE

      RETURN
      END

```

```

cccccccccccccccccccccccccccccccccccccccccccccccccccccccccccc
c
c This subroutine prepares a plot file, starting from
c the interface.
c
cccccccccccccccccccccccccccccccccccccccccccccccccccccccccccc

```

```

c Variable list:
c
c FILE_NUM   A file number
c INDEX(K)   X-axis for graphs
c MAX_Y      Maximum value of NY
c NY         Number of rows
c R_IMAGE(K) An image column in real form
c
cccccccccccccccccccccccccccccccccccccccccccccccccccccccccccc

```

```

      SUBROUTINE PLT_F_INT(INDEX,R_IMAGE,NY,FILE_NUM)

```

```

c   Declare variables.

      INTEGER FILE_NUM,MAX_Y,NY
      REAL INDEX,R_IMAGE

```

```

c   Define parameters.
PARAMETER (MAX_Y=512)

c   Dimension arrays.
DIMENSION INDEX(MAX_Y)
DIMENSION R_IMAGE(MAX_Y)

c   Open output file.
IF (FILE_NUM.EQ.9) THEN
  OPEN (FILE_NUM,FILE='PHASE.PLT',STATUS='NEW')
ELSEIF (FILE_NUM.EQ.10) THEN
  OPEN (FILE_NUM,FILE='FRINGE.PLT',STATUS='NEW')
ELSEIF (FILE_NUM.EQ.11) THEN
  OPEN (FILE_NUM,FILE='N.PLT',STATUS='NEW')
ENDIF

c   Write pixels to file.
WRITE (FILE_NUM,690) NY-1
c   Plot from interface to top of cuvette.
c   Exclude first data point, as the image
c   processor gives a faulty value for its
c   intensity.
DO 630 K=NY,2,-1
c   Convert INDEX from meters to millimeters.
  WRITE(FILE_NUM,691) 1000*INDEX(K),R_IMAGE(K)
630 CONTINUE
CLOSE(FILE_NUM)

c   Format statements.
690 FORMAT (I4)
691 FORMAT (E15.8,E15.8)

RETURN
END

```

```

cccccccccccccccccccccccccccccccccccccccccccccccccccccccccccccccc

```

```

c
c This subroutine writes an image column from an array
c R_IMAGE to a file named N.DAT. The variable SCALE is
c also written.
c

```

```

cccccccccccccccccccccccccccccccccccccccccccccccccccccccccccccccc

```

```

c
c Variable list:
c
c INDEX(K)   X-axis
c MAX_Y     Maximum value of NY
c NY        Number of rows
c R_IMAGE(K) An image column in real form
c SCALE     Image scale, number of pixels in
c           one millimeter
c

```

```

cccccccccccccccccccccccccccccccccccccccccccccccccccccccccccccccc

```

```

SUBROUTINE WRITE_COL(INDEX,R_IMAGE,NY,SCALE)

```

```

c   Declare variables.
      INTEGER MAX_Y,NY
      REAL INDEX,R_IMAGE,SCALE

c   Define parameters.
      PARAMETER (MAX_Y=512)

c   Dimension arrays.
      DIMENSION INDEX(MAX_Y)
      DIMENSION R_IMAGE(MAX_Y)

c   Open output file.
      OPEN (4,FILE='N.DAT',STATUS='NEW')

c   Write pixels to file.
      WRITE (4,289) SCALE
      WRITE (4,290) NY
      DO 770 K=1,NY
        WRITE (4,291) INDEX(K), R_IMAGE(K)
770  CONTINUE
      CLOSE(4)

c   Format statements.
289  FORMAT (E15.8)
290  FORMAT (I4)
291  FORMAT (1X,E15.8,E15.8)

      RETURN
      END

```

**APPENDIX 9**

**PROGRAM CONCEN2**



## PROGRAM CONCEN2

User inputs: Distance between fringes in fringe plot, "FRI2FRI"

Temperature gradient, "GRADIENT"

Window for maximum index of refraction, "WINDOW"

Concentration of water in bulk liquid, "BULK\_C"

File inputs: Refractive index of image column, "N.DAT"

File outputs: Plot of refractive index with temperature effect removed,

"N\_NOTEMP.PLT"

Plot of concentration of image column, "CONCEN.PLT"

Concentration of image column, "CONCEN.DAT"

cc

c  
c Mary E. Magnani  
c 26 June 1991

cc

c  
c File list:  
c  
c CONCEN.DAT      Output: Concentration data  
c CONCEN.PLT      Output: Plot of concentration  
c N.DAT            Input: Index of refraction data  
c N\_NOTEMP.PLT    Output: Plot of index of refraction  
c                   with temperature removed

cc

c  
c This program, CONCEN2, is the second part of a two-  
c part programming package that calculates concentration  
c from phase. This second program converts index of  
c refraction to concentration.

cc

c  
c Variable list:  
c  
c BULK\_C           Bulk concentration of water  
c C\_COEFF          Concentration coefficient in equation  
c                   relating T,C,N  
c CONCEN(K)        Concentration  
c FRI2FRI          Fringe-to-fringe distance in  
c                   FRINGE.PLT, in pixels  
c GRADIENT         Temperature gradient in degrees C/cm  
c MAX\_N            Maximum value of N  
c MAX\_Y            Maximum value of NY  
c N(K)             Index of refraction  
c NY                Number of rows  
c REC\_GRAD         Recommended value for GRADIENT  
c RESPONSE         A response to program question  
c SCALE            Image scale, number of pixels in  
c                   one millimeter  
c T\_COEFF          Temperature coefficient in equation  
c                   relating T,C,N  
c WAVELEN          Wavelength of Helium-Neon laser  
c WIDTH            Width of cuvette  
c WINDOW           Window for maximum index of  
c                   refraction  
c Y(K)             Distance from growth front

cc

PROGRAM CONCEN2

c    Declare variables.  
  
      INTEGER MAX\_Y,NY,RESPONSE  
      REAL BULK\_C,C\_COEFF,CONCEN,FRI2FRI,GRADIENT  
      REAL MAX\_N,N,REC\_GRAD,SCALE,T\_COEFF  
      REAL WAVELEN,WIDTH,WINDOW,Y  
  
c    Define parameters.

```

PARAMETER (C_COEFF=1.63E-3)
PARAMETER (MAX_Y=512)
PARAMETER (T_COEFF=-1.73E-4)
PARAMETER (WAVELEN=6328e-10)
PARAMETER (WIDTH=0.008)

```

c Dimension arrays.

```

DIMENSION CONCEN(MAX_Y)
DIMENSION N(MAX_Y)
DIMENSION Y(MAX_Y)

```

c Read index of refraction data.

```

PRINT*
PRINT*, 'Reading the file named N.DAT ...'
CALL READ_COL(Y,N,NY,SCALE)

```

c Obtain temperature gradient.

5 CONTINUE

```

PRINT*
PRINT*, 'For a recommended temperature '
PRINT*, 'gradient, enter 1.'
PRINT*, 'Enter 2 otherwise.'
READ*, RESPONSE
IF (RESPONSE.EQ.1) THEN
  PRINT*
  PRINT*, 'Enter fringe to fringe distance'
  PRINT*, 'from FRINGE.PLT, in pixels:'
  READ*, FRI2FRI
  REC_GRAD=10*WAVELEN*SCALE/
+   (T_COEFF*WIDTH*FRI2FRI)
  PRINT*
  PRINT*, 'The recommended gradient is',
+   REC_GRAD
  GRADIENT=REC_GRAD
ELSEIF (RESPONSE.EQ.2) THEN
  PRINT*
  PRINT*, 'Enter temperature gradient in'
  PRINT*, 'degrees C per cm, a negative number:'
  READ*, GRADIENT
  ELSE
  PRINT*
  PRINT*, 'Incorrect response, please try again.'
  GO TO 5
ENDIF

```

c Obtain window for maximum index of refraction.

```

PRINT*
PRINT*, 'Use N.PLT to determine a window for'
PRINT*, 'maximum index of refraction. Enter a'
PRINT*, 'distance from the interface in'
PRINT*, 'millimeters.'
READ*, WINDOW

```

c Convert to meters.

```

WINDOW=WINDOW*0.001

```

c Obtain bulk concentration.

```

PRINT*
PRINT*, 'Enter concentration of water in '

```

```

PRINT*, 'the bulk liquid. Example: 72.'
READ*, BULK_C

c Subtract temperature effect from index of
c refraction data, and plot. The maximum index
c of refraction is assigned within WINDOW.

MAX_N=-1.0E12
DO 20 K=NY,1,-1
  N(K)=N(K)+T_COEFF*100*GRADIENT*Y(K)
  IF (N(K).LE.MAX_N) GO TO 20
  IF (Y(K).LE.WINDOW) MAX_N=N(K)
20 CONTINUE
CALL PLOT(Y,N,NY,10)
PRINT*
PRINT*, 'Plot of index of refraction with '
PRINT*, 'temperature effect removed is stored'
PRINT*, 'in file N_NOTEMP.PLT.'

c Calculate concentration.

DO 300 K=1,NY
  CONCEN(K)=BULK_C + (MAX_N-N(K))/C_COEFF
300 CONTINUE
PRINT*
PRINT 310, CONCEN(NY)
310 FORMAT (1X, 'The tip concentration is ',F6.2, '.')

c Prepare plot file.
CALL PLOT(Y,CONCEN,NY,11)
PRINT*
PRINT*, 'Plot of concentration is stored in'
PRINT*, 'file CONCEN.PLT.'

c Prepare output file.
CALL WRITE_COL(Y,CONCEN,NY)
PRINT*
PRINT*, 'Concentration data are stored in'
PRINT*, 'file CONCEN.DAT.'
PRINT*

STOP
END

```

```

cccccccccccccccccccccccccccccccccccccccccccccccccccccccccccc
c
c This subroutine reads an image column from a file to
c the arrays INDEX, R_IMAGE. The variable SCALE is also
c read.
c
cccccccccccccccccccccccccccccccccccccccccccccccccccccccccccc
c
c Variable list:
c
c INDEX(K)      X-axis
c MAX_Y        Maximum value of NY
c NY           Number of rows
c R_IMAGE(K)   An image column in real form
c SCALE        Image scale, number of pixels in
c              one millimeter

```

```

c
cccccccccccccccccccccccccccccccccccccccccccccccccccccccccccc
SUBROUTINE READ_COL(INDEX,R_IMAGE,NY,SCALE)
c Declare variables.
INTEGER MAX_Y,NY
REAL INDEX,R_IMAGE,SCALE
c Define parameters.
PARAMETER (MAX_Y=512)
c Dimension arrays.
DIMENSION INDEX(MAX_Y)
DIMENSION R_IMAGE(MAX_Y)
c Open input file.
OPEN (9,FILE='N.DAT',STATUS='OLD')
c Read pixels into arrays INDEX, R_IMAGE.
READ (9,188) SCALE
READ (9,189) NY
DO 70 K=1,NY
READ (9,190) INDEX(K),R_IMAGE(K)
70 CONTINUE
CLOSE(9)
c Format statements.
188 FORMAT (E15.8)
189 FORMAT (I4)
190 FORMAT (1X,E15.8,E15.8)
RETURN
END

```

```
cccccccccccccccccccccccccccccccccccccccccccccccccccccccccccc
```

```

c
c This subroutine prepares a plot file.
c
cccccccccccccccccccccccccccccccccccccccccccccccccccccccccccc

```

- ```

c Variable list:
c
c FILE_NUM A file number
c INDEX(K) X-axis for graphs
c MAX_Y Maximum value of NY
c NY Number of rows
c R_IMAGE(K) An image column in real form
c

```

```
cc
```

```

SUBROUTINE PLOT(INDEX,R_IMAGE,NY,FILE_NUM)
c Declare variables.

```

```

INTEGER NY,FILE_NUM,MAX_Y
REAL INDEX,R_IMAGE

c Define parameters.

PARAMETER (MAX_Y=512)

c Dimension arrays.

DIMENSION INDEX(MAX_Y)
DIMENSION R_IMAGE(MAX_Y)

c Open output file.

IF (FILE_NUM.EQ.10) THEN
  OPEN (FILE_NUM,FILE='N_NOTEMP.PLT',STATUS='NEW')
ELSEIF (FILE_NUM.EQ.11) THEN
  OPEN (FILE_NUM,FILE='CONCEN.PLT',STATUS='NEW')
ENDIF

c Write pixels to file.

WRITE (FILE_NUM,690) NY
c Plot from growth front to top of cuvette.
DO 630 K=NY,1,-1
c Convert INDEX from meters to millimeters.
WRITE(FILE_NUM,691) 1000*INDEX(K),R_IMAGE(K)
630 CONTINUE
CLOSE(FILE_NUM)

c Format statements.

690 FORMAT (I4)
691 FORMAT (E15.8,E15.8)

RETURN
END

```

```

cc

```

```

c
c This subroutine writes an image column from an array
c R_IMAGE to a file named N.DAT.

```

```

cc

```

```

c
c Variable list:
c
c INDEX(K)    X-axis
c MAX_Y      Maximum value of NY
c NY         Number of rows
c R_IMAGE(K) An image column in real form

```

```

cc

```

```

SUBROUTINE WRITE_COL(INDEX,R_IMAGE,NY)

```

```

c Declare variables.

INTEGER MAX_Y,NY
REAL INDEX,R_IMAGE

```

- c Define parameters.

```
PARAMETER (MAX_Y=512)
```

- c Dimension arrays.

```
DIMENSION INDEX(MAX_Y)  
DIMENSION R_IMAGE(MAX_Y)
```

- c Open output file.

```
OPEN (4,FILE='CONCEN.DAT',STATUS='NEW')
```

- c Write pixels to file.

```
WRITE (4,290) NY  
DO 770 K=1,NY  
    WRITE (4,291) INDEX(K), R_IMAGE(K)  
770 CONTINUE  
CLOSE(4)
```

- c Format statements.

```
290 FORMAT (I4)  
291 FORMAT (1X,E15.8,E15.8)
```

```
RETURN  
END
```

**APPENDIX 10**

**RAW DATA**



## CARRIER IMAGE FOR INTERFEROMETRY

|                        |       |       |       |       |       |
|------------------------|-------|-------|-------|-------|-------|
| Column (pix)           | 66    | 67    | 68    | 69    | 70    |
| Lower cutoff frequency | 64    | 64    | 64    | 64    | 64    |
| Upper cutoff frequency | 87    | 86    | 86    | 86    | 86    |
| Carrier frequency      | 74.21 | 74.21 | 74.21 | 74.22 | 74.21 |

|                        |       |       |       |       |
|------------------------|-------|-------|-------|-------|
| Column (pix)           | 80    | 112   | 155   | 160   |
| Lower cutoff frequency | 66    | 64    | 64    | 64    |
| Upper cutoff frequency | 84    | 84    | 85    | 86    |
| Carrier frequency      | 74.24 | 74.18 | 74.24 | 74.25 |

## BASE PHASE IMAGE FOR INTERFEROMETRY

|                        |       |       |       |       |       |
|------------------------|-------|-------|-------|-------|-------|
| Column (pix)           | 66    | 67    | 68    | 69    | 70    |
| Lower cutoff frequency | 59    | 59    | 59    | 59    | 59    |
| Upper cutoff frequency | 88    | 88    | 88    | 88    | 88    |
| Carrier frequency      | 74.21 | 74.21 | 74.21 | 74.22 | 74.21 |
| Cuvette bottom (pix)   | 399   | 399   | 399   | 399   | 399   |
| Scale (pix/mm)         | 72.5  | 72.5  | 72.5  | 72.5  | 72.5  |

|                        |       |       |       |       |
|------------------------|-------|-------|-------|-------|
| Column (pix)           | 80    | 112   | 155   | 160   |
| Lower cutoff frequency | 62    | 63    | 65    | 65    |
| Upper cutoff frequency | 83    | 88    | 86    | 86    |
| Carrier frequency      | 74.24 | 74.18 | 74.24 | 74.25 |
| Cuvette bottom (pix)   | 398   | 397   | 401   | 400   |
| Scale (pix/mm)         | 72.5  | 72.5  | 72.5  | 72.5  |

## RUNS 47, 48, 49, AND 50 AT 30 SECONDS

| Run                           | 47    | 48    | 49    | 50    |
|-------------------------------|-------|-------|-------|-------|
| Column (pix)                  | 160   | 80    | 68    | 112   |
| Initial interface height (mm) | 0.12  | 0.14  | 0.17  | 0.11  |
| Carrier frequency             | 74.25 | 74.24 | 74.21 | 74.18 |
| Lower cutoff frequency        | 33    | 33    | 34    | 35    |
| Upper cutoff frequency        | 98    | 100   | 99    | 99    |
| Cuvette bottom (pix)          | 400   | 398   | 399   | 397   |
| Interface location (pix)      | 392   | 389   | 390   | 389   |
| Scale (pix/mm)                | 72.5  | 72.5  | 72.5  | 72.5  |
| Window (mm)                   | 2     | 2     | 2     | 2     |
| Temperature gradient (°C/cm)  | 9.77  | 9.87  | 9.87  | 9.97  |
| Bulk concentration (wt%)      | 72.0  | 72.0  | 72.0  | 72.0  |
| Tip concentration (wt%)       | 72.12 | 72.10 | 72.12 | 72.09 |

### RUNS 47, 48, 49, AND 50 AT 55 SECONDS

| Run                           | 47    | 48    | 49    | 50    |
|-------------------------------|-------|-------|-------|-------|
| Column (pix)                  | 160   | 80    | 68    | 112   |
| Initial interface height (mm) | 0.12  | 0.14  | 0.17  | 0.11  |
| Carrier frequency             | 74.25 | 74.24 | 74.21 | 74.18 |
| Lower cutoff frequency        | 32    | 31    | 30    | 34    |
| Upper cutoff frequency        | 101   | 100   | 99    | 100   |
| Cuvette bottom (pix)          | 400   | 398   | 399   | 397   |
| Interface location (pix)      | 392   | 389   | 388   | 390   |
| Scale (pix/mm)                | 72.5  | 72.5  | 72.5  | 72.5  |
| Window (mm)                   | 2     | 2     | 2     | 2     |
| Temperature gradient (°C/cm)  | 10.56 | 10.79 | 10.65 | 10.79 |
| Bulk concentration (wt%)      | 72.0  | 72.0  | 72.0  | 72.0  |
| Tip concentration (wt%)       | 72.22 | 72.20 | 72.20 | 72.17 |

## RUNS 47, 48, 49, AND 50 AT 75 SECONDS

| Run                           | 47    | 48    | 49    | 50    |
|-------------------------------|-------|-------|-------|-------|
| Column (pix)                  | 160   | 80    | 68    | 112   |
| Initial interface height (mm) | 0.12  | 0.14  | 0.17  | 0.11  |
| Carrier frequency             | 74.25 | 74.24 | 74.21 | 74.18 |
| Lower cutoff frequency        | 32    | 26    | 27    | 32    |
| Upper cutoff frequency        | 101   | 98    | 100   | 102   |
| Cuvette bottom (pix)          | 400   | 398   | 399   | 397   |
| Interface location (pix)      | 392   | 390   | 390   | 390   |
| Scale (pix/mm)                | 72.5  | 72.5  | 72.5  | 72.5  |
| Window (mm)                   | 2     | 2     | 2     | 2     |
| Temperature gradient (°C/cm)  | 10.99 | 11.34 | 10.99 | 11.29 |
| Bulk concentration (wt%)      | 72.0  | 72.0  | 72.0  | 72.0  |
| Tip concentration (wt%)       | 72.24 | 72.27 | 72.26 | 72.24 |

## COLUMN COMPARISONS, RUN 47 AT 30 SECONDS

|                               |       |       |       |       |       |
|-------------------------------|-------|-------|-------|-------|-------|
| Column (pix)                  | 66    | 67    | 68    | 69    | 70    |
| Initial interface height (mm) | 0.17  | 0.17  | 0.17  | 0.17  | 0.17  |
| Carrier frequency             | 74.21 | 74.21 | 74.21 | 74.22 | 74.21 |
| Lower cutoff frequency        | 34    | 34    | 34    | 34    | 34    |
| Upper cutoff frequency        | 99    | 99    | 99    | 99    | 99    |
| Cuvette bottom (pix)          | 399   | 399   | 399   | 399   | 399   |
| Interface location (pix)      | 390   | 390   | 390   | 390   | 390   |
| Scale (pix/mm)                | 72.5  | 72.5  | 72.5  | 72.5  | 72.5  |
| Window (mm)                   | 2     | 2     | 2     | 2     | 2     |
| Temperature gradient (°C/cm)  | 9.77  | 9.77  | 9.87  | 9.87  | 9.77  |
| Bulk concentration (wt%)      | 72.0  | 72.0  | 72.0  | 72.0  | 72.0  |
| Tip concentration (wt%)       | 72.12 | 72.12 | 72.12 | 72.13 | 72.12 |

## COMPARISON OF BASE PHASE SUBTRACTION, RUN 48

|                               |       |       |       |       |       |       |
|-------------------------------|-------|-------|-------|-------|-------|-------|
| Time (seconds)                | 30    | 30    | 55    | 55    | 75    | 75    |
| Base phase subtracted?        | Yes   | No    | Yes   | No    | Yes   | No    |
| Column (pix)                  | 80    | 80    | 80    | 80    | 80    | 80    |
| Initial interface height (mm) | 0.14  | 0.14  | 0.14  | 0.14  | 0.14  | 0.14  |
| Carrier frequency             | 74.24 | 74.24 | 74.24 | 74.24 | 74.24 | 74.24 |
| Lower cutoff frequency        | 33    | 33    | 31    | 31    | 26    | 26    |
| Upper cutoff frequency        | 100   | 100   | 100   | 100   | 98    | 98    |
| Cuvette bottom (pix)          | 398   | 398   | 398   | 398   | 398   | 398   |
| Interface location (pix)      | 389   | 389   | 389   | 389   | 390   | 390   |
| Scale (pix/mm)                | 72.5  | 72.5  | 72.5  | 72.5  | 72.5  | 72.5  |
| Window (mm)                   | 2     | 2     | 2     | 2     | 2     | 2     |
| Temperature gradient (°C/cm)  | 9.87  | 9.22  | 10.79 | 10.05 | 11.34 | 10.59 |
| Bulk concentration (wt%)      | 72.0  | 72.0  | 72.0  | 72.0  | 72.0  | 72.0  |
| Tip concentration (wt%)       | 72.10 | 72.09 | 72.20 | 72.19 | 72.27 | 72.26 |

## RUNS 61, 62, 64, AND 65 AT 45 SECONDS

| Run                           | 61    | 62    | 64    | 65    |
|-------------------------------|-------|-------|-------|-------|
| Column (pix)                  | 155   | 155   | 155   | 155   |
| Initial interface height (mm) | 0.32  | 0.32  | 0.30  | 0.30  |
| Carrier frequency             | 74.24 | 74.24 | 74.24 | 74.24 |
| Lower cutoff frequency        | 30    | 24    | 32    | 30    |
| Upper cutoff frequency        | 101   | 100   | 99    | 102   |
| Cuvette bottom (pix)          | 401   | 401   | 401   | 401   |
| Interface location (pix)      | 379   | 379   | 379   | 381   |
| Scale (pix/mm)                | 72.5  | 72.5  | 72.5  | 72.5  |
| Window (mm)                   | 2     | 2     | 2     | 2     |
| Temperature gradient (°C/cm)  | 10.96 | 11.15 | 10.65 | 10.95 |
| Bulk concentration (wt%)      | 72.0  | 72.0  | 72.0  | 72.0  |
| Tip concentration (wt%)       | 72.17 | 72.18 | 72.16 | 72.16 |



## RUNS 61, 62, 64, AND 65 AT 75 SECONDS

| Run                           | 61    | 62    | 64    | 65    |
|-------------------------------|-------|-------|-------|-------|
| Column (pix)                  | 155   | 155   | 155   | 155   |
| Initial interface height (mm) | 0.32  | 0.32  | 0.30  | 0.30  |
| Carrier frequency             | 74.24 | 74.24 | 74.24 | 74.24 |
| Lower cutoff frequency        | 31    | 26    | 30    | 28    |
| Upper cutoff frequency        | 102   | 101   | 100   | 101   |
| Cuvette bottom (pix)          | 401   | 401   | 401   | 401   |
| Interface location (pix)      | 379   | 379   | 379   | 381   |
| Scale (pix/mm)                | 72.5  | 72.5  | 72.5  | 72.5  |
| Window (mm)                   | 2     | 2     | 2     | 2     |
| Temperature gradient (°C/cm)  | 11.45 | 12.04 | 11.33 | 11.45 |
| Bulk concentration (wt%)      | 72.0  | 72.0  | 72.0  | 72.0  |
| Tip concentration (wt%)       | 72.24 | 72.26 | 72.22 | 72.26 |

## INTENSITY METHOD FOR INTERFEROMETRY

|                                  |         |         |
|----------------------------------|---------|---------|
| Time (sec)                       | 45      | 75      |
| Column (pix)                     | 255     | 255     |
| Initial interface height (mm)    | 0.33    | 0.33    |
| Distance from interface (mm) to: |         |         |
| Fringe 1                         | 0.03968 | 0.01323 |
| Fringe 2                         | 0.1587  | 0.07937 |
| Fringe 3                         | 0.6217  | 0.1587  |
| Fringe 4                         | 1.005   | 0.3439  |
| Fringe 5                         | 1.415   | 0.7672  |
| Fringe 6                         | 1.825   | 1.164   |
| Fringe 7                         | -----   | 1.548   |
| Fringe 8                         | -----   | 1.958   |
| Temperature gradient (°C/cm)     | 11.4    | 11.4    |
| Bulk concentration (wt%)         | 72.0    | 72.0    |
| Tip concentration (wt%)          | 72.16   | 72.26   |

## CARRIER IMAGE FOR HOLOGRAPHIC INTERFEROMETRY

|                        |       |
|------------------------|-------|
| Column (pix)           | 272   |
| Lower cutoff frequency | 57    |
| Upper cutoff frequency | 65    |
| Carrier frequency      | 61.05 |

## HOLOGRAPHIC INTERFEROMETRY AT 6 MINUTES 37 SECONDS

|                               |       |
|-------------------------------|-------|
| Column (pix)                  | 165   |
| Initial interface height (mm) | 0.37  |
| Carrier frequency             | 61.05 |
| Lower cutoff frequency        | 33    |
| Upper cutoff frequency        | 93    |
| Cuvette bottom (pix)          | 390   |
| Interface location (pix)      | 354   |
| Scale (pix/mm)                | 95.5  |
| Window (mm)                   | 2     |
| Temperature gradient (°C/cm)  | 16.25 |
| Bulk concentration (wt%)      | 71.5  |
| Tip concentration (wt%)       | 71.70 |

# INTENSITY METHOD FOR HOLOGRAPHIC INTERFEROMETRY

AT 6 MINUTES 37 SECONDS

|                                  |        |
|----------------------------------|--------|
| Column (pix)                     | 184    |
| Initial interface height (mm)    | 0.374  |
| Distance from interface (mm) to: |        |
| Fringe 1                         | 0.1885 |
| Fringe 2                         | 0.6911 |
| Fringe 3                         | 1.194  |
| Fringe 4                         | 1.550  |
| Fringe 5                         | 1.885  |
| Fringe 6                         | 2.220  |
| Fringe 7                         | 2.482  |
| Fringe 8                         | 2.796  |
| Fringe 9                         | 3.089  |
| Fringe 10                        | 3.361  |
| Temperature gradient (°C/cm)     | 16.25  |
| Bulk concentration (wt%)         | 71.5   |
| Tip concentration (wt%)          | 71.71  |

## VITA

Mary E. Magnani (Yesko) was born in 1966 in Toledo, Ohio. In 1974 she moved with her family to Bolingbrook, Illinois. She attended high school at St. Francis Academy in Joliet, Illinois, and was the valedictorian of the graduating class of 1984. A National Merit Scholar, Magnani studied electrical engineering, with a concentration in computer engineering, at Michigan State University. She completed the bachelor of science degree in 1989, graduating with honors.

From 1986 to 1989, Magnani was employed as a co-op engineer in the CAD/CAM/CAE Department of General Dynamics in Detroit. Her work there included computer systems support, software applications projects, and data translation.

In 1989 Magnani began studying engineering science and mechanics at the University of Tennessee Space Institute in Tullahoma. As a graduate research assistant, Magnani was involved with image processing, holographic reconstruction, and materials science experiments. She was a two-time winner of Zonta International's Amelia Earhart Fellowship. In 1991 she completed the master of science degree, graduating with high honors. Magnani is a member of Tau Beta Pi, Eta Kappa Nu, the Institute of Electrical and Electronics Engineers, and the American Institute of Aeronautics and Astronautics, and is an Engineer in Training.

Magnani and her husband Steven married in 1991. She plans to pursue a career in image processing or computer systems development.